# APPLIED COMPUTATIONAL ELECTROMAGNETICS SOCIETY JOURNAL

September 2024
Vol. 39 No. 9
ISSN 1054-4887

**The ACES Journal is abstracted in INSPEC, in Engineering Index, DTIC, Science Citation Index Expanded, the Research Alert, and to Current Contents/Engineering, Computing & Technology.**

The illustrations on the front cover have been obtained from the ARC research group at the Department of Electrical Engineering, Colorado School of Mines

Published, sold and distributed by: River Publishers, Alsbjergvej 10, 9260 Gistrup, Denmark

## SEPTEMBER 2024 REVIEWERS

**Intan Sorfina Zainal Abidin**
**Ankan Bhattacharya**
**Vinh Dang**
**Zaheer Ahmed Dayo**
**Piotr Gas**
**Feyzullah Gulpinar**
**Hector Gutierrez**
**Ahmed Jamal**
**Lida Kouhalvandi**
**Vinoth M**
**Adi Mahmud Jaya Marindra**
**Enrique Melgoza**
**Shahid Modasiya**
**Mirjana Peric**
**Antonella Ragusa**
**Sujith Raman**
**Marek Sawerwain**
**Fusun Oyman Serteller**
**Manthan Shah**
**Cui Zhen Sun**
**Marsellas Waller**
**Haoyan Xue**
**Tao Yuan**
**Xuemei Zheng**

THE APPLIED COMPUTATIONAL ELECTROMAGNETICS SOCIETY JOURNAL

Vol. 39 No. 9 September 2024

## TABLE OF CONTENTS

# A Novel Multi-objective Synthesis Method of Non-uniform Excitation Sparse Square Planar Transmitting Array Antenna for Microwave Wireless Power Transmission

**Jianxiong Li[1], Ranran Zhang[1], and Ziyu Han[2]**

[1]School of Electronic and Information Engineering
Tiangong University, Tianjin 300387, China
lijianxiong@tiangong.edu.cn, zhangranran202203@163.com

[2]School of Electronic Science and Engineering
National University of Defense Technology, Changsha 410000, China
hanziyu23h_@nudt.edu.cn

***Abstract*** **–** A novel multi-objective optimal subarray partitioning synthesis method for non-uniformly excited sparse square planar array (NESSPA) antenna is proposed for the problems of maximizing beam collection efficiency (BCE) and minimizing excitation difference (*diff*) in microwave wireless power transmission (MWPT). The algorithm adopts the multi-objective particle swarm optimization algorithm based on the set of non-dominated solutions (NDSMOPSO) proposed in this paper, which determines the non-dominated solutions in the swarm according to the fitness value and updates the population during the evolution process; the array element positions and excitations are optimized simultaneously in each iteration. In addition, the performance parameter *diff* proposed in this paper can effectively measure the performance of the array; in general, the smaller the *diff*, the better the array performance. The effectiveness of the algorithm is demonstrated through a large number of simulations and, according to the method proposed in this paper compared with other two-step methods, a higher BCE can be obtained with fewer subarrays.

***Index Terms*** **–** Beam collection efficiency (BCE), microwave wireless power transmission (MWPT), multi-objective particle swarm optimization algorithm based on the set of non-dominated solutions (NDSMOPSO), subarray partitioning.

## I. INTRODUCTION

Microwave radio energy transmission is a technology that utilizes microwave devices to convert electrical energy into electromagnetic energy, wirelessly transmits microwave electromagnetic energy in space through a transmitting antenna, and converts the electromagnetic energy into electrical energy, which is rectified, filtered, and other transformations, and then supplied to the electrical load [1]. This is an extensively studied technology for long-distance energy transmission [2], and is widely used in various fields such as space solar power stations [3], large phased arrays [4], space transmission [5], and unmanned aerial vehicles [6–7].The microwave radio energy transmission system has two important components: the transmitting antenna and the rectifying antenna. The transmitting antenna is designed to form an enhanced microwave beam towards a given area while minimizing the radiated power outside the collection area. Improving the beam collection efficiency (BCE) in microwave wireless power transmission (MWPT) systems has been a hot research topic in recent years [8–11]. In order to maximize the BCE to improve the performance of MWPT systems [12–14] transformed the solution formula of BCE into a generalized eigenvalue equation, through which the theoretical maximum BCE and the optimal excitation are calculated. However, the emergence of quasi-Gaussian characteristics of the optimal excitation indicates that each element needs to be equipped with a separate amplifier and phase shifter, and thus the system becomes large, complex, and expensive. In order to reduce the cost, scholars began to study sparse arrays [15–17]. Sparse arrays can reduce the cost to some extent, but designing amplifiers for each array element is still complicated due to the use of non-uniform excitation. Although the cost can be greatly reduced by using uniform excitation, the BCE is reduced too much. In order to maintain a high BCE and further reduce the cost, scholars have started to apply subarray division techniques to sparse arrays [16–22]. Scholars usually divide the process of subarray division into two steps. The first step is to optimize the positions of the elements, and the second step is to optimize the excitations of the elements

*Submitted On: September 19, 2024*
*Accepted On: November 11, 2024*



https://doi.org/10.13052/2024.ACES.J.390901

[19], or to perform the subarray division first and then optimize the positions of the elements [16]. The results obtained from these two-step approaches are usually not optimal. When the second step is completed, perhaps the suboptimal becomes the best. In addition, research on multi-objective optimization mainly focuses on beam direction map synthesis of antenna arrays [23–24]. BCE is closely related to several key indexes in beam direction map synthesis, such as sidelobe level outside the receiving area, the main flap beamwidth, and the directionality.

Aiming at the above problems, this paper proposes an optimization algorithm that combines population updating during the evolution with a multi-objective one-step method. The main innovations of this paper are as follows. The first point is that by using the multi-objective particle swarm optimization algorithm based on non-dominated solutions (NDSMOPSO) introduced in this paper, the proposed method is a one-step optimization algorithm that optimizes both the position of the array element and the excitation in the process of population updating with evolution, and the two indexes of maximizing the BCE and minimizing the excitation difference (*diff*) are selected as the optimization objectives. This one-step algorithm combined with the population update is more effective than two-step algorithms. The second point is that the non-uniformly excited sparse square planar array (NESSPA) model has high optimization degrees of freedom and has the potential to give better results. The last point is that the performance parameter *diff* is proposed in this paper to measure the performance of subarray division. The effectiveness of the method can be demonstrated by several numerical simulations.

The framework of this paper is as follows. Section II describes the derivation of formulas for subarray division. Section III describes the procedure of the NDSMOPSO method and its application to NESSPA synthesis. Section IV reports the numerical simulation results. Section V offers some conclusions.

## II. NESSPA MODEL AND THE FORMULA DERIVATION FOR SUBARRAY PARTITION

The geometric model of the NESSPA MWPT system is shown in Fig. 1. Assume that the aperture of the transmitting array is $L_x \times L_y$, and the total number of array elements is $N = N_x \times N_y$. The array elements are distributed in the XOY plane and the coordinate of the $n$th array element is $(x_n, y_n)$,$1 \le n \le N$. The position coordinates of some elements are listed in Fig. 1. We use $\Psi_r$ and $\Psi_c$ to denote the square receiving area and the circular receiving area, respectively.

The array factor of NESSPA could be written as [14]:

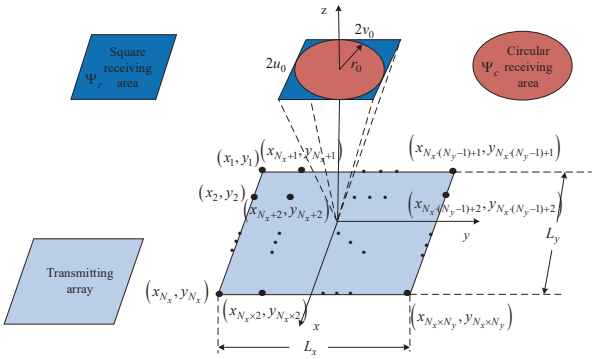


Fig. 1. Geometric model of the NESSPA MWPT system.

$$F(u,v) = \sum_{n=1}^{N} I_n e^{ik(ux_n + vy_n)}, \tag{1}$$

where $k = 2\pi/\lambda$, $\lambda$, and $I_n$ denote the wavenumber, wavelength, and excitation, respectively. $u = \sin\theta\cos\varphi$ and $v = \sin\theta\sin\varphi$ denote the angular coordinates. *BCE* is defined as the proportion of the power collected by the receiving array to the total power generated from the transmitting array, which could be expressed as:

$$BCE \triangleq \frac{P_{\Psi_{r/c}}}{P_{\Omega}} = \frac{\int_{\Psi} |F(u,v)|^2 \, dudv}{\int_{\Omega} |F(u,v)|^2 \, dudv}, \tag{2}$$

where $P_{\Psi_{r/c}/\Omega} = \int_{\Psi_{r/c}/\Omega} |F(u,v)|^2 \, dudv$ represents the power radiating through the area $\Psi_{r/c}/\Omega$.$\Psi_r \triangleq \{(u,v) : -u_0 \le u \le u_0, -v_0 \le v \le v_0\}$, $\Psi_c \triangleq \{(\theta,\varphi) : \theta \le \arcsin(r_0), 0 \le \varphi \le 2\pi\}$, and $\Omega \triangleq \{(u,v) : u^2 + v^2 \le 1\}$. $\Psi_{r/c}$ and $\Omega$ are regions of angular coordinates that identify the radiating area and entire visible range. *BCE* can be rewritten as [14]:

$$BCE = \frac{\mathbf{I}^{\mathrm{H}} A \mathbf{I}}{\mathbf{I}^{\mathrm{H}} B \mathbf{I}}, \tag{3}$$

where $\mathbf{I}$, $A$ and $B$ can be expressed as:

$$\begin{cases} \mathbf{I} = [i_1, i_2, \cdots, i_n, \cdots, i_N]^H; 1 \le n \le N \\ A \triangleq \int_{\Psi} \mathbf{v}(u,v)\, \mathbf{v}(u,v)^H \, dudv \\ B \triangleq \int_{\Omega} \mathbf{v}(u,v)\, \mathbf{v}(u,v)^H \, dudv \end{cases}, \tag{4}$$

where:

$$\mathbf{v}(u,v) = \left[ e^{-jk(ux_1 + vy_1)}, \cdots, e^{-jk(ux_N + vy_N)} \right]^H. \tag{5}$$

Sidelobe level outside (*CSL*) is defined as the highest normalized sidelobe level outside the receiving area $\Psi$ [14], which could be expressed as:

$$CSL(dB) = 10\lg \frac{\max_{\theta,\varphi \notin \Psi} |F(\theta,\varphi)|^2}{\max_{\theta,\varphi \in \Omega} |F(\theta,\varphi)|^2}. \tag{6}$$

Suppose $N$ elements are divided into $M$ subarrays. **SR** denotes the subarray layout matrix, which is a $N \times M$ matrix as follows:

$$\mathbf{SR}=\begin{pmatrix} SR_{11} & SR_{12} & \cdots & SR_{1M} \\ SR_{21} & SR_{22} & \cdots & SR_{2M} \\ \vdots & \vdots & \ddots & \vdots \\ SR_{N1} & SR_{N2} & \cdots & SR_{NM} \end{pmatrix}.$$

$$SR_{nm}=\begin{cases} 1 & The\ nth\ element\ \in\ the\ mth\ subarray \\ 0 & The\ nth\ element\ \notin\ the\ mth\ subarray \end{cases} \tag{7}$$

$n=1,2,\cdots,N;\ m=1,2,\cdots,M$

To satisfy the condition that each array element belongs to only one subarray, the following expression is required:

$$\sum_{m=1}^{M} SR_{nm}=1,(n=1,2,\cdots,N). \tag{8}$$

Assume $\mathbf{I\_sub}=[i\_sub_1,i\_sub_2,\cdots,i\_sub_M]$ denotes the subarray excitation vector. $\mathbf{I^b}=[i_1^b,i_2^b,\cdots,i_{M+1}^b]$ represents the boundary of $M$ subarrays. Thus, the calculation method can be expressed as:

$${i_m}^b=i_{\min}+\frac{i_{\max}-i_{\min}}{M}\times(m-1),(m=1,2,\cdots,M+1), \tag{9}$$

where $i_{\max}$ and $i_{\min}$ represent the minimum and the maximum of $\mathbf{I}$, respectively. Then, $\mathbf{SR}$ can be obtained in the following way:

$$\begin{cases} if\ {i_m}^b\le i_n<{i_{m+1}}^b,\ SR_{nm}=1 \\ elseif\ i_n=i_{\max},\ SR_{nM}=1 \\ else\quad SR_{nm}=0\quad (n=1,2,\cdots,N,m=1,2,\cdots,M) \end{cases}. \tag{10}$$

The excitation of each subarray can be calculated as:

$$i\_sub_m=\frac{\sum_{n=1}^{N} SR_{nm}\cdot i_n}{\sum_{n=1}^{N} SR_{nm}}\quad (m=1,2,\cdots,M). \tag{11}$$

The excitation vector after partitioning the subarray named as $\mathbf{I\_sub\_all}$ can be obtained by:

$$\mathbf{I\_sub\_all}=\mathbf{SR}\cdot\mathbf{I\_sub}. \tag{12}$$

The diff between $\mathbf{I\_sub\_all}$ and $\mathbf{I}$ can be defined as (13), which can be used as a performance indicator:

$$diff=\sum_{n=1}^{N}|\mathbf{I\_sub\_all}(n)-\mathbf{I}(n)|. \tag{13}$$

## III. THE NDSMOPSO METHOD AND ITS APPLICATION FOR SYNTHESIS OF NESSPA

In this section, we will introduce the NESSPA model and the one-step method. By using the one-step method the mathematical model of NESSPA could be expressed as:

$$\begin{cases} find\ [\mathrm{X},\mathrm{I\_sub}]=[x_1,\cdots,x_N,y_1,\cdots,y_N,i\_sub_1,\cdots,i\_sub_M]^T \\ maximize\ BCE_{\max} \\ minimize\ \ diff_{\min} \\ subject\ (a)-L_x/2\le x_n\le L_x/2,n=\{1,2,\cdots,N\}; \\ \qquad (b)-L_y/2\le x_n\le L_y/2,n=\{1,2,\cdots,N\}; \\ \qquad (c)\sqrt{(x_i-x_j)^2+(y_i-y_j)^2}\ge d_{\min}, \\ \qquad\quad i,j\in\{1,2,\cdots,N\},i\ne j; \\ \qquad (d)\,(x_1,y_1)=(-L_x/2,L_y/2); \\ \qquad (e)\,(x_1,y_{end})=(L_x/2,L_y/2); \\ \qquad (f)\,(x_{end},y_1)=(-L_x/2,-L_y/2); \\ \qquad (g)\,(x_{end},y_{end})=(L_x/2,-L_y/2); \\ \qquad (h)\,{i_1}^b<{i_2}^b<\cdots<{i_{M+1}}^b; \end{cases} \tag{14}$$

where $\mathbf{X}=[x_1,x_2,...,x_N,y_1,y_2,...,y_N]$ represents the vectors of horizontal and vertical coordinates of the elements. The optimization goals are maximizing *BCE* and minimizing $diff$. The optimization variables are $\mathbf{X}$ and $\mathbf{I\_sub}$. To achieve an array aperture of $L_x\times L_y$, we restrict the positions of the elements on the four corners (subject: (d), (e), (f), (g)). The distance between any two elements is more than $d_{\min}$(subject: (c)). Normally when $d_{\min}\ge 0.5\lambda$, the mutual coupling between array elements is negligible, and this article does not consider the mutual coupling problem.

Below is a step-by-step procedure description of the one-step method that uses NDSMOPSO. The meanings of some parameters involved are shown in Table 1.

Table 1: Definition of the parameters

| Parameter | Definition |
|---|---|
| $NP$ | number of particles in the population |
| $T$ | maximum number of iterations |
| $t$ | current number of iterations; the variable with subscript $t$ denotes the value of the $t$th iteration |
| $c_1,c_2$ | learning factors |
| $w$ | weight coefficient |
| $v_t$ | updated velocity of the $t$th iteration |
| $d_{\min}$ | minimum array element spacing |

In addition, $gbest\_BCE$ and $gbest\_diff$ are the global optima of *BCE and diff,* respectively, $gbest\_BCE\_x_{t-1}$ and $gbest\_diff\_x_{t-1}$ are the global optimal positions of *BCE* and *diff*, respectively.

**Step 1:** Initializing parameters ($N$, $M$, $t$=0, $T$, $NP$, $\mathbf{X}$, etc.).

**Step 2:** Calculate the fitness value (*BCE* and *diff*) for each particle, perform the stratification of the non-dominated ordering, and identify the particles with non-dominated solutions. Select $gbest\_BCE$ and $gbest\_diff$.

**Step 3:** Update the coordinates$x \in$ X by (15)-(17).

$$w = w_{\max} - (w_{\max} - w_{\min}) \cdot \left(1 - \frac{t}{T}\right), \quad (15)$$

$$\begin{aligned} v_t =& w \times v_{t-1} + c_1 \times rand \\ & \times (pbest\_x_{t-1} - x_{t-1}) + c_2 \times rand \\ & \times (gbest\_BCE\_x_{t-1} + gbest\_diff\_x_{t-1} - 2x_{t-1}) \end{aligned}, \quad (16)$$

$$x_t = x_{t-1} + v_t. \quad (17)$$

**Step 4:** Calculate *BCE* and *diff*. For each particle the *pbest* is updated only if the new solution dominates the current *pbest*.

**Step 5:** Add particles with non-dominated solutions ($l$) to the *NP*. Perform non-dominated sorted stratification to identify particles with non-dominated solutions. Perform sorted stratification of the population ($NP+l$) removing the last $l$ particles. Update *gbest_BCE* and *gbest_diff*.

**Step 6:** If $t = T$, then output the optimal *BCE*, array element positions, subarray incentives, etc., otherwise, return to Step 4.

After the above steps, the minimum *diff* and the maximum *BCE* can be obtained. The innovation of this article is that the proposed integrated optimization method is a combination of population with evolution update and one-step method. What's more, we improved the weight and step size and used multiple learning factors to achieve multi-objective optimization.

## IV. NUMERICAL ANALYSIS

In this part, the validity of the presented algorithm in handling different receiving areas (square and circle) would be tested from two aspects. Firstly, we use the presented algorithm to optimize the NESSPA model under different sparsity of *M* and *N*. Secondly, to prove the behavior of the algorithm and the model introduced in this article, we use some performance parameters to compare the NESSPA model with another four planar array models. The simulation software used in all simulations is MATLAB R2022b.

We use four performance indicators to evaluate the comparison of comprehensive results. They are *BCE*, *CSL*, $\gamma_a$, and $\gamma_e$. $\gamma_a = M/N$ and $\gamma_e = N/N_f$ represent amplifier sparsity and element sparsity, respectively, where $N_f$ denotes the maximum number of array elements that can be accommodated by the array under the condition of $d_{\min} = 0.5\lambda$. In our simulations, $T$ is set to 100 and *NP* is set to 100. $u_0$, $v_0$, and $r_0$ are set to 0.2. $c_1$ and $c_2$ are set to 2. $w_{\max}$ and $w_{\min}$ are set to 0.9 and 0.4, respectively. $\lambda$ is set to 1. $L_x \times L_y$ is set to $5.5\lambda \times 5.5\lambda$.

### A. Synthesis results of the NESSPA model by using NDSMOPSO under different $\gamma_a$ and $\gamma_e$

The first set of simulation in this section involves synthesis of NESSPA with $N = 10 \times 10$ elements. $d_{\min}$ is set to $0.6\lambda$. We performed tests on the influence of different *M* on the behavior of the array. The synthesis findings are displayed in Fig. 2 and Table 2 ($BCE_r$, $CSL_r$ represent the value under the rectangular receiving area, and $BCE_c$, $CSL_c$ represent the value under the circular receiving

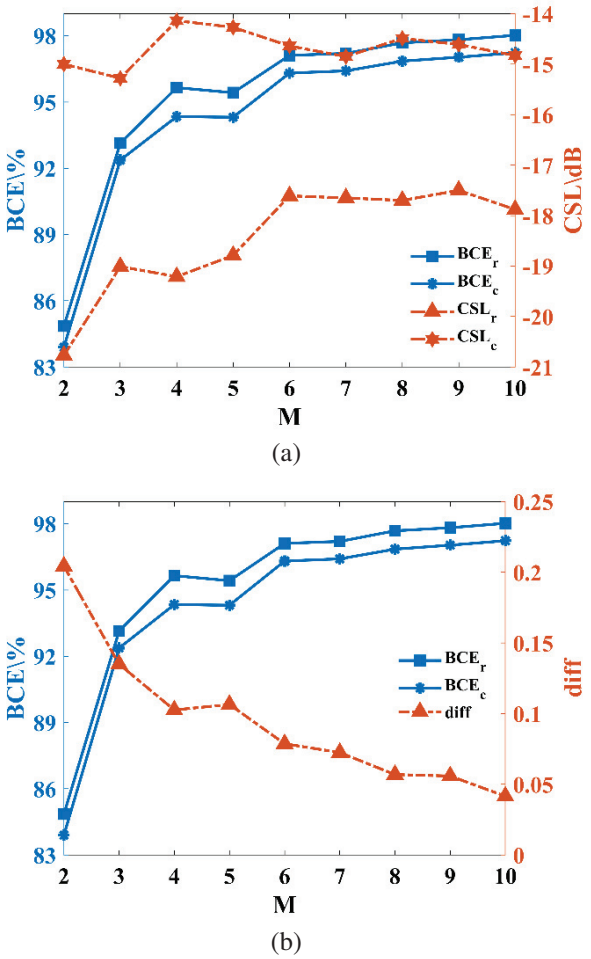


Fig. 2. Results of NESSPA under different *M* at $N = 10 \times 10$: (a) *BCE* and *CSL* and (b) *BCE* and *diff*.

Table 2: Numerical results of NESSPA under different *BCE* (%) and *CSL* (dB)

| *M* | $BCE_r$ | $BCE_c$ | $CSL_r$ | $CSL_c$ | *diff* |
|---|---|---|---|---|---|
| **2** | 84.85 | 83.90 | -20.77 | -15.00 | 0.2044 |
| **3** | 93.14 | 92.37 | -19.01 | -15.28 | 0.1350 |
| **4** | 95.65 | 94.34 | -19.20 | -14.14 | 0.1026 |
| **5** | 95.42 | 94.31 | -18.79 | -14.27 | 0.1065 |
| **6** | 97.11 | 96.31 | -17.61 | -14.64 | 0.0787 |
| **7** | 97.20 | 96.41 | -17.65 | -14.85 | 0.0725 |
| **8** | 97.68 | 96.85 | -17.70 | -14.49 | 0.0569 |
| **9** | 97.82 | 97.03 | -17.50 | -14.61 | 0.0559 |
| **10** | 98.02 | 97.23 | -17.88 | -14.83 | 0.0416 |

area). At $M = 3$, the *BCE* values in the rectangular and circular regions increase significantly, by about 8.3% and 8.5%, respectively ( $BCE_r = 93.14\%, BCE_c = 92.37\%$). The *CSL* in the circular receiving region reaches a minimum ($CSL_c = -15.28dB$). At $M = 4$, the BCE values in the rectangular and circular regions increase by about 2.5% and 2%, respectively ($BCE_r = 95.65\%, BCE_c = 94.34\%$). At $M = 6$, the *BCE* increases again by a small amount ($BCE_r = 97.11\%, BCE_c = 96.31\%$), and thereafter the rise of the BCE tends to stabilize, the change in the *CSL* also leveled off, and the decline in *diff* began to slow. Considering the *BCE* value, *CSL*, performance, and cost together, $M = 6$ is the most suitable when the number of array elements is $10 \times 10$. The analysis of Fig. 2 (b) and Table 2 shows that the smaller the value of *diff*, the better the performance of the array.

The second set of simulation in this section involves synthesis of NESSPA with different $N \in \{8 \times 8, 9 \times 9, 10 \times 10, 11 \times 11\}$, and the corresponding optimal $M$. The synthesis results are displayed in Fig. 3 and Table 3. From Table 3, it can be seen that when $N \in \{8 \times 8, 9 \times 9, 10 \times 10, 11 \times 11\}$, both $BCE_r$ can reach more than 91% and the effectiveness of the NDSMOPSO algorithm can thus be demonstrated. When $N = 9 \times 9$, dividing five subarrays, and when $N = 10 \times 10$, dividing six subarrays are most suitable for the actual fabrication of the MWPT system.

If we take $N = 9 \times 9\,(M = 5, d_{\min} = 0.65\lambda)$ as an example, Fig. 4 shows the power pattern and layout of

Table 3: Numerical results of NESSPA under different $N$

| $N$ | $8\times8$ | $9\times9$ | $10\times10$ | $11\times11$ |
|---|---|---|---|---|
| $M$ | 4 | 5 | 6 | 8 |
| $BCE_r\,(\%)$ | 91.41 | 96.07 | 97.11 | 97.42 |
| $BCE_c\,(\%)$ | 88.83 | 94.68 | 96.31% | 96.73% |
| $CSL_r\,(dB)$ | -16.65 | -17.60 | -17.61 | -17.62 |
| $CSL_c\,(dB)$ | -13.48 | -13.68 | -14.64 | -15.07 |
| *diff* | 0.1504 | 0.1108 | 0.0787 | 0.0519 |

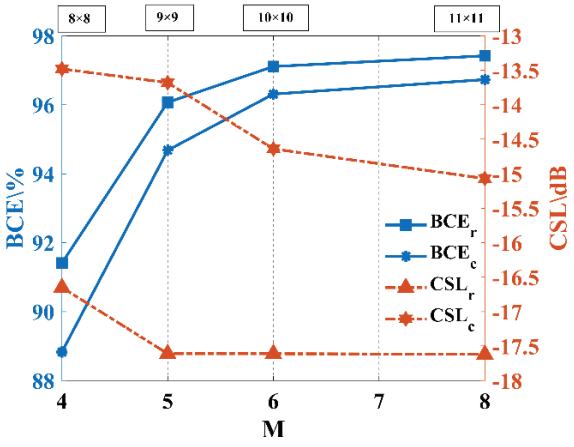


(a)

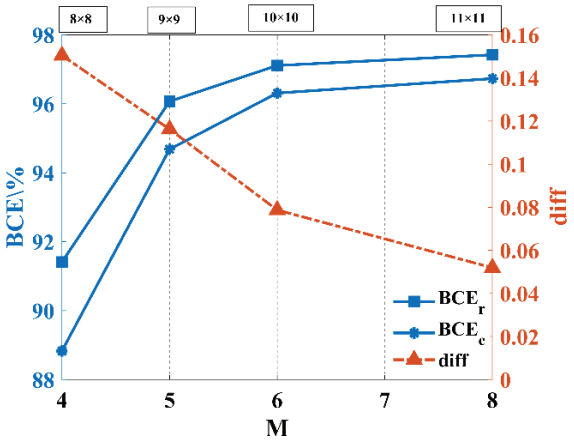


(b)

Fig. 3. Results of NESSPA under different $N$: (a) *BCE* and *CSL* and (b) *BCE* and *diff*.

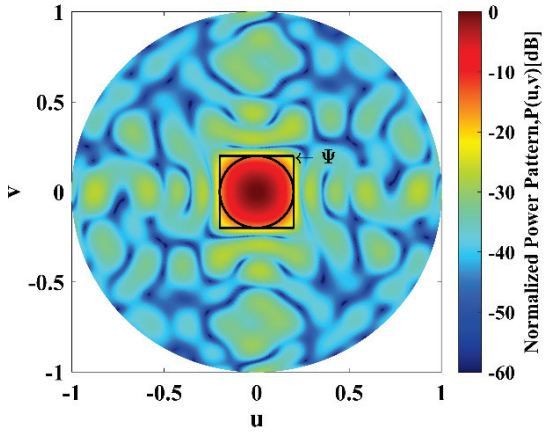


(a)

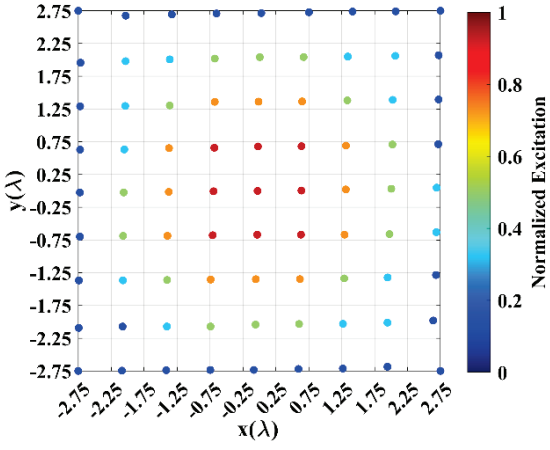


(b)

Fig. 4. Simulation results of NESSPA ($N = 9 \times 9$, $M$=5, *BCE*=96.07%, *CSL*=-17.60dB): (a) layout and excitation and (b) normalized power pattern.

the five subarrays. In Fig. 4 (a), most of the radiated energy is concentrated in the receiving region. Therefore, the method can obtain a better array performance. Figure 5 shows the distribution of array element positions before and after optimization by NDSMOPSO algorithm. NDSMOPSO algorithm determines the non-dominated solution based on the fitness value and updates the population during iteration. Each iteration optimizes the array element positions and excitations at the same time, and the performance of the array is improved after optimization.

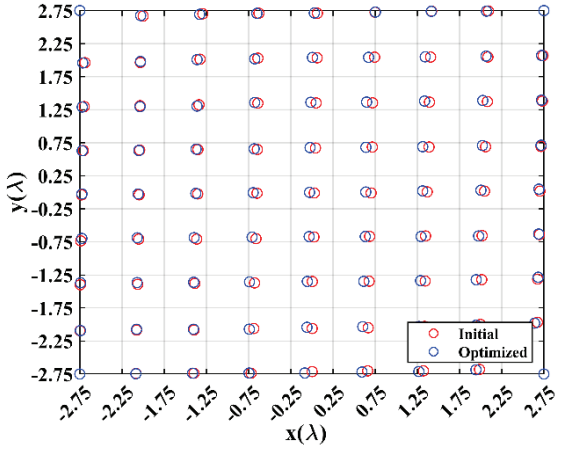


Fig. 5. Distribution of transmitting array element positions before and after algorithm optimization.

The multi-objective fitness curve is shown in Fig. 6. Through Fig. 6, the optimal *BCE* converges at about 20 generations, the optimal *diff* converges at about 25 generations. They all reach convergence within 40 generations, which demonstrates the fast convergence of the method. The good multi-objective optimization performance of the method is also verified.

### B. Comparison of NESSPA with other planar array models in synthesis performance

To gain further validation of the method, we used several comprehensive performance indicators to compare NESSPA with three array optimization models in [8, 13, 17, 22] as shown in Table 4.

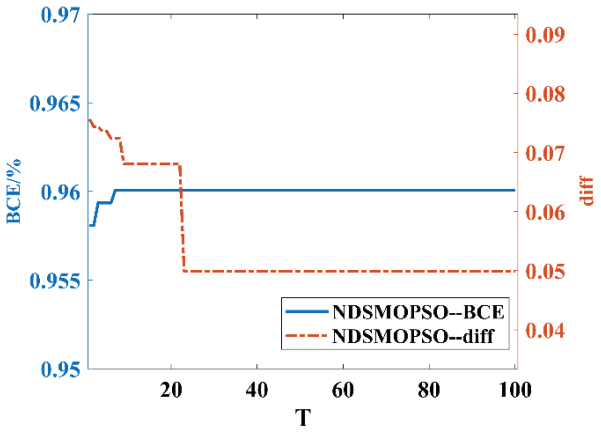


Fig. 6. Comprehensive results of two performance indicators with the number of iterations when $M = 5$.

From Table 4, it can be seen that the uniformly excited unequally spaced planar array synthesis method based on the chaotic particle swarm optimization (CPSO) algorithm proposed in [8] requires only one power amplifier due to the use of uniform excitation, which can significantly reduce the cost, but has a relatively low *BCE* (*BCE*=96.07% > *BCE*=91.06%). A non-uniformly excited planar array model was used in [13] (*BCE*=96.45% > *BCE*=96.07%) but an amplifier needs to be designed for each array element, which leads to an increase in cost. In contrast, the *BCE*=96.07% obtained in this paper is only reduced by 0.38% and the *CSL* is suppressed by 5.33 dB based on the use of fewer array elements and subarrays. Comparing with [22], the synthesized model proposed in this paper can obtain a higher *BCE* with fewer array elements. Compared with [17], the NDSMOPSO proposed in this paper can simultaneously optimize the array element position and excitation during population updating with evolution. With the same number of array elements, a larger *BCE* is obtained by using fewer amplifiers, which can better achieve high efficiency and low cost.

## V. CONCLUSION

In this paper, we propose a one-step optimization method for planar transmitter arrays in MWPT systems

Table 4: Performance comparison of different array modes

| | NESSPA | Ref. [13] | Ref. [22] | Ref. [17] | Ref. [8] |
|---|---|---|---|---|---|
| $N$ | 81 | 100 | 316 | 81 | 100 |
| $M$ | 5 | 100 | 4 | 14 | 1 |
| $\gamma_e$ | 56% | 100% | 79% | 81% | 100% |
| $\gamma_a$ | 6.2% | 100% | 1.2% | 17.28% | 1%5 |
| *BCE* | 96.07% | 96.45% | 92.82% | 95.27% | 91.06% |
| *CSL* (*dB*) | -17.60 | -12.27 | -20.62 | -18.04 | -16.01 |

based on NDSMOPSO. We improved the DWPSO algorithm [25] by adding a multi-objective learning factor while the population is updated with the evolutionary process, and established a one-step optimization mechanism so that the algorithm can optimize the element positions and excitations at the same time in each iteration. By comparing with other two-step subarray delineation methods, the method can achieve higher *BCE* with fewer elements. It is proved that the method can simplify the feeder network and reduce cost.

## REFERENCES


[1] X. Zhu, K. Jin, Q. Hui, W. Gong, and D. Mao, "Long-range wireless microwave power transmission: A review of recent progress," *IEEE Journal of Emerging and Selected Topics in Power Electronics*, vol. 9, no. 4, pp. 4932-4946, Aug. 2021.

[2] P. Lu, K. Huang, Y. Yang, B. Zhang, F. Cheng, and C. Song, "Space matching for highly efficient microwave wireless power transmission systems: Theory, prototype, and experiments," *IEEE Transactions on Microwave Theory and Techniques*, vol. 69, no. 3, pp. 1985-1998, Mar. 2021.

[3] X. Li, B. Duan, L. Song, Y. Zhang, and W. Xu, "Study of stepped amplitude distribution taper for microwave power transmission for SSPS," *IEEE Transactions on Antennas and Propagation*, vol. 65, no. 10, pp. 5396-5405, Oct. 2017.

[4] A. Massa, G. Oliveri, F. Viani, and P. Rocca, "Array designs for long-distance wireless power transmission: State-of-the-art and innovative solutions," *Proceedings of the IEEE*, vol. 101, no. 6, pp. 1464-1481, June 2013.

[5] C. Peng, Z. H. Ye, Y. H. Xia, and C. Yang, "Analysis on space transmission model of the microwave wireless power transfer system," *Frequenz*, vol. 75, no. 11-12, pp. 449-458, 2021.

[6] Y. Song, Y. Liu, W. Xu, X. Yang, and R. Wang, "Research on the multiobjective optimization of microwave wireless power receiving in an unmanned aerial vehicle network," *Complexity*, vol. 2020, no. 1, p. 8882528, 2020.

[7] S.-H. Ahn, Y.-S. Choi, M. Elhefnawy, and W.-S. Lee, "Multi-polarized reconfigurable antenna with ground plane slot and capacitance feeding for UAV-to-everything communications," *Applied Computational Electromagnetics Society (ACES) Journal*, vol. 38, no. 12, pp. 998-1004, Dec. 2023.

[8] X. Li, B. Duan, J. Zhou, L. Song, and Y. Zhang, "Planar array synthesis for optimal microwave power transmission with multiple constraints," *IEEE Antennas and Wireless Propagation Letters*, vol. 16, pp. 70-73, 2017.

[9] F. Yang, S. Yang, Y. Chen, S. Qu, and J. Hu, "An irregular tiled array technique for microwave wireless power transmission," *IEEE Transactions on Vehicular Technology*, vol. 72, no. 4, pp. 5257-5273, Apr. 2023.

[10] Q. H. Zhang, Q. H. Zhang, and Z. Y. Shen, "Planar array subarray division method in microwave wireless power transmission based on PSO&K-means algorithm," *IEEE Open Journal of Antennas and Propagation*, vol. 4, pp. 520-527, 2023.

[11] K. Vodvarka, M. Jurisic Bellotti, and M. Vucic, "Design of uniformly excited unequally spaced antenna arrays by using nonlinear optimization," *IEEE Antennas and Wireless Propagation Letters*, vol. 23, no. 5, pp. 1463-1467, May 2024.

[12] S. Prasad, "On the index for array optimization and the discrete prolate spheroidal functions," *IEEE Transactions on Antennas and Propagation*, vol. 30, no. 5, pp. 1021-1023, Sep. 1982.

[13] G. Oliveri, L. Poli, and A. Massa, "Maximum efficiency beam synthesis of radiating planar arrays for wireless power transmission," *IEEE Transactions on Antennas and Propagation*, vol. 61, no. 5, pp. 2490-2499, May 2013.

[14] S. Kojima, T. Mitani, and N. Shinohara, "Array optimization for maximum beam collection efficiency to an arbitrary receiving plane in the near field," *IEEE Open Journal of Antennas and Propagation*, vol. 2, pp. 95-103, 2021.

[15] J. Li and Z. Han, "Synthesis of sparse square arrays with high beam collection efficiency under minimum element spacing constraints," *Microwave and Optical Technology Letters*, vol. 65, no. 1, pp. 240-246, 2023.

[16] J. Li, J. Pan, and X. Li, "A novel synthesis method of sparse nonuniform-amplitude concentric ring arrays for microwave power transmission," *Progress in Electromagnetics Research C*, vol. 107, pp. 1-15, 2021.

[17] J. Li and S. Chang, "Novel sparse planar array synthesis model for microwave power transmission systems with high efficiency and low cost," *Progress in Electromagnetics Research C*, vol. 115, pp. 245-259, 2021.

[18] J. Li, Z. Han, and C. Guo, "Novel subarray partition algorithm for solving the problem of too low beam collection efficiency caused by dividing a few subarrays," *Progress in Electromagnetics Research M*, vol. 108, pp. 223-235, 2022.

[19] X. Li, B. Duan, and L. Song, "Design of clustered planar arrays for microwave wireless power transmission," *IEEE Transactions on Antennas and Propagation*, vol. 67, no. 1, pp. 606-611, Jan. 2019.

[20] X. Yang, W. Xi, Y. Sun, T. Zeng, T. Long, and T. K. Sarkar, "Optimization of subarray partition for large planar phased array radar based on weighted K-means clustering method," *IEEE Journal of Selected Topics in Signal Processing*, vol. 9, no. 8, pp. 1460-1468, Dec. 2015.

[21] P. Rocca, L. Poli, A. Polo, and A. Massa, "Optimal excitation matching strategy for sub-arrayed phased linear arrays generating arbitrary-shaped beams," *IEEE Transactions on Antennas and Propagation*, vol. 68, no. 6, pp. 4638-4647, June 2020.

[22] X. Sun, X. Li, K. Liu, and C. Liu. "Study on the transmitting array for ground microwave wireless power transmission system," in *2023 IEEE 11th International Conference on Information, Communication and Networks (ICICN)*, Xi'an, China, pp. 659-663, Aug. 2023.

[23] S. Liang, Z. Fang, G. Li, Y. Zhao, X. Liu, and G. Sun, "An improved multiobjective evolutionary algorithm based on decomposition approach and its application in antenna array beam pattern synthesis," *International Journal of Numerical Modelling: Electronic Networks*, *Devices and Fields*, vol. 35, no. 1, p. e2935, 2022.

[24] M. W. Wolff and J. A. Nanzer, "Application of pseudo weights in antenna array optimization and design," *IEEE Antennas and Wireless Propagation Letters*, vol. 23, no. 5, pp. 1478-1482, May 2024.

[25] W. Deng, H. Zhao, X. Yang, J. Xiong, M. Sun, and B. Li, "Study on an improved adaptive PSO algorithm for solving multi-objective gate assignment," *Applied Soft Computing*, vol. 59, pp. 288-302, 2017.

**Jianxiong Li** received the B.Sc. and M.Sc. degrees in Physics in 1991 and 1994, respectively, and obtained the Ph.D. degree in Communication and Information System in 2007, from Tianjin University, Tianjin, China. His main research interests are in computational electromagnetics, wireless communication, and antenna.

**Ranran Zhang** received B.Sc. degree in the School of Physical Science and Information Engineering from Liaocheng University in 2022. She is currently working toward M.Sc. degree in the School of Electronic and Information Engineering from Tiangong University. Her current research interests are electromagnetics, array antennas, and microwave wireless power transmission.

**Ziyu Han** received M.Sc. degree in the School of Electronic and Information Engineering from Tiangong University in 2023. She is currently working toward Ph.D. degree in the National University of Defense Technology, School of Electronic Science. Her research focuses on distributed beamforming, DOA estimation, array signal processing, and intelligent optimization algorithms.

# A Dual-polarized Reflectarray Antenna for High-speed Ka-band Satellite Communications

**Ahmet Hulusi Gülseren[1], Selda Yılmaz[2], Aytaç Alparslan[3], and Nurhan Türker Tokan[2]**

[1]Department of Electrical-Electronics Engineering
Aydın Adnan Menderes University, Aydın 09010, Türkiye
agulseren@adu.edu.tr

[2]Department of Electronics and Communication Engineering
Yildiz Technical University, İstanbul 34220, Türkiye
selda.yilmaz@memorial.com.tr, nturker@yildiz.edu.tr

[3]Department of Electrical and Electronics Engineering
Trakya University, Edirne 22030, Türkiye
aytacalparslan@trakya.edu.tr

***Abstract –*** A small-sized reflectarray antenna array with compact production specifications is designed and fabricated for high-speed Ka-band communication systems. In the design phase, firstly, the reflection characteristics of unit cells used in the reflective surface are obtained by the full wave computational analysis tool, CST Microwave Studio. Secondly, an aperture efficiency analysis is carried out to determine the physical size of the reflectarray and the distances between the feeding antenna and the individual unit cells. Then, the entire reflectarray antenna is analyzed by array theory to obtain geometrical dimensions to be used in the fabrication phase. These results are verified by CST Microwave Studio and similar fabrication guidelines are obtained for both TE and TM polarizations. In the fabrication phase, the carefully tailored design parameters of the unit cells are used to build the antenna and measure important parameters such as radiation patterns, gain, cross polarization levels and $S_{11}$ parameters, which agree with the results obtained in the design phase. The proposed reflectarray antenna makes it possible to support dual-polarized multi-beams in the range 18-20 GHz with stable gain behavior, which makes it possible to use it in high speed 5G satellite communication systems.

***Index Terms –*** Antennas, reflectarrays, satellite communication.

## I. INTRODUCTION

The popularity of reflectarray antennas have increased in parallel with improvements in 5G/6G satellite technologies which made it possible to obtain faster communication standards with lower delays [1–5]. Reflectarray antennas are also suitable to be used in a wide range of frequency bands employed in different types of satellites. For instance, a reflectarray antenna was designed using the pattern synthesis method to fulfill the coverage requirements of Direct Broadcast Systems (DBS) in South America in the Ku-band and to obtain the phase distribution at different frequencies in the Transmit (Tx) and Receive (Rx) bands [6]. In another study, a reflectarray antenna was used in a medium Earth orbit remote sensing satellite system by using a Yagi-Uda array as the feeding mechanism in the X-band [7]. Recently, reflectarray antennas have gained popularity in satellite communication studies due to their features such as low cost, ease of production and eliminating the necessity of complex feeding circuits [8, 9]. These features are realized in dual-polarized reflectarray antennas that can be combined with other structures to be used in applications such as transmit-receive reflectarrays, reflect-transmit arrays and plane wave generators [6, 10, 11]. In addition, a linearly polarized reflectarray and a circularly polarized transmit array are combined to have the characteristics of both [6, 12–14]. As itemized by the applications above, designing and manufacturing reflectarray antennas are among the most popular recent research subjects in aerospace communication systems.

When designing antenna systems for satellite communications, performance, weight, volume, cost and multifunctionality must be considered. Therefore, to use reflectarray antennas in such systems, it is important that the designs are dual polarized, support multi-beams, and operate at different frequencies with low-cost and small-sized production specifications. In dual-polarized reflectarray antenna systems, symmetrical structures are generally favored. For such antennas, single-layer structures are preferred for ease of fabrication and cost [10, 15, 16].

*Submitted On: September 19, 2024*
*Accepted On: October 17, 2024*
https://doi.org/10.13052/2024.ACES.J.390902

Dual polarization studies are carried out not only in linear polarization but also in circular polarization [17, 18]. The reconfigurable dual-polarized reflectarray antenna is constructed using a single-band, symmetrically rotated subarray to keep the cross polarization levels low [19]. A dual-polarized reconfigurable reflectarray antenna has been designed using independent phase control obtained by adding p-i-n diodes as an active component to the meta-surface elements [19]. While designing the unit cell of the reflectarray in [20], the thickness of the liquid crystal layer was reduced without loss of performance. In another dual-polarized application, a tightly coupled reflectarray antenna consisting of unit cells with $x$ and $y$ polarizations is designed [21], where the reflecting surface for each polarization consists of different number of elements. In another study, an X-band dual-polarized reflectarray antenna using shared aperture technology that has only one substrate between the two metal layers is designed [10], where the number of substrates is reduced when combining the advantages of the elements above and below the substrate. Another method for designing a broadband dual-polarized and dual beam reflectarray antenna is to use a 1-bit unit cell [15]. Generally, a rectangular horn antenna is used as the feed antenna in reflectarray antenna applications, but other antenna models can also be used [6, 14, 22]. In addition, reflectarray antennas can operate simultaneously for one or more bands on two [17, 23–25] or more frequencies [8].

In this work, a reflectarray antenna is designed, fabricated and measured to be used in downlink frequencies of Ka-band Satellite Communication (SATCOM) [26]. When designing the reflectarray antenna, a single-layer dual-polarized unit cell layout, which was analyzed only numerically in [27], is used. Here, the geometrical parameters of the unit cells are optimized to be used in Ka-band 5G high speed satellites with low-cost and small-sized fabrication specifications. For 18 GHz, the proposed structure has a directivity of 21.72 dBi, a gain of 20.99 dBi and a total efficiency of 84.58%. Very similar results are obtained for TE and TM modes. The antenna gain shows stable characteristics in the 18-22 GHz frequency band. As seen in the results, the reflectarray antenna designed in this paper is a strong candidate to be used in high speed 5G satellite communication systems.

This paper is organized as follows. In section II, the novel unit cell is introduced, and the phase variations obtained by changing the dimensions of the elements in the unit cell are given. In the third section, the characteristics of the feed horn antenna are presented, and the optimum dimensions of the reflective surface are determined by using the aperture efficiencies. Based on these dimensions, a novel reflective surface is designed. In section IV, the designed reflectarray antenna is analyzed by CST Microwave Studio [28] and the array theory method and the results are compared. The parameter measurements of the fabricated reflectarray antenna are shared in the fifth section and the main contributions of this paper are summarized in section VI.

## II. UNIT CELL DESIGN

When designing a reflectarray antenna, the unit cells should be accurately analyzed since the performance of whole system depends directly on the unit cell performance. A unit cell structure with symmetry in both principal planes is used for the dual-polarized reflectarray antenna with an off-axis feed. This structure was recently analyzed, only numerically, in a different setting with an on-axis feed [27]. The proposed unit cell geometry is depicted in Fig. 1. As seen in the figure, each unit cell is made up of a cross dipole and four L-shaped elements. The proposed unit cell is printed on a $H_s = 0.51$ mm thickness Arlon DiClad 880 substrate with the relative electrical permittivity of 2.2. To achieve the desired phase difference characteristics, a gap between the substrate and the ground plane is left as free-space with thickness $H_a = 1$ mm. A single-layer structure is preferred in the design of the unit cell due to simple and low-cost fabrication. Design parameters of the element are exhibited in the figure and the values of the parameters are listed in Table 1 . Since the unit cell is rectangular and has identical profile along $xz$- and $yz$-planes, the phase of the unit cell for the TE- and TM-polarization is controlled by the lengths of the dipoles. Thus, corresponding phase shift characteristic is obtained by varying the $L_a$ parameter. Analysis of the unit cell is carried out in CST Microwave Studio.

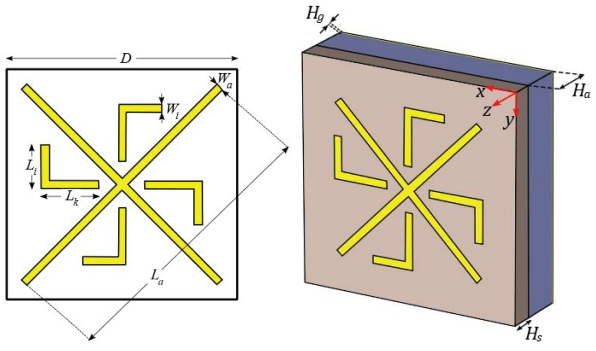


Fig. 1. Unit cell of the dual-polarized reflectarray antenna: (a) top view and (b) perspective view.

Periodicity of the unit cell [$D$ parameter in Fig. 1 (a)] should be chosen by considering the required phase shift at the operation band. Besides providing enough space

Table 1: Parameters of the unit cell

| Parameter | Value (mm) |
|---|---|
| $D$ | 7.5 |
| $W_a$ | 0.25 |
| $W_i$ | 0.25 |
| $L_i$ | 1.4 |
| $L_k$ | 1.86 |
| $H_s$ | 0.51 |
| $H_a$ | 1 |
| $H_g$ | 0.035 |

to obtain the phase shift, its value should be chosen to avoid grating lobes at the higher frequencies of the band. The following equation may be used to determine the periodicity of the unit cell [29]:

$$D \leq \frac{\lambda}{1+sin\theta}, \quad (1)$$

where $\lambda$ is the wavelength in free-space and $\theta$ is the angle of beam radiation with respect to the normal direction of the reflectarray. According to the expression given in equation (1), the horizontal and vertical dimensions of the unit cell at 18 GHz must not exceed 11.1 mm for $\theta = 30^{\circ}$. By choosing $D = 7.5$mm in the proposed unit cell, it is aimed to direct the main beam towards larger reflection angles. The final values of the parameters are determined after an optimization process.

To observe the effects of the unit cell parameters, a comprehensive parametric analysis is carried out. Although they are not reported here for the sake of brevity, important conclusions of the parametric analysis are given. The substrate material plays a critical role in the phase characteristics of the unit cell. Phase variation of the unit cell for different air gap and substrate thicknesses as the function of parameter $L_a$ is given in Fig. 2.

According to Fig. 2 (a), the maximum phase variation at 18 GHz is achieved when there is no air layer between the Arlon substrate and the ground plane ($H_a = 0$). However, an abrupt decrease is observed in this case. When elements with nonlinear S-shaped phase curves are used in the reflectarray design, they cause narrow operation bands and high variations at different frequencies. Thus, air layer thickness is chosen as 1 mm by virtue of the fact that the phase difference is more, and the phase curve is closer to linear. The total phase variation of the structure for $H_a = 1$ mm is about 320°. Phase characteristics of the unit cell for different substrate thickness values are exhibited in Fig. 2 (b). The phase variations reveal that as the substrate thickness increases, the amount of phase range decreases and the phase curve gets closer to linear. Maximum phase change is observed for $H_s = 0.254$ mm. Since this thickness is very thin and may cause problems at the surface etching stage of the reflectarray manufacturing process, this thickness is not favored. Among the other thicknesses of Arlon DiClad 880 substrate, $H_s = 0.508$ mm is chosen.

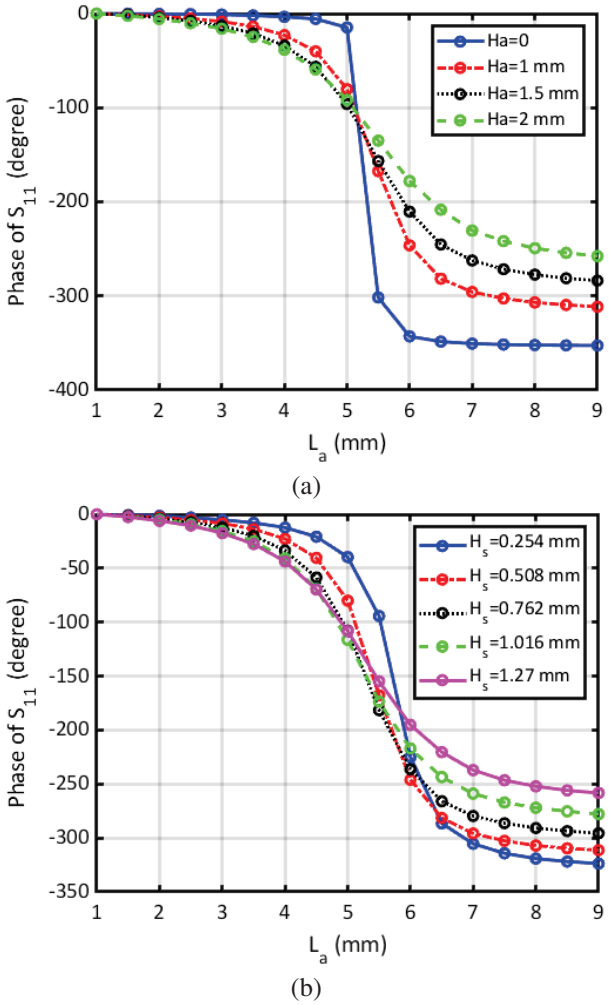


Fig. 2. Phase characteristics of the unit cell as a function of parameter $L_a$ at 18 GHz for different (a) air gap values ($H_a$) and (b) substrate thickness values ($H_s$).

## III. REFLECTARRAY DESIGN

### A. Feed antenna: Double ridged horn antenna

As the feed antenna of the system, an OBH180400-15 double ridged horn antenna operating at 18-40 GHz frequency band is used. The broadband feed is linear polarized with high polarization purity. Right-angle double ridge waveguide (WRD180) to coaxial adapter (2.92 mm female) is used for the cable connection. Simulated reflection coefficient variation of the feed antenna is given in Fig. 3.

$S_{11}$ variation of the horn antenna shows that good impedance matching is achieved above cutoff frequency of the double ridged waveguide. The photograph of the feed antenna is given as an inset in Fig. 3.

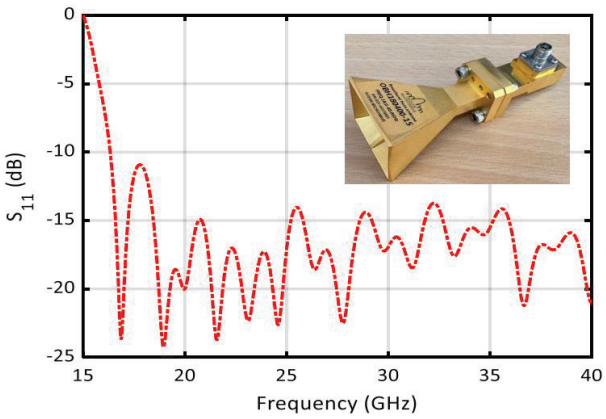


Fig. 3. Reflection coefficient variation of the double ridged horn antenna.

The three-dimensional radiation pattern of the feed antenna at 18 GHz is shown in Fig. 4, where the beam direction is also demonstrated.

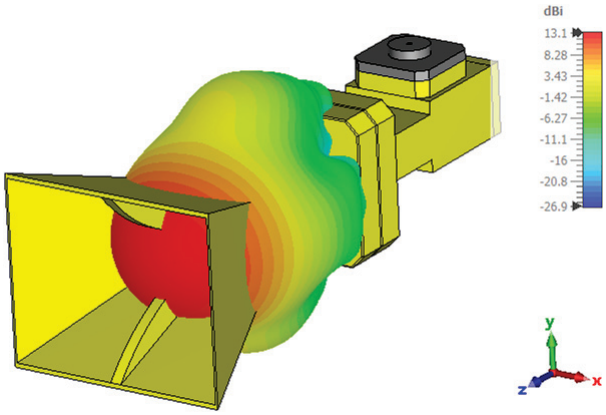


Fig. 4. 3D far-field radiation pattern of the feed antenna at 18 GHz.

The gain and phase center of the horn antenna are 13.1 dBi and 13.84 mm towards inside from the center of the horn aperture along the z-axis. In the reflectarray system, the phase center of the feed antenna should coincide with the predetermined feed position by aperture efficiency analysis. The gain and position of the feed antenna are critical factors for maximizing aperture efficiency.

### B. Aperture efficiency

Aperture efficiency analysis is carried out to determine the physical size of the reflective surface and the distance of the feed antenna's phase center from the reflective surface. The aperture efficiency of the reflectarray, $\eta_a$, is calculated by the product of illumination and spillover efficiencies [30]. Illumination efficiency, $\eta_i$, measures how uniform the field amplitude is distributed on the antenna aperture, whereas the spillover efficiency, $\eta_s$, is defined as the ratio between the total radiated power and the incident power on the reflectarray [31]. These two parameters are calculated as a function of the shape of the reflectarray and the feeding source.

Radiation patterns of the feed antenna are given in Fig. 5 in two principal planes. Since the aperture of the horn feed antenna is rectangular, the patterns are different in $\phi = 0^\circ$ and $\phi = 90^\circ$ planes. When determining the $q$ parameter of the $\cos^q$ pattern, $q$ is chosen by considering the H-plane pattern, which has a wider beam compared to the E-plane. The 3 dB beamwidth of the antenna are approximately 38° and 32° in H- and E-planes, respectively. By using the $\cos^q$ model for the H-plane of the feed antenna pattern, $q$ parameter of the feed antenna is found to be 6.3.

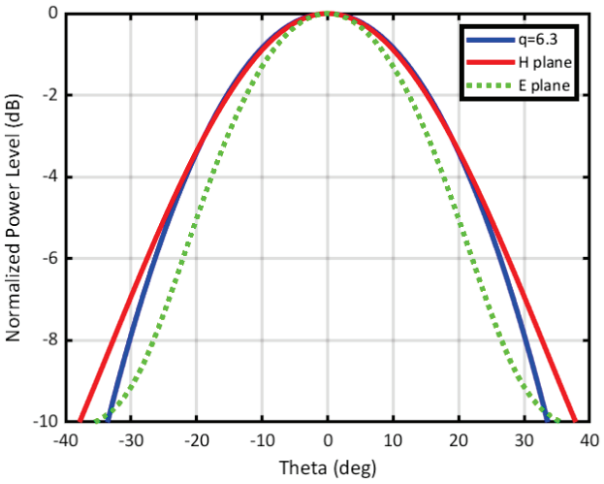


Fig. 5. Normalized power levels of the feed antenna. $cos^q$ model with $q = 6.3$ is depicted by a solid blue line.

For the reflectarray system shown in Fig. 6, the spillover efficiency ($\eta_s$) is calculated by the ratio of the total power radiated by the feed antenna to the power incident on the reflective surface as given below:

$$\eta_s = \frac{\iint_A \overrightarrow{P}(\overrightarrow{r}_{f,mn}).d\overrightarrow{s}}{\iint_{sphere} \overrightarrow{P}(\overrightarrow{r}_{f,mn}).d\overrightarrow{s}}, \tag{2}$$

where $\overrightarrow{P}(\overrightarrow{r}_{f,mn})$ is the Poynting vector. By using a numerical approach, the following equation can be used to solve for array apertures in the polar coordinate plane [31]:

$$\eta_s = \frac{2q+1}{2\pi} \int_0^{2\pi} \int_0^{D/2} (H/r_{f,mn}^3) \left(\frac{r_f^2 + r_{f,mn}^2 - r_{mn}{}^2}{2\, r_f\, r_{f,mn}}\right)^{2q} \rho d\rho d\varphi, \tag{3}$$

where $H$ is the perpendicular distance between the phase center of the feed antenna and the reflective surface.

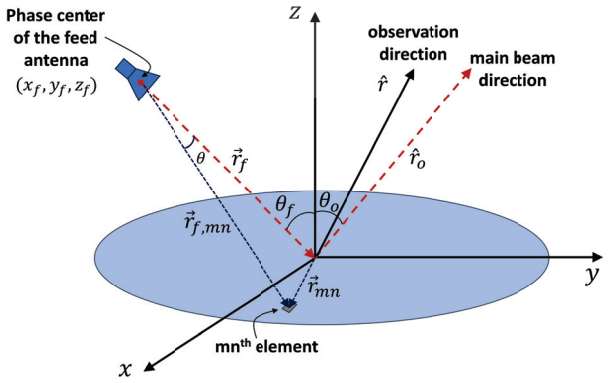


Fig. 6. Reflectarray system configuration.

Illumination efficiency ($\eta_i$) is calculated as follows:

$$\eta_i = \frac{1}{A_a}\frac{\left|\iint_A I(A')\,dA'\right|^2}{\iint_A |I(A')|^2 dA'}, \tag{4}$$

where $I(A')$ stands for the amplitude distribution over the reflective surface, which depends on feed antenna pattern and reflectarray element pattern. Alternatively, the following formula can be used to solve for the array apertures in the polar coordinate plane numerically [31]:

$$\eta_i = \frac{4}{\pi D^2}\frac{\left[\int_0^{2\pi}\int_0^{D/2}\left(\frac{1}{r_{f,mn}^{1+q_e}}\right)\left(\frac{r_f^2+r_{f,mn}^2-r_{mn}^2}{2r_f r_{f,mn}}\right)^q \rho\,d\rho\,d\varphi\right]^2}{\int_0^{2\pi}\int_0^{D/2}\left(\frac{1}{r_{f,mn}^{2+2q_e}}\right)\left(\frac{r_f^2+r_{f,mn}^2-r_{mn}^2}{2r_f r_{f,mn}}\right)^{2q} \rho\,d\rho\,d\varphi} x^2\,y'', \tag{5}$$

where $q_e$ belongs to the element pattern and is usually chosen as 1 for ease of operation. Formulations given in equations (2-5) can be used in the case of on-axis feeding for the circular aperture. Mostly, off-axis feeds are preferred in reflectarray systems to avoid feed blockage. However, in the case of offset feed, the beam would cut the reflecting surface elliptically. Thus, the following boundary condition should be applied [31]:

$$x^2 + \left(y\cos\theta_f\right)^2 = \left(y\sin\theta_f + \frac{H}{\cos\theta_f}\right)^2 \tan^2\alpha\; x^2 y'', \tag{6}$$

where $\alpha$ is the angle that represents half aperture angle of the feed beam.

By using the novel dual-polarized unit cell introduced in this paper, an off-axis fed reflectarray system whose feed is located at $\theta = 15^\circ$ (z-axis is along the reflectarray surface normal) and beam is oriented towards $\theta = -15^\circ$ in $\phi = 0^\circ$ plane is designed. The spillover ($\eta_s$), illumination ($\eta_i$) and aperture ($\eta_a = \eta_i \times \eta_s$) efficiency values of the reflectarray system are given in Fig. 7 as a function of the reflectarray diameter $D$ for the feed antenna elevation value from the reflective surface of $H = 260$ mm.

As seen in Fig. 7, $\eta_a$ has its highest value at $D = 300$ mm. In this case, the reflective surface consists of

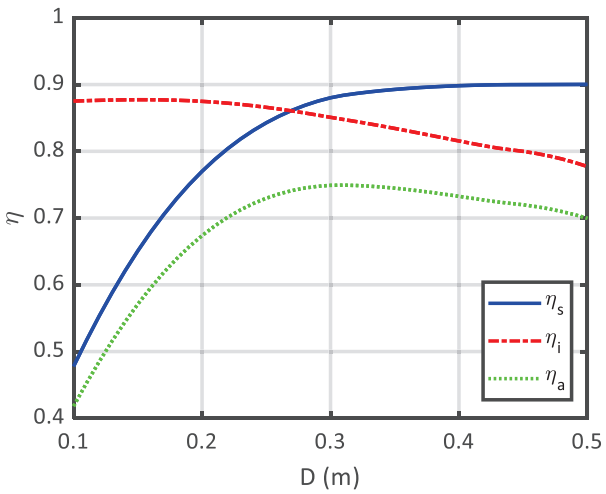


Fig. 7. Efficiency as a function of the reflectarray diameter $D$ for the off-axis fed reflectarray.

40×40 cells. Since the RAM and processor capacity of the workstation (HP Z820 Intel(R) Xeon(R) workstation with 2.4 GHz processor and 64 GB RAM) used for the simulations cannot handle this processing load, the reflective surface has been reduced to 25×25 cells by sacrificing efficiency. This compromise results in reduced aperture efficiency of 0.65.

### C. Reflective surface design

Each unit cell is used as an individual reflector when designing the reflective surface of the reflectarray antenna. The finely tuned geometrical features of the unit cells are used to atone for the phase delay generated due to the path differences between the feed antenna and individual unit cells. To design a reflective surface with maximum directivity with off-axis operation, the following equations are used to calculate the required phase shift for each unit cell:

$$\psi_{mn} = k_0\left(r_{f,mn} - \overrightarrow{r}_{mn}.\hat{r}_0\right) + \psi_o, \tag{7}$$

$$r_{f,mn} = \sqrt{(x_{mn}-r_{f_x})^2 + (y_{mn}-r_{f_y})^2 + (z_{mn}-r_{f_z})^2}, \tag{8}$$

where $\psi_{mn}$ is the reflection phase and $r_{f,mn}$ is the distance between the feed antenna and the $mn$th element. When calculating the relations given above, $\overrightarrow{r}_{mn}$ defines the position vector of the $mn$th element, and the unit vector $\hat{r}_0$ represents the direction of the main beam [32] as shown in Fig. 6. Since a relative reflection phase is needed, $\psi_o$ is added in (7), where $k_0$ is the wavenumber of free-space. The unit cell $mn$ and the feed antenna are located at $(x_{mn}, y_{mn}, z_{mn})$ and $(r_{f_x}, r_{f_y}, r_{f_z})$, respectively.

The necessary phase distribution for steering the beam towards a predefined direction is obtained by using the equations above. The phase values are quantized when designing the reflective surface and smaller

quantization steps are used in the fast-decaying regions. To achieve optimum directivity, a phase range of 360 degrees is required. With the dual-polarized novel unit cell, a phase range of 360 degrees is obtained with 1 mm $\leq L_a \leq$ 9 mm. The unit cell phase distribution of the reflective surface consisting of 25×25 cells is shown in Fig. 8 (a). The reflectarray with the corresponding unit cells geometry that gives the calculated phase value is given in Fig. 8 (b).

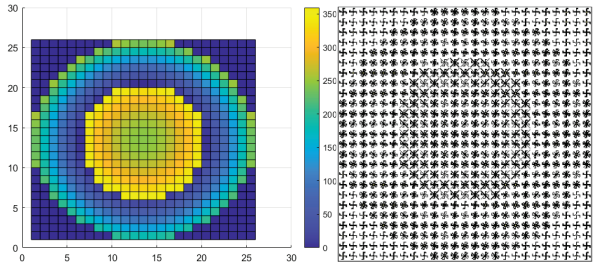

(a) (b)

Fig. 8. Reflective surface of the reflectarray: (a) phase distribution and (b) reflectarray with corresponding unit cells geometry.

## IV. ANALYSIS RESULTS

A reflectarray with 25×25 dual-polarized unit cells was analyzed with a full-wave electromagnetic wave analysis tool based on finite-integration technique [28]. The problem space consists of about 134 million unknowns. Array theory, which is a robust analysis technique for electrically large antennas, gives very fast results compared to other analysis methods. 3D simulation programs especially take a while, whereas array theory calculates the far-field radiation pattern of the reflectarray antenna in seconds. The far-field radiation pattern of a reflectarray antenna consisting of $M \times N$ elements is calculated by [32]:

$$E(\hat{r}) = \sum_{m=1}^{M} \sum_{n=1}^{N} \overrightarrow{A}_{mn}(\hat{r}) . \overrightarrow{I}(\overrightarrow{r}_{mn}), \tag{9}$$

$$\hat{r} = \hat{x}\, sin\theta\, cos\varphi + \hat{y}\, sin\theta\, sin\varphi + \hat{z}\, cos\theta\ , \tag{10}$$

where $\overrightarrow{A}_{mn}$ and $\overrightarrow{I}$ are the vector functions defined for the unit cell patterns and the unit cell excitations and the remaining vectors and angles in the equations are defined in Fig. 6. The scalar element pattern function is given with $\cos^{qe}$ model as follows:

$$A_{mn}(\theta,\varphi) \triangleq cos^{qe}\, e^{jk(\overrightarrow{r}_{mn}.\hat{r})}. \tag{11}$$

The incident field and the element property are used to define element excitation function, $I(r_{m,n})$ defined by:

$$I(r_{m,n}) = \frac{cos^{q}\theta_f(m,n)}{\left|\overrightarrow{r}_{mn} - \overrightarrow{r}_f\right|} . e^{-jk(\left|\overrightarrow{r}_{mn} - \overrightarrow{r}_f\right|)} . |\Gamma_{mn}|\, e^{j\phi_{mn}}, \tag{12}$$

where $|\Gamma_{mn}|$ isn directly obtained from the unit cell analysis. Finally, the radiation pattern of the reflectarray is obtained as:

$$E(\theta,\varphi) = \sum_{m=1}^{M} \sum_{n=1}^{N} cos^{qe} \frac{cos^{q}\theta_f(m,n)}{\left|\overrightarrow{r}_{mn} - \overrightarrow{r}_f\right|} \tag{13}$$

$$e^{-jk\left(\left|\overrightarrow{r}_{mn} - \overrightarrow{r}_f\right| - \overrightarrow{r}_{mn}.\hat{r}\right)} cos^{qe}\theta_e(m,n) e^{j\phi_{mn}}\ .$$

General pattern shape indicators, especially the main beamwidth and the beam direction, are obtained successfully by the array theory. However, the cross polarization characteristics of the antenna are not calculated by array theory since the feed polarizations are not included and a simplified $\cos^q$ model is used. To get the radiation pattern data in different polarizations, full wave simulations are performed using CST Microwave Studio. Normalized radiation patterns of the dual-polarized reflectarray antenna designed for high-speed Ka-band satellite communications are given in Fig. 9 for TE and

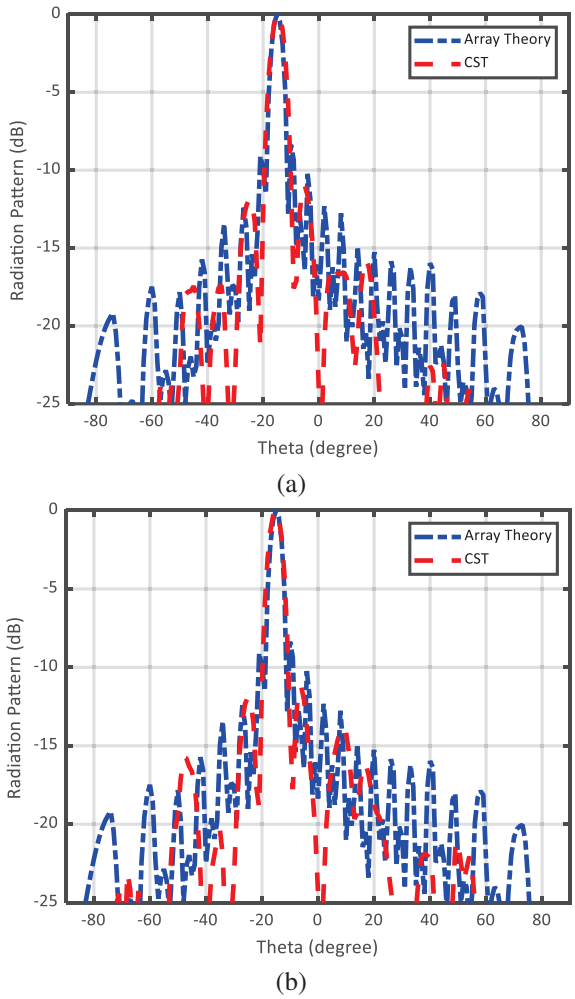


Fig. 9. Normalized radiation patterns at 18 GHz: (a) TE and (b) TM polarization.

TM polarizations. The feed phase center is located at (69.67 mm, 0, 260 mm) with respect to the center of the reflectarray. Gain of 21 and 21.6 dBi is observed in TE and TM modes, respectively.

It is observed that array theory and simulation results are almost overlapping for both modes and in both cases the main beam is directed to $\theta = -15^0$. Moreover, TE and TM mode patterns are almost identical with main beams directed towards $\theta = -15^0$. This proves that the reflectarray works in dual mode successfully. The effect of the holder is investigated by full wave analysis of the whole structure. Figure 10 shows the 3D radiation pattern in TE mode. The gain pattern, which is obtained by including the holder in the simulations, has a maximum value of 20.5 dBi. Inclusion of the holder to the simulations has lowered the gain about 0.5 dB and increased the side lobe level of the pattern. Since the unit cell structure used in this design is symmetrical in the $x$ and $y$ directions, TE and TM modes are identical.

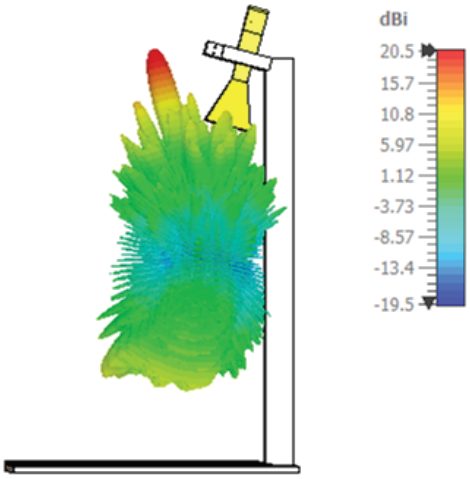


Fig. 10. Three-dimensional radiation pattern of reflectarray antenna in TE mode. The pattern is obtained by including the holder with PLA (polylactic acid) material.

## V. EXPERIMENTAL VERIFICATION

### A. Fabrication

The reflectarray prototype consisting of 25×25 dual-polarized unit cells is fabricated by a chemical etching technique. Arlon DiClad 880 with 0.51 mm dielectric thickness and 35 μm copper thickness is used as the printed circuit board. The reflectarray prototype which has 187.5 mm × 187.5 mm physical area is shown in Fig. 11 (a) with an expanded view of a unit cell. The ground plane of the reflectarray is generated by covering the top surface of the flat holder plate by conductive tape. An air layer with 1 mm thickness is ensured between the substrate and the ground plane by using 0.5 mm nuts. A double ridged horn antenna (OBH180400-15 from Ocean Microwave) operating in the $18-40$ GHz frequency band is used as the feed antenna. The phase center of the horn antenna at 18 GHz is located to (69.67 mm, 0, 260 mm) coordinates with respect to the center of the reflectarray. A holder that is designed to keep the feed antenna and reflectarray stationary in their designated positions is printed with a PLA filament by using an additive manufacturing technique. Four holes are drilled in the corners of the reflectarray and 5M screws are used to fix the reflectarray to the holder mechanism as shown in Fig. 11 (b). The arm of the holder grips the horn antenna with a clamp that orients the main beam of the feed antenna towards the center of the reflectarray with $\theta = 15^\circ$.

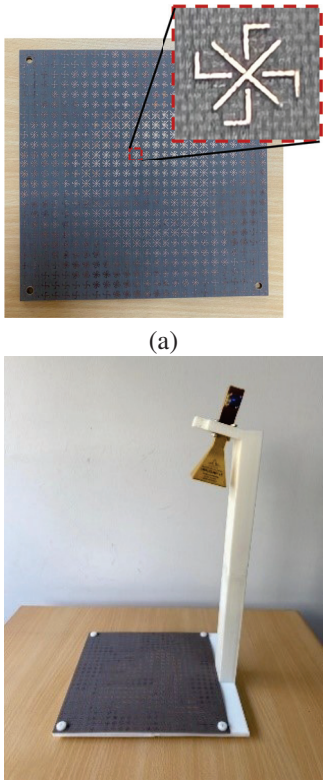

(a)

(b)

Fig. 11. Fabricated reflectarray system: (a) reflectarray prototype and (b) reflectarray system.

### B. Measurement results

Co- and X-polarized radiation patterns, antenna gain and reflection coefficients of the reflectarray system are measured in a full anechoic chamber in the 17-23 GHz frequency band. An NSI-RF-SG42 horn antenna is used as the reference antenna in the measurements. The measurements are performed with 1° resolution within $-90^\circ \leq \theta \leq 90^\circ$ angular range at the steering plane of the reflectarray. The measurement setup in the anechoic chamber is shown in Fig. 12.

Reflection coefficient variation of the reflectarray system is given in Fig. 13. The reflectarray has good impedance matching characteristics with $S_{11}$ lower than $-10$ dB above 18.5 GHz except for a slight increase in the $19.7-20.05$ GHz band. At 18 GHz, about $-7$ dB reflection coefficient level is observed at the measurement, which wasn't the case in the simulations. This deviation from simulated response is attributed to the introduction of the connector. Co- and X-polarized radiation patterns are demonstrated in Fig. 14 at 18.5 and 19 GHz. It is clearly observed that the main beam of the measured patterns is towards $\theta = 15^\circ$ in the $\phi = 90^\circ$ plane. The observed sidelobe levels are higher compared to the simulation results. In the measurement process, the absorbers around the reflectarray were removed to fit the reflectarray system. The higher sidelobes that were not observed in the simulations are attributed to the conductor region where the bottom of the reflectarray was implanted. Measured gain and cross polarization levels are given in Fig. 15. Although the antenna was

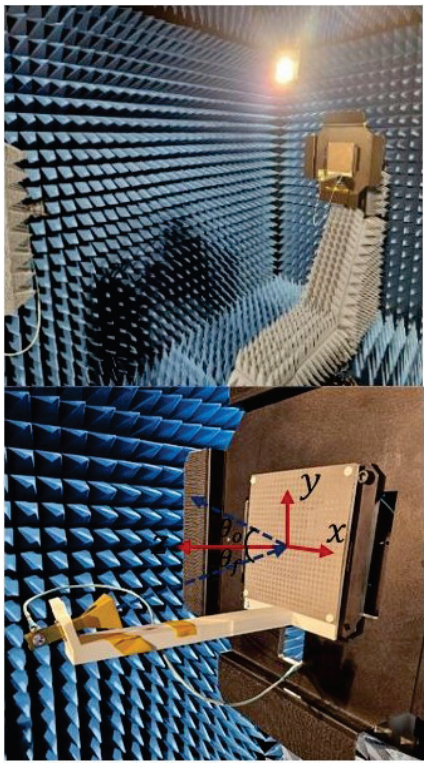


Fig. 12. Measurement setup of the dual-polarized Ka-band reflectarray system. Beam steering is observed on the $\phi = 90^\circ$ plane.

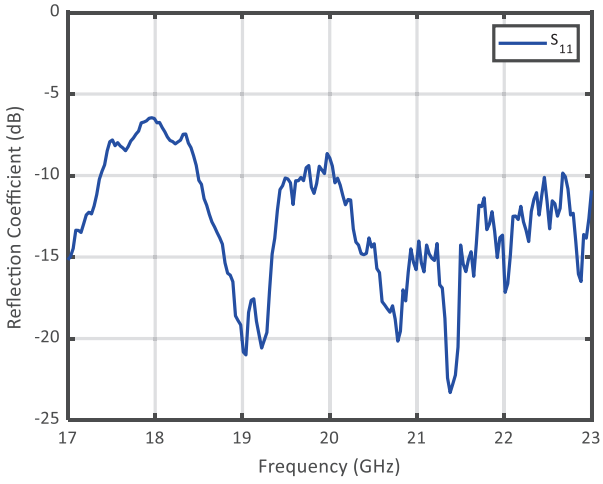


Fig. 13. Measured $S_{11}$ parameter variation of the reflectarray system as a function of frequency.

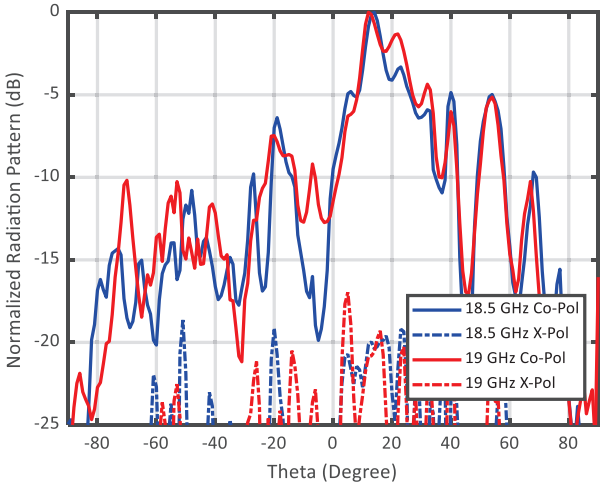


Fig. 14. Measured normalized patterns of the reflectarray system on the $\phi = 90^\circ$ plane. Solid lines (—) and dash-dot lines (– -) belong to Co-polarized and X-polarized patterns, respectively.

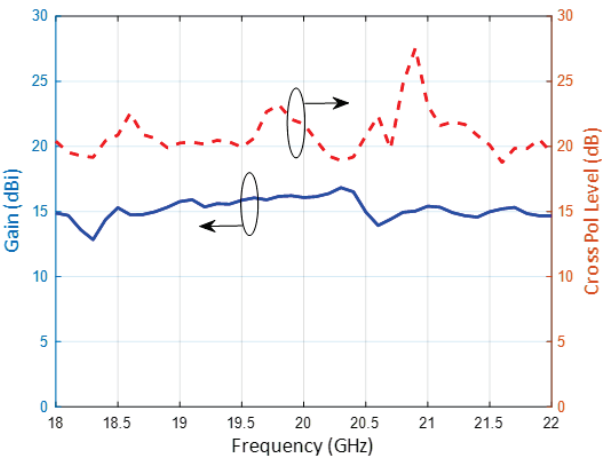


Fig. 15. Measured gain and cross polarization level variations.

optimized to operate at 18 GHz, the antenna gain shows stable characteristics in the whole frequency range. Measured cross polarization patterns are at low levels. Mostly it is above 20 dB in the $18-22$ GHz range. The radiation performance of the reflectarray may be enhanced in terms of sidelobe and efficiency by enlarging the physical reflectarray size since larger dimensions reduce effects such as edge diffraction, specular reflection and feed blockage.

## VI. CONCLUSION

In the transition of 5G to 6G networks, satellites having faster communication standards with lower delays will play a critical role in providing coverage and resilience. Reflectarray antennas are suitable to be used in a wide range of frequency bands employed in different types of satellites. In this work, a novel single-layer dual-polarized unit cell is proposed for a dual-polarized reflectarray antenna operating at SATCOM Ka-Band downlink frequencies to be used in 5G/6G antennas. The unit cell is constructed as the combination of a cross dipole and four L-shaped elements. At 18 GHz, the designed structure has a simulated directivity of 21.72 dBi, a gain of 20.99 dBi and total efficiency of 84.58%. Very similar results are obtained for TE and TM modes. A prototype consisting of $25\times25$ dual-polarized unit cells was fabricated using Arlon DiClad 880 PCB with 0.51 mm dielectric thickness and 35 μm copper thickness and the reflectarray system was measured in a full anechoic chamber. The antenna gain showed stable characteristics in the 18-22 GHz frequency band. It was observed in the simulation and measurement results that the reflectarray consisting of the proposed unit cells produces pencil beams with $\theta = 15^\circ$ orientation. The results show that the proposed reflectarray system can be used in high speed 5G satellite communication systems.

## ACKNOWLEDGMENT

This work was supported by The Research Fund of Yildiz Technical University (Project Number: FBA-2021-4493). The authors wish to acknowledge Dr. İbrahim Tekin and SUNUM (Sabanci University NanoTechnology Research and Application Center, Istanbul, Türkiye) staff for their assistance with the measurements.

## REFERENCES

[1] M. H. Dahri, M. I. Abbasi, M. H. Jamaluddin, and M. R. Kamarudin, "A review of high gain and high efficiency reflectarrays for 5G communications," *IEEE Access*, vol. 6, pp. 5973-5985, 2018.

[2] P. Mei, S. Zhang, and G. F. Pedersen, "A low-cost, high-efficiency and full-metal reflectarray antenna with mechanically 2-D beam-steerable capabilities for 5G applications," *IEEE Trans. Antennas Propag.,* vol. 68, no. 10, pp. 6997-7006, Oct. 2020.

[3] Y. Cui, R. Bahr, S. A. Nauroze, T. Cheng, T. S. Almoneef, and M. M. Tentzeris, "3D printed 'Kirigami'-inspired deployable bi-focal beam-scanning dielectric reflectarray antenna for mm-wave applications," *IEEE Trans. Antennas Propag*., vol. 70, no. 9, pp. 7683-7690, Sep. 2022.

[4] P. Mei, S. Zhang, and G. F. Pedersen, "A wideband 3-D printed reflectarray antenna with mechanically reconfigurable polarization," *IEEE Antennas Wirel. Propag. Lett.,* vol. 19, no. 10, pp. 1798-1802, Oct. 2020.

[5] H. Kim, S. Oh, S. Bang, H. Yang, B. Kim, and J. Oh, "Independently polarization manipulable liquid-crystal-based reflective metasurface for 5G reflectarray and reconfigurable intelligent surface," *IEEE Trans. Antennas Propagat*., vol. 71, no. 8, pp. 6606-6616, Aug. 2023.

[6] J. A. Encinar, M. Arrebola, L. F. de la Fuente, and G. Toso, "A transmit-receive reflectarray antenna for direct broadcast satellite applications," *IEEE Trans. Antennas Propagat*., vol. 59, no. 9, pp. 3255-3264, Sep. 2011.

[7] S. A. M. Soliman, E. M. Eldesouki, and A. M. Attiya, "Analysis and design of an X-band reflectarray antenna for remote sensing satellite system," *Sensors*, vol. 22, no. 3, p. 1166, Feb. 2022.

[8] R. Deng, S. Xu, F. Yang, and M. Li, "An FSS-backed Ku/Ka quad-band reflectarray antenna for satellite communications," *IEEE Trans. Antennas Propag.*, vol. 66, no. 8, pp. 4353-4358, Aug. 2018.

[9] M. Bozzi, S. Germani, and L. Perregrini, "Performance comparison of different element shapes used in printed reflectarrays," *IEEE Antennas Wireless Propag. Lett*., vol. 2, pp. 219-222, 2003.

[10] W. Song, Q. Xue, Y. Cai, N. Guo, K. Liu, S. Li, and H. Ding, "A single-layer reflect-transmit-array antenna with polarization-dependent operation," *IEEE Access*, vol. 9, pp. 167928-167935, Nov. 2021.

[11] Á. F. Vaquero, R. Florencio, M. R. Pino, and M. Arrebola, "Dual-polarized near-field plane wave generator using an offset-optics reflectarray mm-wave band," *IEEE Trans. Antennas Propag*., vol. 70, no. 12, pp. 12370-12375, Dec. 2022.

[12] B. Xi, Y. Cai, Y. Wang, S. Yang, R. Zang, and L. Zhang, "Design of a dual-polarized reflect-transmit-array," *Microw. Opt. Technol. Lett*., vol. 62, no. 2, pp. 949-955, Feb. 2020.

[13] S. Yang, Z. Yan, T. Zhang, M. Cai, F. Fan, and X. Li, "Multifunctional tri-band dual-polarized antenna combining transmitarray and reflectarray," *IEEE Trans. Antennas Propag*., vol. 69, no. 9, pp. 6016-6021, Sep. 2021.

[14] C. C. Chung, F. P. Lai, S. X. Huang, and Y. S. Chen, "Anisotropic metasurface with asymmetric propagation of electromagnetic waves and enhancements of antenna gain," *IEEE Access*, vol. 9, pp. 90295-90305, 2021.

[15] J. Yin, Q. Lou, H. Wang, Z. N. Chen, and W. Hong, "Broadband dual-polarized single-layer reflectarray antenna with independently controllable 1-bit dual beams," *IEEE Trans. Antennas Propag*., vol. 69, no. 6, pp. 3294-3302, June 2021.

[16] Y. Liu, H. Wang, and X. Dong, "Design of a dual polarized broadband single-layer reflectarray based on square spiral element," *Progress in Electromagnetics Research M.*, vol. 72, pp. 23-30, Aug. 2018.

[17] R. Florencio, D. Martinez-de-Rioja, E. Martinez-de-Rioja, J. A. Encinar, R. R. Boix, and V. Losada, "Design of Ku- and Ka-band flat dual circular polarized reflectarrays by combining variable rotation technique and element size variation," *Electronics*, vol. 9, no. 6, p. 985, June 2020.

[18] S. Mener, R. Gillard, R. Sauleau, A. Bellion, and P. Potier, "Dual circularly polarized reflectarray with independent control of polarizations," *IEEE Trans. Antennas Propag*., vol. 63, no. 4, pp. 1877-1881, Apr. 2015.

[19] N. Zhang, K. Chen, J. Zhao, Q. Hu, K. Tang, J. Zhao, T. Jiang, and Y. Feng, "A dual-polarized reconfigurable reflectarray antenna based on dual-channel programmable metasurface," *IEEE Trans. Antennas Propag*., vol. 70, no. 9, pp. 7403-7412, Sep. 2022.

[20] P. Aghabeyki, Y. Cai, G. Deng, Z.-H. Tan, and S. Zhang, "A dual-polarized reconfigurable reflectarray with a thin liquid crystal layer and 2-D beam scanning," *IEEE Trans. Antennas Propag.*, vol. 71, no. 4, pp. 3282-3293, Apr. 2023.

[21] W. Li, H. Tu, Y. He, L. Zhang, S.-W. Wong, and S. Gao, "A novel wideband tightly coupled dual-polarized reflectarray antenna," *IEEE Trans. Antennas Propag*., vol. 71, no. 6, pp. 5422-5427, June 2023.

[22] L. X. Wu, Q. Hu, X. Y. Luo, J. Zhao, T. Jiang, K. Chen, and Y. Feng, "Wideband dual-feed dual-polarized reflectarray antenna using anisotropic metasurface," *IEEE Antennas Wirel. Propag. Lett*., vol. 21, no. 1, pp. 129-133, Jan. 2022.

[23] I. Aryanian, A. Ahmadi, M. Rabbani, S. Hassibi, and M. Karimipour, "Design and fabrication of a dual-polarized, dual-band reflectarray using optimal phase distribution," *Turk. J. Elec. Eng. & Comp. Sci.*, pp. 878-888, Mar. 2019.

[24] S. Li, Y. Cao, Y. B. Zhang, and T. Wu, "Dual polarized reflectarray antenna for operation in X and Ku bands," *Microwave Opt. Technol. Lett*., vol. 64, no. 7, pp. 1272-1279, Mar. 2022.

[25] M. Abdollahvand, K. Forooraghi, J. A. Encinar, Z. Atlasbaf, and E. Martinez-de-Rioja, "A 20/30 GHz reflectarray backed by FSS for shared aperture Ku/Ka-band satellite communication antennas," *IEEE Antennas Wirel. Propag. Lett*., vol. 19, no. 4, pp. 566-570, Apr. 2020.

[26] C. McLain, S. Panthi, M. Sturza, and J. Hetrick, "High throughput Ku-band satellites for aeronautical applications," in *MILCOM 2012 - 2012 IEEE Military Communications Conference*, Orlando, FL, pp. 1-6, 2012.

[27] S. Yılmaz, A. H. Gülseren, and N. T. Tokan, "Dual-polarized reflectarray for high-speed satellite communication," in *2023 10th International Conference on Recent Advances in Air and Space Technologies (RAST),* Istanbul, Turkiye, pp. 1-5, 2023.

[28] CST Microwave Studio [Online]. Available: http://www.cst.com/2023.

[29] E. Nido, "New advances on multi-frequency and multi-beam reflectarrays with application to satellite antennas in Ka-band," Doctoral thesis, Universidad Politécnica De Madrid, Madrid, 2018.

[30] J. Huang, "Analysis of a microstrip reflectarray antenna for microspacecraft application," *Telecommunications and Data Acquisition Progress Report*, vol. 120, pp. 153-173, Feb. 1994.

[31] A. Yu, F. Yang, A. Z. Elsherbeni, J. Huang, and Y. Rahmat-Samii, "Aperture efficiency analysis of reflectarray antennas," *Microw. Opt. Technol. Lett*., vol. 52, no. 2, pp. 364-372, Dec. 2009.

[32] P. Nayeri, "Advanced design methodologies and novel applications of reflectarray antennas reflectarray antennas," Electronic Theses and Dissertations, University of Mississippi, 2012.

**Ahmet Hulusi Gülseren** received the B.S degree, M.S degree and Ph.D. degree in Electronics and Communications Engineering from Yildiz Technical University (YTU), Istanbul, Turkey, in 2014, 2018 and 2024 respectively. In 2016, he joined the faculty of Electrical and Electronics Engineering Department of Aydın Adnan Menderes University, Aydın, Türkiye, where he is currently research assistant. His research interests include antennas, metamaterials and microwave circuits.

**Selda Yilmaz** was born in 1994. She received the B.S. and M.S. degrees from the Yildiz Technical University, in Istanbul, in 2016 and in 2023, both in Electronic and Communication Engineering. Her research interest is antenna communication.

**Aytaç Alparslan** received the B.S. and M.S. degrees in electrical and Electronic Engineering from Koç University, İstanbul, Türkiye, in 2006 and 2008, respectively, and the Ph.D. degree in Information Technology and Electrical Engineering from ETH Zürich in 2013. From 2013 to 2014, he was a postdoctoral fellow at the Institute of Electromagnetic Fields at ETH Zürich. In 2014, he joined the faculty of Electrical and Electronics Engineering Department of Trakya University, Edirne, Türkiye, where he is currently an associate professor. His research interests include computational electromagnetics, metamaterials, layered media and plasmonics.

**Nurhan Türker Tokan** received her B.Sc. degree in Electronics and Communications Engineering from Kocaeli University in 2002 and her M.Sc. and Ph.D. degrees in Communication Engineering from Yildiz Technical University (YTU), Istanbul, Turkey, in 2004 and 2009, respectively. From May 2003 to May 2009, she worked as a research assistant in the Electromagnetic Fields and Microwave Technique Section of the Electronics and Comm. Eng. Dept. of YTU, Istanbul, Turkey. Between May 2009 and April 2015, she worked as an assistant professor and between April 2015 and August 2021, she worked as an associate professor in the Electronics and Comm. Eng. Dept. of YTU. Since August 2020, she has been working as a professor at the same department. From October 2011 to October 2012, she was Postdoctoral researcher in the EEMCS Department of Delft University of Technology, Delft, Netherlands. From October 2012 to May 2013, she was a Postdoctoral Fellow supported by European Science Foundation at the Institute of Electronics and Telecommunications (IETR), University of Rennes 1, Rennes, France. She is the author or coauthor of more than 50 papers published in peer-reviewed international journals and conference proceedings. Her current research interests are analysis and design of antennas with emphasis on dielectric lens antennas and wideband antennas, microwave circuits and intelligent systems.

# Optimized Deep Graph Shallow Attention Neural Network Based Four-port Multiple-input-multiple-output Antenna Design for Sub-6 GHz 5G Applications

**E. Suganya[1], T. Anita Jones Mary Pushpa[1], and T. Prabhu[2]**

[1]Department of Electronics and Communication Engineering
Karunya Institute of Technology and Sciences, Coimbatore 641114, Tamil Nadu, India
suganyae@karunya.edu.in, anitajones@karunya.edu

[2]Department of Electronics and Communication
Presidency University, Bengaluru, Karnataka 560064, India
prabhu@presidencyuniversity.in

***Abstract*** **–** This paper proposes a novel, four-port multiple-input-multiple-output antenna system that is considered for sub-6 GHz 5G applications. A compact multi-band circular printed monopole antenna (MCPMA) is designed for determining the appropriate dimensions of size 110.16×360 mm. The device operates from 0.6 to 1 GHz. To improve cell isolation, four slits are positioned at an angle on the common ground. Deep graph shallow attention neural network with adaptive gold rush optimization algorithm (DGSANN-AGROA) is employed to create a model establishing the relationship among transmission coefficients and antenna geometric parameters. Following this, an adaptive gold rush optimization algorithm (AGROA) is utilized to enhance the antenna array's decoupling. It showcases pattern diversity, a valuable characteristic for multiple-input-multiple-output implementation. Simulations were conducted using HFSS19 software versions, followed by an evaluation of the introduced antenna in MATLAB. The multiple-input-multiple-output antenna demonstrates favorable diversity characteristics with acceptable diversity gain (>9.5 dB) and envelope correlation coefficient (ECC) (≤0.009).

***Index Terms*** **–** Circular printed monopole antenna, deep learning, gold rush optimization, multiple-input-multiple-output, peak gain, return loss.

## I. INTRODUCTION

As the number of consumers continues to rise and wireless communication technology evolves rapidly, there is a growing demand for higher throughput and channel capacity. Integrating multiple antennas into a single portable device emerges as a viable solution, promising an enhancement in communication network quality and transmission rates [1–3]. The technology central to 5G research, known as multiple-input-multiple-output (MIMO), plays a crucial role in addressing these needs [4, 5]. Several countries have already taken the lead by 5G networks.

Introducing an electromagnetic bandgap (EBG) structure between four widely spaced monopole antennas achieves a mutual coupling reduction [6, 7]. The antenna demonstrates an envelope correlation coefficient (ECC) of 0.3. Simplifying fabrication has been created but operates above 2.0 GHz [8]. In order to fulfil the needs of the sub-1 GHz and sub-6 GHz, a MIMO implementation featuring a four-port radiating antenna is introduced, utilizing coplanar waveguide (CPW) feeding [9]. The antenna features four radiating elements with multiple ports, particularly targeting the sub-6 GHz 5G NR frequencies. In this paper, a MIMO implementation featuring a four-port common radiating element antenna fed by CPW. The major contributions are as follows:

- The antenna with stub loading exhibits an omnidirectional radiation pattern, providing a pattern diversity well-psuited for implementing MIMO systems.
- The antenna's circularly polarized feature enables it to mitigate multipath fading and provides flexibility in polarization, unlike a linearly polarized antenna.
- The outcomes of optimization using deep learning closely resemble those obtained through simulation and experimentation. Also, indicating that the suggested design is well-suited for 5G communication, due to its high diversity gain (DG), low ECC and significant isolation among radiators.

The manuscript is organized as follows. Section II presents a literature survey related to the proposed

*Submitted On: March 4, 2024*
*Accepted On: October 17, 2024*



https://doi.org/10.13052/2024.ACES.J.390903

methodology. Section III provides an in-depth explanation of the proposed methodology. Section IV showcases the results and discussions. In section V, the entire paper is concluded.

## II. RELATED WORKS

Wu et al. [10] introduced a MIMO antenna with an asymptote-shaped design. The design achieves polarization diversity by arranging the antenna elements orthogonally to one another. As a result, the antenna proves to be highly suitable for various applications, such as indoor positioning and tracking.

Ali and Ibrahim [11] suggested a flower-shaped MIMO antenna. The MIMO antenna was suitable for integration into portable electronic devices, enabling their operation for a wide range of applications requiring broad frequency bands.

Sarkar et al. [12] suggested an electromagnetic modelling framework for ultra-wideband (UWB) MIMO antennas. These machine learning models were implemented and evaluated to assess their performance within the modelling framework.

Elabd and Al-Gburi [13] suggested a specific absorption rate (SAR) assessment for millimeter-wave 5G smartphones. The constructed antennas showed enhancements in the overall active DG, reflection coefficient (RC) and average gain. The simulation and test results exhibited commendable alignment within the desired frequency range, suggesting the potential applicability of the design in millimeter-wave 5G smartphones.

### A. Problem statement

The MIMO antenna described in existing works employs a T-shaped decoupling structure between cells, effectively achieving isolation exceeding 24 dB. In the traditional MIMO antenna design, polarization diversity and a docking floor operation contribute to an average isolation level exceeding 26 dB within the operational range. However, this antenna has drawbacks, including high ECC and excessive size. Conventional microstrip antennas commonly exhibit limitations like narrow frequency bands and variations in parameters based on the dielectric substrate. As a result, they are generally less favored in the design of antennas. In order to achieve a compact design, antennas in MIMO systems are positioned closely together. However, this proximity gives rise to the unwanted mutual coupling effect, leading to a degradation in the overall performance of the system. These motivated us to do this research work based on deep graph shallow attention neural network with adaptive gold rush optimization algorithm.

## III. PROPOSED METHODOLOGY

As the consumer base expands and wireless communication technology advances rapidly, the demand for increased throughput and channel capacity has become paramount. Integrating multiple antennas into a single portable device emerges as a viable solution, ultimately enhancing both the communication network's quality and transmission rates. Consequently, the pivotal role of MIMO technology in the forefront of 5G research becomes evident. This paper introduces the four-port MIMO antenna, termed the deep graph shallow attention neural network with adaptive gold rush optimization algorithm (DGSANN-AGROA). When it is designed with a multi-band circular printed monopole antenna (MCPMA) configuration, careful consideration of several critical parameters is imperative.

Key design elements include resonant frequency, RC, impedance bandwidth, stub position, parameters associated with the displacement of the ground plane to the right or left, and the antenna's feed position. These design parameters significantly influence the performance characteristics of the MIMO system. Therefore, optimization of these parameters is achieved using DGSANN-AGROA to enhance predictive accuracy. The resulting optimized stub-loaded antenna features four radiating elements, providing pattern diversity conducive to MIMO implementation. Subsequently, simulations were conducted using HFSS19 software versions. The analysis encompasses performance metrics, including ECC and DG.

In the proposed design, integration of a deep graph shallow attention neural network (DGSANN) with an adaptive gold rush optimization algorithm (AGROA) is crucial for achieving balanced and robust performance across key parameters. To further enhance the antenna configuration, characteristic mode analysis (CMA) is employed. CMA, widely utilized for modal significance interpretation, is instrumental in optimizing antenna placement, bandwidth enhancement and decoupling, ultimately crafting a multiband antenna capable of operating within the 0.6-6.0 GHz range to meet higher-band communication needs.

### A. Optimization to accomplish circularized polarization via the deep learning algorithm

As the number of antennas grows in higher-order MIMO design, there is a proportional increase in both required resources and costs. This phenomenon is recognized as a fundamental drawback of higher-order MIMO systems. Expanding the number of antennas in higher-order MIMO design results in an escalation of necessary resources and costs. Figure 1 illustrates the workflow of the introduced method.

Simulation results suggest that modifying the geometric values of parasitic elements (PEs) while preserving their structures has minimal impact on $S_{11}$. As a result, the suggested DGSANN system must accurately represent the mapping relationship among the

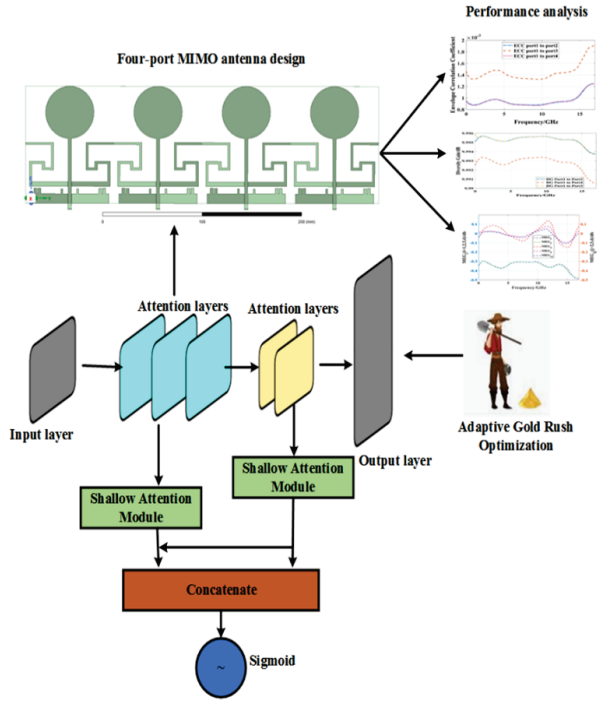


Fig. 1. Procedure of introduced antenna design.

geometric variables of PEs and the antennas $S_{21}$, excluding consideration of $S_{11}$. Following initial DGSANN training, AGROA aids predictions. The fitness function aligns with the predicted objective. Due to incomplete DGSANN training, predictions are imprecise. These are incorporated into DGSANN training and testing data, effectively reducing the number of training samples and significantly enhancing prediction accuracy. These design parameters collectively play a crucial role in shaping the MIMO system's performance characteristics. DGSANN is a combination of a graph neural network with a shallow attention module.

*1. Graph shallow attention neural network (GSANN)*

The graph attention network (GAN) presents a structure based on multi-head attention to comprehend the node's higher-level features in a graph through the utilization of a shallow attention strategy. Each attention head possesses its own set of parameters. The majority of both training and testing datasets comprises small parameters, resulting in substantial information loss during the repeated down-sampling in convolutional neural networks (CNNs). In the realm of MIMO antenna design, addressing this issue is essential. Shallow features $(s_f)$ play a vital role due to their high resolutions, offering distinct object boundaries crucial for precise prediction.

Let us consider the impact of feedline ($L_F$) on modal resonance frequency ($F_{m1}$) and the percentage change in resonance frequency ($\Delta F$) for four cases. By choosing $L_F/P_1$ appropriately (where $P_1$ is the radius), control over $F_{m1}$ and $\Delta F$ is achieved to meet design requirements. Increasing $L_F$ from 0 on a fixed $P_1$ reduces the fundamental mode resonance frequency ($F_{m1}$) for the circular printed monopole, observed consistently across all $P_1$ cases. By raising $L_F/P_1$, $F_{m1}$ decreases for a given $P_1$. The figures also illustrate the $L_F/P_1$ effect on $\Delta F$ change, which stabilizes around 10% for larger values. Notably, operating at a specific $F_{m1}$ requires a smaller feed length for a larger monopole radius and vice versa. This flexibility in choosing $P_1$ and $L_F$ provides an additional design parameter for crafting a compact monopole antenna.

Following the strategy guide, a CPW-fed antenna along with $P_1$=35 mm is chosen. $F_{m1}$ at ($L_F/P_1$=0) is about 3 GHz, reduced to around 1.05 GHz with $L_F$=65 mm ($L_F/P_1$=2). Further lowering $F_{m1}$ is achieved through additional metallic strip loading. Let us consider the impact of adding a metallic sheet $(S_L \times S_W)$ on $F_{m1}$ and multimodal resonance frequencies $F_{mn}$ ($n$=1,2,3...) controlling bandwidth. Five modal frequencies, excluding mode#4 with $M_S < 0.5$, are displayed. These modes satisfy $M_S \geq 0.85$ over a wide frequency band. Additionally, $F_{m1}$ at 0.652 GHz can be harnessed for a substantial sub-1 GHz bandwidth. $M_S$, the metallic strip $S_W \times 2S_L$, becomes the ground plane modified with a slit ($s$) for the SMA connector.

These features have limitations related to the receptive field and may be overshadowed by background noise, posing challenges for direct utilization. To tackle this, let us introduce the shallow attention module (SAM) which utilizes coarse-boundary deep features $(d_f)$ to filter out background noise from $(s_f)$.

The multi-layer's input GAN consists of the node feature matrix $Y \in \Re^{M\times D}$ and the adjacency matrix $B \in \Re^{M\times M}$ which represents the connections between nodes.

The iteration process is defined:

$$I^{(\ell+1)} = \sigma\left(\tilde{E}^{-\frac{1}{2}}\tilde{B}\tilde{E}^{-\frac{1}{2}}I^{(\ell)}MI^{(\ell)}\right), \tag{1}$$

where $\tilde{B} = \tilde{B} + L_M$ ($L_M$ denotes the identity matrix), the activation function is given as $\sigma$, $\tilde{E}_{jj} = \sum_j \tilde{B}_{jj}$ and the learnable parameter is denoted as $M$. The outcome $S \in \Re^{M\times G}$ is mathematically defined:

$$S = \tilde{E}^{-\frac{1}{2}}\tilde{B}\tilde{E}^{-\frac{1}{2}}Y\Theta, \tag{2}$$

where $\Theta \in \Re^{D\times G}$and the feature maps are denoted $G$.

The mathematical model for GSANN is given in:

$$Attention = \rho\left(u_p\left(d_f\right)\right), \tag{3}$$

$$s_f = Attention \otimes s_f, \tag{4}$$

where $u_p(\cdot)$ denotes the up-sampling operation, $\rho(\cdot)$ represents the ReLU function and $\otimes$ indicates element-wise multiplication. Following SAM, shallow features $(s_f)$ undergo a significant enhancement, becoming clearer and offering crucial cues for small parameters. SAM also plays a vital role in achieving feature balance

across various blocks. The computation of output features for nodes is expressed in:

$$g'_j = \left\| n=1,\ldots.N \left( \beta^n_{j,i} M g_j + \sum_{i \in M(j)} \beta^n_{j,i} M g_i \right) \right\|, \quad (5)$$

where $g'_j$ is the output feature, $\|\|$ concatenates the outcomes from various attention strategies, $W$ represents the count of attention heads and $M \in \Re^{D' \times D}$ is a weight matrix. The attention coefficient $\beta_{j,i}$, which signifies the relationship among every input node $j$ and its first-order neighbor, is computed by:

$$\beta_{j,i} = \frac{\exp\left(elu\left(b^T \left[Mg_j \| Mg_i\right]\right)\right)}{\sum_{r \in V(j)} \exp\left(elu\left(b^T \left[Mg_j \| Mg_r\right]\right)\right)}, \quad (6)$$

where exp represents the exponential function, $Mg_j, Mg_i$ and $Mg_r$ denote matrix of nodes $i, j$ and $r$, $\Sigma r \in V(j)$ is the sum over all nodes $r$ that are neighbors of node $j$, $b^T \in \Re^{D'}$ represents a learnable weight vector, $T$ is its appropriate transpose, and $elu$ is a activation function where $x$ equals 0 when $y$ is negative. Subsequently, the $softmax$ function is used to normalize all neighbor nodes $i$ of $j$, which is mentioned in:

$$\rho_t = softmax\left(M_{out} \cdot b^t + a_{out}\right), \quad (7)$$

where $\rho_t$ represents the probability of $t$, and $M_{out}$ denotes the weight matrix and $a_{out}$ denotes the bias vector. The variables $b^t$ correspond to the embedding features learned by preceding layers.

The GAN-based system employs three consecutive GAN layers, each initiated by the ReLU operation. Traditionally, GANs are utilized for node classification, where the outcomes are node-level feature vectors. To derive graph-level features, employ max pooling method collective features from all nodes within the graph and assess their performance.

Evaluation reveals that incorporating a max pooling layer within the GAN-based architecture yields superior results compared to other pooling methods. Consequently, we integrate a global max pooling layer after the final GAN layer to effectively extract and represent the overall features.

By employing combinations with labels, the model was trained using cross-entropy as the loss function. The goal is to minimize the loss throughout the training process:

$$L = minimum\left( -\sum_{j=1}^{V} \log Q_{t_j} + \frac{2}{\eta} \|\Theta\| \right), \quad (8)$$

where $L$ is the loss, $\Theta$ denotes the set encompassing all bias and trainable weight parameters within the system. $V$ represents the total number of samples, $t_j$ signifies the $j$th sample's label, and $\eta$ represents an L2 regularization hyper-parameter. In this work, the optimal parameters are extracted with the help of AGROA approach.

### B. AGROA for enhancing the antenna array's decoupling

A significant historical occurrence related to gold is the gold rush, signifying a remarkable influx of individuals aspiring to amass wealth [14].

Table 1 provides the pseudocode for the GRO method. The mathematical model for the fitness function is:

$$Fitness\_function = \min\left(R_f, R_c, S_p\right), \quad (9)$$

where $R_f$ denotes the resonant frequency, $R_c$ represents RC, and $S_p$ is the stub position. Cost function minimization in antenna design is crucial for optimizing key performance parameters such as $R_f$, $R_c$, $B$ and $S_p$. The resonant frequency is targeted to ensure the antenna operates effectively at the intended frequency, while the reflection coefficient is minimized to achieve better impedance matching and reduce power loss. Stub positions are optimized for fine-tuning impedance and other performance metrics. The cost function combines these parameters into a single metric that the optimization algorithm minimizes, balancing trade-offs and guiding adjustments to find the best configuration. By minimizing deviations from desired values for $R_f$, $R_c$ and $S_p$, the cost function

Table 1: Pseudocode of AGROA

Initialize the population of gold prospectors $Y_j, j = 1,2,\ldots,M$

Initialize the new positions of gold prospectors $Y_{new_j} = Y_j, j = 1,2,\ldots,M$

Initialize $t, t_1, t_2$

$Y*$ is the optimal search agent

while $t \le \max iteration$ do

for all search agent $j$ do

compute the present search agent's fitness function ( $F$ ) at $Y_{new_j}$ (new position)

Update the current position of the search agent $Y_j$ derived from (9)

$$\vec{Y}_j(t+1) = \overrightarrow{Y_{new_j}}(t+1) if\ F\left(\overrightarrow{Y_{new_j}}(t+1)\right) < F\left(\vec{Y}_j(t)\right) \quad (9)$$

Update optimal search agent $Y*$

end

Update $t_1, t_2$ $t_e$ (location) using (10)

$$t_e = \left(\frac{maximum_{iteration} - iteration}{maximum_{iteration} - 1}\right)^e \left(2 - \frac{1}{maximum_{iterstion}}\right) + \frac{1}{maximum_{iterstion}} \quad (10)$$

Update the $p$ is calculated using (11),

$$p = 1 - \left(1.01 \times t^3 / Maximum\_iteration^3\right) \quad (11)$$

for all search agent $j$ do

compute present search agent's $Y_{new_j}$ next position with three primary concepts

end

$t \leftarrow t + 1$;

end

return $Y*$;

ensures no parameter becomes a significant weak point, leading to a well-rounded, robust and reliable antenna design. This approach systematically enhances antenna performance across all critical aspects for promoting robust and reliable performance.

In this paper, DGSANN-AGROA is used to design a novel four-port MIMO antenna system that is considered for sub-6 GHz 5G applications. Following this, an AGROA is utilized to enhance the antenna array's decoupling.

## IV. RESULTS AND DISCUSSIONS

Simulations are performed using HFSS19 software, followed by an assessment of the introduced antenna in MATLAB. The performance measures which are utilized to show the effectiveness of the introduced antenna design are gain, ECC and DG.

Table 2 provides the introduced antenna design parameters.

The antenna component, the surface current density ($I_r$) at the frequency $F_{m1} =$ 0.643 GHz, and the RC of the antenna are illustrated in Figs. 2 (a, b). Figure 2 (b) presents a depiction of the antenna modified with stub loading. To improve the bandwidth, the antenna's impedance matching range is improved by introducing stubs $R1$, $R2$ and $R3$, as illustrated in Fig. 2 (b). These stubs improve the impedance matching range, allowing the antenna to achieve better performance over a wider frequency range.

As an outcome of these modifications, the antenna exhibits resonance at an exceptionally minimum frequency of 0.605 GHz, accompanied by a 34% fractional bandwidth. This means the antenna can operate effectively over a broader range of frequencies, making it more adaptable to different applications. The use of stub loading is key to this performance enhancement, as it allows for precise tuning of the resonant frequency and a significant increase in operational bandwidth.

Table 2: Design parameters of introduced antenna

| **Parameters** | $L_s$ | $W_s$ | $R_1$ | $L_f$ | $W_F$ | $G_L$ | $G_W$ | $g$ | $L_p$ | $g_1$ |
|---|---|---|---|---|---|---|---|---|---|---|
| **Value** $(mm)$ | 110.16 | 80 | 24.6564 | 52 | 3.24 | 38 | 9 | 1.62 | 7 | 0.5 |
| **Parameters** | $R_1$ | $R_2$ | $R_3$ | $S_1$ | $S_2$ | $S_3$ | $S_4$ | $S_5$ | $S_6$ | $S_7$ |
| **Value** $(mm^2)$ | 5.2136 × 2.97 | 5.0976 × 3.3156 | 4.6764 × 1.9548 | 39 × 4.2444 | 16.9992 × 2.29608 | 13.0032 × 2.29608 | 6.00372 × 2.6352 | 9.3528 × 2.1168 | 23.8032 × 2.1168 | 28 × 2 |

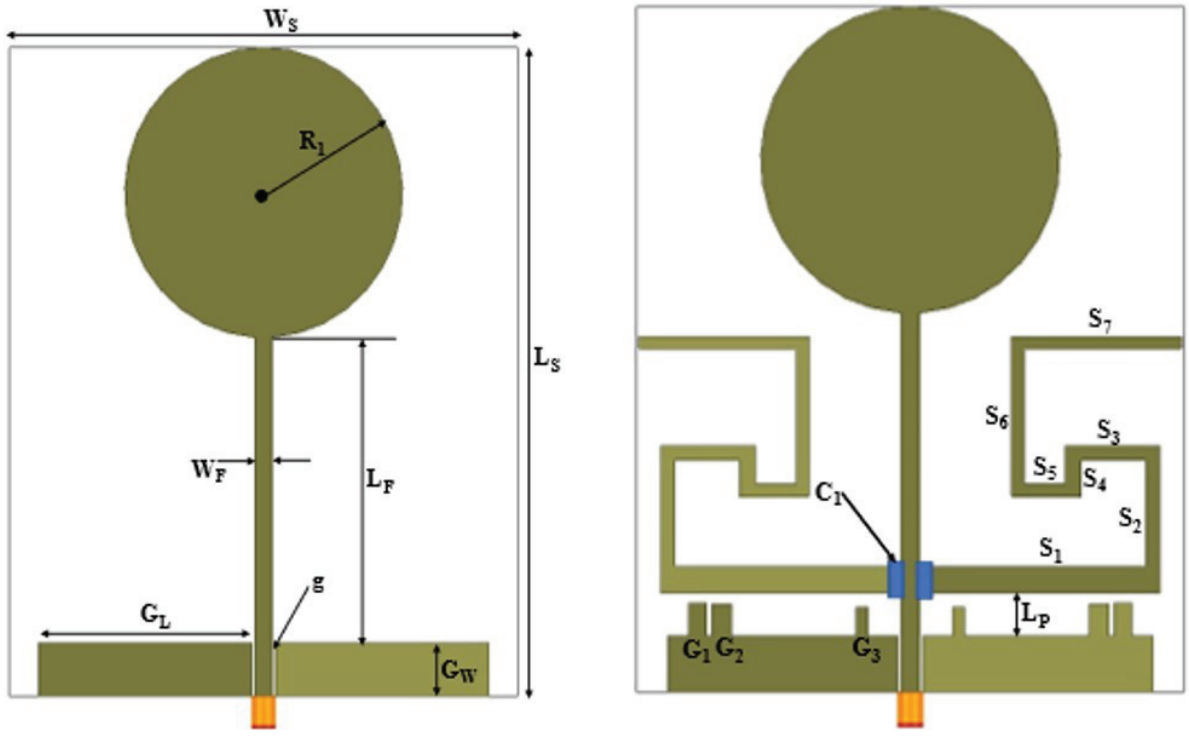


(a) (b)

Fig. 2. Antenna (a) structure and (b) circular printed monopole.

The resonant frequency and operational bandwidth are subjected to modification through the application of stub loading, as indicated in reference [15]. The parameters of Fig. 2 are: $W_s$ is the total antenna's area, $R_I$ be the printed circular monopole's radius, $W_F$ is the feed-line width, $L_f$ represents the feed-line, $G_W$ is denoted as ground plane width, $g$ denotes ground, the length of ground plane is given as $G_L$, $(S_1 - S_7)$ are the stubs, $(R_1 - R_3)$ is represented as ground stubs, $C_1$ denotes capacitances, and length of the projecting part of the monopole is given as $L_p$.

Due to frequency limitations, the antenna's 2D radiation patterns at 3.7 and 6.9 GHz were exclusively measured at all four ports using the standard horn. The results exhibit reasonable coverage yet, at 6.9 GHz, elevated cross-polarization occurs due to the anechoic chamber's limited noise floor. Despite some deviation caused by substrate sagging and mechanical support issues, the measurements offer valuable insights regarding the overall radiation characteristics of the antenna. Figure 3 illustrates the 2D radiation pattern of the introduced antenna.

The axial ratio of the introduced circularly polarized antenna was measured at 3.7 GHz and 6.9 GHz using a standard antenna. At 3.7 GHz, the antenna exhibited reasonable coverage, with the axial ratio likely below 3 dB, indicating good circular polarization performance. However, at 6.9 GHz, the measurements showed elevated cross-polarization due to the limited noise floor. This suggests a higher axial ratio at this frequency, which impacts the ideality of circular polarization. Causing interference, nulls, zones of weak or no signal, could also be identified, impacting desired coverage areas. Analyzing beamwidth, the angle of strong signal, is crucial. A narrow beam might be ideal for satellite communication but unsuitable for a cell tower needing broad coverage. Asymmetry in the pattern, potentially caused by imperfections or nearby objects, can lead to uneven signal strength. Figure 3 (a) illustrates the lobes for port 1 may have a specific orientation, indicating

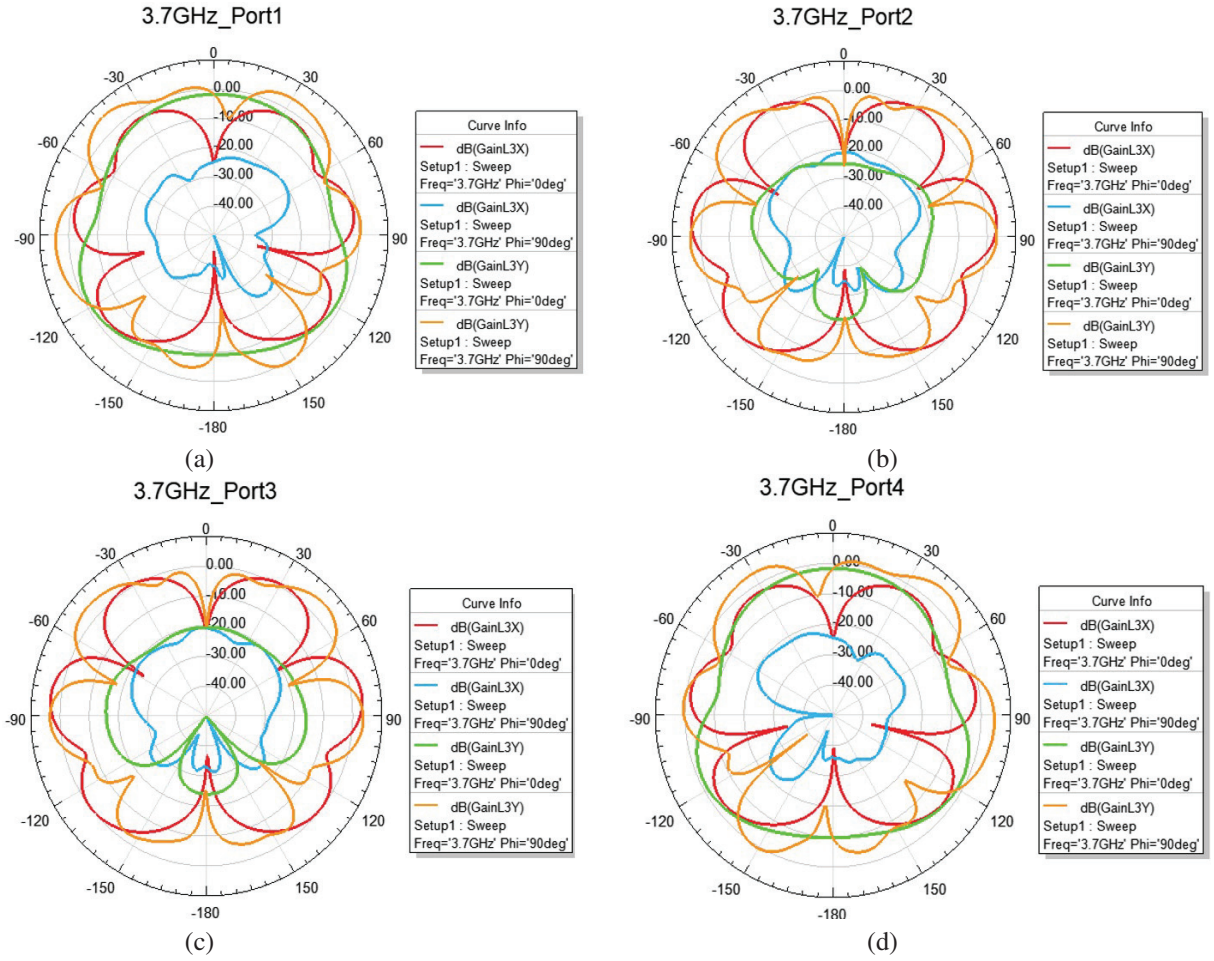


Fig. 3. *Continued*

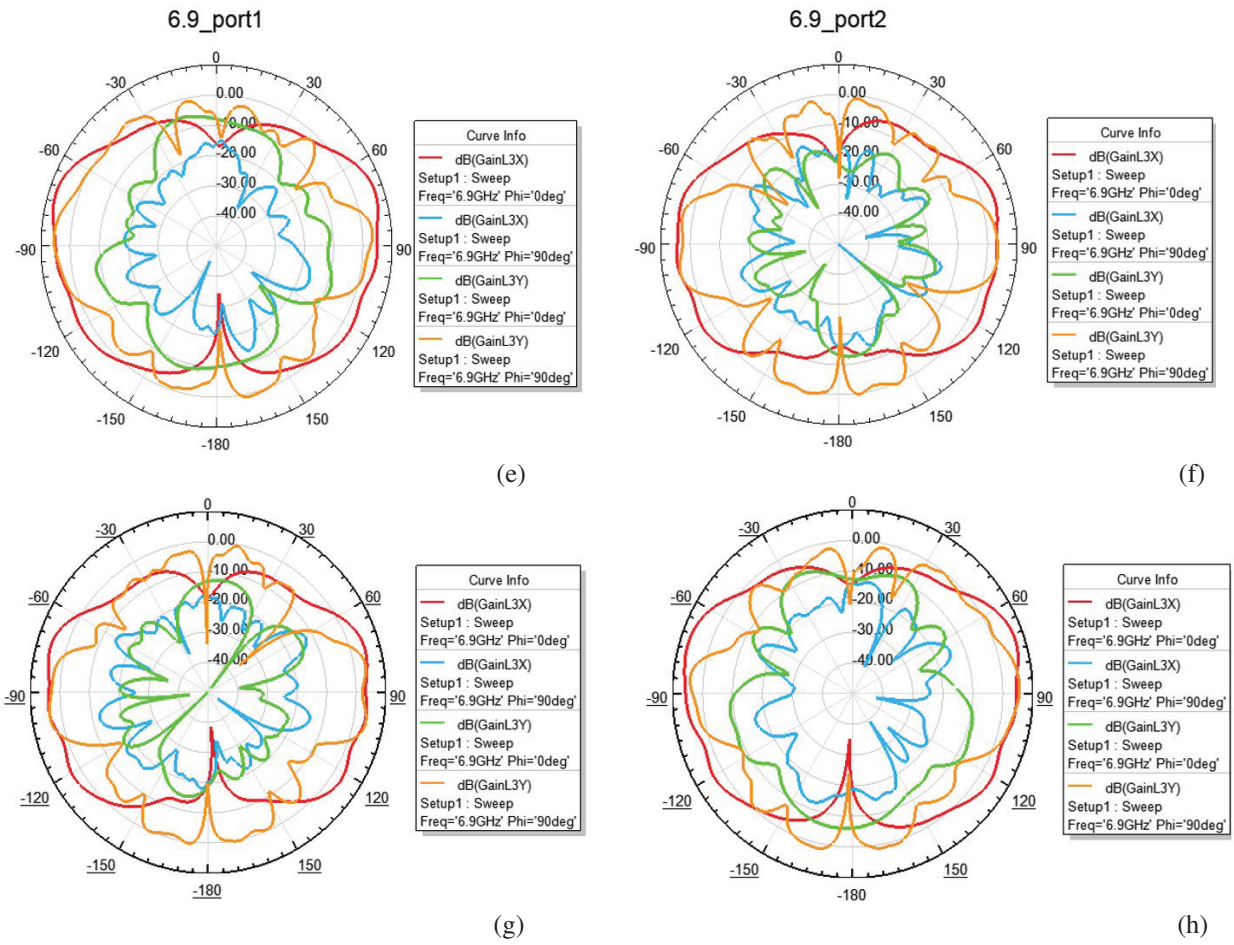


Fig. 3. Computed 2D radiation pattern: (a) port 1, (b) port 2, (c) port 3, (d) port 4 at 3.7 GHz, (e) port 1, (f) port 2, (g) port 3, and (h) port 4 at 6.9 GHz.

stronger radiation in particular directions. Figure 3 (b) demonstrates the shape of the lobes might differ, with port 2 having wider or narrower lobes compared to port 1. In Fig. 3 (c), the pattern of port 3 appears more consistent across different phi angles, whereas port 4 shows more variation. Figure 3 (d) port 4 shows more complexity in the side lobe structure, indicating potential differences in antenna design. The port radiation pattern in Fig. 3 (e) should exhibit a symmetrical distribution.

Figure 3 (f) is similar to port 1. This port should also show a symmetrical radiation pattern, ensuring good coverage without significant nulls or weak zones.

The pattern in Fig. 3 (g) should be checked for uniformity and any deviations that might indicate interference or reflection issues. The radiation pattern symmetry and coverage in Fig. 3 (h) are crucial for ensuring consistent signal strength and minimal interference.

In Fig. 4 (a), ECC curves show correlation levels between port 1 and other ports. Figure 4 (b) displays ECC curves among the remaining ports (2, 3, 4) meeting the MIMO system requirements for antenna correlation parameters. The ECC values are critical for determining the performance of MIMO systems, as it measures the correlation between signals received or transmitted by different antenna elements. All ports are excited at a frequency of 3.5 GHz. ECC values should ideally be below 0.5. In this graph, due to the antennas being placed adjacent to each other, antenna pairs 1 and 2 show higher correlation compared to pair 1 and 3, and pair 1 and 4. However, at desired frequencies like 1 GHz, 3.7 GHz and 6.9 GHz, the ECC values remain below 0.31. These low ECC values signify minimal correlation, validating the antenna's suitability for MIMO applications.

If all the ports are excited, ECC values should be below 0.5. This minimal correlation is essential for ensuring efficient MIMO performance, as it allows for better signal diversity and improved data throughput. Thus, antenna design effectively meets the

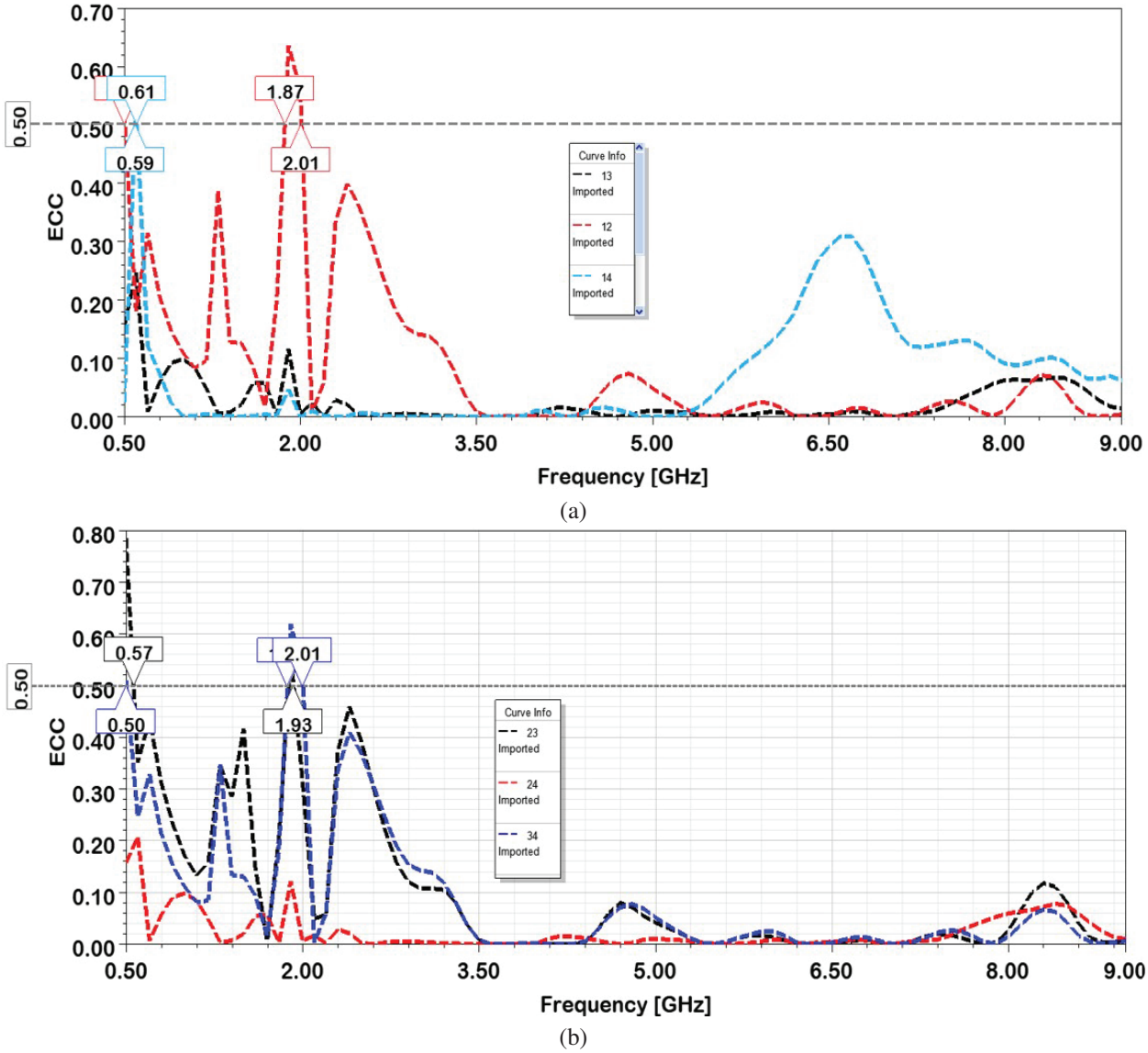


Fig. 4. Envelope correlation coefficient among (a) port 1 and others and (b) ports 2, 3, and 4.

requirements for MIMO systems, demonstrating its suitability for applications that demand high-performance multi-antenna configurations. In Fig. 4 (b), due to the antennas being placed adjacent to each other, pair 2 and 3, and pair 3 and 4, exhibit higher correlation compared to pair 2 and 4.

DG is a vital parameter characterizing the diversity features of the model. It quantifies improvement in signal quality due to the use of multiple antennas to receive or transmit the signal. High DG values indicate effective mitigation of fading and signal degradation, which are common in wireless communication environments. As indicated in Fig. 5, the DG at ports 1 and 2 for the proposed antenna surpasses 100 dB. This is a remarkably high value, indicating that the antenna system has excellent diversity performance. Such a high DG suggests that the antennas are capable of effectively combining signals from different paths, reducing the impact of signal fading and improving overall signal reliability and quality. This observation suggests that MIMO antennas exhibit strong diversity properties, emphasizing their capability to enhance performance in diverse signal conditions. Table 3 provides a comparison of ECC metrics between the proposed method and existing methods.

The antenna was fabricated using an EP42 auto prototyping machine from Everprecision PCB. It was subsequently tested in the anechoic chamber at the Antenna

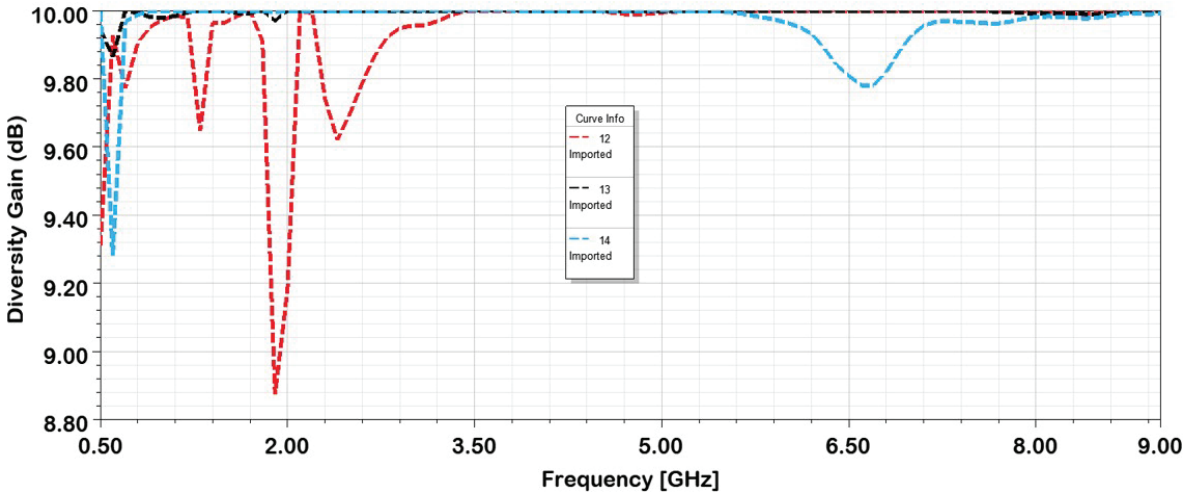


(a)

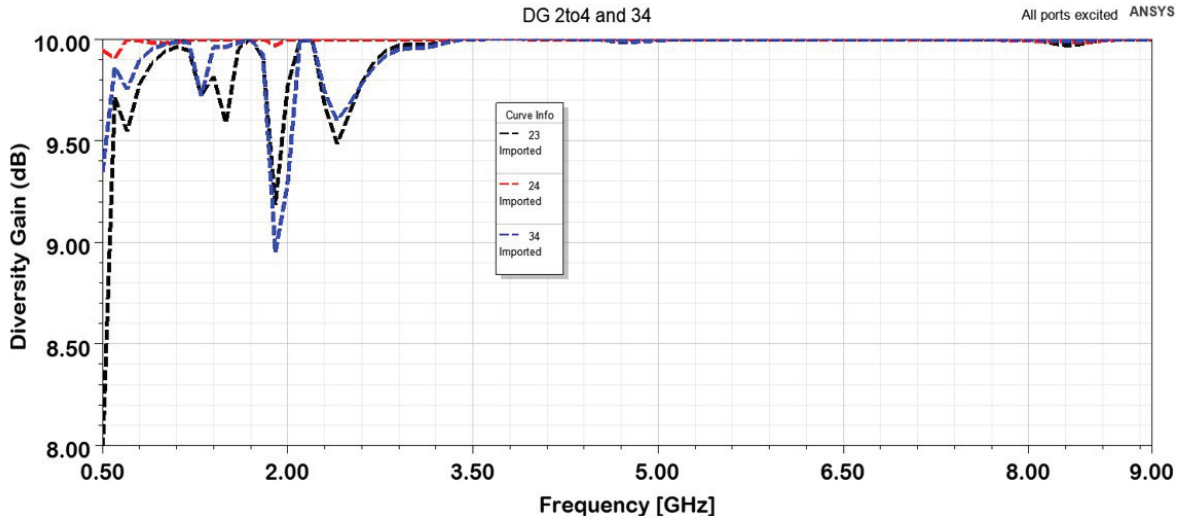


(b)

Fig. 5. Diversity gain among (a) port 1 and (b) port 2.

Table 3: Four-port antenna design comparison

| Four-port Antenna Design | ECC/dB |
|---|---|
| Koch fractal element (four-port antenna) [16] | <0.4 |
| Four-port MIMO antenna [17] | <0.0408 |
| Four-port millimeter wave MIMO antenna [18] | <0.50 |
| DGSANN-AGROA (proposed) | 0.009 |

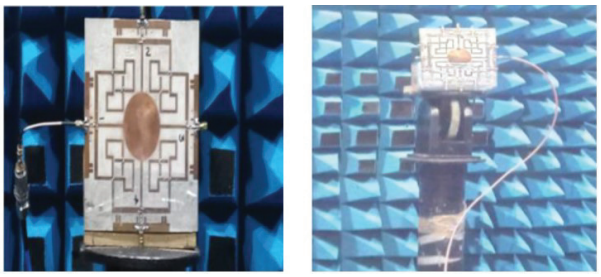

(a) (b)

Fig. 6. Antenna: (a) fabricated prototype and (b) under testing in the anechoic chamber.

and Microwave Design laboratory. The resulting planar four-port antenna is illustrated in Fig. 6.

Figure 7 illustrates the cost complexity comparison of the proposed method with existing methods. This line graph depicts the performance of three algorithms: Snow Geese Algorithm (SGA) [19], Botox Optimization Algorithm (BOA) [20] and Adaptive Gold Rush Optimization Algorithm (AGROA). The graph tracks the aver-

age cost function as the number of iterations increases. AGROA appears superior as its cost function decreases more significantly: 20-22 seconds is needed to train the network.

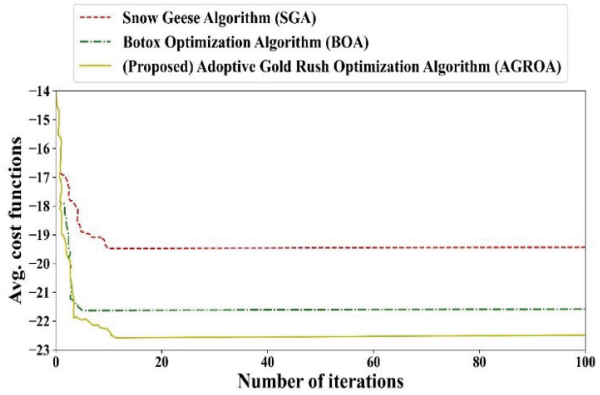


Fig. 7. Comparison of cost complexity.

Figure 8 (a) demonstrates the impact of stub loading on the $(Z(Re))$ real and $(Z(Im))$ imaginary parts of impedance. The addition of $S1-S3$ to the small ground plane ($S_W = 8.4$mm) increases inductance, improving $Z(Im)$ and enhancing impedance matching. This modification also alters $Z(Re)$. Figures 8 (b,c) compare the magnitude of RC with and without $R1-R3$, illustrating that the increased $Z(Im)$ leads to an improved $-6$ dB impedance matching level above 3.9 GHz across a wide range.

From the observations in Fig. 9, it is evident that slight shifts occur in the RC at various end ports for the antenna at varying frequencies. However, good matching is achieved in other regions. Note, $S(2,1), S(3,2)$ and $S(3,4)$ maintain an isolation below -11.77 dB, $S(3,1), S(4,2)$ maintain an isolation below

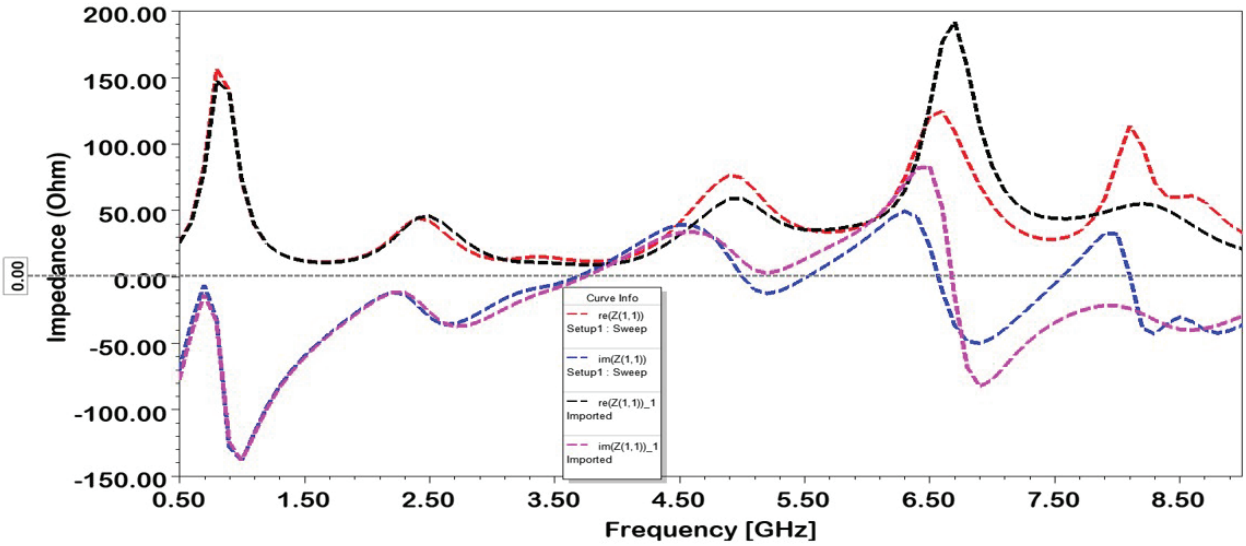


(a)

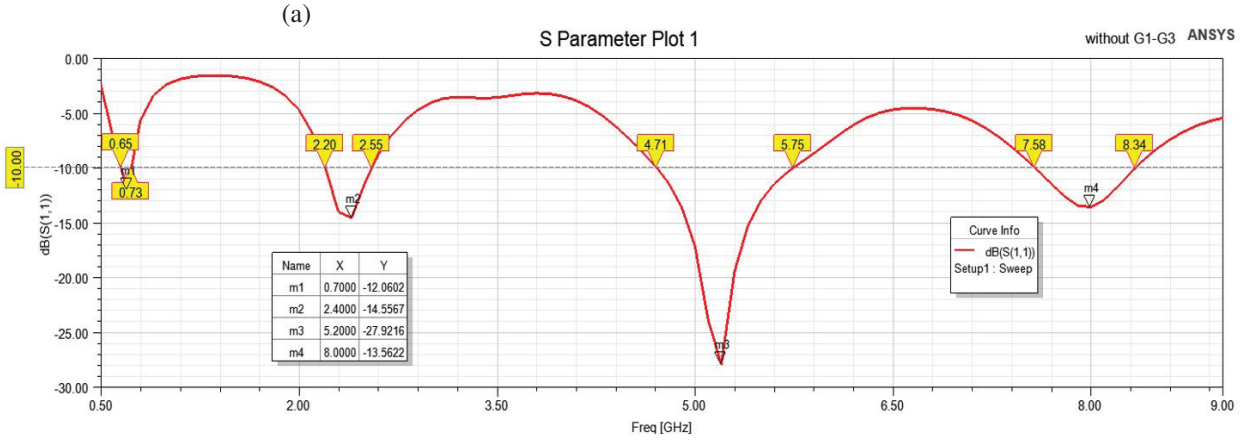


(b)

Fig. 8. *Continued*

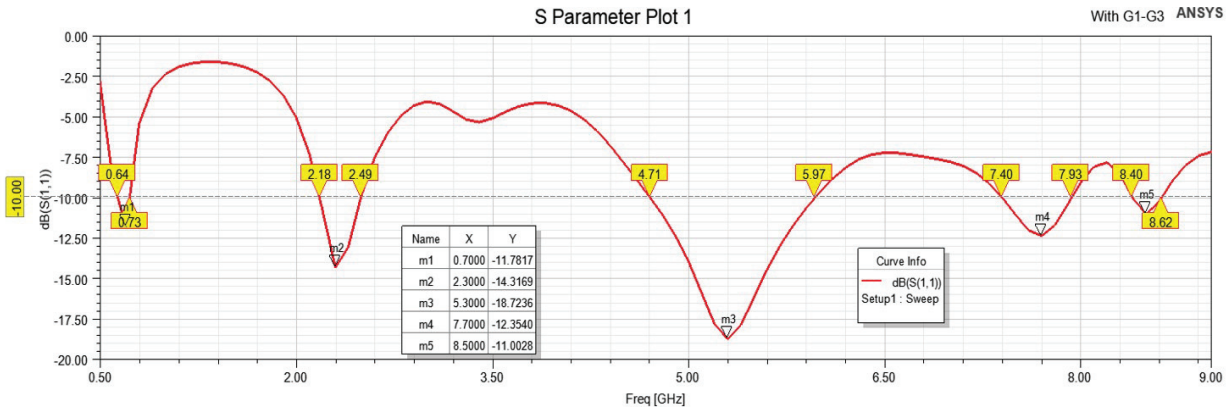


(c)

Fig. 8. Ground stubs effect: (a) impedance (b) RC (without $R1 - R3$) and (c) RC (with $R1 - R3$).

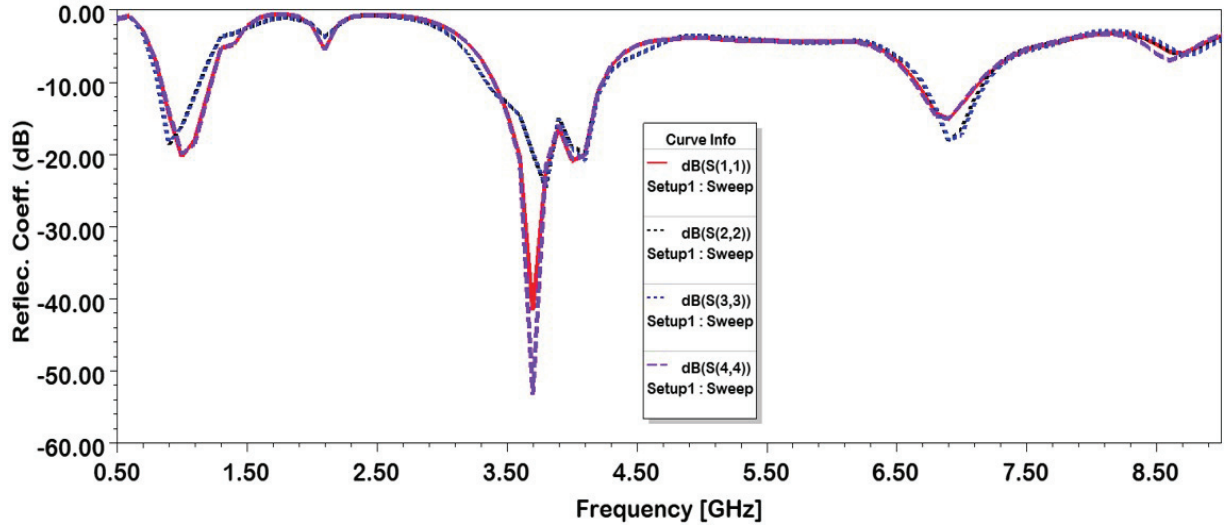


(a)

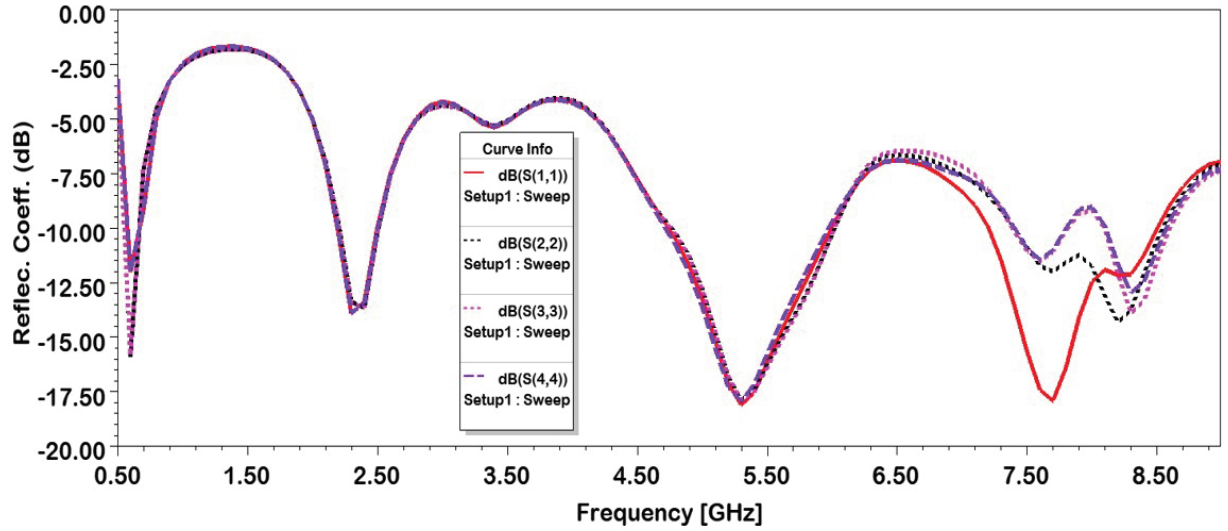


(b)

Fig. 9. MIMO antenna S-parameters: (a) RC with strips and (b) RC without strips.

-21.66 dB and $S(4,1)$ maintains an isolation below -29.33 dB.

## V. CONCLUSION

This paper presents the design of a compact four-port MIMO antenna with strong isolation capabilities. The proposed MIMO antennas achieve an isolation of -29.33 dB without compromising the overall antenna size. Simulated results show that the newly introduced antenna maintains a consistent omnidirectional radiation pattern, demonstrating outstanding gain, efficiency and high isolation as a four-port system. Furthermore, the MIMO antenna demonstrates favorable diversity characteristics with acceptable DG ($>$9.5 dB) and ECC ($\leq$0.009), establishing its excellence as a MIMO antenna with exceptional performance. A four-port antenna setup with a co-surfaced ground plane holds promise as a design for creating conformal and three-dimensional MIMO antennas in the future.

## REFERENCES


[1] B. Baz, D. Jansari, S. P. Lavadiya, and S. K. Patel, "Miniaturized and high gain circularly slotted 4×4 MIMO antenna with diversity performance analysis for 5G/Wi-Fi/WLAN wireless communication applications," *Results in Engineering*, vol. 20, p. 101505, 2023.

[2] M. Munir, S. H Kiani, H. Savci, D. A. Sehrai, F. Muhammad, A. Ali, H. Mostafa, and N. O. Parchin, "mmWave polarization diversity wideband multiple-input/multiple-output antenna system with symmetrical geometry for future compact devices," *Symmetry*, vol. 15, no. 9, p. 1641, 2023.

[3] P. Tiwari, V. Gahlaut, M. Kaushik, A. Shastri, V. Arya, I. Elfergani, C. Zebiri, and J. Rodriguez, "Enhancing performance of millimeter wave MIMO antenna with a decoupling and common defected ground approach," *Technologies*, vol. 11, no. 5, p. 142, 2023.

[4] D. Burghal, Y. Li, P. Madadi, Y. Hu, J. Jeon, J. Cho, A. F. Molisch, and J. Zhang, "Enhanced AI based CSI prediction solutions for massive MIMO in 5G and 6G systems," *IEEE Access*, vol. 11, pp. 117910-117825, 2023.

[5] S. S. Tyokighir, J. Mom, K. E. Ukhurebor, and G. Igwue, "New developments and trends in 5G technologies: Applications and concepts," *Bulletin of Electrical Engineering and Informatics*, vol. 13, no. 1, pp. 254-263, 2024.

[6] A. D. Tadesse, O. P. Acharya, and S. Sahu, "Wideband MIMO antenna mutual coupling reduction with electromagnetic band-gap structure," *IETE Journal of Research*, vol. 69, no. 9, pp. 6014-6021, 2023.

[7] A. Ali, M. Munir, M. M. Nasralla, M. Esmail, A. J. A. Al-Gburi, and F. A. Bhatti, "Design process of a compact tri-band MIMO antenna with wideband characteristics for sub-6 GHz, Ku-band, and millimeter-wave applications," *Ain Shams Engineering Journal*, vol. 15, no. 3, p. 102579, 2024.

[8] F. Taher, H. A. Hamadi, M. S. Alzaidi, H. Alhumyani, D. Elkamchouchi, Y. Elkamshoushy, M. T. Haweel, M. F. A. Sree, and S. Y. A. Fatah, "Design and analysis of circular polarized two-port MIMO antennas with various antenna element orientations," *Micromachines*, vol. 14, no. 2, p. 380, 2023.

[9] S. Ghosh, G. S. Baghel, and M. V. Swati, "Design of a highly-isolated, high-gain, compact 4-port MIMO antenna loaded with CSRR and DGS for millimeter wave 5G communications," *AEU-International Journal of Electronics and Communications*, vol. 169, p. 154721, 2023.

[10] A. Wu, Y. Tao, P. Zhang, Z. Zhang, and Z. Fang, "A compact high-isolation four-element MIMO antenna with asymptote-shaped structure," *Sensors*, vol. 23, no. 5, p. 2484, 2023.

[11] W. A. Ali and R. A. Ibrahim, "Highly compact 4×4 flower-shaped MIMO antenna for wideband communications," *Applied Sciences*, vol. 13, no. 6, p. 3532, 2023.

[12] D. Sarkar, T. Khan, Jayadeva, and A. A. Kishk, "Machine learning assisted hybrid electromagnetic modeling framework and its applications to UWB MIMO antennas," *IEEE Access*, vol. 11, pp. 19645-19656, 2023.

[13] R. H. Elabd and A. J. Al-Gburi, "SAR assessment of miniaturized wideband MIMO antenna structure for millimeter wave 5G smartphones," *Microelectronic Engineering*, vol. 282, p. 112098, 2023.

[14] K. Zolf, "Gold rush optimizer: A new population-based metaheuristic algorithm," *Operations Research and Decisions*, vol. 33, no. 1, pp. 113-150, 2023.

[15] S. Modak and T. Khan, "A slotted UWB-MIMO antenna with quadruple band-notch characteristics using mushroom EBG structure," *AEU-International Journal of Electronics and Communications*, vol. 134, p. 153673, 2021.

[16] A. Kumar, V. Prakash, and S. C. Padhy, "Four port MIMO antenna for IoT applications in public safety band and sub-6 GHz TDD 5G band," *Engineering Research Express*, vol. 6, no. 1, 2024.

[17] M. Srinubabu and N. V. Rajasekhar, "Enhancing diversity and isolation performance for a

four-port MIMO antenna in FR-1 5G frequency bands," *IETE Journal of Research*, vol. 70, no. 8, pp. 1-16, 2024.

[18] M. Sharma, A. Kumar, V. Kikan, G. Jaitly, S. Bhardwaj, and T. Bano, "Conformal ultra-compact narrowband 60.0 GHz four-port millimeter wave MIMO antenna for wearable short-range 5G application," *Wireless Networks*, vol. 30, no. 3, pp. 1-17, 2024.

[19] A. Q. Tian, F. F. Liu, and H. X. Lv, "Snow Geese Algorithm: A novel migration-inspired meta-heuristic algorithm for constrained engineering optimization problems," *Applied Mathematical Modelling*, vol. 126, no. 8, pp. 327-347, 2024.

[20] M. Hubálovská, Š. Hubálovský, and P. Trojovský, "Botox Optimization Algorithm: A new human-based metaheuristic algorithm for solving optimization problems," *Biomimetics*, vol. 9, no. 3, p. 137, 2024.

**E. Suganya** received her B.E. in electronics and communication engineering from the Bannari Amman Institute of Technology, Tamil Nadu, India, in 2009 and M.E. in communication systems from the Kumaraguru College of Technology, Tamil Nadu, India, in 2012. She is currently pursuing her Ph.D. in electronics and communication engineering at Karunya Institute of Technology and Sciences, India. She is an Assistant Professor in the Department of Electronics and Communication Engineering at Nitte Meenakshi Institute of Technology (NMIT), Bengaluru, India. She is a member of IEEE, ISTE and IAENG. Her area of interest includes planar antenna design, MIMO communication and wireless communication.

**T. Anita Jones Mary Pushpa** received her B.E. in electronics and communication engineering from Madurai Kamaraj University, Tamil Nadu, India, in 1998 and M.E. in communication systems from Madurai Kamaraj University, Tamil Nadu, India, in 1999. She completed her Ph.D. in information and communication engineering from Anna University, India, in 2014. She is an Associate Professor in the Department of Electronics and Communication Engineering at Karunya Institute of Technology and Sciences, India. She is a life member of IETE. Her area of interest includes miniaturized antennas and microwave communication.

**T. Prabhu** received the B.E. degree in electronics and communication engineering from Anna University, Chennai, India, in 2009 and M.E. degree in communication systems from Anna University, Chennai, India, in 2011. He completed his Ph.D. degree in information and communication engineering from Anna University, India, in 2021. He started his career at Cognizant Technology Solutions for two years and then joined in SNS College of Technology and worked for nine years. During this period, he has organized Faculty Development Programme, Workshop, Seminar, Webinars and Training Programme. He has published papers in *SCI*, *Scopus* and *UGC* journals. He also presented many technical papers in national and international conferences. He is an active member in IEEE, theIRED, IAENG and ISRD. His area of interest includes antenna design and MIMO communication. Currently, he is working as an Assistant Professor in Department of Electronics and Communication Engineering at Presidency University, Bengaluru, India.

# Bandwidth and Gain Improvement of a Circularly Polarized Slot Antenna Using Nonuniform Metasurface

**Qiang Chen, Jun Yang, Changhui He, Liang Hong, Tianci Yan, Fangli Yu, Di Zhang, and Min Huang**

Air Force Early Warning Academy
Wuhan, Hubei 430019, China
1062620145@qq.com, yangjem@126.com, 513442678@qq.com, 197222036@qq.com, 84802610@qq.com, yufangli_aewa@163.com, deeafeu@163.com, huangmin_hm@163.com

***Abstract –*** This paper presents a novel design of a circularly polarized antenna based on a nonuniform metasurface (NMS). The original antenna comprises a uniform metasurface (UMS) layer and a slot antenna below. In order to achieve circularly polarized (CP) radiation, an oblique slot is etched on the center patch, and the size ratio between the center patch and the surrounding patches is adjusted to create the NMS. To further enhance the CP properties, an improved NMS (INMS) is proposed, consisting of four units with corners removed, building upon the original NMS design. Simulation results demonstrate that the proposed antenna design offers an S11 bandwidth ranging from 4.39 to 7.21 GHz, with a 3 dB axial ratio (AR) bandwidth spanning from 5.43 GHz to 6.76 GHz. Compared to the original UMS-based antenna, the INMS design shows an average gain increase of 1.21 dB, with a peak gain of 9.49 dBic. Furthermore, utilizing characteristic mode analysis (CMA), this paper explores the modal behaviors when applying the NMS to the antenna. The results indicate that this configuration excites two orthogonal modes, leading to CP radiation and the emergence of an additional AR minimum point. These factors contribute to the broader bandwidth observed in the proposed antenna design. The outstanding radiation performance of the proposed antenna design makes it suitable for various applications, including military and civilian communication, as well as point-to-point links.

***Index Terms –*** Characteristic mode analysis, circularly polarized, low profile, nonuniform metasurface.

## I. INTRODUCTION

Circularly polarized (CP) antennas are essential for wireless communication systems and point-to-point links due to their ability to mitigate multi-path effects and polarization mismatch. The growing demand for CP antennas that offer high gain, wideband coverage, and a wide 3 dB axial ratio (AR) angle has prompted the exploration of different design techniques. One such technique is the use of metasurface, which have proven to be highly effective in generating and enhancing CP radiation. Consequently, a significant number of antennas based on metasurface have been developed and wideband CP properties successfully demonstrated [1–8].

A nonuniform metasurface (NMS) was employed in a 2×2 CP antenna array arrangement, as explored in a separate study [9]. The design incorporated a Wilkinson power divider feed network, showcasing remarkable bandwidth capabilities. Specifically, it achieved an impressive 3 dB axial ratio bandwidth (ARBW) of 33.13% (7-9.78 GHz) and a wide instantaneous bandwidth (IBW) of 49.6% (6.05-10.04 GHz). This investigation effectively highlighted the potential of utilizing NMS configurations to enhance the radiation properties of CP antennas.

In a separate investigation [9], researchers explored the use of an NMS in a 2×2 CP antenna array. The design incorporated a Wilkinson power divider feed network and demonstrated impressive bandwidth capabilities. It achieved an instantaneous bandwidth (IBW) of 49.6% (6.05-10.04 GHz) and a 3 dB ARBW of 33.13% (7-9.78 GHz). These results effectively showcased the potential of NMS arrangements in enhancing the radiation properties of CP antennas. This study's findings have significant implications for advancing the development of high-performance antennas in wireless communication applications. By utilizing NMS, antenna designs can support wider frequency ranges and improved polarization properties, leading to enhanced performance in wireless communication systems. This research contributes to the exploration of innovative approaches to optimize antenna performance and increase the efficiency of wireless communication systems.

It should be noted that previous works [4–9] did not take into account the gain and 3 dB AR beamwidth. Moreover, the bandwidths of metasurface-based antennas were found to be limited. To address these

*Submitted On: December 7, 2023*
*Accepted On: October 10, 2024*

https://doi.org/10.13052/2024.ACES.J.390904

limitations, an NMS design can be utilized to precisely control the distribution of the electromagnetic field. This approach enables the antenna to enhance its radiation properties, achieving high gain and wide bandwidth. By ensuring the antenna radiates with the desired polarization, remarkable radiation properties can be achieved. This research contributes to the exploration of innovative approaches to optimize antenna performance and increase the efficiency of wireless communication systems.

This paper presents an innovative NMS design that combines the central patches of 2×2 corner-cut slotted patches with the surrounding corner-cut patches. Extensive simulations and precise measurements are conducted to validate the effectiveness of this design, showing remarkable agreement. Moreover, the paper utilized characteristic mode analysis (CMA) to analyze the radiated performance, which is in accordance with the simulated and measured results.

## II. EVOLUTION DESIGN OF THE NONUNIFORM METASURFACE ELEMENT

In the design process, the antenna with UMS is proposed. The UMS-based antenna's geometric dimensions are shown in Fig. 1, consisting of two layers of dielectric substrates, two layers of metal coatings and a feeding line. The layers in order from top to bottom are the UMS layer, dielectric substrate #1, ground plane with slot, dielectric substrate #2 and feeding line. Dielectric substrates #1 and #2 are made of the same material (Duroid) and sized 55×55 mm, with electromagnetic parameters $\varepsilon_r = 2.2$ and $\tan\delta = 0.0009$. The heights of substrates #1 and #2 are denoted as $h_a$ and $h_s$, respectively. The

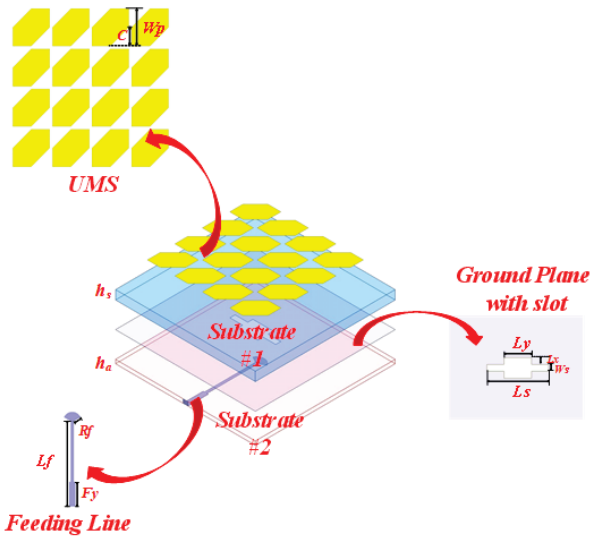


Fig. 1. Antenna configuration: Perspective view in 3D, UMS, feeding line and ground plane with slot.

UMS layer consists of a 4×4 array of corner-cut square patch, with asymmetric structure for circular polarization radiation. The metal ground of dielectric substrate #2 is etched with a regular rectangular notched slot, and the specific dimensional parameters are shown in Table 1. Both layers of dielectric substrates are of the same size. The feeding line is positioned on each side of the slot in the dielectric substrate. During the radiation process of the antenna, microwave energy is initially transferred to the UMS layer through the regular rectangular slot, and the UMS is then utilized for amplitude and phase modulation of electromagnetic waves, resulting in the conversion from linear polarization to circular polarization.

Table 1: Optimal variable of proposed INMS-based antenna

| Dimension | Size (mm) | Dimension | Size (mm) |
|---|---|---|---|
| $L_p$ | 55 | $W_p$ | 12.5 |
| $T_x$ | 2 | $C$ | 6 |
| $T_y$ | 9 | $C_N$ | 5 |
| $W_{p2}$ | 10 | $W_s$ | 2 |
| $L_x$ | 2 | $L_s$ | 18 |
| $L_y$ | 4 | $R_f$ | 3 |
| $L_f$ | 28 | $F_y$ | 0.5 |
| $C_M$ | 6 | $h_s$ | 3.5 |
| $h_a$ | 1.5 | | |

As demonstrated by the simulated results depicted in Fig. 2 by Ansys HFSS, the S11 less than -10 dB ranges from 4.77 GHz to 6.43 GHz, 6.75 GHz to 8.45 GHz and 9.08 GHz to 9.59 GHz, which meets the requirements for the antenna's external radiation. At 6.12 GHz, the antenna achieves a peak gain of 8.99 dB. Within the frequency range of 5.95-6.25 GHz, AR falls below the 3 dB line, enabling CP radiation. However, due to the limitations of the UMS structure in controlling electromagnetic wavefronts, the UMS-based antenna's performance is relatively poor. The reflection coefficient bandwidth is discontinuous, the AR bandwidth is narrow and the circular polarization effect is not satisfactory, making it difficult to meet the requirements of broadband design.

Hence, to further improve the antenna's circular polarization radiation performance, NMS should be employed. As Fig. 3 depicts, the next step involves etching 45° angled rectangular slots on the central 2×2 corner-cut square patches, which aims to increase the capability for linear-to-circular polarization conversion. With the right-angled slot tilted at 45° on the upper right side, the antenna's CP radiation was facilitated. Through simulation analysis with Ansys HFSS, it was found that when the length of the angled slot is 9 mm and the width is 2 mm, the antenna exhibits improved AR bandwidth and S11 bandwidth.

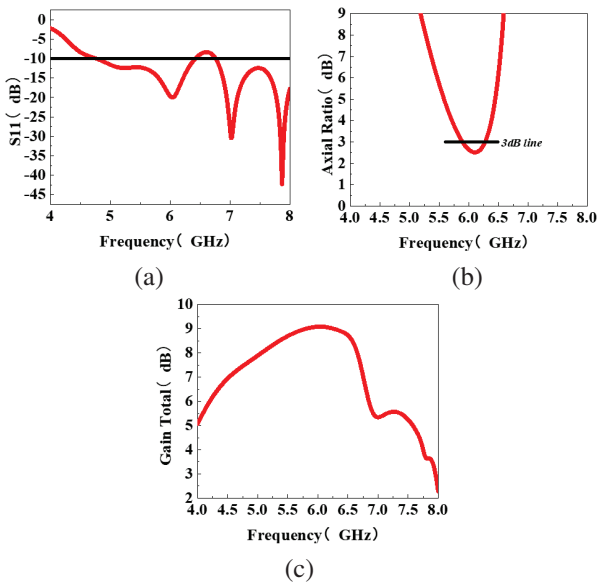


Fig. 2. Simulations of the UMS-based antenna: (a) S11, (b) Axial Ratio, and (c) Gain Total.

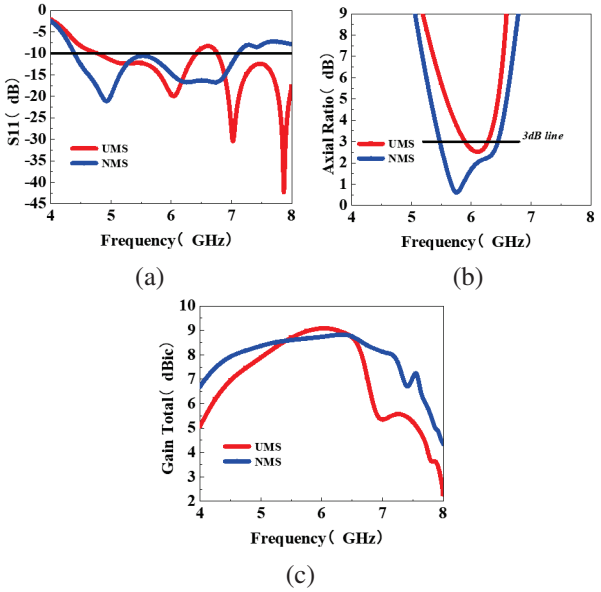


Fig. 4. Simulation of NMS-based antenna: (a) S11, (b) Axial Ratio, and (c) Gain Total.

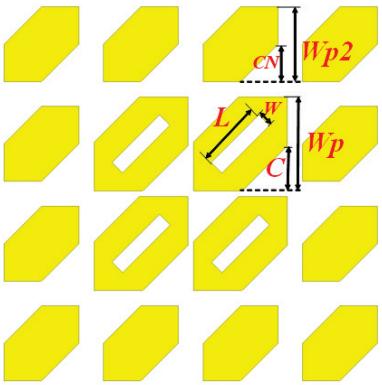


Fig. 3. Configuration of the NMS.

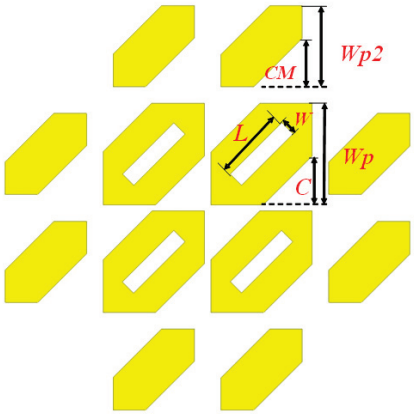


Fig. 5. Configuration of the improved NMS.

The NMS-based antenna was simulated in HFSS, and the results are plotted in Fig. 4. The results show that the proposed design achieves a S11 bandwidth of 2.72 GHz, which ranges from 4.39 GHz to 7.11 GHz and a 3 dB AR bandwidth of 0.97 GHz, which ranges from 5.47 GHz to 6.44 GHz, with the minimum value below 1 dB. The simulated results have successfully proven NMS's capability of improving the radiation performance of the antenna. Compared to the UMS-based design, the radiation performance and circular polarization properties of the antenna were greatly enhanced.

It can be observed that the S11 bandwidth is 2.76 GHz, ranging from 4.39 GHz to 7.15 GHz, which has been broadened as a result of the corner cut on the NMS. This design modification effectively enhances the material's performance by reducing reflections and improving impedance matching, leading to more efficient energy transmission. Additionally, the AR bandwidth has significantly improved, totaling 1.33 GHz and ranging from 5.43 to 6.76 GHz. This enhancement is crucial for applications that require circular polarization, as a lower AR signifies better polarization retention. Together, these improvements indicate that the modified NMS design is well-suited for advanced communication systems and radar applications, where signal integrity across a wide frequency range is essential.

In addition, the normalized radiation patterns in the far-field at 4.7 GHz display remarkably minimal cross-polarizations and a negligible back lobe in both the *xoz* and *yoz* planes, as depicted in Fig. 7. The radiation

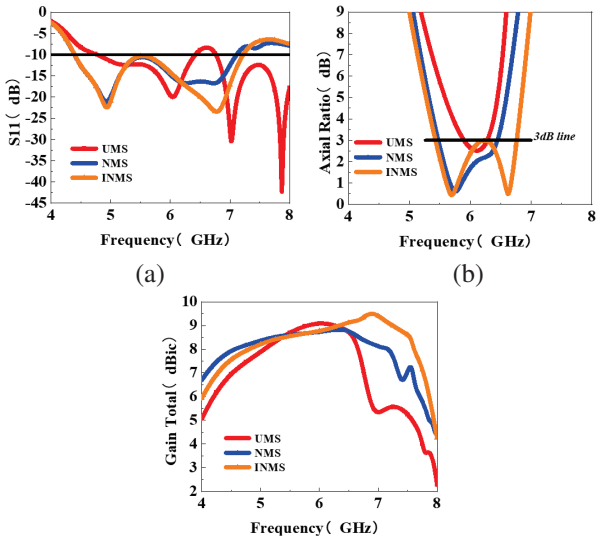


Fig. 6. Simulation of the INMS-based antenna: (a) S11, (b) Axial Ratio, and (c) Gain Total.

pattern of the improved NMS (INMS)-based antenna is stable and essentially symmetric, with a much lower level of cross-polarization than co-polarization. Within the CP operating bandwidth in two orthogonal planes, the designed antenna demonstrates excellent wideband LHCP radiation properties, with cross-polarization levels below -30 dB and back lobe level below -10 dB, resulting in effective forward radiation and enhanced directivity. Thus, the INMS-based antenna demonstrates fair CP radiation properties.

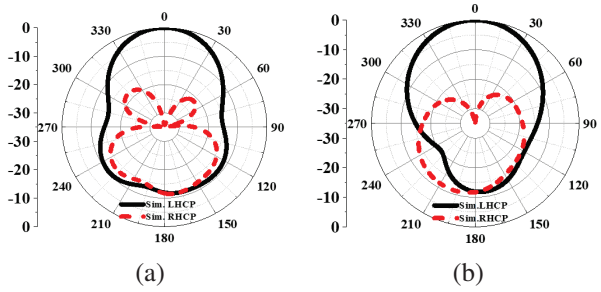


Fig. 7. Simulated radiation pattern in the (a) *xoz* plane and (b) *yoz* plane at 5.7 GHz.

## III. ANALYSIS OF MODE BEHAVIORS OF THE NONUNIFORM METASURFACE ELEMENT USING CMA

The NMS design's radiation performance was further elucidated by employing CMA to enhance the antenna's properties. This was achieved by calculating the inherent properties of the conductor structure without the addition of excitation. Of particular note is that various parameters derived through CMA can be used to analyze whether an antenna can generate CP radiation. To generate the corresponding CP radiation, it is necessary to excite two orthogonal modes simultaneously during CMA and satisfy the following five prerequisites: (1) MS values of the two modes should be relatively large and both greater than 0.707; (2) MS values of the two modes should be close; (3) phases of the two modes should have an approximate phase difference of 90 degrees; (4) current surface performed by the two modes should be directed orthogonally; and (5) maximum radiation directions of the two modes should be aligned. MS values, CA, surface currents and radiation patterns were further examined utilizing the multilayer solver in CST2022.

For NMS, the MS values and the CAs of mode 1 and mode 2 were calculated as illustrated in Fig. 8. Mode

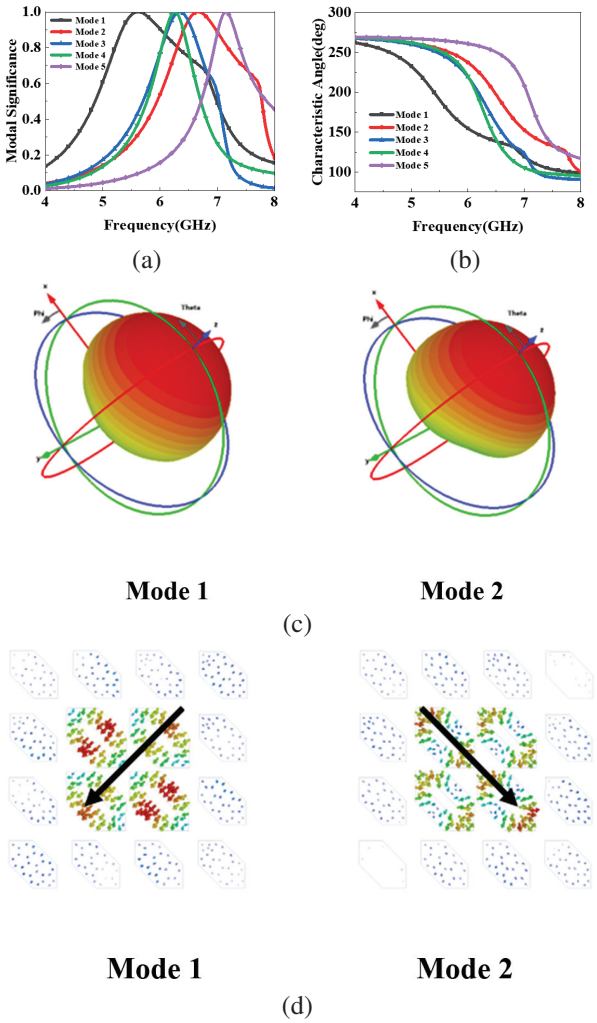


Fig. 8. Mode behaviors of NMS-based antenna: (a) MS values, (b) CAs, (c) radiation pattern at 6 GHz of mode 1 and mode 2, and (d) surface currents.

1 and mode 2 are resonant at 5.61 GHz and 6.66 GHz, respectively, and the phase difference of the two modes CAs are about 90 degrees, with their corresponding frequency points falling within the covered resonance band, which indicates that the two modes can be seen as a pair of potentially orthogonal modes. To further explore whether it can achieve circular polarization or not, the surface currents and the broadside radiation pattern of modes 1 and 2 are depicted in Fig. 8. The surface current of mode 1 distributes mainly along the diagonal direction from up right to down left, while mode 2 distributes in a perpendicular direction. In the meantime, the far-field radiation patterns of mode 1 and mode 2 had a similar broadside orientation, aligned with the *z*-axis, which means that the NMS-based antenna can realize wideband CP radiation.

In addition, the modal behaviors of INMS were also investigated in the design process in order to attain enhanced properties. As the results showed in Fig. 9, the first five modal behaviors of INMS were simulated, which indicates that the INMS resonates at 5.61, 6.35, 6.25, 6.65 and 7.13 GHz, corresponding to the MS values that reach to 1. It is obvious that mode 1 and mode 4 should be chosen as the operation modes because their bandwidth, which is greater than 0.707, falls within the operating band. By analyzing the simulated results, it is further found that the CAs of the mode 1 and mode 4 maintain a 90 degrees phase difference, which indicates the potential to achieve CP properties. The surface current and radiation pattern are also investigated, as depicted in Fig. 9. Obviously, for mode 1, the maximum current directs from down left to up right, while the surface current of mode 4 is along the diagonal direction, while other modes were found to have an anomalous current. It can be also observed that mode 1 and mode 4 share a similar radiation pattern along the z-axis. Therefore, we can deduce that mode 1 and mode 4 are a set of orthogonal modes capable of achieving CP properties.

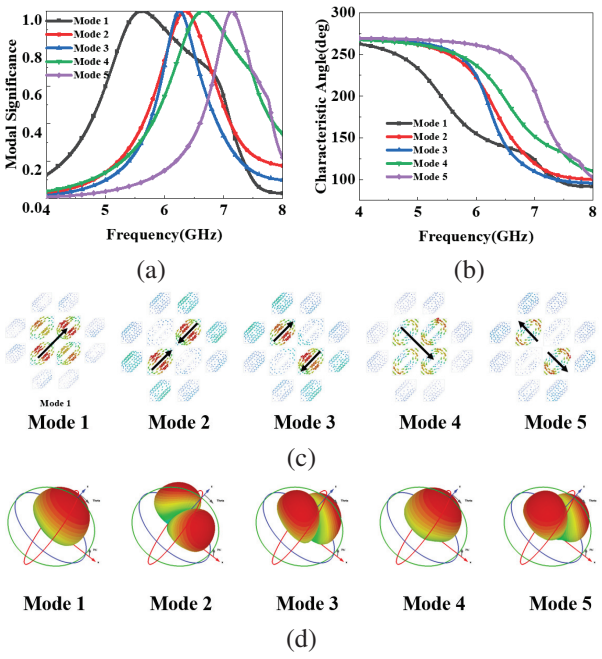


Fig. 9. Modal behaviors of proposed INMS: (a) MS values, (b) CAs, (c) surface currents, and (d) radiation pattern at 6 GHz for the first five modes.

## IV. RESULTS OF SIMULATED AND MEASURED

To assess the performance of the proposed INMS-based antenna, simulations were conducted in HFSS. Additionally, measurements were carried out in an anechoic chamber using a vector network analyzer to validate the accuracy of the design.

The results, depicted in Fig. 10 (a), showcased the S11 bandwidth below -10 dB of 2.76 GHz, ranging from 4.39 GHz to 7.15 GHz. Although there were slight disparities between the simulated and measured frequencies, they fell within an acceptable range. The designed antenna exhibited a measured AR bandwidth of 1.33 GHz, ranging from 5.43 GHz to 6.76 GHz, closely aligning with the simulation results, shown an Fig. 10 (b). Remarkably, all frequencies remained within the operating band, demonstrating exceptional radiation performance across a wide frequency range. Figure 10 (b) provides further evidence of the design's effectiveness, as the AR values remained consistently flat at a low level

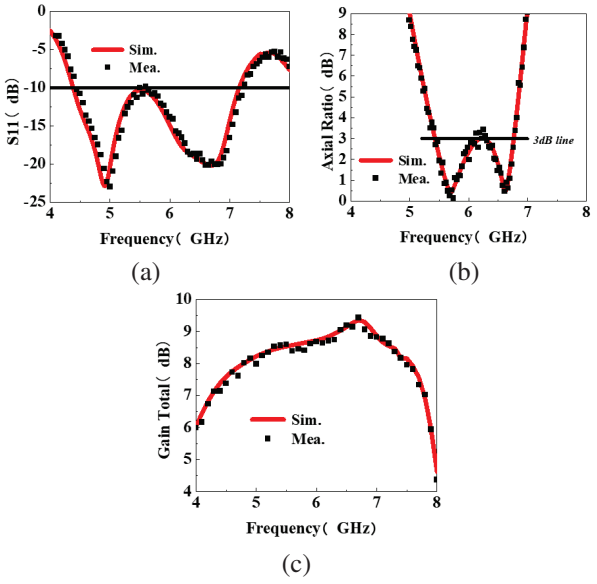


Fig. 10. Simulated and measured results of INMS MS-based antenna: (a) S11, (b) Axial Ratio, and (c) Gain Total within the main lobe.

Table 2: Performance comparison of the recently reported CP antennas

| Ref. | Size ($\lambda_0{}^3$) | 3 dB AR BW (GHz) | Peak Gain (dBic) | 3dB AR Angle Range | Operating Bandwidth (GHz) |
|---|---|---|---|---|---|
| **Proposed** | **1 ×1×0.1** | **5.43-6.76** | **9.35** | **-52° to 42°** | **4.39-7.15** |
| **[9]** | 2×2×0.08 | 7-9.78 | 13.17 | null | 6.05-10.04 |
| **[10]** | 0.67×0.67×0.06 | 1.3-2.1 | 8.7 | null | 1.4-2.1 |
| **[11]** | 2.6×2.63×0.36 | 9.8-10.2 | 13.4 | -10° to 10° | 9.86-10.14 |
| **[12]** | 2.0×2.0×0.6 | 7.3-7.6 | 15.1 | null | 7.3-7.6 |
| **[13]** | 2.0×2.0×0.88 | 4.12-6.39 | 14.5 | | 3.82-6.01 |
| **[14]** | 3×3×0.19 | 9.7-10.3 | 17.8 | -15° to 15° | 9.8-10.2 |

of averagely 1.89 dB throughout the operating band. Furthermore, as depicted in Fig. 10 (c), the maximum gain measured in the main lobe reached 9.35 dB at 6.72 GHz, falling within the operating band covered by the 3 dB AR bands. This outstanding performance signifies the antenna's capability in terms of CP radiation. Additionally, the gain values exhibited stability and consistency across the operated bands, resulting in a flat response.

In Fig. 11, the radiation pattern at 5.7 GHz was analyzed. It was found that the antenna demonstrated a low cross-polarization level of less than -30 dB in both the *xoz* and *yoz* planes, indicating successful CP radiation. Furthermore, the side lobe values were at least 10 dB lower than those of the main lobe, suggesting an excellent radiation performance.

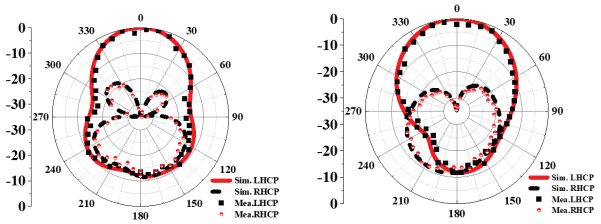


(a) (b)

Fig. 11. Simulated and measured radiation patterns at 5.7 GHz in the (a) *xoz* plane and (b) *yoz* plane.

Figure 12 presents AR versus angle at 5.7 GHz. The *yoz* plane exhibited a wide-angle range of CP property, with ARs that were lower than 3 dB exhibiting a beamwidth of 94°, ranging from −52° to +42°, while performance in the *xoz* plane was 71°, ranging from −32° to +39°, achieving a satisfactory CP property. To further validate the effectiveness of the proposed design, a comprehensive comparison was made with other recently proposed metasurface-based antennas, as listed in Table 2. The results clearly demonstrate that the proposed antenna outperforms its counterparts in terms of radiation properties. Remarkably, this superior performance is achieved within a compact size of 1λ0×1λ0×0.1λ0, making it highly desirable for various applications. In conclusion, the analysis of the radiation pattern and AR, along with the comparison with other antennas, highlight the exceptional radiation characteristics and compact size of the proposed antenna design. These findings further validate its effectiveness and underscore its potential for a wide range of applications.

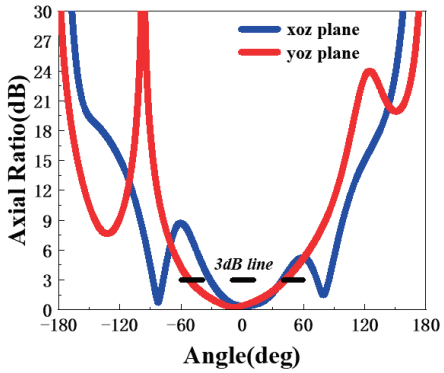


Fig. 12. Simulated Axial Ratio values versus angle in the *xoz* and *yoz* planes at 5.7 GHz.

## V. CONCLUSION

Proposed in this research paper is a novel circularly polarized antenna design that incorporates a nonuniform metasurface. The principal element of this antenna is a UMS layer, which is composed of an arrangement of 4×4 corner-cut patches and a slot antenna located below. To bolster CP radiation, the NMS was introduced into the design of the antenna, which consists of a 2×2 arrangement of central corner-cut slotted patches and the surrounding corner-cut patches. Through extensive simulations, the proposed antenna's remarkable radiation properties are confirmed. By utilizing CMA, the radiation performance of INMS is further analyzed. Based on the CMA results, the INMS exhibits a broader CP band than the UMS due to its ability to satisfy a broader frequency range of MS and CA. Beyond its exceptional radiation properties, the proposed antenna exhibits potential for employment in communication and

point-to-point links systems. This research contributes significantly to the progression and refinement of CP antenna design.

## ACKNOWLEDGEMENT

This work was supported by the Natural Science Foundation of Hubei Province under Grant 2023AFB452.

## REFERENCES

[1] K. Li, Y. Liu, Y. Jia, and Y. J. Guo, "A circularly polarized high gain antenna with low RCS over a wideband using chessboard polarization conversion metasurfaces," *IEEE Trans. Antennas Propag.,* vol. 65, no. 8, pp. 4288-4292, 2017.

[2] Y. Huang, L. Yang, J. Li, Y. Wang, and G. Wen, "Polarization conversion of metasurface for the application of wide band low-profile circular polarization slot antenna," *Appl. Phys. Lett.,* vol. 109, no. 5, p. 054101, 2016.

[3] Z. G. Liu, Z. X. Cao, and L. N. Wu, "Compact low-profile circularly polarized Fabry-Perot resonator antenna fed by linearly microstrip patch," *IEEE Antennas Wirel. Propag. Lett.,* vol. 16, pp. 524-527, 2016.

[4] Z. Wu, L. Li, Y. Li, and X. Chen, "Metasurface superstrate antenna with wideband circular polarization for satellite communication application," *IEEE Antennas Wireless Propag. Lett.,* vol. 10, pp. 907-910, 2015.

[5] H. L. Zhu, S. W. Cheung, K. L. Chung, and T. I. Yuk, "Linear-to-circular polarization conversion using metasurface," *IEEE Trans. Antennas Propag.,* vol. 61, no. 9, pp. 4615-4623, 2013.

[6] Q. Chen and H. Zhang, "Dual-patch polarization conversion metasurface-based wideband circular polarization slot antenna," *IEEE Access,* vol. 6, pp. 74772-74777, 2018.

[7] P. Xie, G. Wang, H. Li, and J. Liang, "A dual-polarized two-dimensional beam-steering Fabry-Perot cavity antenna with a reconfigurable partially reflecting surface," *IEEE Antennas Wireless Propag. Lett.,* vol. 16, pp. 2370-2374, 2017.

[8] Q. Chen and H. Zhang, "High-gain circularly polarized Fabry-Pérot patch array antenna with wideband low-radar-cross-section property," *IEEE Access,* vol. 7, pp. 8885-8889, 2019.

[9] X. Gao, S. Yin, G. Wang, C. Xue, and X. Xie, "Broadband low-RCS circularly polarized antenna realized by nonuniform metasurface," *IEEE Antennas Wireless Propag. Lett.,* vol. 21, no. 12, pp. 2417-2421, 2022.

[10] J. Cui, X. Zhao, and W. Sheng, "Low profile and broadband circularly polarized metasurface antenna based on nonuniform array," *AEU-International Journal of Electronics and Communications,* vol. 156, p. 154386, 2022.

[11] N. Hussain, S. I. Naqvi, W. A. Awan, and T. T. Le, "A metasurface-based wideband bidirectional same sense circularly polarized antenna," *Int. J. RF Microw. Comput. Aided Eng.,* vol. 30, p. 22262, 2020.

[12] Y. Cheng and Y. Dong, "Bandwidth enhanced circularly polarized Fabry-Perot cavity antenna using metal strips," *IEEE Access,* vol. 8, pp. 60189-60198, 2020.

[13] F. Qin, S. Gao, G. Y. Wei, Q. Luo, C. Mao, C. Gu, J. Xu, and J. Li, "Wideband circularly polarized Fabry-Perot antenna [antenna applications corner]," *IEEE Antennas and Propagation Magazine,* vol. 57, no. 5, pp. 127-135, 2015.

[14] N. Hussain, M. Jeong, J. Park, and N. Kim, "A broadband circularly polarized Fabry-Perot resonant antenna using a single-layered PRS for 5G MIMO applications," *IEEE Access,* vol. 7, pp. 42897-42907, 2019.

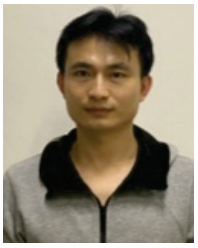

**Qiang Chen** was born in Jiangxi, China. He received the master's and Ph.D. degree from Air Force Engineering University (AFEU), Xi'an, China, in 2015 and 2019, respectively. He is currently a lecturer with Air Force Early Warning Academy, Wuhan, Hubei, China. His research interests include microwave circuits, antennas and arrays.

**Jun Yang** was born in 1973. He received his Ph.D. degree from Air Force Engineering University, Xian, China, in 2003. Currently, he is an associate professor at the Air Force Early Warning Academy, Wuhan, China. His research interests cover radar systems, radar imaging and compressed sensing.

**Changhui He** was born in 1973. She received the master's degree from Central China Normal University. She is currently an associate professor at Air Force Early Warning Institute. She is interested in electromagnetic field, microwave technology, and antenna design. Ms He has

published over 20 technical papers and authored one book. She holds four national invention patents.

**Liang Hong** was born in Wuhan, China. He received the B.S. and M.S. degrees from Huazhong University of Science and Technology, Wuhan, China, in 2005 and 2011, respectively. His research interests include microwave devices and microwave technology.

**Tianci Yan** was born in Hubei, China. He received the B.S. from Air Force Early Warning Academy, Wuhan, China, in 2023. His research interests include microwave devices and microwave technology.

**Fangli Yu** was born in China, in 1983. He received the B.E. degree from the Air Force Early Warning Academy, Wuhan, China. He is currently a Ph.D. Candidate in the School of Information and Engineering, Wuhan University of Technology. His current research interest is radar signal processing.

**Di Zhang** received the B.S., M.S. and Ph.D. degrees from Air Force Engineering University (AFEU), Xi'an, China, in 2013, 2015, and 2019, respectively. He is currently a lecturer with Air Force Early Warning Academy. His research interests include RF orbital angular momentum antennas, reflect array antennas and metasurface.

**Min Huang** graduated from Taiyuan University of Technology with a master's degree in physical electronics. She is now an instructor at the Air Force Early Warning Academy. Her research interests are electromagnetic fields and microwave technology.

# Transformation Optics-based Antenna for Focusing OAM Beams

**Jia-Tong Jing, Wei Song, and Xin-Qing Sheng**

Institute of Radio Frequency Technology and Software
Beijing Institute of Technology, Beijing 100081, China
3120215362@bit.edu.cn, wsong@bit.edu.cn, xsheng@bit.edu.cn

***Abstract –*** In this article, a metamaterial horn antenna based on transformation optics (TO) is presented to generate a focused orbital angular momentum (OAM) beam. By applying the coordinate transformation, a metamaterial insertion inside the horn is designed to concentrate the radiated OAM beam. The TO-based insertion is further realized by using split ring resonators (SRRs). The metamaterial antenna is fabricated and measured to verify the design. A 13$^{o}$ reduction in the main lobe angle is realized in measurement by SRRs.

***Index Terms –*** Main lobe angle, metamaterial, orbital angular momentum, split ring resonator, transformation optics.

## I. INTRODUCTION

The orbital angular momentum (OAM) wave carries the rotation phase factor $\exp(il\varphi)$ , where $l$ represents the OAM mode number [1, 2]. Due to mode orthogonality, OAM waves have wide applications, including enhancing network capacity [3, 4], improving resolution of images [5], and resisting eavesdropping [6].

However, the maximum beam intensity in an OAM beam is with a deviation angle from the direction of wave propagation. Thus, the conical beam intensity causes the beam energy to spread rapidly with the propagation distance [7]. According to the communication principle of the OAM waves, the best communication link can be obtained only if the maximum power area is covered by the receiving antenna. That means to receive more beam power and improve power efficiency, the aperture of the antennas will be linearly dependent on the communication distance, which may make the system impractically bulky for long-distance communication. Therefore, OAM wave applications are limited to short-distance transmission in wireless communication systems [8], or special treatment must be involved [9]. To solve this problem, it is important to focus the beam and reduce the cone-apex angle of beam energy.

In the radio frequency regime, OAM beams can be generated through various means, e.g., through modulating plane waves by metamaterials [10–14], through modulated feeding of antenna arrays [15], and by making use of the eigenmodes of conventional single antennas [16]. Among the OAM antennas, the horn antenna has the advantages of easy fabrication, high power handling, and stable phase center [9]. More importantly, it can generate OAM beams with a mode purity as high as 87% [9]. However, when designing horn antennas as the transceivers with focused beams, there are two difficulties. First, focused beams require a large horn, which means increasing the length and radiation aperture of the horn simultaneously [10]. Second, a horn antenna cannot be designed arbitrarily large while maintaining the purity of the radiated modes as the feeding waveguide modes.

To address this problem, transformation optics (TO) can be a candidate solution. By applying coordinate transformation to the form-invariant Maxwell's equations, a TO-based filling for an OAM horn antenna was designed [17], with the function of focusing OAM beams validated through numerical simulations [18]. The electromagnetic medium dictated by TO is normally inhomogeneous and anisotropic. To realize such parameters in the real world remains an interesting topic. Among many metamaterial types, a frequency selective surface (FSS) is a two-dimensional periodic array exhibiting its filter characteristics to transmit (band-pass) and/or reflect (band-stop) electromagnetic waves (EMW) [19, 20]. A split ring resonator (SRR) is one of the techniques to control the resonant frequency location and effect of the size reduction of the antenna design [21]. In this paper, we proposed to realize the TO-based filling by SRR, and validate the OAM beam focusing function of the TO-based filling both by numerical and physical experiments.

## II. TO-BASED METAMATERIAL MODEL

Consider two spaces for coordinate transformation. A standard conical horn antenna is defined in the virtual space. As illustrated in Fig. 1 (b), this antenna has a radiation aperture $a$ and a feeding circular waveguide of radius $r_0$. Its frustum of cone is height $d$. $a$ can be determined conventionally [19]. In the physical space, a proposed horn antenna has the same height and the same feeding waveguide. Only the radiation aperture $a'$ is larger, as illustrated in Fig. 1 (a).

*Submitted On: July 14, 2023*
*Accepted On: October 17, 2024*

https://doi.org/10.13052/2024.ACES.J.390905

Overlapping the cross-sections of the two antennas provides the convenience of setting up the mapping between the two spaces. As plotted in Fig. 1 (c), overlapping the origins and $z(z')$-axis of the two spaces as $O$ and $z$-axis, the extensions of segments $MN$ and $M'N'$ intersect the $z$-axis at points $P(0,0,-c)$ and $P'(0,0,-c')$, respectively. Here $c = r_0 d/(a - r_0)$ and $c' = r_0 d/(a' - r_0)$. Thus, the transformation from the virtual space to the physical space is expressed as:

$$\begin{cases} \rho' = \rho \cdot \frac{c'+z}{c+z} \cdot \frac{c}{c'} \\ \varphi' = \varphi \\ z' = z \end{cases}, \tag{1}$$

where $c' = r_0 d/(a' - r_0)$ and $c = r_0 d/(a - r_0)$.

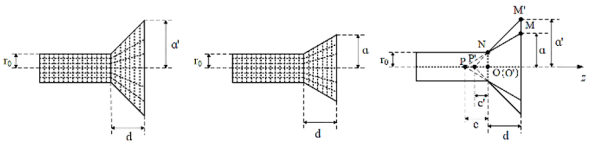


(a) (b) (c)

Fig. 1. Coordinate transformation scheme of the proposed horn antenna (*xoy* cross-section): (a) TO-based horn antenna in the physical space, (b) transformation target of the TO-based horn antenna in the virtual space, which is a standard horn antenna, and (c) overlapping cross-sections of the two antennas.

Following the approach in [19], the mapping from the virtual coordinate system to the physical coordinate system dictates a frustum cone space with the following radius-dependent, anisotropic relative permittivity and permeability:

$$\varepsilon_\rho = \mu_\rho = 1, \tag{2}$$

$$\varepsilon_\varphi = \mu_\varphi = 1, \tag{3}$$

$$\varepsilon_z = \mu_z = \left(\frac{c'+z}{c+z} \cdot \frac{c}{c'}\right)^2. \tag{4}$$

Equations (2)-(4) show that all permittivity and permeability components are positive, which are much easier to realize through artificial metamaterials than through negative material components.

The antenna geometric dimensions in this paper are as follows: $r_0 = 41.81$ mm, $a = 120$ mm, $a' = 240$ mm, and $d = 244.3$ mm.

Among many kinds of metamaterials [20, 21], we chose the classical SRRs to realize the prescribed $\mu_z$ value. The substrate used in the SRRs is FR-4, whose permittivity is 4.3 and loss tangent is 0.017. On the top and bottom sides of the FR-4 substrate, the printed split rings are oriented with a rotational angle of 90°, to reduce the polarization sensitivity of the metamaterial, as shown in Fig. 2 (a,b).

The unit cells of the metamaterial were designed with the commercial software CST Microwave Studio. The operating frequency is 5 GHz. With the constitutive parameters' retrieval algorithm [22], the anisotropic constitutive parameters can be obtained. For example, to retrieve $\mu_z$, we first set the unit cell model as in Fig. 2 (c), and assign the periodic boundary conditions to the lateral walls in both the $y$- and $z$-directions. Then a TM polarized plane wave incidence from the $+x$-direction (with the magnetic field along the $z$-direction) was introduced. Then $\mu_z$ can be retrieved from the simulated $S$ parameters. $\varepsilon_x$ and $\varepsilon_y$ values can be obtained similarly. To keep this paper concise, only the simulation result of layer 11 was plotted as an example in Fig. 2 (d-f). The retrieved $\mu_x$, $\mu_y$, and $\mu_z$ coincide with the design target (2)-(4) at 5 GHz. The imaginary parts of $\varepsilon_x$ and $\varepsilon_y$ are 0. It is noted that the real parts of $\varepsilon_x$ and $\varepsilon_y$ differ from the design target (2) and (3), which may cause the difference between the measurement based on the SRR realized model and the numerical results based on the TO dictated model. However, this difference is inevitable because of the existence of the dielectric substrate in the unit cell. Similar

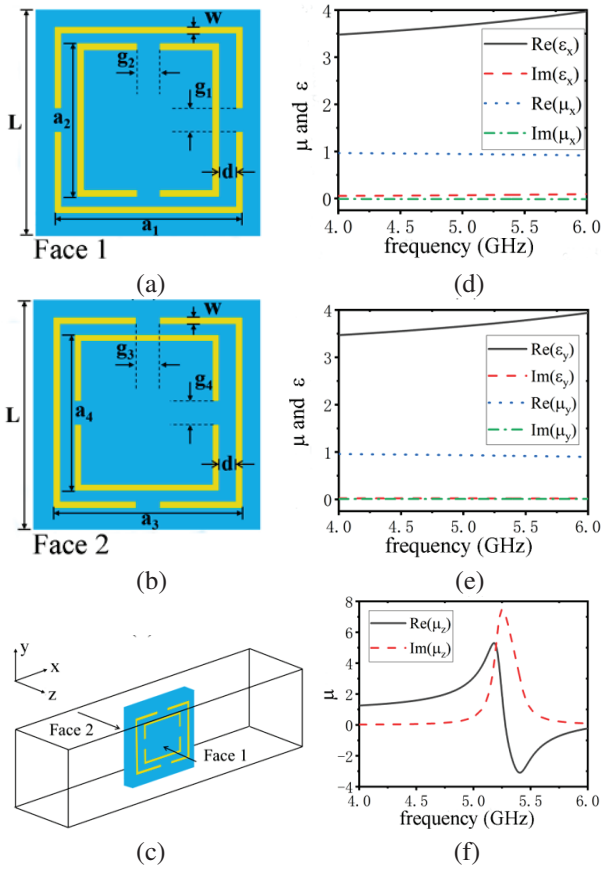


Fig. 2. (a) Geometry of the metamaterial unit-cell face 1, (b) geometry of the metamaterial unit-cell face 2, (c) unit-cell simulation scheme, (d-f) retrieved constitutive parameters of layer 11, (d) $\varepsilon_x$, $\mu_x$, (e) $\varepsilon_y$, $\mu_y$, and (f) $\mu_z$.

situations exist in the other layers. Therefore, it is necessary to evaluate the metamaterials-based design.

In Table 1, we list the structure parameters of SRRs and the SRR-realized $\mu_z$ of each layer. From Table 1, it is seen that the permeability of every layer changes gradually. Thus, it is expected that the SRR realized medium will not introduce significant reflection.

Table 1: Size and $\mu_z$ of every layer

| Layer | Z (mm) | L (mm) | d (mm) | w (mm) | Re ($\mu_z$) |
|---|---|---|---|---|---|
| 1 | 0 | 0 | 0 | 0 | 1 |
| 2 | 10 | 5 | 0.3 | 0.1 | 1.28 |
| 3 | 20 | 5 | 0.1 | 0.1 | 1.62 |
| 4 | 30 | 5 | 0.1 | 0.1 | 1.62 |
| 5 | 40 | 5 | 0.1 | 0.2 | 1.85 |
| 6 | 50 | 5 | 0.4 | 0.3 | 2.01 |
| 7 | 60 | 5 | 0.3 | 0.2 | 2.46 |
| 8 | 70 | 5 | 0.3 | 0.2 | 2.46 |
| 9 | 80 | 5 | 0.3 | 0.2 | 2.46 |
| 10 | 90 | 5 | 0.4 | 0.3 | 2.76 |
| 11 | 100 | 5 | 0.4 | 0.3 | 2.76 |
| 12 | 110 | 5 | 0.2 | 0.4 | 2.91 |
| 13 | 120 | 5 | 0.1 | 0.3 | 3.02 |
| 14 | 130 | 5 | 0.1 | 0.2 | 3.12 |
| 15 | 140 | 5 | 0.1 | 0.1 | 3.21 |
| 16 | 150 | 5 | 0.5 | 0.2 | 3.29 |
| 17 | 160 | 5 | 0.1 | 0.5 | 3.38 |
| 18 | 170 | 5 | 0.3 | 0.4 | 3.51 |
| 19 | 180 | 5 | 0.3 | 0.4 | 3.51 |
| 20 | 190 | 5 | 0.1 | 0.4 | 3.67 |
| 21 | 200 | 5 | 0.4 | 0.3 | 3.77 |
| 22 | 210 | 5 | 0.2 | 0.3 | 3.80 |
| 23 | 220 | 5 | 0.2 | 0.3 | 3.80 |
| 24 | 230 | 5 | 0.3 | 0.2 | 3.91 |
| 25 | 240 | 5 | 0.2 | 0.3 | 4.04 |

## III. FULL-WAVE SIMULATIONS

In this section, the proposed antenna with the TO-based filing realized by the SRR material is investigated using CST Microwave Studio. Limited by computing resources, the model of the horn antenna is only filled with the first five layers of SRR filling. A reference antenna is obtained by simply removing the SRR filling from the proposed antenna. The simulated S11 results are plotted in Fig. 3. Due to the reflection between each layer in the SRR insertion, the proposed antenna has an impedance band of 4.6-5.5 GHz (a relative bandwidth of 18%), which is narrower than the unfilled antenna.

OAM waves of mode $l = 1$ are exited in the feeding waveguides of the two antennas. Observation planes are

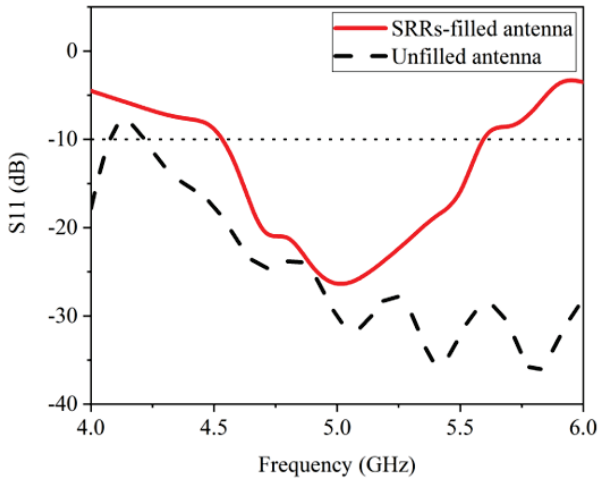


Fig. 3. Simulated S11 of the SRR-filled horn antenna and unfilled horn antenna.

defined $2\lambda$ away from the radiation aperture of each horn antenna. The simulated amplitude of $E$-field is shown in Figs. 4 (a) and (c). An apparent low amplitude zone can be found in the beam center, which is a characteristic feature of the OAM beam. Additionally, we can see that the energy is more focused for the cases of the SRR-filled antennas. In all cases, an obvious spiral phase distribution corresponding to OAM of order $+1$ can be observed, as shown in Figs. 4 (b) and (d).

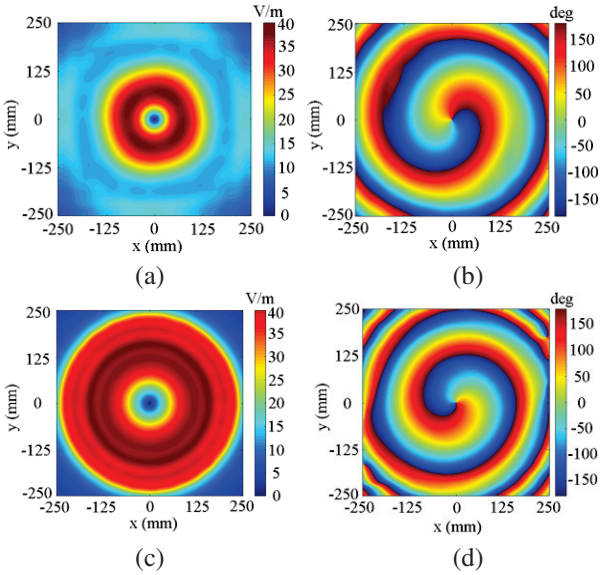


Fig. 4. Measured amplitude distribution and phase pattern: (a,b) the SRR-filled horn antenna and (c,d) the unfilled horn antenna.

From the above phase information, OAM mode purities are calculated on different concentric integration

contours on the observation planes [23]. These contours are indicated by radius $r$ in Fig. 5. It shows that the SRR-filled horn antenna has a mode purity comparable to that of the unfilled antenna, indicating that the layered metamaterial does not degrade the mode purity.

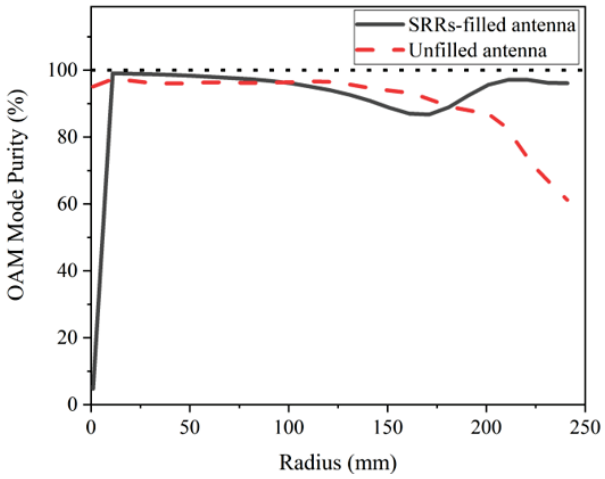


Fig. 5. OAM mode purity of the antennas.

The simulated gains of the antennas at 5 GHz are plotted in Fig. 6, with the main lobe angle summarized in Table 2. In the SRR-filled antenna, there is a reduction of 6.5° in the main lobe angle in the E-plane and H-plane compared with the unfilled antenna. In addition, it can be seen that the maximum gain of the SRR-filled antenna is lower than the unfilled one. This is attributed to the lossy FR-4 substrate used in the filling.

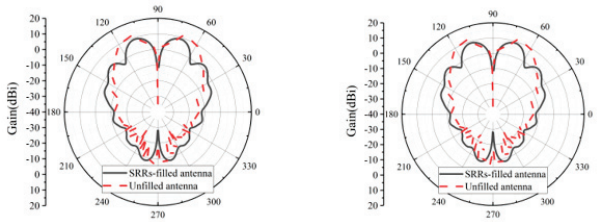


(a) (b)

Fig. 6. Simulated gain of the antenna: (a) E-plane and (b) H-plane.

Table 2: Simulated main lobe angle for the L = 1 OAM beam

| Cases | E-plane | | H-plane | |
|---|---|---|---|---|
| | Angle (°) | **Gain (dBi)** | Angle (°) | **Gain (dBi)** |
| SRR-filled antenna | 17 | 8.9 | 17 | 8.9 |
| Unfilled antenna | 23.5 | 11.6 | 23.5 | 11.6 |

## IV. EXPERIMENTAL RESULTS

To verify the design, the horn antenna, as illustrated in Fig. 1, was fabricated. Its photograph is shown in Fig. 7 (a). Two SMA connectors are used to feed the horn antenna with equal magnitude and a $+90^{o}$ phase difference to generate the OAM mode. The first 11 layers of metamaterial in Table 1 were fabricated, as shown in Fig. 7 (b).

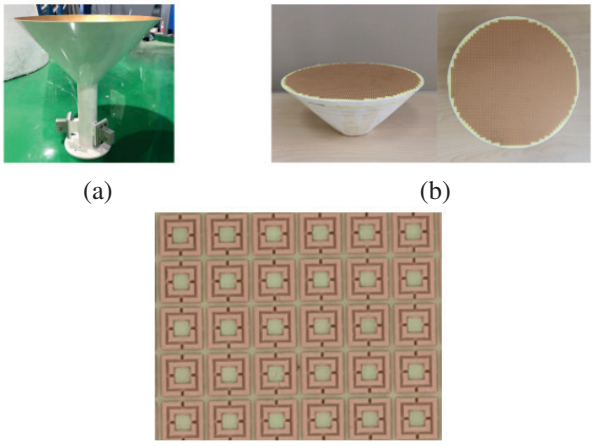

(a) (b)

(c)

Fig. 7. (a) Fabricated horn antenna, (b) fabricated metamaterial, and (c) unit cell layout of the metamaterial.

First, the reflection coefficients of the SRR-filled antenna and the unfilled antenna are measured (Fig. 8). The reflection coefficients for the two antennas are comparable with an operating band centered at 5 GHz, demonstrating that TO-based filling does not introduce extra reflection.

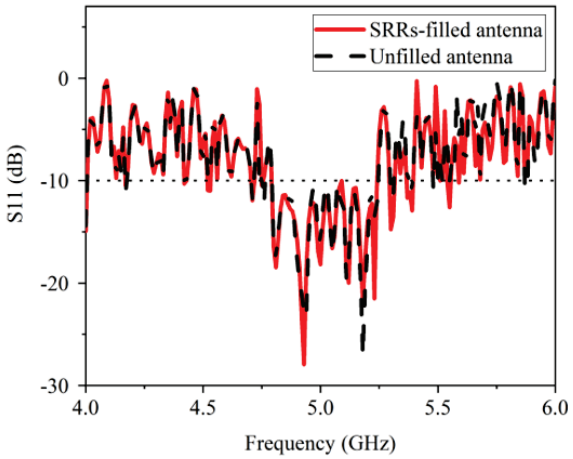


Fig. 8. Measurement results of S11 from the antennas.

The near-field measurement setup is shown in Fig. 9. An open waveguide is used as a probe to measure the phase and field intensity. Scanning is performed in a planar zone for both horizontal polarization and vertical polarization.

For all the antennas to be scanned, observation planes are defined $2\lambda$ away from the radiation aperture of the horns. The measured amplitude distribution and phase pattern are shown in Fig. 10. Similar to the simulation results in Fig. 4, an OAM null zone can be found in the beam center. Additionally, we can see that the energy distribution is in a better regularly circular form for the case of the SRR-filled antenna. Obvious spiral phase distributions corresponding to OAM of order $+1$ can be observed for both antennas, which is consistent with the simulation results in Fig. 4. Only the H-polarization measurement results are plotted in Fig. 10. Similar results for the V-polarization can be obtained and are not plotted here.

From the phase information, OAM mode purities are calculated again as a function of the contour radius $r$,

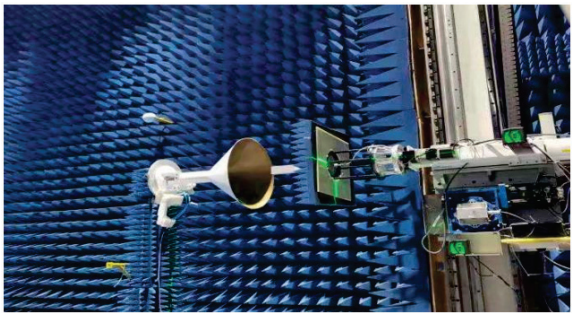

Fig. 9. Near-field measurement setup.

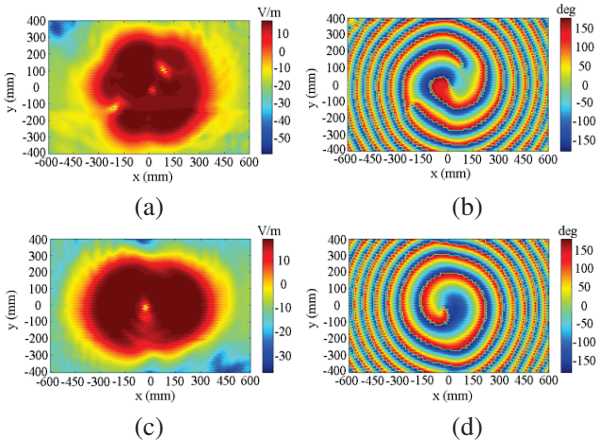


Fig. 10. Measured amplitude distribution and phase pattern: (a) amplitude, SRR-filled antenna, (b) phase pattern, SRR-filled antenna, (c) amplitude, unfilled antenna, and (d) phase pattern, unfilled antenna.

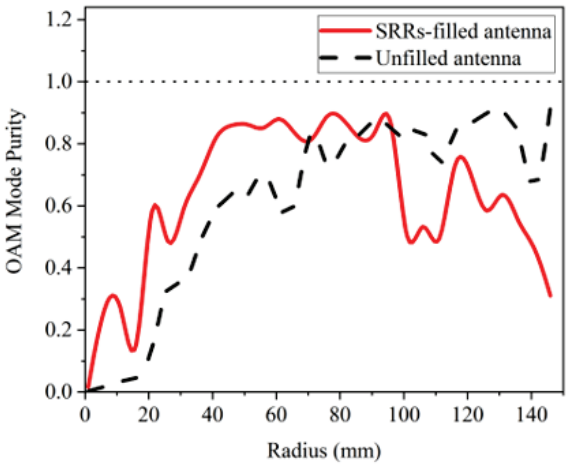


Fig. 11. OAM mode purity of the antennas.

as shown in Fig. 11. It shows that the SRR-filled horn antenna has a mode purity of over 80% in the range of 40 mm $\leq r \leq$ 90 mm with a maximum of 88.9% reached at $r = 76$ mm. It is comparable to the mode purity of the unfilled antenna.

The gains of the antennas are measured with the system setup shown in Fig. 12. The measured gains at 5 GHz are depicted in Fig. 13. The key information of the main lobe angle is summarized in Table 3.

Compared with the unfilled horn antenna, the SRR-filled antenna has a reduction of 13°on the main lobe

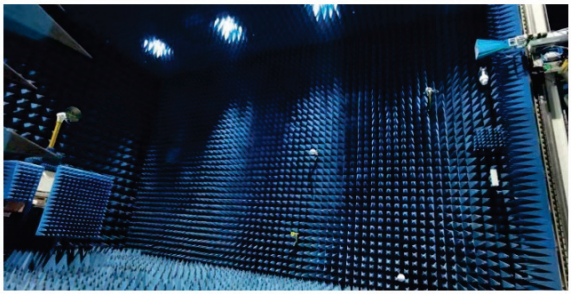

Fig. 12. Far-field measurement setup.

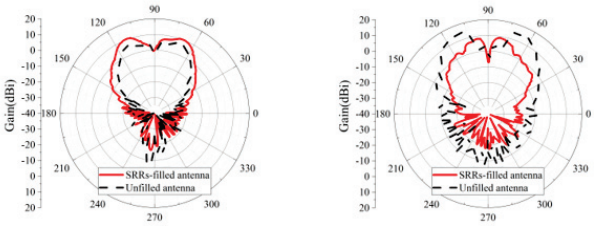


Fig. 13. Gain of the antennas: (a) E-plane and (b) H-plane.

Table 3: Measured main lobe angle for the L = 1 OAM beam

| | **E-plane** | **H-plane** |
|---|---|---|
| **Cases** | Angle (°) | Angle (°) |
| SRR-filled antenna | 20 | 11 |
| Unfilled antenna | 20 | 24 |

Table 4: Comparison with other designs

| **Ref.** | **[11]** | **[15]** | **This Work** |
|---|---|---|---|
| Type | HMS | CUCA | TOMS |
| Angle | - | 15 | 11 |
| OAM purity | 84% | - | 90.5% |

angle in the H-plane. However, in the E-plane, the lobe angles of the two antennas are similar.

Further investigation shows the different performance in measurement and simulation origins from the feeding of the antennas. In the simulations, ideal waveguide ports are defined at the end of the circular waveguides and the antennas are circular polarized. However, as the fabricated antennas are fed with a pair of waveguide ports, the antennas become linearly polarized and, thus, the gains in E- and H-planes lost symmetry. Table 4 shows the comparison of the proposed transformation optics metasurface (TOMS) and other designs, including Huygens' metasurface (HMS) [11] and concentric uniform circular array (CUCA) [15]. We know the proposed work can reduce the cone-apex angle of the beam energy, while maintaining high OAM purity.

To conclude, the reduction on main lobe angle in the H-plane measurement results show that the layered SRR-filled antenna can generate focused OAM beams.

In this paper, we only consider the TE polarized wave. For the TM wave, the metamaterial must be designed with desirable $\varepsilon_z$, while $\mu_z$ can be arbitrary. The desirable $\varepsilon_z$ can be realized by wire medium and be explored in the future.

## V. CONCLUSION

In this study, a SRR-filled horn antenna is proposed to generate a focused OAM beam. Transformation optics was utilized to obtain an inhomogeneous transformation medium for focusing the OAM beam. To validate the proposed approach, we fabricated and measured the proposed antenna based on a double-sided split ring resonator. By inserting SRR-filling, the OAM mode purity is well-preserved, and the OAM main lobe angle can be reduced by 13°, which agrees with the simulation results. The focused OAM beam can be a preferable feature in the OAM wireless communication systems.

## ACKNOWLEDGMENT

This work is supported by BIT-BRFFR Joint Research Program, under Grant No. BITBLR2020015.

## REFERENCES

[1] S. M. Mohammadi, L. K. Daldorff, J. E. Bergman, R. L. Karlsson, B. Thid´e, K. Forozesh, T. D. Carozzi, and B. Isham, "Orbital angular momentum in radio—a system study," *IEEE Trans. Antennas Propag*., vol. 58, no. 2, pp. 565-572, 2009.

[2] Y. Shuang, H. Zhao, W. Ji, T. J. Cui, and L. Li, "Programmable high-order OAM-carrying beams for direct-modulation wireless communications," *IEEE J. Emerg. Sel. Topics Circuits Syst.*, vol. 10, no. 1, pp. 29-37, 2020.

[3] Y. Yagi, H. Sasaki, T. Yamada, and D. Lee, "200 Gb/s wireless transmission using dual-polarized OAM-MIMO multiplexing with uniform circular array on 28 GHz band," *IEEE Antennas Wireless Propag. Lett.*, vol. 20, no. 5, pp. 833-837, 2021.

[4] H. Yang, S. Zheng, H. Zhang, T. He, N. Li, Z. Yang, Z. Lyu, Y. He, L. Zhang, and X. Yu, "Metasurface-based high-speed photonic THz OAM communication system," *Journal of Lightwave Technology*, vol. 42, no. 15, pp. 5080-5087, 2024.

[5] Z. Luo, Y. Liao, and M. Xing, "Target imaging and anti-jamming with frequency agile OAM radar," *IEEE Geoscience and Remote Sensing Letters*, vol. 21, pp. 1-5, 2024.

[6] J. Chen, Z. Liang, K. Liu, J. Liu, Y. Jing, and B. Xiang, "Phase-encoding truncated orbital angular momentum modes for high-security and high-capacity information encryption," *Journal of Lightwave Technology*, vol. 42, no. 10, pp. 3677-3683, 2024.

[7] S. M. Mohammadi, L. K. Daldorff, K. Forozesh, B. Thid´e, J. E. Bergman, B. Isham, R. Karlsson, and T. Carozzi, "Orbital angular momentum in radio: Measurement methods," *Radio Science*, vol. 45, no. 4, pp. 1-14, 2010.

[8] R. Lyu, W. Cheng, W. Zhang, and F. Qin, "OAM-NFC: A short-range high capacity transmission scheme," in *ICC 2020-2020 IEEE International Conference on Communications (ICC),* Dublin, pp. 1-6, 2020.

[9] Y. Yao, X. Liang, W. Zhu, J. Geng, and R. Jin, "Experiments of orbital angular momentum phase properties for long-distance transmission," *IEEE Access*, vol. 7, pp. 62689-62694, 2019.

[10] H. Liu, H. Xue, Y. Liu, Q. Feng, and L. Li, "Generation of high-order Bessel orbital angular momentum vortex beam using a single-layer reflective metasurface," *IEEE Access*, vol. 8, pp. 126504-126510, 2020.

[11] D. Su, H. Zhang, H. Xiao, W. Song, H. Xiong, D. Xiao, and X. Wang, "Generation of enhanced focused airy orbital angular momentum beam with metal-only Huygens' metasurface," *IEEE*

*Transactions on Circuits and Systems II: Express Briefs*, vol. 71, no. 8, pp. 3875-3879, 2024.

[12] J. Guo, C. Shen, J. Hu, Y. Zhu, C. Zhang, and S. Wei, "Generation of power-exponent-phase vortex beam arrays based on all-dielectric metasurfaces," *IEEE Photonics Journal*," vol. 16, no. 2, pp. 1-6, 2024.

[13] R. Xi, L. Li, and T. Zhang, "A high-gain orbital angular momentum antenna array based on parasitic composite slabs," in *2018 International Applied Computational Electromagnetics Society Symposium - China (ACES)*, Beijing, China, pp. 1-2, 2018.

[14] M. K. T. Al-Nuaimi, W. G. Whittow, G.-L. Huang, and R.-S. Chen," Generation of narrow divergence angle OAM beams for mmwave communication links using metasurface," in *2024 18th European Conference on Antennas and Propagation (EuCAP),* Glasgow, UK, pp. 1-5, 2024.

[15] S. Guo, Z. He, and R. Chen, "Generation and numerical simulation of the focused OAM beams," *Engineering Analysis with Boundary Elements*, vol. 135, pp. 359-368, 2022.

[16] J. Ren and K. W. Leung, "Generation of high-purity millimeter-wave orbital angular momentum modes using horn antenna: theory and implementation," arXiv preprint arXiv:1710.00035, 2017.

[17] J.-T. Jing, W. Song, and X.-Q. Sheng, "Transformation optics-based horn antenna for focusing orbital angular momentum beams," *International Journal of RF and Microwave Computer-Aided Engineering*, vol. 30, no. 11, p. e22408, 2020.

[18] J. B. Pendry, D. Schurig, and D. R. Smith, "Controlling electromagnetic fields," *Science*, vol. 312, no. 5781, pp. 1780-1782, 2006.

[19] J. Kraus and R. Marhefka, *Antennas: For All Applications*. Maidenhead: McGraw-Hill Publishing, 2004.

[20] A. Yelizarov, I. Nazarov, A. Skuridin, and E. Zakirova, "Computer model of a frequency-selective surface on mushroom-shaped metamaterial," in *2020 Systems of Signal Synchronization, Generating and Processing in Telecommunications (SYNCHROINFO)*, pp. 1-4, 2020.

[21] H. Sedghi and H. Rezazadeh, "A broadband asymmetric microwave metamaterial based on LC and standing-wave resonances," *Physics Letters A*, vol. 384, no. 29, p. 126758, 2020.

[22] X. Chen, T. M. Grzegorczyk, B.-I. Wu, J. Pacheco Jr, and J. A. Kong, "Robust method to retrieve the constitutive effective parameters of metamaterials," *Physical Review E*, vol. 70, no. 1, p. 016608, 2004.

[23] T. Yuan, Y. Cheng, H. Wang, and Y. Qin, "Mode characteristics of vortical radio wave generated by circular phased array: Theoretical and experimental results," *IEEE Trans. Antennas Propag.*, vol. 65, no. 2, pp. 688-695, 2017.

**Jia-Tong Jing** received the B.E., M.S. degrees from Beijing Institute of Technology, Beijing, China, in 2018 and 2021. He is currently pursuing the Ph.D. degree in Institute of Radio Frequency Technology and Software from Beijing Institute of Technology. His current research interests include metamaterial and computational electromagnetics.

**Wei Song** received the B.S. degree from Northeastern University, Shenyang, China, in 2002, and the M.S. and Ph.D. degrees from Queen Mary University of London, UK, in 2003 and 2008, respectively. She is currently an Associate Professor with the School of Information and Electronics, Beijing Institute of Technology, Beijing, China. She has authored or co-authored over 20 papers in refereed journals and international conferences, and has co-authored a monograph in computational electromagnetics. Her current research interests include high-performance methods in computational electromagnetics, EM property analysis, and metamaterial-based antenna design.

**Xin-Qing Sheng** received the B.S., M.S., and Ph.D. degrees from the University of Science and Technology of China (USTC), Hefei, China, in 1991, 1994, and 1996, respectively. Sheng is a Chang-Jiang Professor of the School of Information and Electronic at the Beijing Institute of Technology. Sheng has authored and co-authored over 150 papers in refereed journals, and three books: *Essentials of Computational Electromagnetics* (Singapore: IEEE Press-Wiley, 2012), *A Brief Treatise on Computational Electromagnetics* (Beijing: Science Press, 2004), and *A Treatise on Electromagnetic Wave* (Beijing: Science Press, 2007). Sheng has authored SINOCOM, a simulation software for scattering by complex targets. His research interests include computational electromagnetics, scattering and antenna analysis, electromagnetic compatibility, and microwave imaging.

# A Novel Reconfigurable Chipless RFID Tag Based on Notch Filter

**Li Zhang[1], Ajay K. Poddar[2], Ulrich L. Rohde[2], and Mei Song Tong[1]**

[1]Department of Electronic Science and Technology, Tongji University
Shanghai 201804, China
1910692@tongji.edu.cn, mstong@tongji.edu.cn

[2]Synergy Microwave Corporation, 201 McLean Boulevard
Paterson, NJ 07504, USA
akpoddar@ieee.org, u.l.rohde@ieee.org

***Abstract –*** A novel reconfigurable chipless RFID tag to enhance encoding capacity is proposed in this paper. The entire transmission network includes four non-interacting ports that are independent separately. The reconfigurability can be realized by combining different ports to get different encoding results. To increase the anti-interference capability of the tag, a method of cross-combination for unit coders is proposed according to the spacing distances of the unit coders. The encoding ability of about 8-bit information can be obtained by using the compact tag structure with a dimension of $70 \times 70$ mm$^2$ and the encoding capacity can be increased by increasing the number of unit coders. Code "1" or "0" is defined by arranging the appearance or disappearance of a unit coder. Typical encoding examples are presented and the simulation results match well with the measurement results, demonstrating the effectiveness of the proposed tag. The proposed tag can be used for structural health monitoring with the advantages of battery-free, large information capacity, and flexible usage.

***Index Terms –*** Chipless RFID, encoding capacity, notch filter, reconfigurable RFID, tag antenna.

## I. INTRODUCTION

Radio frequency identification (RFID) technology is a kind of wireless information tracking and identification technology and it has been widely used in various industries and people's lives, such as traffic control, asset management, and health care, logistics, transportation, etc. [1]. The tag is a vital component in the RFID system and its primary function is to transmit the stored information when requested. Traditionally, the RFID tag includes a special silicon chip used for storing the information of attached targets so that more information can be stored. However, the inclusion of silicon chip will significantly increase the cost of the tag and many cost-sensitive applications like cheap and large-amount fast-selling products may not be able to accept [2]. To remarkably lower the cost, the chipless RFID tag has been developed. Because the chip is removed, no complex and costly operation is required to connect the chip to an antenna, so that the design and fabrication can be greatly simplified. As a new branch of RFID technology, the chipless RFID has received a wide attention and has also been extensively applied in recent years [3–6].

There have been many different designs for the chipless RFID tags which can be found in the literature [7–10]. However, the chipless RFID tag has a very limited capacity of storing information since no chip is used as a storage and the tag antenna usually has a weak coding capacity because it is hard to obtain good responses used for encoding information [11, 12]. To enhance the coding capacity, one has proposed some effective encoding techniques and they can be categorized into time-domain-based, frequency-domain-based, phase-domain-based, and image-domain-based encoding methods, respectively [13–16]. In practice, the frequency-domain-based and phase-domain-based encoding methods could be the favorable choices due to their easier fabrication and more efficient detection [17–25].

We employ the frequency-domain-based method to propose a novel reconfigurable chipless RFID tag so as to enhance its coding capacity. The tag includes four independent ports with an isolation and its reconfigurability is achieved by using different port combinations with different coding results. There are eight unit coders which are clockwisely arranged on the microstrip lines in the tag. When the detection signal is loaded to one of the four ports, then we can obtain an output signal from the other port. The four frequency attenuations will be generated by the four unit coders, but the detection signal will not be impacted by the unit coders close to the other two ports. By setting the presence or absence of unit coders, we can obtain

*Submitted On: November 27, 2023*
*Accepted On: November 17, 2024*



https://doi.org/10.13052/2024.ACES.J.390906

Code "1" or Code "0" in the corresponding coding bandwidth.

The proposed tag has been extensively simulated by using the well-known HFSS for the $S$ parameters which are the transmission coefficients between every two ports, i.e. $S_{12}$, $S_{13}$, $S_{14}$, $S_{23}$, $S_{24}$, and $S_{34}$ and the optimal geometric parameters are obtained by using the HFSS optimization. The final size of the tag is only $70 \times 70$ mm$^2$ which is relatively small compared with other similar chipless RFID tags. We also fabricate the tag based on the optimal geometric parameters and then measure its $S$ parameters by using a vector network analyzer (VNA). It is found that the simulated results are in good agreement with the experimental results, verifying the performance of the designed tag. The tag includes eight unit coders which can store 8-bit data. If we need $2^8$ codes, only $2^8/6$ tags are designed, so the coding capacity can be significantly increased. Note that there is not the code of 11111111 because it will be degenerated to the code 00000000. Also, when the number of coders is increased, the coding capacity can be further expanded with a small increase of costs. Furthermore, the tag has a high degree of isolation between different ports because we use a cross combination for unit coders in terms of their spacings, and such a cross combination can greatly enhance the anti-interference ability of the tag.

## II. NOTCH FILTER

We use the notch filter which is the first-order prototype circuit based on series-inductance-capacitance resonant circuits [26] in the design of tags. The inductance and capacitance values can be calculated by the following equations after the filter circuit is transformed from a lowpass to a bandstop:

$$L_s = \frac{1}{W w_c C_c w_0}, \tag{1}$$

$$C_s = \frac{W w_c C_c}{w_0}, \tag{2}$$

where $L_s$ is the inductance while $C_s$ is the capacitance and the subscript "s" denotes "series". Also, $W$, $w_0$, and $w_c$ represent the relative bandwidth, the center frequency of the stopband, and the cutoff frequency, respectively. From the principle of microstrip lines, we know that an open-ended microstrip line with a length of $\lambda/4$ can be seen as an equivalent series-RLC resonant circuit and its resistance ($R$), inductance ($L$), and capacitance ($C$) can be determined by:

$$R = Z_{0i}\alpha l_i, \tag{3}$$

$$L = \frac{\pi Z_{0i}}{4\omega_i}, \tag{4}$$

$$C = \frac{4}{\pi Z_{0i}\omega_i}, \tag{5}$$

where $Z_{0i}$, $\alpha$, $l_i$, $\omega_i$ are the characteristic impedance of the open-ended microstrip line, the attenuation coefficient, the length of open-ended microstrip line, and angular frequency, respectively. Also, the capacitance $C_c$ in (1) and (2) can be calculated by the following analogy formulas:

$$C = \left(\frac{R_0}{R_0'}\right)\left(\frac{\omega_0'}{\omega_0}\right)C', \tag{6}$$

$$C_c = \left(\frac{R_0}{R_0'}\right)\left(\frac{\omega_c'}{\omega_c}\right)C_c', \tag{7}$$

where $\omega_c' = 1$ is the normalized cutoff frequency of the lowpass prototype filter. Substituting (7) to (1), we can calculate the inductance $L_s$ by:

$$L_s = \frac{g_i}{W Z_{0o}\omega_0}, \tag{8}$$

where $Z_{0o}$ is the characteristic impedance of the microstrip transmission line and $g_i$ is the value of Butterworth filter's inductance or capacitance which is given by:

$$g_i = 2\sin\left[\frac{(2i-1)\pi}{2n}\right]. \tag{9}$$

Thus, the microstrip circuit of the notch filter used in the chipless RFID tag can be designed by using the above equations, i.e. (5), (8), and (9), which are summarized as follows:

$$R = Z_{0i}\alpha l_i, \tag{10}$$

$$L = \frac{Z_{0i}}{8f}, \tag{11}$$

$$C = \frac{2}{Z_{0i}\pi^2 f}, \tag{12}$$

$$Z_{0i} = \frac{2Z_{0o}}{\Delta W \pi}, \tag{13}$$

$$Z_{0i} = F(f_i, w_{si}, \varepsilon_r, t, h), \tag{14}$$

$$Z_{0o} = F(f_o, w_{so}, \varepsilon_r, t, h), \tag{15}$$

where $Z_{0i}$, $f_i$, $w_{si}$, and $l_i$ are the characteristic impedance, working frequency, width and length of the $i$th open-ended microstrip line, respectively. Here, $f_i = w_i/2\pi$. Also, $w_{so}$, $f_o$, and $\Delta W$ are the width of microstrip transmission line, the central frequency, and fractional bandwidth. In addition, $\varepsilon_r$, $t$, and $h$ are the common parameters in the microstrip transmission line, which are the permittivity, thickness of coating copper, and thickness of substrate, respectively. Moreover, $F$ is a common function used to calculate the characteristic impedance. After obtaining the RLC values, we can apply the RLC circuit to design the microstrip circuit by using the well-known software ADS.

## III. DESIGN AND ANALYSIS

Figure 1 shows a physical structure of the proposed reconfigurable chipless RFID tag which consists of a substrate, a ground plane, two crossed microstrip lines, and eight open-ended microstrip lines. We define the eight open-ended microstrip lines as eight unit coders, which are distributed on the two crossed microstrip

lines in a clockwise direction. Actually, the electrical lengths of eight unit coders can be changed by using the quarter-wavelength bandstop filter theory. Also, the real lengths of eight unit coders are calculated, respectively, by using the formulas of notch-filter theory in section II. In order to better understand the calculating process for the dimensions of coders, we summarize the calculating steps as shown in Fig. 3.

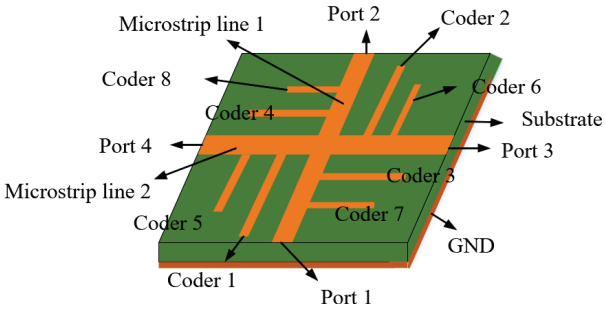


Fig. 1. Physical structure.

Note that the final length and width of the coders are obtained by optimizing these parameters through the simulations of well-known HFSS. The optimized lengths $l_i$ and widths $w_i$ $(i = 1, 2, \cdots, 8)$ of the eight coders are presented in Fig. 2 and their values are summarized in Table 1. Since one coder can produce one resonant frequency, eight coders can generate eight resonant frequencies with their bandwidths and they can be used to

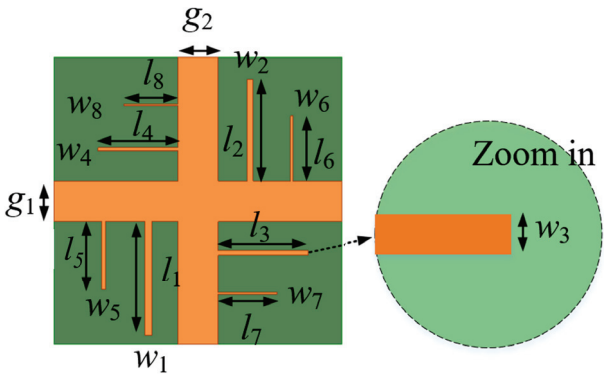


Fig. 2. Top view of the tag.

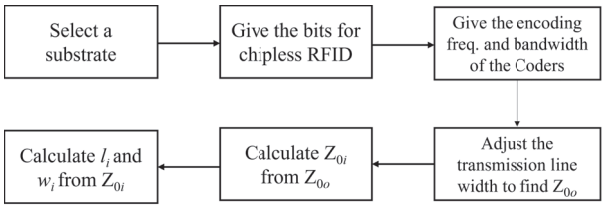


Fig. 3. Calculating process for the dimensions of coders.

Table 1: Optimized lengths and widths of the coders (Unit: mm)

| $l_1$ | $l_2$ | $l_3$ | $l_4$ | $l_5$ | $l_6$ | $l_7$ | $l_8$ |
|---|---|---|---|---|---|---|---|
| 28 | 24.7 | 21.8 | 19.4 | 16.9 | 15.8 | 14.3 | 13.1 |
| $w_1$ | $w_2$ | $w_3$ | $w_4$ | $w_5$ | $w_6$ | $w_7$ | $w_8$ |
| 1.7 | 1.34 | 1.1 | 0.8 | 1.0 | 0.52 | 0.42 | 0.31 |

encode information when excited. The correspondence between the lengths of coders and encoding frequencies is shown in Fig. 4. In order to miniaturize the tag, we set the widths of two microstrip transmission lines as $g_1 = 9.8$ mm and $g_2 = 9.8$ mm, respectively, and set the total length and width of the tag as $L = 70$ mm and $W = 70$ mm, respectively. Considering the favorable properties of Rogers RT/duroid 5880 (tm) as a dielectric medium, it is used as the substrate material in the tag and its relative permittivity, dielectric loss tangent, and thickness are 2.2, 0.0009, and 0.508 mm, respectively. As a high-frequency laminate used for stripline and microstrip circuit structures, Rogers RT/duroid 5880 (tm) is a microfiber-reinforced polytetrafluoroethylene (PTFE) composite material that can maintain a consistent dielectric constant between different layers of the laminate and keep unchanged over a wide frequency range. In addition, the material has the merits of low electrical loss, low moisture absorption, and excellent chemical resistance.

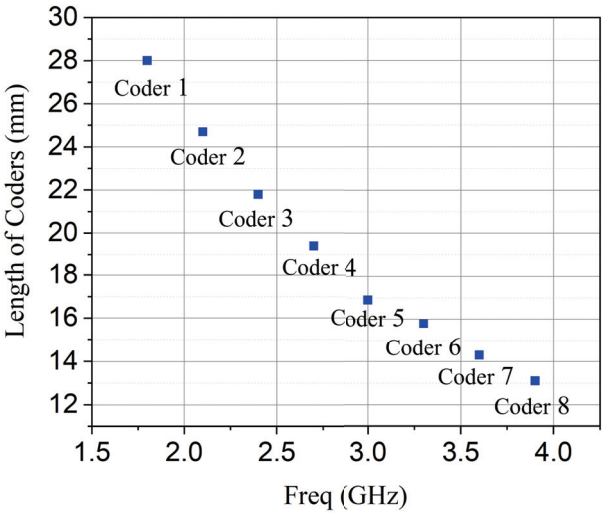


Fig. 4. Lengths of coders (mm) versus encoding frequency.

The pairing of the eight coders is illustrated in Fig. 5. Specifically, Coder 1 is paired with Coder 5, Coder 2 with Coder 6, Coder 3 with Coder 7, and Coder 4 with Coder 8, respectively. These pairings are denoted as Couple 1, Couple 2, Couple 3, and Couple 4, respectively. Such a pairing scheme can minimize the coupling

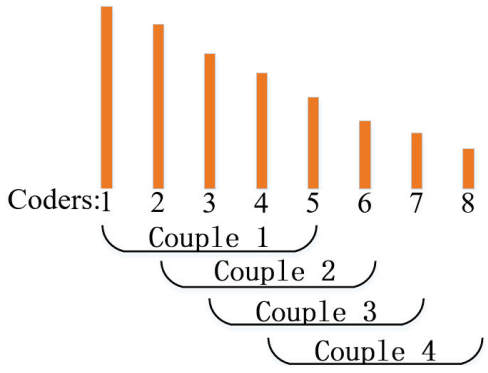


Fig. 5. Coupling schematic diagram of unit coders.

interference between unit coders and waste of spectrum resource. If the coders are paired in order, for example, Coder 1 and Coder 2 are paired in the same microstrip line, they can easily produce a coupling interference and even cause an encoding error because the lengths of the two unit coders are close and they could produce similar resonant frequencies. On the other hand, we should minimize the frequency bandwidth in case the spectrum resource is wasted, hence the gap of neighboring resonant frequencies should not be far away excessively. As a trade-off, we select a total frequency range from 1.8 to 3.9 GHz as the encoding bandwidth. Eight resonant frequencies with an average interval can be obtained by selecting appropriate dimensions for the coders and they are 1.8 GHz, 2.1 GHz, 2.4 GHz, 2.7 GHz, 3.0 GHz, 3.3 GHz, 3.6 GHz, and 3.9 GHz, respectively.

To demonstrate the proposed encoding scheme, we present an example with the code of 00110011 and it is shown in Fig. 6. In the figure, Code "1" and Code "0" are achieved in the corresponding encoding bandwidths by setting the appearance and disappearance of corresponding unit coders, respectively. The appearance of a unit coder will produce a notch in the figure and we define −30 dB as a threshold. If the notch is below −30 dB, then the corresponding code is designated as "1", otherwise the code is designated as "0".

## IV. SIMULATED AND MEASURED RESULTS

Figure 8 shows the fabricated tag antenna sample and the coaxial connectors are welded to four feeding ports. The tag is fabricated under laboratory conditions by the etching method which is a subtraction process [27]. In the measurement experiment, as shown in the Fig. 9, we connect the Vector Network Analyzer (VNA) with chipless RFID tag using two coaxial lines, and we measure the $S$ parameter (transmission coefficient) values of every two ports $S_{12}$, $S_{13}$, $S_{14}$, $S_{23}$, $S_{24}$, $S_{34}$. We define the number here as the port number. For example, $S_{12}$ indicates the transmission coefficient between Port 1 and Port 2.

To verify the independent port, all the coding cases of connecting two ports are presented, respectively. It can be seen from Fig. 7, no matter which two ports are connected, their deep notches (the coding frequencies) from attenuated frequencies are within a specific same range. Although some deep notches of *coders* have small deviations, they are all within the coding frequency band 1.95∼2.25 GHz. For example, the Coder 2 deep notch has a gap of about 20 MHz between the purple curve and the blue curve, and there is also a gap of about 20 MHz between the purple curve and the red curve. But it will not affect the encoding results, and such small differences are acceptable.

The software HFSS is applied in the simulations and Fig. 10 shows the transmission coefficient $S_{12}$ of the proposed reconfigurable chipless tag. When we connect Port

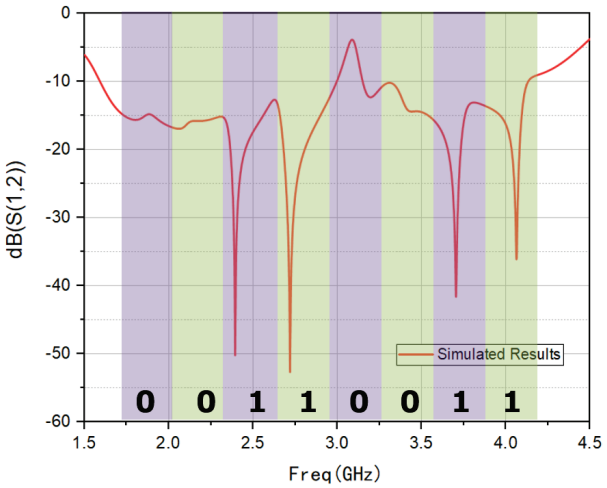


Fig. 6. A coding display with the code of 00110011.

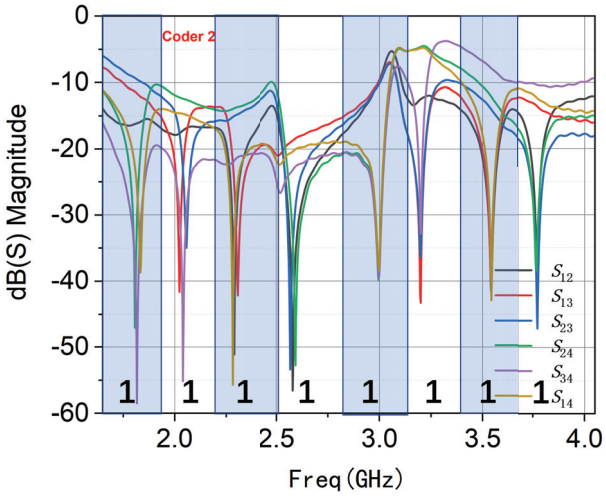


Fig. 7. Port independence verification.

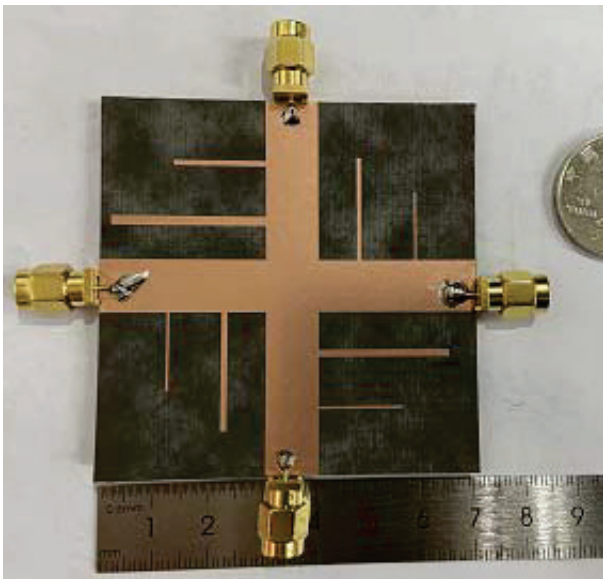

Fig. 8. Fabricated tag antenna sample.

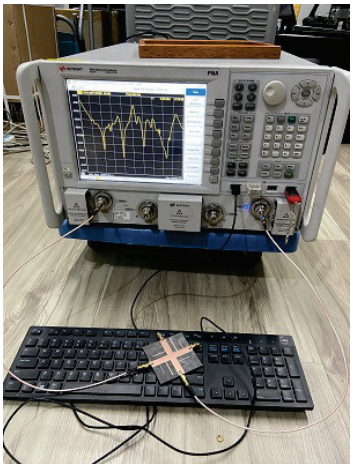

Fig. 9. Photo of device connection.

1 and Port 2, the four Coders, namely, Coder 3, Coder 4, Coder 7, and Coder 8 are excited, and corresponding four resonant frequencies of 2.39 GHz, 2.72 GHz, 3.70 GHz and 4.06 GHz can be obtained with the code of 00110011. At the same time, the other four coders are not influenced. So, it has a good isolation effect as well, which realize the chipless tag's anti-interference ability. The other five codes can be obtained by connecting other ports. Those are 01100110, 10101010, 01010101, 10011001 and 11001100, respectively. All of these codes are depicted in Figs. 10–15.

Traditionally, the structure of chipless RFID tag is not able to be changed after the tag being designed and fabricated and one tag can only produce one code. The proposed tag with 8 unit coders can produce 6 codes

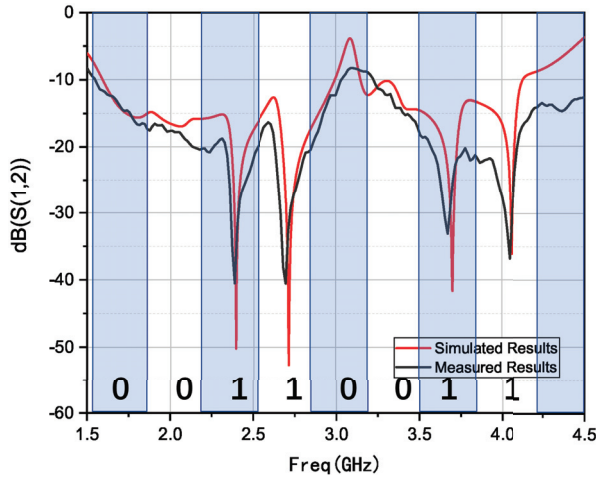


Fig. 10. Transmission coefficient by connecting Port 1 and Port 2 and the code is 00110011.

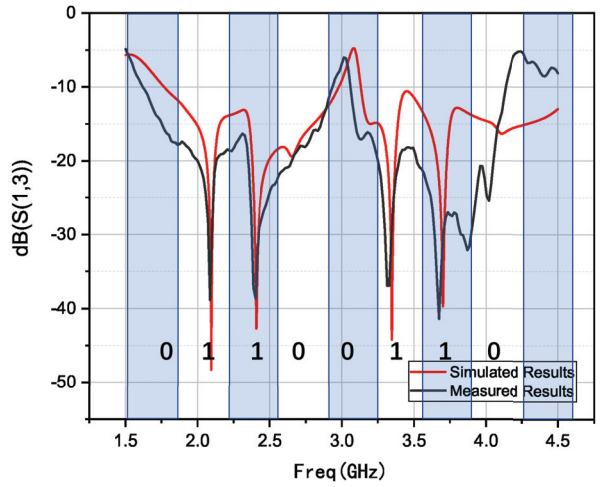


Fig. 11. Transmission coefficient by connecting Port 1 and Port 3 and the code is 01100110.

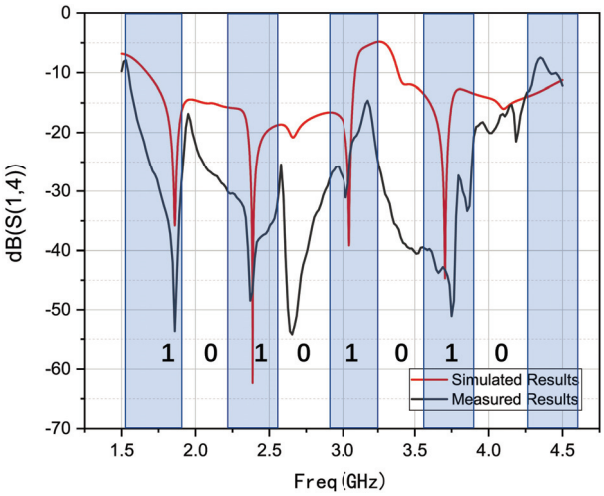


Fig. 12. Transmission coefficient by connecting Port 1 and Port 4 and the code is 10101010.

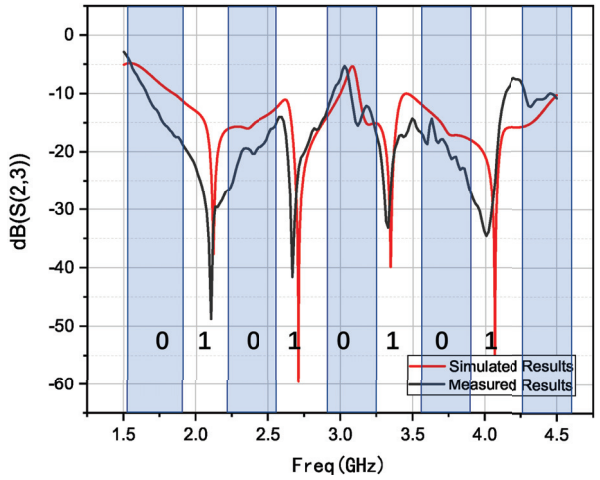


Fig. 13. Transmission coefficient by connecting Port 2 and Port 3 and the code is 01010101.

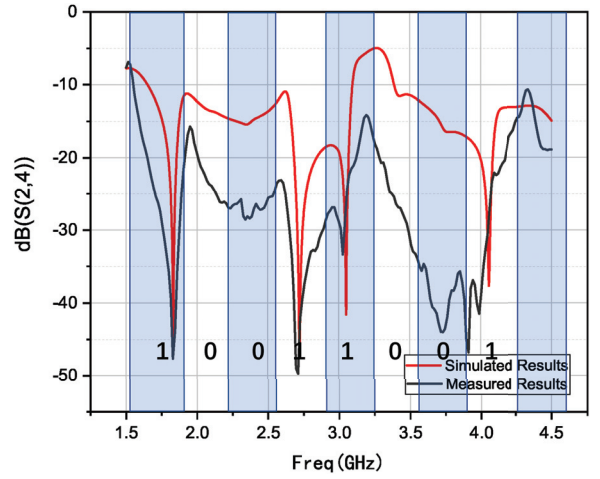


Fig. 14. Transmission coefficient by connecting Port 2 and Port 4 and the code is 10011001.

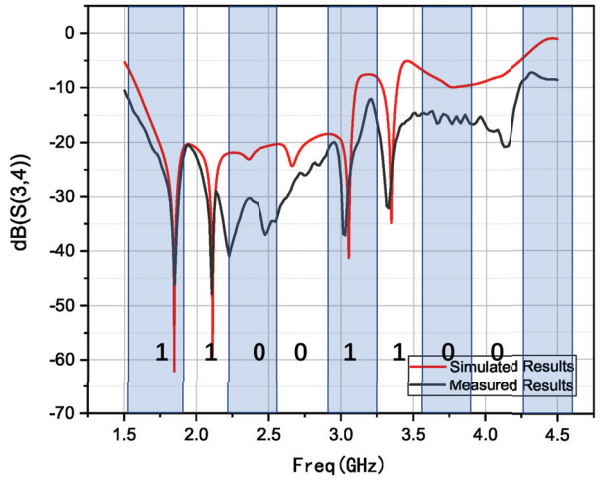


Fig. 15. Transmission coefficient by connecting Port 3 and Port 4 and the code is 11001100.

by connecting different ports. So only one-type tag is needed to design in actual application if we need 6 codes. Meanwhile, the code "1" or "0" can be obtained in the corresponding encoding band by arranging the presence or absence of unit coders. So the proposed tag can encode 8-bit data. Since one 8-bit tag can produce $2^8$ codes, we only need to design $2^8/6$ electronic tags, significantly enhancing the coding capacity.

The aforementioned experiments employed a vector network analyzer of Keysight which is connected to two coaxial cables to conduct the wired measurement. For cross-validation, we performed a second set of wired measurements as shown in Fig. 16, utilizing a Rohde & Schwarz vector network analyzer and replacing the previous coaxial cables with specialized test cables designed for network analyzers. These cables have a characteristic impedance of 50 ohms, a propagation velocity of 76%, and a maximum operating frequency of 26.5 GHz. They are characterized by low insertion loss and high durability, which helps to mitigate the issue of significant measurement errors.

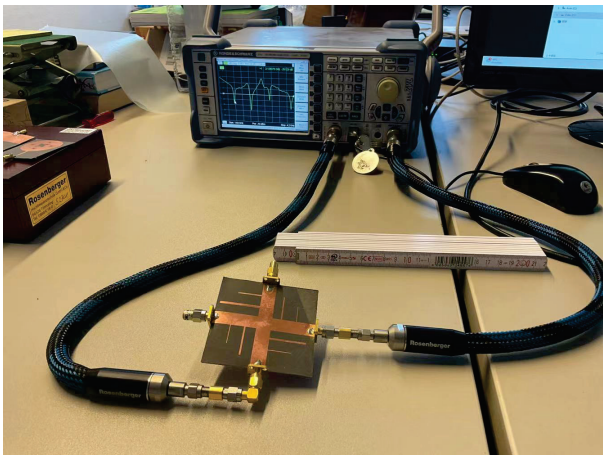

Fig. 16. Wired measurement via a Rohde & Schwarz vector network analyzer.

Additionally, we conducted wireless measurements. Figure 17 illustrates the scenario of performing the wireless measurements, including two orthogonally polarized conical log-periodic antennas as the transmitting and receiving antennas, respectively. Two ultra-wideband monopole antennas are vertically integrated into the designed miniaturized tag. The conical log-periodic antennas are connected to the ports of a chipless reader to measure the transmission coefficient response of the integrated tag. The measurement distance between the antennas and tag is approximately 15 cm.

Figures 18–23 display the comparison between the results of the second wired measurements and the wireless measurements. The results indicate a good

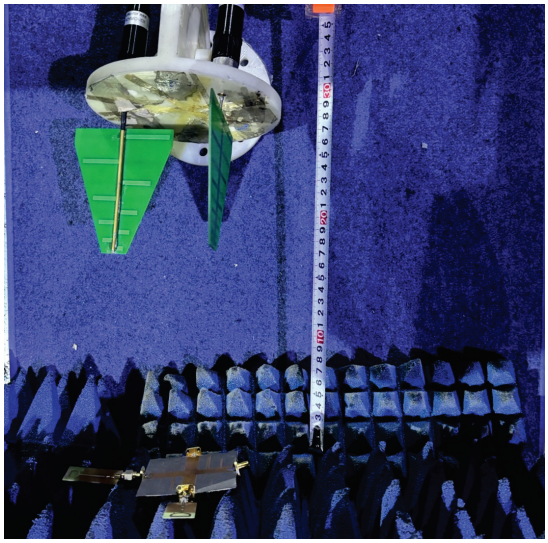

Fig. 17. Scenario of performing the wireless measurement.

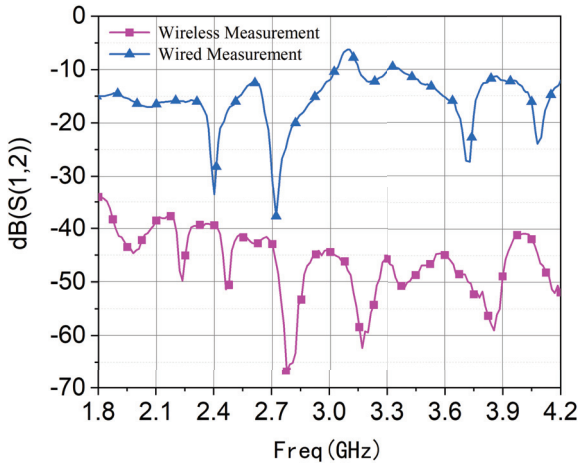


Fig. 18. $S_{12}$ of wired and wireless measurement.

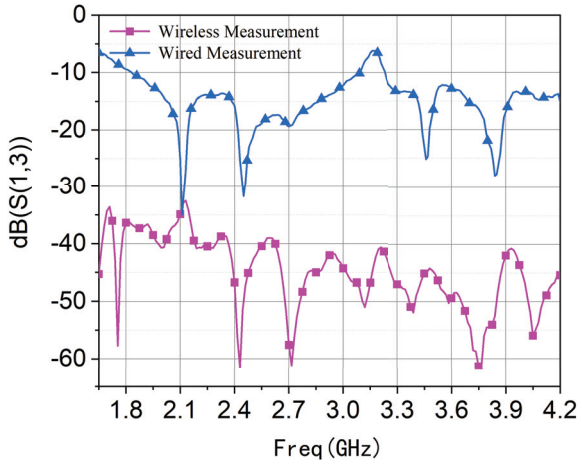


Fig. 19. $S_{13}$ of wired and wireless measurement.

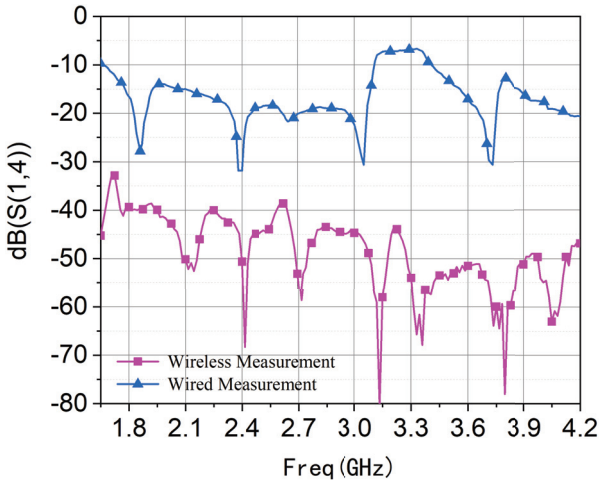


Fig. 20. $S_{14}$ of wired and wireless measurement.

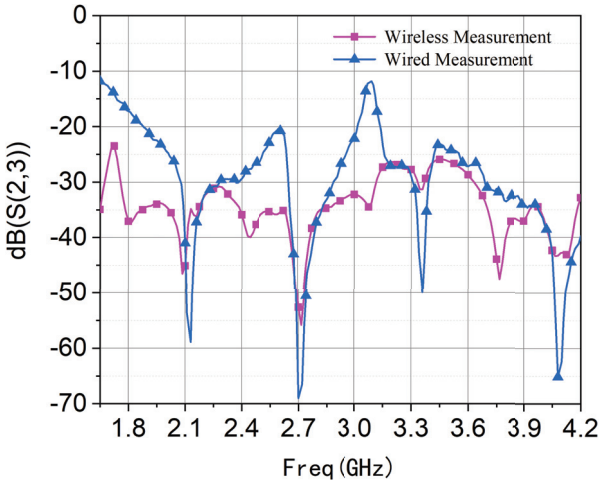


Fig. 21. $S_{23}$ of wired and wireless measurement.

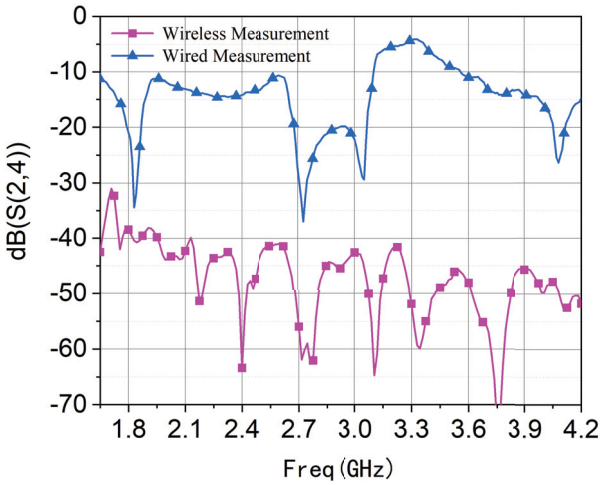


Fig. 22. $S_{24}$ of wired and wireless measurement.

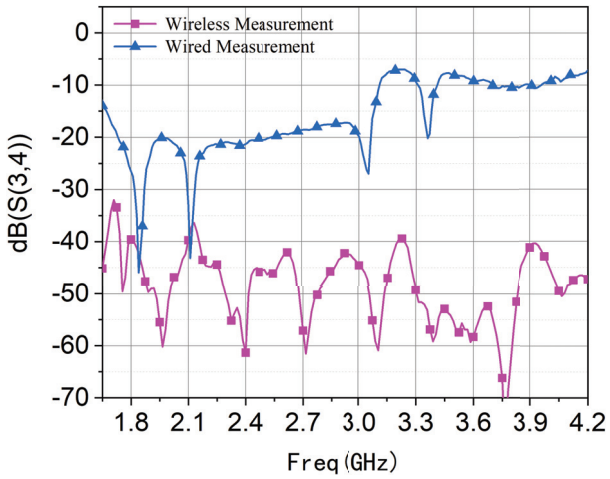


Fig. 23. $S_{34}$ of wired and wireless measurement.

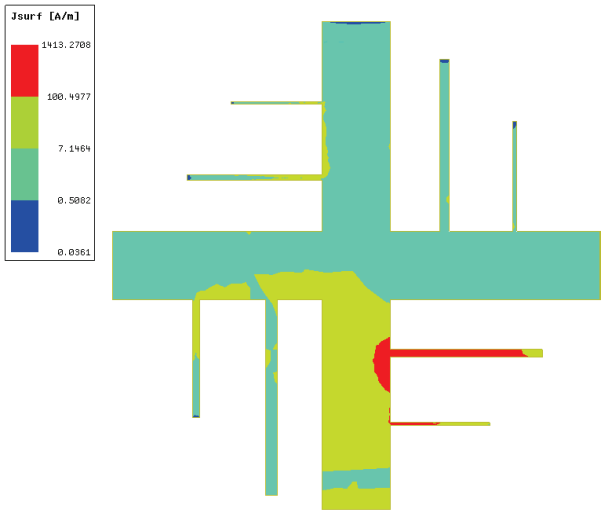


Fig. 24. Surface current distribution at the frequency of 2.39 GHz.

agreement between the wired and wireless measurement outcomes. However, due to the presence of background noise, there is a certain discrepancy between the results of the wired and wireless measurements. Additionally, some resonant points exhibit errors, possibly due to the fact that the cables and connectors used to connect the VNA and the antennas may introduce additional losses in actual measurements. These losses might not have been fully considered in the simulations, leading to discrepancies between the measured and simulated results. Particularly at high frequencies, the losses in the cables become more pronounced.

Table 2 shows the comparison of the tag we proposed in this work with other chipless tags reported. Although the proposed tag has a relatively low encoding density, it still can reduce the size of the tag compared to structures where encoding units are placed on both sides of the microstrip line. This is because our proposed structure connects the coding unit (Coder) in a clockwise rotation on the cross-microstrip line. Moreover, it possesses reconfigurability, and the material used is the commonly utilized Rogers RT/duroid 5880, which is relatively cost-effective.

The surface current distributions generate the electromagnetic signals and thus impact the coding quality. Figures 24–27 present the surface current distributions on the tag at different frequencies, where the red region represents a larger current density. From the current distributions, we can clearly see the activated states of the tag. Taking the current distribution generated for connecting ports 1 and 2 as an example. When we perform the parameter sweep analysis at the frequency of 2.39 GHz, 2.27 GHz, 3.70 GHz, and 4.06 GHz, respectively, we can obtain the corresponding working codes, i.e. Coder 3, Coder 4, Coder 7, and Coder 8, respectively. There should be one coder activated for each frequency theoretically and the red region indicates that the coders are strongly excited. From Figs. 24–27, we can validate this conclusion, even though there are the cases that two coders are simultaneously activated at the same frequency. However, this does not affect the other

Table 2: Comparison between the proposed tag and other chipless tags

| Tag Type | Encode Density | Size (mm × mm) | Reconfigurability | Substrate Material | Reference |
|---|---|---|---|---|---|
| Re-transmission | 0.4 bit/cm$^2$ | 30×70 | No | $SnO_2$/G | [28] |
| RCS | 0.45 bit/cm$^2$ | 21×21 | No | FR-4 | [29] |
| RCS | 28.6 bit/cm$^2$ | 3.5×4 | No | Taconic TLX-0(high cost) | [30] |
| RCS | 745.1 bit/$\lambda_g^2$ | 6.4×3.4 | Yes | Rogers RO4003 | [2] |
| Re-transmission | 0.16 bit/cm$^2$ | 70×70 | Yes | Rogers RT/duroid 5880 | our work |

$\lambda_g$ is the guided wavelength at the lowest resonant frequency.

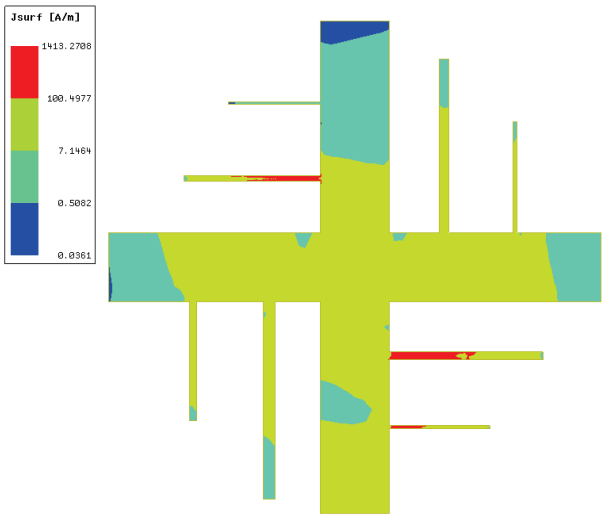


Fig. 25. Surface current distribution at the frequency of 2.72 GHz.

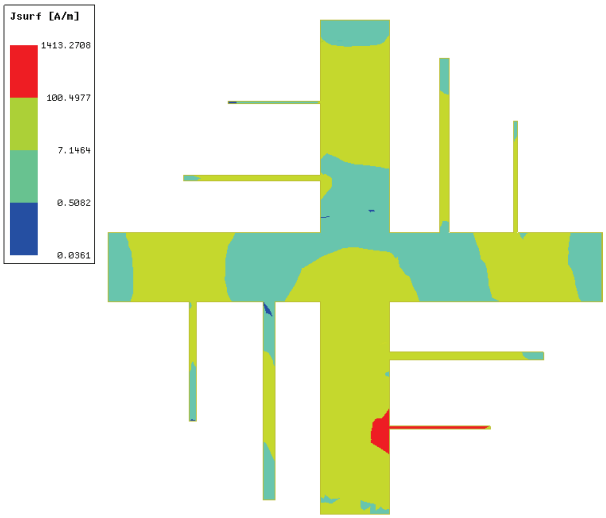


Fig. 26. Surface current distribution at the frequency of 3.70 GHz.

four coders, so the simultaneous activation is acceptable. Taking Fig. 27 as an example, we can see that Coder 7 and Coder 8 are simultaneously activated, but the encoding result remains 00110011, which is unchanged. This is because the other four coders are located at another microstrip line and they will not be affected. In addition, since the tag is fabricated using an etching method with chemical solution in a limited laboratory environment, there is a big discrepancy between the measurement results and simulation results. If we use a Laser Direct Structuring (LDS) method to fabricate the tag, the discrepancy can be greatly reduced because the LDS method can more precisely control the geometry and placement of conductive elements.

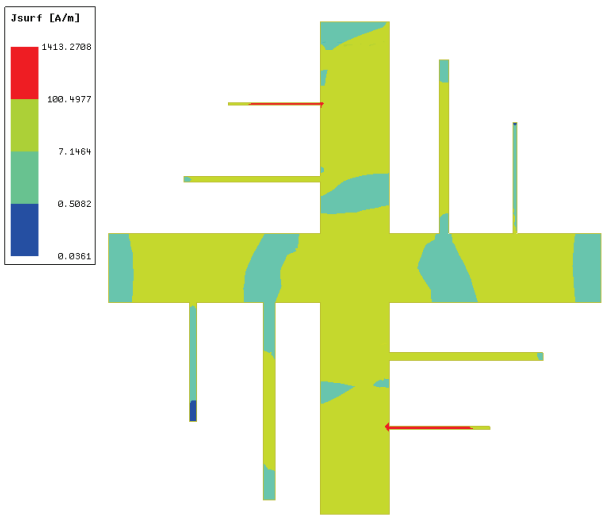


Fig. 27. Surface current distribution at the frequency of 4.06 GHz.

## V. CONCLUSION

This paper proposes a novel reconfigurable chipless RFID tag based on a notch filter. The tag consists of four separated and noninteracted ports and the reconfigurability of encoding results is achieved by combining different ports. Also, the tag has a strong anti-interference capability because the cross-combination of unit coders is used based on their spacings. The tag can encode the information with about 8 bits by using Code "1" or "0" to represent the appearance or disappearance of the unit coders, respectively, and the encoding capacity can be further enhanced if using more unit coders. The tag has a compact structure whose size is only $70 \times 70$ mm$^2$. The encode density of the tag are 0.16 bit/cm$^2$. We present typical encoding examples to illustrate the proposed tag and its good performance has been verified by both simulation results and measurement results.

## REFERENCES

[1] S. M. Chiang, E. H. Lim, P. S. Chee, Y. H. Lee, and F. L. Bong, "Dipolar tag antenna with a top-loading inductive channel with broad range frequency tuning capability," *IEEE Transactions on Antennas and Propagation*, vol. 70, no. 3, pp. 1653-1662, Mar. 2022.

[2] L. Wang, T. Liu, J. Siden, and G. Wang, "Design of chipless RFID tag by using miniaturized open-loop resonators," *IEEE Transactions on Antennas and Propagation*, vol. 66, no. 2, pp. 618-626, Feb. 2018.

[3] N. Javed, M. A. Azam, and Y. Amin, "Chipless RFID multisensor for temperature sensing and crack monitoring in an IOT environment," *IEEE Sensors Letters*, vol. 5, no. 6, pp. 1-4, June 2021.

[4] L. Corchia, G. Monti, E. D. Benedetto, and L. Tarricone, "A chipless humidity sensor for wearable applications," *in IEEE International Conference on RFID Technology and Applications*, Pisa, Italy, Sep. 2019.

[5] A. M. J. Marindra and G. Y. Tian, "Chipless RFID sensor tag for metal crack detection and characterization," *IEEE Transactions on Microwave Theory and Techniques*, vol. 66, no. 5, pp. 2452-2462, May 2018.

[6] L. Y. Liu, A. K. Poddar, U. L. Rohde, and M. S. Tong, "A novel flexible chipless RFID tag sensor for monitoring environmental humidity," *IEEE Sensors Journal*, vol. 23, no. 24, pp. 31237-31249, Dec. 2023.

[7] Y. Gao, M. Mahmoodi, and R. Zoughi, "Design of a novel frequency-coded chipless RFID tag," *IEEE Open Journal of Instrumentation and Measurement*, vol. 1, pp. 1-9, 2022.

[8] M. Noman, U. A. Haider, A. M. Hashmi, H. Ullah, A. I. Najam, and F. A. Tahir, "A novel design methodology to realize a single byte chipless RFID tag by loading a square open-loop resonator with micro-metallic cells," *IEEE Journal of Microwaves*, vol. 3, no. 1, pp. 43-51, Jan. 2023.

[9] M. T. Tu, P. Cheong, and W. W. Choi, "Defected ground structure with half-wavelength spiral resonator of ultrawide band chipless RFID tag," *IEEE Journal of Radio Frequency Identification*, vol. 3, no. 3, pp. 121-126, Sep. 2019.

[10] A. Vena, A. A. Babar, L. Sydänheimo, M. M. Tentzeris, and L. Ukkonen, "A novel near-transparent ask-reconfigurable inkjet-printed chipless RFID tag," *IEEE Antennas and Wireless Propagation Letters*, vol. 12, pp. 753-756, 2013.

[11] M. S. Reynolds, "A 500°C tolerant ultra-high temperature 2.4 GHz 32 bit chipless RFID tag with a mechanical BPSK modulator," in *2017 IEEE International Conference on RFID (RFID)*, Phoenix, AZ, pp. 144-148, 2017.

[12] B. Kubina, M. Schusler, C. Mandel, A. Mehmood, and R. Jakoby, "Wireless high-temperature sensing with a chipless tag based on a dielectric resonator antenna," in *SENSORS, 2013 IEEE*, Baltimore, MD, pp. 1-4, 2013.

[13] V. P. Plessky, W. Steichen, S. Harma, and C. S. Hartmann, "PS-1 SAW RFID tag with reduced size," in *2006 IEEE Ultrasonics Symposium*, Vancouver, BC, Canada, pp. 2389-2392, 2006.

[14] A. Chamarti and K. Varahramyan, "Transmission delay line based ID generation circuit for RFID applications," *IEEE Microwave and Wireless Components Letters*, vol. 16, no. 11, pp. 588-590, Nov. 2006.

[15] M. Donelli, "A chipless RFID system based on substrate impedance waveguide resonators (SIW)," in *2017 IEEE-APS Topical Conference on Antennas and Propagation in Wireless Communications (APWC)*, Verona, Italy, pp. 29-32, 2017.

[16] C. Feng, X. Chen, L. Han, L. Li, G. Han, and W. Zhang, "Angle-based Y-shaped chipless radio frequency identification tag," *IET Microwaves Antennas and Propagation*, vol. 9, no. 15, pp. 1778-1785, Dec. 2015.

[17] Y. J. Zhang, R. X. Gao, Y. He, and M. S. Tong, "Effective design of microstrip-line chipless RFID tags based on filter theory," *IEEE Transactions on Antennas and Propagation*, vol. 67, no. 3, pp. 1428-1436, Nov. 2019.

[18] L. Zhang, H. H. Su, and M. S. Tong, "A novel design of surface acoustic wave-based chipless radio frequency identification tag based on multiphysics modeling," *International Journal of Numerical Modelling: Electronic Networks, Devices and Fields*, vol. 34, no. 6, pp. 1-10, Oct. 2021.

[19] Q. Gu, G. C. Wan, C. Gao, and M. S. Tong, "Frequency-coded chipless RFID tag based on spiral resonators," in *2016 Progress in Electromagnetics Research Symposium (PIERS)*, Shanghai, China, pp. 844-846, 2016.

[20] G. C. Wan, Q. Gu, X. R. Zhang, and M. S. Tong, "Frequency-coded chipless RFID tag based on hybrid coding technique," in *2017 IEEE International Symposium on Antennas and Propagation & USNC/URSI National Radio Science Meeting*, San Diego, CA, USA, pp. 2519-2520, 2017.

[21] G. C. Wan, Y. K. Kuang, Q. Xu, and M. S. Tong, "A novel chipless RFID tag based on backscattering principle," in *2018 Progress in Electromagnetics Research Symposium (PIERS-Toyama)*, Toyama, Japan, pp. 1295-1298, 2018.

[22] X. Y. Guo, G. C. Wan, Y. M. Gao, and M. S. Tong, "A novel temperature sensor based on chipless RFID tags," in *2020 IEEE MTT-S International Conference on Numerical Electromagnetic and Multiphysics Modeling and Optimization (NEMO)*, Hangzhou, China, pp. 1-3, 2020.

[23] L. Zhang, M. M. Li, and M. S. Tong, "A chipless ultra-wideband RFID tag based on cylindrical dielectric resonator," in *2021 IEEE International Symposium on Antennas and Propagation and USNC-URSI Radio Science Meeting (APS/URSI)*, Singapore, Singapore, pp. 381-382, 2021.

[24] J. Li, L. Shi, X. Jin, Q. Zhang, Y. Ran, Q. Lei, Y. Ma, Y. Liu, J. Xiao, and J. Wang, "Efficient and explicit Fourier modal method for ultrathin metallic gratings," *Chinese Journal of Electronics*, vol. 31, no. 6, pp. 1155-1160, Nov. 2022.

[25] C. Jia, Z. He, D. Ding, L. Guan, X. Ai, J. Liu, and X. Chen, "Characteristic mode analysis for thin dielectric sheets with alternative surface integral equation," *Chinese Journal of Electronics*, vol. 31, no. 6, pp. 1181-1188, Nov. 2022.

[26] I. Hunter, *Theory and Design of Microwave Filters*, London, U.K.: IET, 2001.

[27] J. Birkenshaw, *Printed Electronics*. Surrey: Pira International, 2004.

[28] B. Tao, L. Feng, F. Miao, and Y. Zang, "High sensitivity chipless RFID humidity sensor tags are based on $SnO_2$/G nanomaterials," *Vacuum*, vol. 202, p. 111126, Aug. 2022.

[29] P. P. Sahu, D. P. Mishra, T. K. Das, and S. K. Behera, "Design of a chipless RFID tag for 2.4 GHz and 5.8 GHz ISM band applications," in *2020 IEEE International Students' Conference on Electrical, Electronics and Computer Science (SCEECS)*, Bhopal, India, pp. 1-4, 2020.

[30] O. Necibi, S. Naoui, and A. Gharsallah, "Design of a chipless RFID tag based on the frequency shift technique for K band," in *2016 2nd International Conference on Advanced Technologies for Signal and Image Processing (ATSIP)*, Monastir, Tunisia, pp. 816-819, 2016.

**Li Zhang** received the B.S. degree in information and computer science from Henan Agriculture University, Zhengzhou, China, in 2008, and the M.S. degree in electronic science and technology from Tongji University, Shanghai, China, in 2015. Since 2019, she started to pursue the Ph.D. degree in electronic science and technology, Tongji University, Shanghai, China, and is expected to receive the Ph.D. degree in January 2025. From September 2022 to September 2024, She was a visiting/exchange Ph.D. Student with the Technical University of Munich, Munich, Germany. Her current research interests include antenna technology and computational electromagnetics. Ms. Zhang was a recipient of the China Scholarship Council in 2021 and the National Scholarship in 2022.

**Ajay K. Poddar** is an IEEE Fellow and member of IEEE Eta-Kappa-Nu, has been working as a Chief Scientist at Synergy Microwave, NJ, USA, for the last 23 years, responsible for the design and development of signal generation and signal processing electronics, RF-MEMS, and Metamaterial-Sensors/Electronics for industrial, medical, space applications. He is also a visiting professor at the University Of Oradea, Romania, Indian Institute of Technology Jammu, India, and a guest lecturer at the Technical University Munich, Germany. Previously (1991-2001), he was a Senior Scientist and Program Manager at DRDO (Defense Research and Development Organization), Ministry of Defense, India, and a visiting Professor at the University of Pune, India. Dr. Poddar graduated from IIT-Delhi, India; his Doctorate (Dr.-Ing.) from Technical University Berlin, Germany; Post Doctorate (Dr.-Ing. habil) from Brandenburg Technical University Cottbus, Germany. He has received over a dozen awards, to name a few 2015 IEEE IFCS Cady Award in recognition of his outstanding scientific contributions to a host of frequency-generating and frequency-controlled electronics and timing devices for industrial, medical, and space applications, and recipient of the 2018 IEEE MGA Innovation Award for his dedicated volunteering service to members, chapters and humanitarian projects, recipient 2015 IEEE R1 Award for "Outstanding Scientific Contributions, Leadership and Service", recipient 2009 IEEE R1 Award for "Outstanding Leadership and Contributions in the Research, Design, and Development of Microwave Systems", and selected in the list of Divine Innovator "Divine Innovation: 10 Technologies Changing the Future of Passive and Control Components" (Photo shows on Cover page, Microwave Journal, November 2011). Recently, Dr. Poddar received the 2023 RCA Armstrong Medal Award for his three decades of scientific research work in signal generation and signal processing electronics for the application in modern radios and test and measurement equipment. Dr. Poddar published 350 plus scientific papers in journals, magazines, and conference proceedings, co-authored six technical books/chapters, and 40 plus patents for scientific and technological innovations. For the past 30 years, he has supervised many PhD students worldwide, served as an Editor of many Technical Journals, and currently serving in several scientific committees, professional societies, and voluntary organizations.

**Ulrich L. Rohde** is a Partner of Rohde & Schwarz, Munich Germany; Chairman of Synergy Microwave Corp., Paterson, New Jersey; President of Communications Consulting Corporation; serving as an honorary member of the Senate of the University of the Armed Forces Munich, Germany, honorary member of the Senate of the Brandenburg University of Technology Cottbus–Senftenberg, Germany.

Dr. Rohde is serving as a full Professor of Radio and Microwave Theory and Techniques at the University of Oradea and several other universities worldwide, to name a few: Honorary Professor IIT-Delhi, Honorary Chair Professor IIT-Jammu, Professor at the University of Oradea for microwave technology, an honorary professor at the BTU Cottbus-Senftenberg University of Technology, and professor at the German Armed Forces University Munich (Technical Informatics).

Rohde has published 400+ scientific papers, co-authored over dozen books, with John Wiley and Springer, and holds 50 plus patents; received several awards, to name a few recent awards: recipient of 2023 IEEE Communications Society Distinguished Industry Leader Award, 2023 IEEE Antennas and Propagation Society Distinguished Industry Leader Award, 2022 IEEE Photonics Society Engineering Achievement Award, 2021 Cross of Merit of the Federal Republic of Germany, 2020 IEEE Region 1 Technological Innovation Award, 2019 IETE Fellow Award, 2019 IEEE CAS Industrial Pioneer Award; 2017 RCA Lifetime achievement award, 2017 IEEE-Cady Award, 2017 IEEE APS Distinguish achievement award, 2017 Wireless Innovation Forum Leadership Award, 2016 IEEE MTT-S Applications Award, 2015 IEEE-Rabi Award, 2015 IEEE Region-1 Award, and 2014 IEEE-Sawyer Award.

Dr. Ulrich Rohde is the recipient of the "2021 Cross of Merit of the Federal Republic of Germany". The Order of Merit of the Federal Republic of Germany, also known as the Federal Cross of Merit, is the highest tribute the Federal Republic of Germany can pay to individuals for services to the nation. In December 2022, The Indian National Academy of Engineering (INAE) inducted Dr. Ulrich Rohde as a fellow during ceremonies for "outstanding contributions to engineering and also your dynamic leadership in the engineering domain, which has immensely contributed to the faster development of the country." Dr. Rohde is only the third foreign fellow elected by the INAE, preceded by Dr. Jeffrey Wineland, who won a Nobel Prize in Physics.

**Mei Song Tong** received the B.S. and M.S. Degrees from Huazhong University of Science and Technology, Wuhan, China, respectively, and Ph.D. degree from Arizona State University, Tempe, Arizona, USA, all in electrical engineering. He is currently the Distinguished Professor and Head of Department of Electronic Science and Technology, and Vice Dean of College of Microelectronics, Tongji University, Shanghai, China. He has also held an adjunct professorship at the University of Illinois at Urbana-Champaign, Urbana, Illinois, USA, and an honorary professorship at the University of Hong Kong, China. He has published more than 700 papers in refereed journals and conference proceedings and co-authored 8 books or book chapters. His research interests include electromagnetic field theory, antenna theory and design, simulation and design of RF/microwave circuits and devices, interconnect and packaging analysis, inverse electromagnetic scattering for imaging, and computational electromagnetics.

Prof. Tong is a Fellow of the Electromagnetics Academy, Fellow of the Japan Society for the Promotion of Science (JSPS), and Senior Member (Commission B) of the USNC/URSI. He has been the chair of Shanghai Chapter since 2014 and the chair of SIGHT committee in 2018, respectively, in IEEE Antennas and Propagation Society. He has served as an associate editor or guest editor for several well-known international journals, including *IEEE Antennas and Propagation Magazine, IEEE Transactions on Antennas and Propagation, IEEE Transactions on Components, Packaging and Manufacturing Technology, International Journal of Numerical Modeling: Electronic Networks, Devices and Fields, Progress in Electromagnetics Research*, and *Journal of Electromagnetic Waves and Applications*, etc. He also frequently served as a session organizer/chair, technical program committee member/chair, and general chair for some prestigious international conferences. He was the recipient of a Visiting Professorship Award from Kyoto University, Japan, in 2012, and from University of Hong Kong, China, 2013. He advised and coauthored 15 papers that received the Best Student Paper Award from different international conferences. He was the recipient of the Travel Fellowship Award of USNC/URSI for the 31th General Assembly and Scientific Symposium (GASS) in 2014, Advance Award of Science and Technology of Shanghai Municipal Government in 2015, Fellowship Award of JSPS in 2016, Innovation Award of Universities'

Achievements of Ministry of Education of China in 2017, Innovation Achievement Award of Industry-Academia-Research Collaboration of China in 2019, "Jinqiao" Award of Technology Market Association of China in 2020, Baosteel Education Award of China in 2021, Carl Friedrich von Siemens Research Award of the Alexander von Humboldt Foundation of Germany in 2023, and Technical Achievement Award of Applied Computational Electromagnetic Society (ACES) of USA in 2024. In 2018, he was selected as the Distinguished Lecturer (DL) of IEEE Antennas and Propagation Society for 2019-2022.

# Modeling and Analysis of a Proposed AC-DC C-Core Heteropolar Radial Hybrid Magnetic Bearing

**N. Boutra[1], R. Mehasni[1], and M. Feliachi[2]**

[1]Laboratoire d'électrotechnique de Constantine (LEC)
Université des frères Mentouri Constantine 1, Route Ain Elbey, 25000 Constantine, Algérie
boutra.nacir@gmail.com, Algérieboutra.nacir@gmail.com, mehasni@yahoo.fr

[2]Laboratoire IREENA (UR 4642)
Nantes Université, CRTT, 37 boulevard de l'Université, CS 90406, 44600 Saint-Nazaire, France
mouloud.feliachi@univ-nantes.fr, Francemouloud.feliachi@univ-nantes.fr

***Abstract* –** In this study, a new C-Core heteropolar radial hybrid magnetic bearing (HRHMB) driven by a three-phase power inverter is proposed. The use of a three-phase inverter driving technology improves the performance of magnetic bearings in terms of cost and power consumption. The force-current and the force-displacement characteristics of the proposed HRHMB are linear and the magnetic field coupling between the X and Y directions is significantly reduced. To analyze the proposed HRHMB, the configuration, working principle and required mathematical model based on the equivalent magnetic circuit (EMC) method are firstly presented. Then the load capacity and important parameters design are deduced. A comparison between the results obtained by the used analytical approach and those given by the finite element method (FEM) allowed verification of the developed mathematical model's accuracy. Compared with the twelve-pole HRHMB, the proposed HRHMB improves bearing capacity, reduces mass, and enhances cost efficiency and performance, making it highly suitable for large journal diameter applications.

***Index Terms* –** Heteropolar, hybrid magnetic bearing, magnetic circuit decoupling, second air gap, three-phase inverter driving.

## I. INTRODUCTION

Many application areas make use of magnetic bearings (MBs). By using applied electromagnetic forces, they can keep rotors in levitation. Compared to mechanical bearings, they allow for the removal of frictional losses, extending the system's lifespan [1, 2]. In addition to their capacity to avoid environment pollution, they can also reduce vibrations and limit maintenance. The cited advantages have allowed MB technology to be increasingly exploited in high-speed rotating equipment [3–6]. The hybrid magnetic bearing (HMB) combines the advantages of low loss of passive MB and the control ability of active MB [7–9]. HMBs are characterized by the presence of copper coils and permanent magnets (PMs). PMs create the biased field which is modulated by the electromagnetic field generated by coils to produce a controllable magnetic force between the rotor and each ferromagnetic pole. Homopolar and heteropolar are the two kinds of radial hybrid magnetic bearing (RHMB) that are largely used and studied [10–12]. The homopolar type has the advantage of low power consumption. In this one, the PM is inserted between two stators to create the bias flux in the axial direction. The double stator design is inherently more complex than the single stator design. In contrast, the heteropolar radial hybrid magnetic bearing (HRHMB) with a single stator has a lower axial length, compact structure, and simple mechanical construction. In [13–15], three novel decoupling HRHMB structures with second air gap are presented. The control flux generated by the coils is separated from the PM, which considerably reduces the power loss. A novel structure of HRHMB has been proposed with small volume compared to the classical structure where an analytical model is developed to investigate its performance [16]. In [17], a comparison of main performance indexes such as rotor core loss, displacement stiffness and current stiffness between a novel proposed HRHMB and conventional one under the same constraints is made.

Compared with RHMBs driven by four or two power amplifiers, the three-pole and six-pole RHMBs are designed to improve space utilization and reduce volume. Researchers agree that it is very attractive to design a MB driven by a three-phase inverter because of the low cost and low power consumption [18, 19]. Three-phase inverter drive technology is used in three-pole [20, 21], six-pole [18, 22] and twelve-pole MBs [23] if the sum of the current equals zero. The disadvantages of three-pole and six-pole RHMBs are the strong nonlinearity between

*Submitted On: March 20, 2023*
*Accepted On: November 18, 2024*

https://doi.org/10.13052/2024.ACES.J.390907

the magnetic force and the control current and the magnetic coupling between the two directions X and Y that makes control of the rotor position more complex.

To meet practical engineering demands, efficient MBs are crucial for the reliable and secure functioning of rotor systems. In this paper, a new HRHMB, specifically suitable for large journal diameter applications, is introduced. By optimizing the structure, we aim to significantly reduce the mass of the MB, resulting in decreased material usage and reduced production costs.

This paper proposes a new HRHMB structure driven by a three-phase inverter with a second air gap. This structure combines the benefits of decoupling HRHMBs with those of RHMBs driven by a three-phase inverter, and overcomes the shortcomings caused by the non-symmetrical traditional three-pole and six-pole structures. The new structure offers the dual advantages of a lower power amplifier requirement and weak magnetic field coupling between the X and Y directions. The linearity of the force-current and force-displacement characteristic facilitates the implementation of a simple control mechanism.

Construction and operation of the proposed HRHMB are thoroughly examined. The configuration is modeled using the equivalent magnetic circuit (EMC) approach to determine force-current and force-displacement properties. Various design parameters are then determined based on the EMC. The analytical model's results are contrasted with those obtained via the finite element method (FEM). Compared to twelve-pole HRHMB, the suggested construction demonstrates a higher bearing capacity. Consequently, the proposed HRHMB not only meets the prerequisite of sufficient bearing capacity but also offers a cost-effective and technically sound solution for large journal diameter applications.

## II. STRUCTURE AND MATHEMATICAL MODEL

### A. Structure

In this work a new structure of a HRHMB is proposed. The structure shown in Fig. 1 contains a laminated stator and rotor to reduce its eddy current loss. Six C-Core magnetic poles are windings and are arranged symmetrically. The yokes between adjacent two C-Core poles are made of non-magnetic material. Six identical PMs radially magnetized in NSSNNSSNNSSN configuration are inserted in the six C-Core poles to produce bias fluxes. Three phase coils, where each one is composed of four windings, are connected in series and wrapped around four poles ($P_{11}$, $P_{12}$, $P_{21}$, and $P_{22}$ belong to $P$-phase, $P = A, B, C$). The coils are driven by a three-phase inverter to produce control fluxes. This driving mode reduces the cost construction and switching loss compared with power amplifiers driving mode. With the introduction of the second air gap, the control flux is directed away from the PM. If the three coils are not energized and the rotor is perfectly in the equilibrium position, the resultant magnetic force generated by PMs and acting on the rotor is zero, due to the symmetrical structure. When energizing the coils, the produced magnetic field will be superposed with bias flux. These two fields are additive in the two ferromagnetic poles and subtractive in the two opposite poles which creates a magnetic force acting on the rotor in the direction between the two opposite ferromagnetic poles. If the magnetic fluxes generated by $A$-phase are taken as an example, the two fields are additive in $A_{12}$ and $A_{21}$ and are subtractive in $A_{21}$ and $A_{22}$. Thus, the magnetic force is the result of the force in ($A_{11}A_{22}$) direction and the force in ($A_{12}A_{21}$) direction.

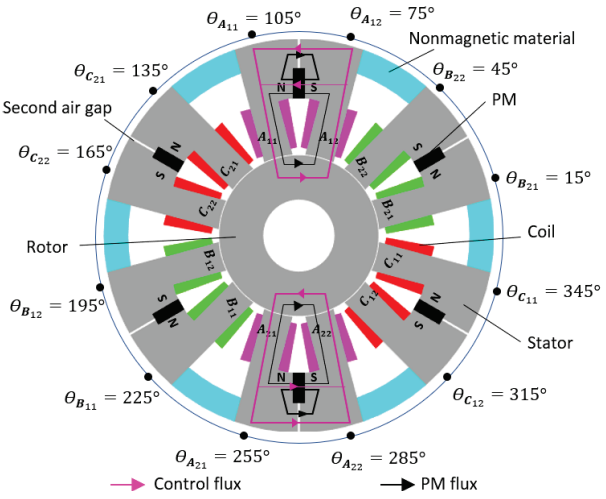


Fig. 1. Structure of proposed heteropolar radial hybrid magnetic bearing.

### B. Mathematical model

The path of the PM magnetic circuit and the electric magnetic circuit of the $A_{11} - A_{22}$ C-Core formed by two poles ($A_{11}$ $A_{22}$) is shown in Fig. 2. Here we neglect factors such as reluctance of the iron core, the eddy current loss and magnetic flux leakage.

For the six C-Core poles, $\Phi_{pA_1}$, $\Phi_{pA_2}$, $\Phi_{pB_1}$, $\Phi_{pB_2}$, $\Phi_{pC_1}$ and $\Phi_{pC_2}$ are the magnetic fluxes in air gaps generated by the PM, $\Phi_{eA_1}$, $\Phi_{eA_2}$, $\Phi_{eB_1}$, $\Phi_{eB_2}$, $\Phi_{eC_1}$ and $\Phi_{eC_2}$ are the magnetic fluxes in air gaps generated by control currents, $N$ is the number of turns in single coil, $i_A$, $i_B$ and $i_C$ are the currents in the three-phase coils, $F_p$ is the magnetomotive force of the PM, $R_p$ is the reluctance of the PM and $R_s$ is the reluctance of the second air gap. The air gap reluctances $R_l$ ($l \in L = [A_{11}, A_{12}, A_{21}, A_{22}, B_{11}, B_{12}, B_{21}, B_{22}, C_{11}, C_{12}, C_{21}, C_{22}]$ ) can be

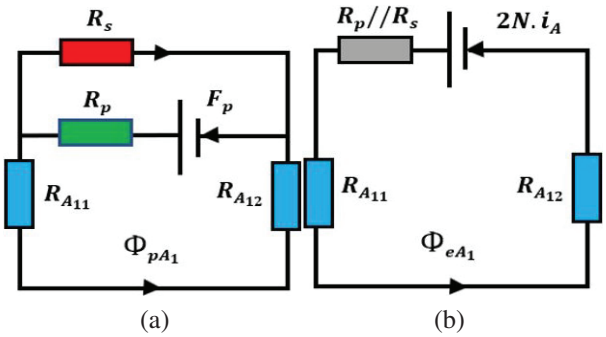


Fig. 2. Equivalent magnetic circuits of the $A_{11}-A_{22}$ C-Core pole (a) PM bias flux circuit and (b) control flux circuit.

expressed as:

$$R_l = \frac{g_0 - \cos(\theta_l)\, x - \sin(\theta_l)\, y}{\mu_0 A_\mathrm{p}}, \tag{1}$$

where $g_0$ is the air gap length, $\mu_0$ is the permeability of a vacuum, $A_\mathrm{p}$ is the section area of the pole, and $x$ and $y$ are the eventual rotor displacements in X and Y directions, respectively. $\Phi_l$ is the polar angle of the $l$-pole axis.

Based on the EMC method, the PM fluxes can be calculated as:

$$\Phi_{pl_k} = \frac{F_p R_s}{\left(\left(R_{l_{k1}}+R_{l_{k2}}\right)\left(R_p+R_\mathrm{s}\right)+R_p R_\mathrm{s}\right).c_\mathrm{p}}, \tag{2}$$

where $c_\mathrm{p}$ is the correction factor of the PM magnetic circuit, $l = A,B,C$ and $k = 1,2$.

The electromagnetic fluxes can be expressed as:

$$\Phi_{el_k} = \frac{2N(R_p+R_s)}{\left(\left(R_{l_{k1}}+R_{l_{k2}}\right)\left(R_p+R_\mathrm{s}\right)+R_p R_\mathrm{s}\right).c_\mathrm{e}} i_l, \tag{3}$$

where $c_\mathrm{e}$ is the correction factor of electromagnetic magnetic circuit, $l = A,B,C$ and $k = 1,2$.

Taking $K_{l_k} = \frac{2N(R_p+R_s)}{\left(\left(R_{l_{k1}}+R_{l_{k2}}\right)\left(R_p+R_\mathrm{s}\right)+R_p R_\mathrm{s}\right).c_\mathrm{e}}$, equation (3) can be rewritten as:

$$\Phi_{el_k} = K_{l_k} i_l. \tag{4}$$

The virtual work method is applied to acquire the magnetic forces for the twelve poles. The forces generated in the air gap poles can be calculated as:

$$\begin{cases} F_{A_{11}} = F_{A_{12}} = \frac{\left(\Phi_{pA_1}+K_{A_1} i_A\right)^2}{2\mu_0 A_\mathrm{p}} \\ F_{A_{21}} = F_{A_{22}} = \frac{\left(\Phi_{pA_2}-K_{A_2} i_A\right)^2}{2\mu_0 A_\mathrm{p}} \\ F_{B_{11}} = F_{B_{12}} = \frac{\left(\Phi_{pB_1}+K_{B_1} i_B\right)^2}{2\mu_0 A_\mathrm{p}} \\ F_{B_{21}} = F_{B_{22}} = \frac{\left(\Phi_{pB_2}-K_{B_2} i_B\right)^2}{2\mu_0 A_\mathrm{p}} \\ F_{C_{11}} = F_{C_{12}} = \frac{\left(\Phi_{pC_1}+K_{C_1} i_C\right)^2}{2\mu_0 A_\mathrm{p}} \\ F_{C_{21}} = F_{C_{22}} = \frac{\left(\Phi_{pC_2}-K_{C_2} i_C\right)^2}{2\mu_0 A_\mathrm{p}} \end{cases}. \tag{5}$$

Projecting the forces in equation (5) into the $x$-axis and $y$-axis, respectively, each phase generates two directional forces. The six magnetic suspension forces can be expressed as:

$$\begin{cases} F_{X_A} = 0 \\ F_{X_B} = (\cos 45^\circ + \cos 15^\circ)(F_{B_{21}} - F_{B_{11}}) \\ F_{X_C} = (\cos 45^\circ + \cos 15^\circ)(F_{C_{12}} - F_{C_{21}}) \\ F_{Y_A} = 2\cos 15^\circ\ (F_{A_{11}} - F_{A_{21}}). \\ F_{Y_B} = (\cos 45^\circ + \cos 75^\circ)\ (F_{B_{21}} - F_{B_{11}}) \\ F_{Y_C} = (\cos 45^\circ + \cos 75^\circ)\ (F_{C_{21}} - F_{C_{11}}) \end{cases}. \tag{6}$$

The magnetic forces in the X and Y directions are expressed as:

$$\begin{cases} F_x = F_{X_B} + F_{X_C} \\ F_y = F_{Y_A} + F_{Y_B} + F_{Y_C} \end{cases}. \tag{7}$$

The three-phase current $i_A$, $i_B$ and $i_C$ can be transformed to two-phase control currents $i_x$ and $i_y$ by the Clark transformation:

$$\begin{cases} i_y = \sqrt{\frac{2}{3}}\left(i_\mathrm{A} - \frac{1}{2} i_\mathrm{B} - \frac{1}{2} i_\mathrm{C}\right) \\ i_x = \sqrt{\frac{2}{3}}\left(\frac{\sqrt{3}}{2} i_\mathrm{C} - \frac{\sqrt{3}}{2} i_\mathrm{B}\right) \end{cases}. \tag{8}$$

To estimate the force-displacement stiffness $k_x$ and $k_y$ and force-current stiffness $k_{i_x}$ and $k_{i_y}$ in the X and Y directions, respectively, radial suspension forces near the equilibrium position are linearized using the first-order Taylor expansion as:

$$\begin{cases} F_x = k_{i_x} i_x + k_x \mathrm{y} \\ F_y = k_{i_y} i_y + k_y \mathrm{y} \end{cases}. \tag{9}$$

The stiffness coefficients $k_x$, $k_y$, $k_{i_x}$, and $k_{i_y}$ are given by:

$$\begin{cases} k_{i_x} = k_{i_y} = \frac{\left(3+\sqrt{3}\right)\Phi_0 K_0}{\mu_0 A_p} \\ k_x = k_y = \frac{\left(\sqrt{6}+\sqrt{2}\right)^2 \mu_0 A_\mathrm{p}}{4} {\Phi_0}^2 \left[\frac{l_p + l_s}{l_p l_s + 2g_0\left(l_p + l_s\right)}\right] \end{cases}. \tag{10}$$

$\Phi_0$ and $K_0$ are given by:

$$\begin{cases} \Phi_0 = \Phi_{pl_k}(x=0, y=0) \\ K_0 = K_{l_k}(x=0, y=0) \end{cases}. \tag{11}$$

## III. RADIAL LOAD CAPACITY ANALYSIS

When the rotor is in the central position, the flux densities in the air gap poles are equal to the bias flux density $B_0$, which is equal to half of the saturation flux density $B_s$.

The suspension force $F_y$ is maximum when the current $i_y = i_{y\max}$. According to (8) and as the sum of the three-phase current is zero, it can be taken that $i_{y\max} = \frac{\sqrt{3} i_{\mathrm{Amax}}}{\sqrt{2}} = -0.5\frac{\sqrt{3} i_{\mathrm{Bmax}}}{\sqrt{2}} = -0.5\frac{\sqrt{3} i_{\mathrm{Cmax}}}{\sqrt{2}}$. In this condition, we have $\Phi_0 = K_0\, i_{Amax} = 0.5 B_s A_\mathrm{p}$, which gives:

$$F_{ymax} = \sqrt{\frac{3}{2}}\frac{\left(3+\sqrt{3}\right)\Phi_0{}^2}{\mu_0 A_p} = \frac{3\left(\sqrt{6}+\sqrt{2}\right) A_\mathrm{p} {B_s}^2}{8\mu_0}. \tag{12}$$

The suspension force $F_x$ is only determined by the flux densities in the air gaps $B_{11}$, $B_{12}$, $B_{21}$, $B_{21}$, $C_{11}$, $C_{12}$, $C_{21}$, and $C_{21}$. $F_x$ is maximum when the current $I_x = I_{x\max}$, flux density $B_{B_1} = B_s$ and flux density $B_{A_2} = 0$. If we make $i_y = 0$, it can be taken that

$i_{xmax} = -i_{Bmax}/\sqrt{2} = i_{Cmax}/\sqrt{2}$, according to equation (8). In this condition, we have $\Phi_0 = K_0 I_{Bmax}$, which gives:

$$F_{xmax} = \sqrt{2}\frac{(3+\sqrt{3})\,\Phi_0{}^2}{\mu_0 A_p} = \frac{\left(\sqrt{6}+3\sqrt{2}\right)A_p B_s{}^2}{4\mu_0}. \tag{13}$$

The maximum suspension forces in each direction of the proposed structure are compared to those given by six-pole and twelve-pole structures (see Table 1).

Table 1: Maximum suspension force in each direction

| Load Capacity | Twelve-Pole Structure | Proposed Structure |
|---|---|---|
| X direction | $0.75\ \frac{A_p B_s{}^2}{\mu_0}$ | $1.673\ \frac{A_p B_s{}^2}{\mu_0}$ |
| Y positive direction | $0.867\ \frac{A_p B_s{}^2}{\mu_0}$ | $1.449\ \frac{A_p B_s{}^2}{\mu_0}$ |
| Y negative direction | $0.867\ \frac{A_p B_s{}^2}{\mu_0}$ | $1.449\ \frac{A_p B_s{}^2}{\mu_0}$ |

Compared to the twelve-pole HRHMBs [23], the maximum load capacity $F_{max}$ of the proposed C-Core HRHMB is increased by 1.93 times. Taking $F_{ymax} =$ 600 N, the dependence of the load capacity on the orientation angle is shown in Fig. 3. The radius of the polar plot indicates load capacity at an orientation angle. It can be seen from Fig. 3 that the minimum value of the maximums of the suspension forces is obtained at the orientation angles located in the six centers of the six C-Core poles. The maximum load capacity of the proposed bearing is the maximum force in the Y direction ($F_{max} = F_{ymax}$).

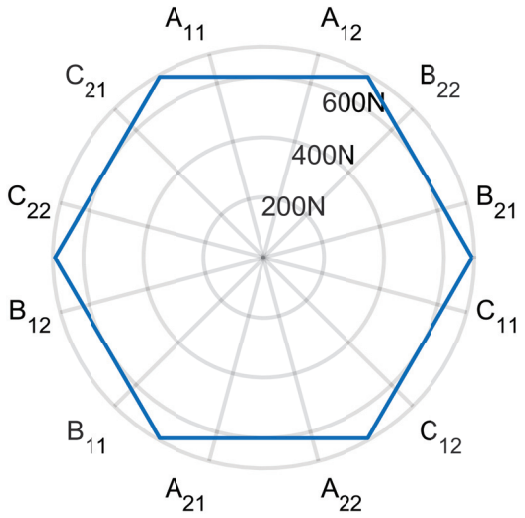


Fig. 3. Load capacity of the proposed hybrid magnetic bearing as a function of orientation angle.

The load capacity of the HRHMB is primarily determined by the required pole section area. Using FEM, we compared the two types of magnetic bearings with the same pole section area (rotor diameter and pole width) and bias flux. In this comparison, the pole width varies between 10 mm and 40 mm, the pole section covers 50% of the journal, and the aspect ratio (axial length/outer diameter of the rotor) is 0.5. Figure 4 shows total mass versus load capacity. We can conclude from this figure that the new HRHMB has a lower mass compared to the twelve-pole. When the load capacity of the twelve-pole structure reaches its maximum value of 3661 N with a pole width of 40 mm, the total mass of the novel HRHMB decreases by 38% for the same load capacity. Therefore, as the journal diameter increases linearly with the increase in pole width, the proposed HRHMB is suitable for applications involving large journal diameters.

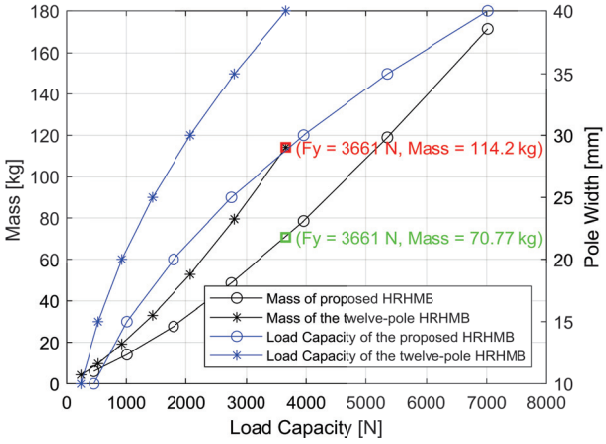


Fig. 4. Total mass versus load capacity.

## IV. PARAMETER DESIGN

### A. Magnetic pole area

According to equation (12), the area of the magnetic pole can be expressed as:

$$A_p = W_p l = \frac{\mu_0 F_{ymax}}{1.449\ B_s{}^2}, \tag{14}$$

where $W_p$ is the width of the pole and $l$ is the axial length. $W_p$ is taken to be equal to half of one-twelfth of the inner stator perimeter length and defined as:

$$W_p = 0.5\frac{\pi D_{is}}{12}, \tag{15}$$

where $D_{is}$ is the inner diameter of the stator.

### B. Second air gap

To obtain the optimal value of $R_s$ that maximises the Y direction force $F_y$, the force-current stiffness $k_{i_y}$ in equation (9) can be treated as the objective function with variable $R_s$. We solved the equation thus:

$$\frac{\partial k_{i_y}}{\partial R_s} = \frac{(3+\sqrt{3})}{\mu_0 S_p}\frac{\partial\,(\Phi_0 K_0)}{\partial R_s} = 0. \tag{16}$$

The optimal value of the reluctance of the second air gap can be given by:

$$R_s = \frac{2R_pR_g}{R_p - 2R_g} . \quad (17)$$

### C. PM dimensions

The bias flux density $B_0$ is chosen to be equal to half of the saturation flux density $B_s$ to maximize the load capacity. For the rotor equilibrium position, the flux densities in the air gaps are equal to the bias flux density. According to equations (2) and (17), the width of the PM can be calculated as:

$$l_p = \frac{B_s c_p}{\mu_r \mu_0 H_c} , \quad (18)$$

where $\mu_r$ is the relative permeability of the PM and $H_c = F_p/l_p$ is the coercivity of the PM. The design parameters of the proposed HRHMB are shown in Table 2.

Table 2: Parameters of the proposed HRHMB

| Parameter | Symbol | Value |
|---|---|---|
| Radial air gap length | $g_0$ | 0.4 mm |
| Second air gap length | $g_s$ | 1 mm |
| Saturation induction density | $B_s$ | 1 T |
| Magnetic pole width | $W_p$ | 10.4 mm |
| Outer diameter of stator | $D_{os}$ | 183 mm |
| Inter diameter of stator | $D_{is}$ | 80 mm |
| Axial length | $l$ | 50 mm |
| PM height | $h_p$ | 10.7 mm |
| PM width | $l_p$ | 6 mm |
| Number of turns | $N$ | 232 |
| Load capacity | $F_{max}$ | 600 N |

## V. VERIFICATION OF THE PERFORMANCE OF THE PROPOSED HRHMB

To verify the performance of the proposed RHMB in comparison to the existing structures, a numerical simulation based on application of the 2D FEM has been achieved. The distribution of the magnetic field that permits the computation of different characteristics on which our analysis is based is presented in Fig. 5.

Figure 5 (a) shows the distribution of magnetic field provided only by PM without rotor eccentricity. We can see that the flux density is symmetrically distributed. When energizing the coils in the Y direction ($i_x = 0$, $i_y = i_{ymax}$), the symmetry of the distribution of the magnetic field will be lost (see Fig. 5 (b)). The magnetic field in the Y positive direction is enhanced whereas the magnetic field in the Y negative direction is reduced.

Figure 6 (a) shows the effect of displacement of the rotor on air gap flux density when the coils are not energized. Without rotor displacement (no eccentricity), we

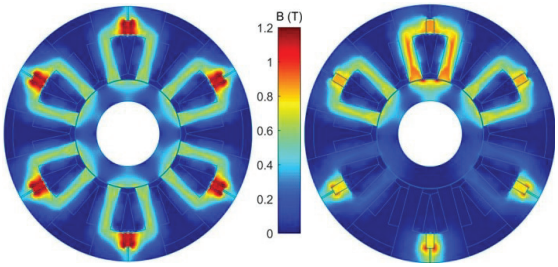


(a) (b)

Fig. 5. Distribution of flux densities (a) PM bias flux density and (b) superposition of PM bias flux and control flux ($i_x = 0, i_y = i_{ymax}$).

have obtained identical air gap flux density at the poles and symmetrical distribution in view of the two axes. The bias flux in each air gap is 0.5 T, which verifies the design requirements. However, when the rotor displaces in the Y positive direction, it can be seen that the air gap flux densities under poles $A_{11}$, $A_{12}$, $B_{21}$, $B_{22}$, $C_{21}$ and $C_{22}$ increases while the air gap flux densities under poles $A_{21}$, $A_{22}$, $B_{11}$, $B_{12}$, $C_{11}$ and $C_{12}$ decreases. However, the flux density waveform is not uniformly distributed because of the non-uniformity of the air gap.

Figure 6 (b) shows the effect of coil current on the air gap density when the rotor is at the equilibrium position. It can be shown that with increasing coil current $i_y$, the flux density of each part in Y positive direction is increased while the flux density of each part in Y negative direction is decreased. It can be seen for example that the bias and control fluxes are additive in poles $A_{11}, A_{12}$, $B_{21}, B_{22}$, $C_{21}$ and $C_{22}$ and subtractive in the opposite poles $A_{21}, A_{22}, B_{11}, B_{12}, C_{11}$ and $C_{12}$.

To verify the accuracy of the achieved modeling of the proposed HRHMB, the analytically and numerically

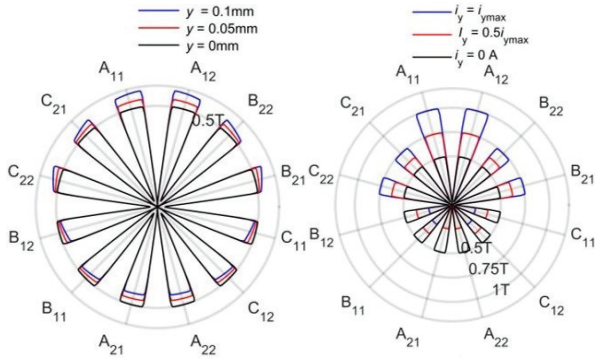


(a) (b)

Fig. 6. Polar flux density waveform in the air gap (a) $y$-displacement of rotor without coils energizing and (b) variation of $i_y$ without rotor eccentricity.

obtained results concerning the force-current and force-displacement characteristics are compared and presented in Fig. 6. Figure 7 shows that magnetic force is almost linearly proportional to control current and displacement. Comparison of analytical and numerical values of current and displacement stiffness is listed in Table 3.

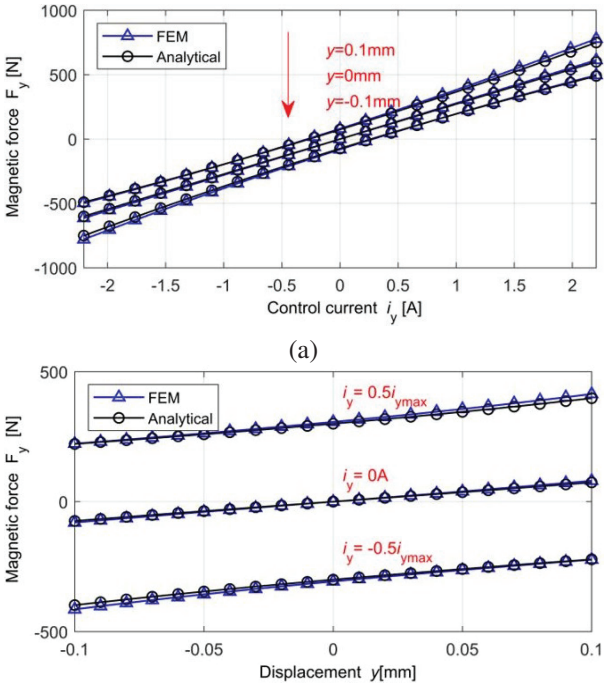


Fig. 7. $F_y$ components as a function of control current and rotor displacement (a) force-current relationship and (b) force-displacement relationship.

Table 3: Comparison of analytical and numerical stiffness of the proposed HRHMB

| Stiffness | Analytical | Numerical | Error |
|---|---|---|---|
| $k_{i_y}$ (N/A) | 272.17 | 278.38 | 2.23% |
| $k_y$ (N/mm) | 735.03 | 796.10 | 7.67% |

The maximum error between the analytical and numerical results is 7.67% for the displacement stiffness. This error is mainly related to the local saturation of the iron core that is not considered in the analytical computation. Based on all of the aforementioned findings, it can be concluded that the developed analytical model can be properly used for the design of the proposed HRHMB.

Variations of the magnetic force components as a function of the two control currents $i_x$ and $i_y$ are presented in Fig. 8. These results have been obtained for a current $i_x$ changing from $-2.54$ A to 2.54 A and a current $i_y$ changing from $-2.2$ A to 2.2 A. It can be observed

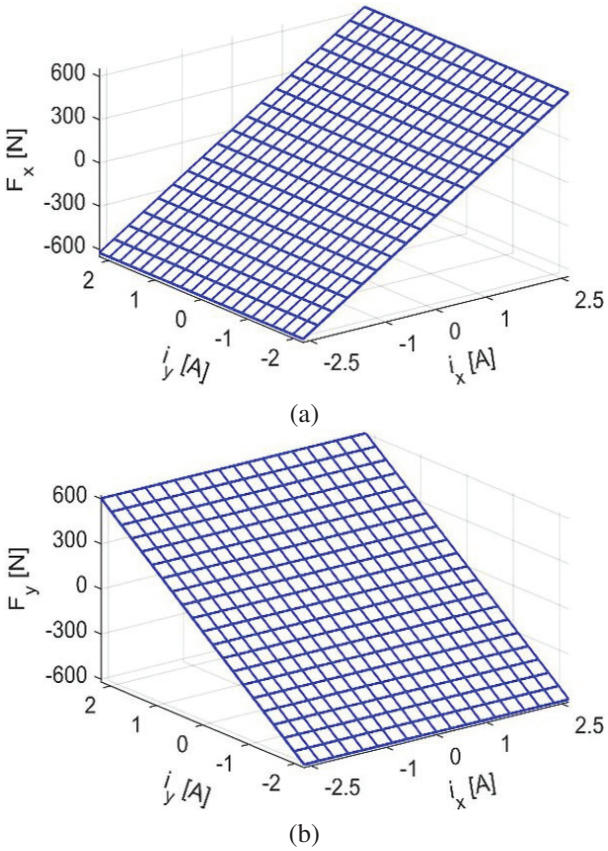


Fig. 8. Force-current dependence (a) variation of the $F_x$ component and (b) variation of the $F_y$ components.

that the magnetic force $F_x$ is almost proportional to the coil current $i_x$ and independent of $i_y$. Also, the magnetic force $F_y$ is almost proportional to the coil current $i_y$ and independent of $i_x$.

To identify the nature of dependency between force and rotor eccentricity, we have estimated the effect of rotor displacement on the force components $F_x$ and $F_y$. The obtained results are presented in Fig. 9.

The results shown in Fig. 9 have been obtained by considering eccentricities in X and Y directions varying from $-0.1$ mm to 0.1 mm. It can be seen that a linear dependency exists between the force components and the displacement. Moreover, the magnetic force $F_x$ does not depend on $y$ displacement and the magnetic force $F_y$ does not depend on $x$ displacement.

To examine variations of the magnetic force $F_y$ due to X direction displacements and X direction control currents, we compute the coupling ratios defined as:

$$\begin{cases} \alpha(x,y) = \frac{F_y(x,y) - F_y(0,y)}{F_y(0,y)} \times 100\% \\ \beta(i_x,i_y) = \frac{F_y(i_x,i_y) - F_y(0,i_y)}{F_y(0,i_y)} \times 100\% \end{cases}. \quad (19)$$

Figure 10 (a) illustrates variation of the coupling ratios $\alpha(x,y)$ with the different rotor displacements in

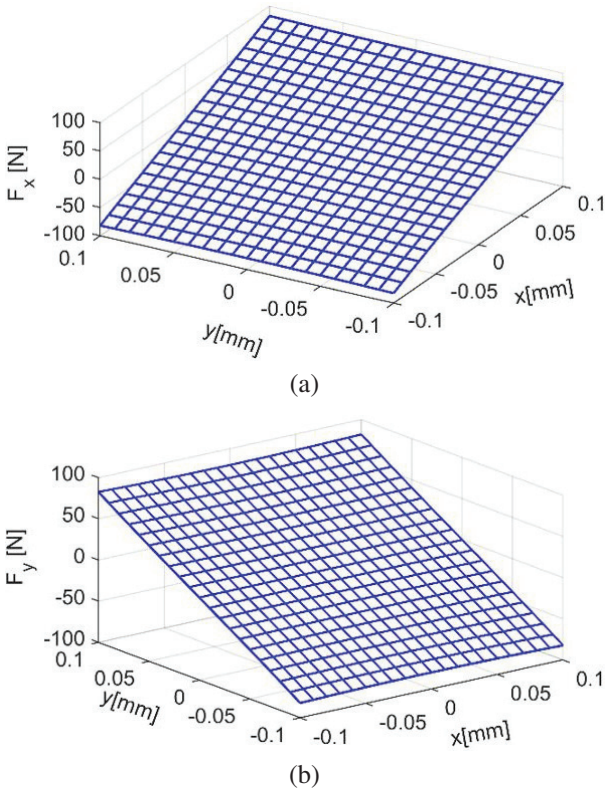


Fig. 9. Force-displacement relationship (a) $F_x$ variations and (b) $F_y$ variations.

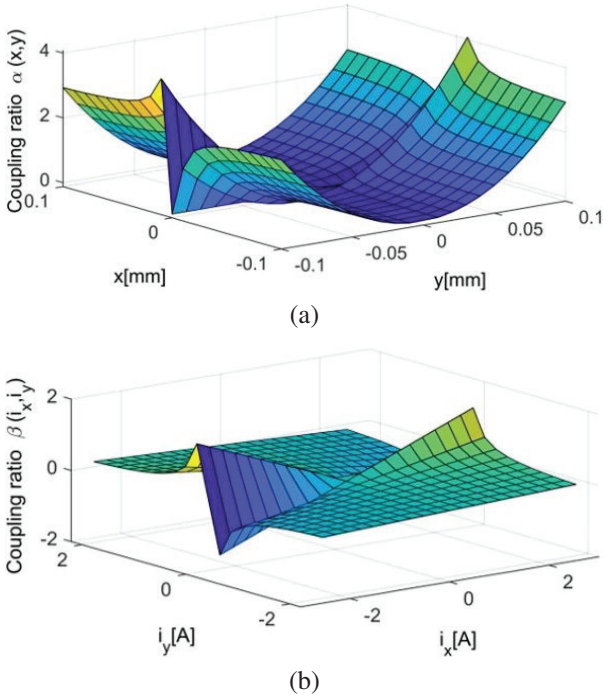


Fig. 10. Magnetic force coupling (a) caused by rotor displacement and (b) caused by control current.

the X and Y directions when all coils are not energized. As shown, rotor displacements in the X direction have minimal impact on the magnetic force in the Y direction, with the maximum coupling effect less than 4.08%.

Figure 10 (b) shows the variation of the coupling ratios $\beta\,(i_x, i_y)$ when the rotor is at the equilibrium position. Results indicate that the maximum coupling effect occurs when the control current $i_x$ is substantial while the control current $i_y$ is zero, with the maximum coupling effect less than 1.47%. These two coupling ratios indicate that the magnetic forces in the X and Y directions of the designed magnetic bearing are nearly independent of each other.

## VI. CONCLUSION

In this paper, a new structure for HRHMB driven by a three-phase inverter is presented. The EMC method is used to analyze the linearity and the coupling characteristics of the proposed magnetic bearing. FEM analysis has permitted verification of the performance of the HRHMB validation of such an analysis. Compared to the existing HRHMB, the proposed HRHMB retains the advantages of the existing bearing and overcomes their drawbacks. The proposed HRHMB offers the advantage that there is very weak magnetic coupling between the X and Y directions. Moreover, the linear proportionality between the magnetic force and the control current facilitates the control. The proposed HRHMB demonstrates a higher load capacity compared to the twelve-pole given the same biased flux and journal diameter. Additionally, it offers an effective and reliable solution for applications with larger journal diameters.

## REFERENCES

[1] G. Schweitzer and E. Maslen, *Magnetic Bearings: Theory, Design, and Application to Rotating Machinery*. Berlin, Germany: Springer-Verlag, 2009.

[2] T. Fan, J. Yu, Z. Sun, X. Liu, X. Zhang, J. Zhao, X. Yan, H. Zuo, and Z. Shi, "Theory and simulation of linearized force coefficients for active magnetic bearings with multiple magnetic poles," *Applied Computational Electromagnetics Society Journal (ACES),* vol. 34, no. 04, pp. 598-604, 2019.

[3] K. Asami, A. Chiba, M. A. Rahman, T. Hoshino, and A. Nakajima, "Stiffness analysis of a magnetically suspended bearingless motor with permanent magnet passive positioning," *IEEE Transactions on Magnetics*, vol. 41, no. 10, pp. 3820-3822, Oct. 2005.

[4] G. G. Sotelo, R. de Andrade, and A. C. Ferreira, "Magnetic bearing sets for a flywheel system," *IEEE Transactions on Applied Superconductivity*, vol. 17, no. 2, pp. 2150-2153, 2007.

[5] J. Denk, D. Stoiber, H. Köpken, and H. Walter, "Industrialization of AMB system with standard drive technology," *IEEE Transactions on Magnetics*, vol. 45, no. 12, pp. 5319-5325, Dec. 2009.
[6] F. Jiancheng, S. Jinji, X. Yanliang, and W. Xi, "A new structure for permanent-magnet-biased axial hybrid magnetic bearings," *IEEE Transactions on Magnetics*, vol. 45, no. 12, pp. 5319-5325, Dec. 2009.
[7] A. V. Filatov and E. H. Maslen, "Passive magnetic bearing for flywheel energy storage systems," *IEEE Transactions on Magnetics*, vol. 37, no. 6, pp. 3913-3924, Nov. 2001.
[8] M. A. Pichot, J. P. Kajs, B. R. Murphy, A. Ouroua, B. M. Rech, and R. J. Hayes, "Active magnetic bearings for energy storage systems for combat vehicles," *IEEE Transactions on Magnetics*, vol. 37, no. 1, pp. 318-323, Nov. 2001.
[9] E. Y. Hou and K. Liu, "A novel structure for low-loss radial hybrid magnetic bearing," *IEEE Transactions on Magnetics,* vol. 47, no. 1, pp. 4725-4733, Jan. 2011.
[10] F. Jiancheng, W. Xi, W. Tong, T. Enqiong, and F. Yahong, "Homopolar 2-pole radial permanent-magnet biased magnetic bearing with low rotating loss," *IEEE Transactions on Magnetics*, vol. 48, no. 8, pp. 2293-2303, Aug. 2012.
[11] K. Kang and A. Palazzolo, "Homopolar magnetic bearing saturation effects on rotating machinery vibration," *IEEE Transactions on Magnetics,* vol. 48, no. 6, pp. 1984-1994, June 2012.
[12] S. Jinji and F. Jiancheng, "A novel structure of permanent-magnet-biased radial hybrid magnetic bearing," *Journal of Magnetism and Magnetic Materials*, vol. 323, no. 2, pp. 202-208, Jan. 2011.
[13] S. Xu and J. Sun, "Decoupling structure for heteropolar permanent magnet biased radial magnetic bearing with subsidiary air-gap," *IEEE Transactions on Magnetics*, vol. 50, no. 8, pp. 1-8, Aug. 2014.
[14] J. Fang and C. Wang, "Design and optimization of a radial hybrid magnetic bearing with separate poles for magnetically suspended inertially stabilized platform," *IEEE Transactions on Magnetics*, vol. 50, no. 5, pp. 1-11, May 2014.
[15] H. Wang, B. Xue, and S. Tang, "Modeling and analysis of E-Core permanent magnet biased radial magnetic bearing," *International Journal of Applied Electromagnetics and Mechanics*, vol. 49, no. 2, pp. 179-193, 2015.
[16] L. Wu, D. Wang, Z. Su, K. Wang, and X. Zhang, "Analytical model of radial permanent magnet biased magnetic bearing with assist poles," *IEEE Transactions on Applied Superconductivity*, vol. 26, no. 7, pp. 1-5, Oct. 2016.
[17] R. Zhu, W. Xu, C. Ye, and J. Zhu, "Novel heteropolar radial hybrid magnetic bearing with low rotor core loss," *IEEE Transactions on Magnetics*, vol. 53, no. 11, pp. 1-5, Nov. 2017.
[18] L. Ji, L. Xu, and C. Jin, "Research on a low power consumption six-pole heteropolar hybrid magnetic bearing," *IEEE Transactions on Magnetics*, vol. 49, no. 8, pp. 4918-4926, Aug. 2013.
[19] W. Zhang and H. Zhu, "Radial magnetic bearings: An overview," *Results in Physics*, vol. 7, pp. 3756-3766, 2017.
[20] H. Zhu, S. Ding, and J. Jv, "Modeling for three-pole radial hybrid magnetic bearing considering edge effect," *Energies*, vol. 9, no. 5, pp. 1-15, May 2016.
[21] J. Ju and H. Zhu, "Radial force-current characteristics analysis of three-pole radial-axial hybrid magnetic bearings and their structure improvement," *Energies*, vol. 9, no. 9, pp. 1-17, Sep. 2016.
[22] M. Wu, H. Zhu, H. Zhang, and W. Zhang, "Modeling and multilevel design optimization of an AC-DC three-degree-of-freedom hybrid magnetic bearing," *IEEE Transactions on Industrial Electronics*, vol. 70, no. 1, pp. 233-242, Jan. 2023.
[23] G. Liu, H. Zhu, M. Wu, and W. Zhang, "Principle and performance analysis for heterpolar permanent magnet biased radial hybrid magnetic bearing," *IEEE Transactions on Applied Superconductivity*, vol. 30, no. 4, pp. 1-4, June 2020.

**Nacir Boutra** was born in Ain M'lila, Algeria. He received the B.S. and M.S. degrees in Electrical Engineering from the University of Constantine, Algeria, in 2007 and 2010, respectively. He is currently working toward the Ph.D. degree at the Department of Electrical Engineering, in the same University, member of the LEC laboratory. His current research interests include magnetic bearing, numerical and analytical methods.

**Rabia Mehasni** was born in Grarem, Algeria, in 1970. He received the Ph.D. in Electrical Engineering from the University of Constantine, Algeria, in 2007. He has been with the Department of Electrical Engineering, University of Constantine, since 2000. He is currently Research Director at the LEC Laboratory. He has published in the field of magnetic separation. His

research interests are in the field of numerical methods and modeling techniques to approach multidisciplinary problems.

**Mouloud Feliachi** is native of Biskra (Algeria). He is an Engineer of the "Ecole Nationale Polytechnique", Algiers (1976), a Ph.D. of the "Conservatoire National des Arts et Métiers", Paris (1981), and "Docteur d'Etat Es-Sciences Physiques" of "Institut National Polytechnique", Grenoble (1986), all in Electrical Engineering. In 1987, he worked as an Engineer for the Leroy Somer company in Orléans. In 1988, he joined the University of Nantes (Institut Universitaire de Technologie - Saint-Nazaire) where he is Professor. He was Scientific Director of LRTI-Lab and Head of the Modeling and Simulation team in GE44-Lab. He is currently leading a Franch Algerian thematic network of research in Inductics, within IREENA Lab. His research interests are in hybrid analytical and numerical modeling of low frequency electromagnetic phenomena with emphasis on multiphysics and eddy current non-destructive testing and evaluation.

# Calculative Method on Electromechanical Strength for Rectangular and T-Shaped Rail over a Flat Surface Armature

**M. N. Saravana Kumar[1], R. Murugan[2], J. Lydia[3], and S. Leones Sherwin Vimalraj[4]**

[1]Department of Electronics and Communication Engineering
Kings Engineering College, Chennai, Tamil Nadu, India
dr.mnskphd@gmail.com

[2]Department of Electrical and Electronics Engineering
Bharath Institute of Higher Education and Research, Chennai, Tamil Nadu, India
ramumurugan_r@rediffmail.com

[3]Department of Electrical and Electronics Engineering
Easwari Engineering College, Chennai, Tamil Nadu, India
lydia.jeec@gmail.com

[4]Department of Electronics and Communication Engineering
Panimalar Engineering College, Chennai, Tamil Nadu, India
sherwin_leo@yahoo.com

***Abstract*** **–** The electromagnetic railgun launching (EMRL) system is a type of long-range projectile launch that does not require any chemical propellant and can accelerate masses ranging from milligrams to kilograms to velocities of more than several kilometers per second. To make the rail stronger, electromechanical strength analysis was performed by calculating the area's moment of inertia and critical velocity. One of the most essential mechanical aspects of rails is their moment of inertia, which has a direct impact on critical velocity and launch performance. Geometry and material both have an impact on the rails' electromechanical performance. This paper describes the increase in electromechanical performance achieved by constructing two types of rail cross-sections - rectangular rails and T-shaped rails - based on structural analysis and current distribution from coupled electromagnetic (EM) simulation. The investigation found that T-shaped rails have higher moments of inertia than rectangular rails for the same cross-sectional area and width. However, the mechanical performance differences between the two geometries are not significant. Therefore, the advantage of larger moments of inertia for a given cross-sectional area is limited. EM analysis has been extended to a 3-D finite element method (FEM) for both rails by linking it with Simplorer using the Maxwell-Simplorer coupled (MSC) method with a flat surface C-shaped armature. When compared to rectangular and T-shaped rails, the T-shaped rail has a lower current density at the inner curvature but a greater at the contact interface.

***Index Terms*** **–** Area's moment of inertia, armature velocity, critical velocity, dynamic analysis, electromagnetic railgun launching, electromechanical strength, Maxwell-Simplorer coupled.

## I. INTRODUCTION

That a significant dynamic response with a moving armature might happen during railgun launch is a challenging event, because the rails are exposed to a hostile load environment. The rail-armature interface experiences significant contact pressure variations, which can cause damage under certain situations. High current density in railguns can cause high temperatures, resulting in strength loss, melting and erosion. Thus, launch performance depends on the mechanical characteristics as well as the current distribution of the rails.

Geometry and material are key factors influencing electromechanical performance. Zhou et al. [1] have scrutinized railgun key parameters such as height, width and separation between the rails for different cross-sections of rails. They investigated the changes in thickness, width, spacing and other rail geometric parameters which affect inductance gradient (L'), current density (J) and magnetic flux density (B). They implemented finite element analysis for examining the key parameters for different rail cross-sections. They assumed the rail is brass, 1 MA current and 60 Hz frequency. They simulated the geometries under Eddy current A.C. analysis and determined the result for geometries cross-sections of rail. Keshtkar [2] examined the effect of key

*Submitted On: September 12, 2023*
*Accepted On: October 25, 2024*

https://doi.org/10.13052/2024.ACES.J.390908

parameters on varying the dimensional parameters of the railgun. Models of two-dimensional (2-D) finite element simulations were performed for the various w (width), h (height) and s (separation) values. L' values for different geometrical parameters were calculated, and a table presented. Keshtkar concluded that to increase L' the thickness and width of rails must be decreased whereas separation between rails ought to increase. Jin et al. [3] designed a cross-sectional geometry for calculating the area's moment of inertia, one of the important properties of the rails that affects the critical velocity as well as the launch. They concluded that a convex rail cross-section shows larger inertia moment and current density distribution is smaller at the bore-side rail surface but greater at the contact surface, especially at the trailing edge of the armature.

The three-dimensional structure illustrated in Fig. 1 represents the dimensional parameters by considered rail to be at finite length with an armature placed between the rails to complete the current path. When the current flowing in Rail_1 passes through the armature it is returned back through Rail_2 and completes the circuit. As a result, a magnetic field is established in the space between the rails. This field interacts with the current to produce Lorentz forces.

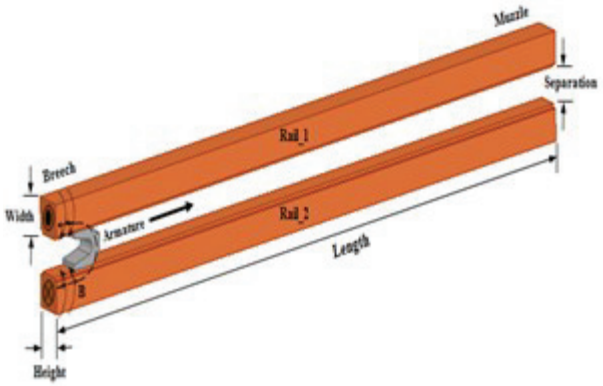


Fig. 1. Schematic three-dimensional geometric model of a railgun.

This paper investigates the moment of inertia for cross-sections of rectangular and T-shaped rails. Finite element method (FEM) simulations of rail dynamics are conducted for different rail types under identical conditions. The Maxwell-Simplorer coupled (MSC) technique is used for electromagnetic (EM) simulations to estimate current distributions.

## II. STRUCTURAL ANALYSIS OF EM RAILS

During the railgun launch action, the rail receives a huge peak value and a brief duration of current pulses. The skin effect causes the pulse current to scatter in a very thin layer near the surface of each conductor. This complicates the EM study of the railgun. This study uses the finite element method to calculate the railgun inductance gradient.

Because real equipment is rather sophisticated, the simulation model in this research is simplified using the following assumptions. The two rails are spatially symmetrical, with identical constructions and materials. In comparison to the rail's height and width, the rail's length is adequate to construct a 2-D equivalent model. A 2-D model can be further simplified by considering the field distribution's perfect symmetry [4].

The differential form of Maxwell's equation is:

$$\nabla H = J + \frac{\partial D}{\partial t}, \tag{1}$$

$$B = \nabla A, \tag{2}$$

$$\nabla E = -\frac{\partial B}{\partial t}. \tag{3}$$

Therefore:

$$E = -\nabla\phi - \frac{\partial A}{\partial t}, \tag{4}$$

and Eddy current density:

$$J_e = -\sigma\left(\nabla\phi + \frac{\partial A}{\partial t}\right). \tag{5}$$

The rail is supplied with a short period of high magnitude 300 kA pulsed current, resulting in a non-uniform current distribution and a hotspot at the rails' inner corners. The rail will undergo many alterations during armature motion as a result of contact pressure and contact damage. This causes a rise in temperature, loss of mechanical strength, melting and erosion [3, 5]. The mechanical strength of the rail cross-section is explored by finding the area moment of inertia and critical velocity which determines the most efficient rail cross-section that might be used for EM launch.

Area cross-section is considered to be 1500 mm$^2$, and Fig. 2 depicts the dimensional parameters. For a rectangular rail the cross-sections are H=40 mm, W=37.5 mm. For a T-shaped rail the cross-sections are H=40 mm, W=38.5 mm, m=4 mm and d=30 mm [6, 7]. A comparison was done between the essential characteristics of the rectangular and the T-shaped rail cross-sections, which minimized the current hotspot appropriate for launch.

The cross-sectional area for the rectangular rail:

$$A_{\text{Rect}} = WH. \tag{6}$$

The cross-sectional area for the T-shaped rail:

$$A_{T\_Shaped} = W - mH + md. \tag{7}$$

Table 1 shows the design essential parameters such as inductance gradient (L'), current density (J), magnetic flux density (B) and Lorentz force (F) for the two rails. According to researchers [8, 9], both the rectangular and T-shaped rail cross-sections have an acceptable induc-

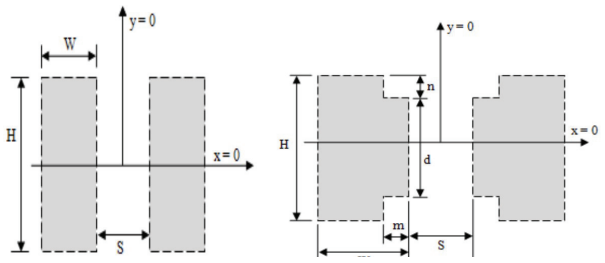


Fig. 2. Cross-sectional geometry of rectangular and T-shaped rails.

Table 1: Comparison of L', J, B and F over the rectangular and T-shaped rail cross-sections

| Rail Cross-Section | L' ($\mu$H/m) | J$\times 10^{10}$ (A/m$^2$) | B [T] | F (kN) |
|---|---|---|---|---|
| Rectangular | 0.46305 | 0.54381 | 4.6284 | 132.801 |
| T-shaped | 0.48481 | 0.34753 | 5.8247 | 129.387 |

tance gradient value. As a result, the current density concentration is limited across both rails.

The area's moment of inertia for rectangular and T-shaped rail cross-section under consideration can be calculated by the following equations:

1. Moment of inertia for rectangular rail cross-section along the X'$_1$-X$_1$ and Y'$_1$-Y$_1$ axis as shown in Fig. 3.

$$I_{x1} = \frac{WH^3}{12}, \tag{8}$$

$$I_{y1} = \frac{HW^3}{12}. \tag{9}$$

Centroid for rectangular rail cross-section:

$$\overline{X_1} = \frac{W}{2}, \tag{10}$$

$$\overline{Y_1} = \frac{H}{2}. \tag{11}$$

2. Moment of inertia for T-shaped rail cross-section along the X'$_2$-X$_2$ and Y'$_2$-Y$_2$ axis as shown in Fig. 4.

$$I_{x2} = \frac{(W-m)H^3 + md^3}{12}, \tag{12}$$

$$I_{y2} = \frac{H(W-m)^3 + dm^3}{12} + A_{21}\left(x_{21} - \overline{X_2}\right)^2 + A_{21}\left(x_{22} - \overline{X_2}\right)^2. \tag{13}$$

Centroid for rectangular convex rail cross-section:

$$\overline{X_2} = \frac{A_{21}x_{21} + A_{22}x_{22}}{A_{T\_Shaped}}, \tag{14}$$

$$\overline{Y_2} = \frac{A_{21}y_{21} + A_{22}y_{22}}{A_{T\_Shaped}}, \tag{15}$$

where:

$$A_{21} = (W-m)H,$$
$$A_{22} = md,$$
$$x_{21} = \frac{(W-m)}{2},$$
$$x_{22} = (W-m) + \frac{m}{2},$$
$$y_{21} = y_{22} = \frac{H}{2}.$$

Railgun launches can cause the rail to respond dynamically due to magnetic pressure. When the armature reaches its critical velocity, resonance might develop, causing high-amplitude tension and strain during passage and potentially damaging the rails [10]. Timoshenko [12] investigated the vibration of Bernoulli-Euler beams on an elastic base. Lewis and Nechitailo [11] proposed an expression for critical velocity, based on [12].

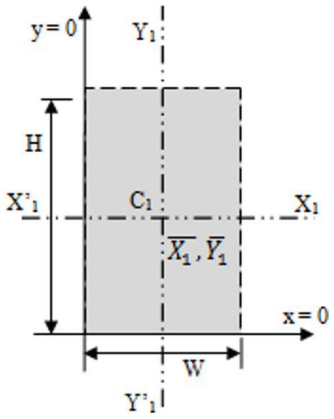


Fig. 3. Cross-section of rectangular rail.

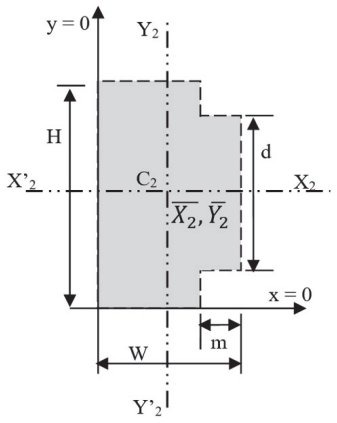


Fig. 4. Cross-section of T-shaped rail.

Rails' critical velocity:

$$V_{cr} = \sqrt{\frac{2\sqrt{EI_yK_f}}{\rho A}}, \tag{16}$$

where $E$ is the modulus of elasticity, $I_y$ is the moment of inertia of the beam cross-section, $\rho$ is the density of the rail material and $A$ is the rail cross-sectional area.

The normalized rail critical velocity at the time of launch can be calculated by using equation (16). Though the mechanical strength of the rail purely depends on the material property. So, the material chosen for the rail was [1–4] having modulus of elasticity ($E$) as 117 GPa, moment of inertia ($I_x$) of the beam cross-section, density ($\rho$) of the rail material as 8933 kg/m$^3$, rail cross-sectional area ($A$) as 1500 mm$^2$ and foundation stiffness ($K_f$) as $6\times10^9$ N/m$^2$. The resultant values of inertia moment for all rail cross-sectional geometries are tabulated. For a comparative approach, the simulated values and calculated values of moment of inertia are shown in Table 2.

Table 2: Comparison of moment of inertia

| Rail Cross-Section | Centroidal Axis (mm) | Moment of Inertia, $I_y$ ($\times 10^5$ mm$^4$) | | $V_{cr}$ (m/s) |
|---|---|---|---|---|
| | | Simulated (Using ANSYS Tool) | Calculated (Using Empirical Equations) | |
| Rectangular | (18.75, 20) | 1.7578 | 1.7429 | 128.78 |
| T-shaped | (18.79, 20) | 1.7795 | 1.7524 | 129.18 |

Table 2 indicates that the found equations for determining the area's moment of inertia produce the same results as those acquired through simulation. The T-shaped rail cross-section has a greater mechanical strength of 1.7 mm$^4$ and a critical velocity of 129 m/s, indicating its ability to resist launch.

## III. DYNAMIC ANALYSIS ON EM RAILGUN USING MSC METHOD

Railgun armature plays a crucial function in the EM launching process. Two types of armatures were chosen for experimental consideration: C-shaped armature and brush armature. At the end of the simulation, the C-shaped armature demonstrated higher efficiency than the brush armature. Higher current concentration in the armature causes a rise in local temperature, resulting in loss of mechanical strength and even melting [13]. The armature is built so that it may be correctly aligned with the rectangular and T-shaped railgun for a 1 meter rail.

The three-dimensional geometry was initialized by properly selecting the properties of the materials copper for rail with conductivity $5.8\times10^7$ (S/m) with a relative permeability of 0.999991 and aluminum for armature with conductivity $3.5\times10^7$ (S/m) with a relative permeability of 1.0. The boundary conditions and excitation of rails about 300 kA are assigned to the railgun by meshing it properly. The parameter sweep is used to calculate current density and magnetic field strength as the armature position moves in increments until it exits the rails. The ANSYS Maxwell EM solver is coupled with Simplorer to accomplish the MSC method, and simulation flow is clearly represented in Fig. 5.

Figure 6 depicts a 30×40 mm flat surface armature that has been proposed to improve railgun performance by meeting the required railgun essential criteria such

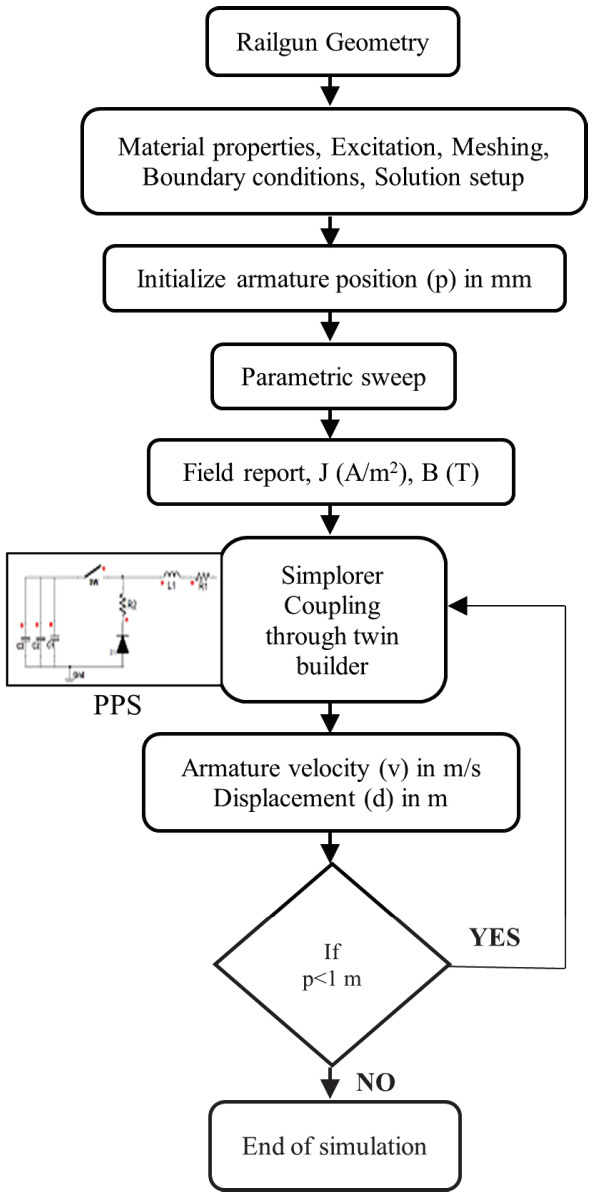


Fig. 5. Design chart of MSC method.

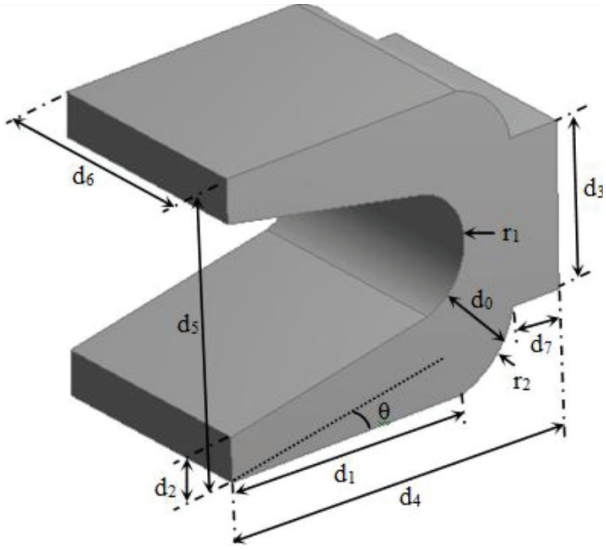


Fig. 6. A 30×40 mm flat surface C-shaped armature.

as minimal current density concentration and maximum EM armature force.

Wing angle of the armature tail ($\theta$ =11.7°), thickness of the armature ($d_0$ =13 mm), length of the armature tail ($d_1$ =35 mm), thickness of the armature tail ($d_2$ =6 mm), height of the armature spearhead ($d_3$ =22 mm), length of the armature ($d_4$ =50 mm), width of the armature ($d_5$ =40 mm), height of the armature ($d_6$ =30 mm), thickness of the armature spearhead ($d_7$ =7 mm), curvature radius of the armature throat ($r_1$ =8 mm) and curvature radius joining leading edge to armature spearhead ($r_2$ =11 mm). During the pre-processing stage the meshing is properly configured with 28234 domain elements, 5940 boundary elements and 790 edge elements. Degrees of freedom (DOF) for flat surface C-shaped armature are 18629 with internal DOF's as 4882.

Figure 7 depicts the pulsed power supply (PPS) system with pulsed capacitor circuit, switching circuit and pulse shaping elements that is outfitted with the railgun to generate 300 kA capacitive discharge pulse current, as shown in Fig. 8, to improve railgun performance analysis.

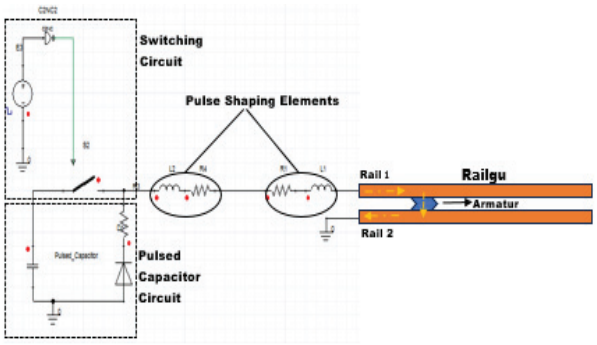


Fig. 7. Pulsed power supply system.

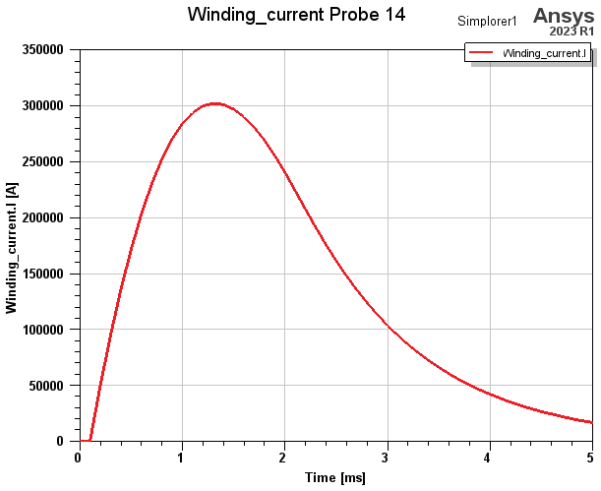


Fig. 8. Capacitor discharge current.

The railgun model being fed with 300 kA of pulsed current from 0 to 2 ms and then reduced from 2 ms to 5 ms is illustrated in Fig. 7. This calculates the current density concentration between the armature and the rail for an armature distance of 40 mm from the rail's breech end.

Figure 9 depicts the electrical equivalent circuit model of a railgun, which is used to determine the velocity and distance traveled by the projectile using the ANSYS coupled Simplorer. The subsystem model is provided with capacitor bank-based PPS, and the resulting emerging force causes the armature to move. The armature's location is sensed and given back to the subsystem model by computing its velocity and displacement.

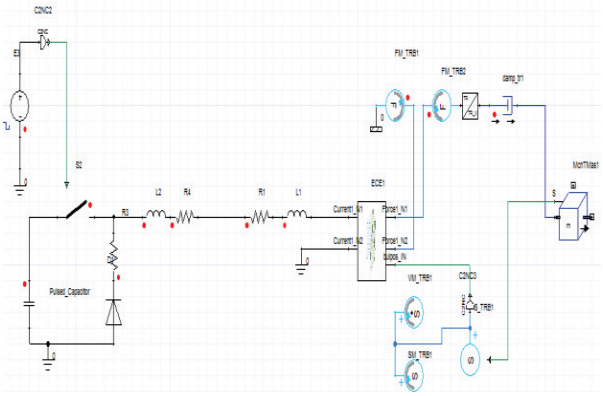

Fig. 9. MSC method of computational system.

The closed loop model contains a discharge capacitor C1, input resistance R1, pulse shaping inductance equivalent model of the railgun system, a translational mass "MASS_TRB1", a translational motion setting "S_TRB1" and time-controlled switches S1 and S2. The railgun will act as a subsystem which is initialized by current excitation which passes through the rails and the bullet. The output of the rail model is the Lorentz force "FORCE1_N" that is generated on the armature. This generated force propels the mass with the delta change in position to the delta change in time which is sensed and recorded by the displacement sensor "SM_TRB1". This process is carried out until the bullet exits the rails.

## IV. ELECTROMAGNETIC POST PROCESSING RESULTS

In the post processing stage, EM field plots and output parameter graphical plots can be obtained. To compute the armature velocity, a project variable has been developed for a flat surface C-shaped armature with an armature volume of $3.3039\times10^{-005}$ $m^3$ and an armature density of 1816.045 kg/$m^3$ for a 60 gram armature.

On observing the field plots from Figs. 10–13, the current density concentration over the center curvature of the armature of the rectangular railgun is greater ($1.1790\times10^9$ A/$m^2$) compared with the T-shaped railgun ($1.0706\times10^9$ A/$m^2$). The current hotspot in the center curve of the armature causes melting due to temperature rise, resulting in damage to the armature before it leaves the muzzle.

Figures 14 and 15 show the velocity and acceleration graphs for the rectangular and T-shaped railguns with 60 grams armature. For both types of railguns, the velocity obtained is nearly equivalent to 1 km/s for 60 grams of armature. When the parameters m and d of the T-shaped railgun are further dimensioned, the current density concentration will be reduced by raising the value of uniform current distribution to obtain maximum velocity.

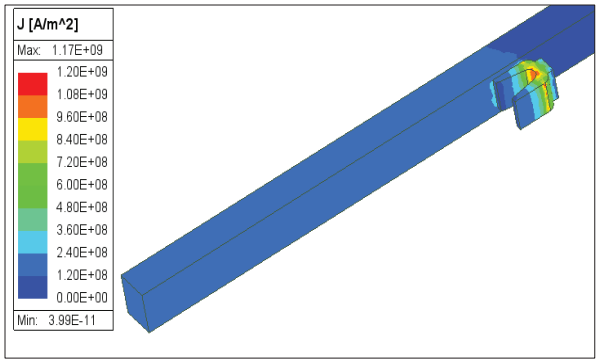


Fig. 10. Current density field plot for rectangular railgun at armature distance of 40 mm.

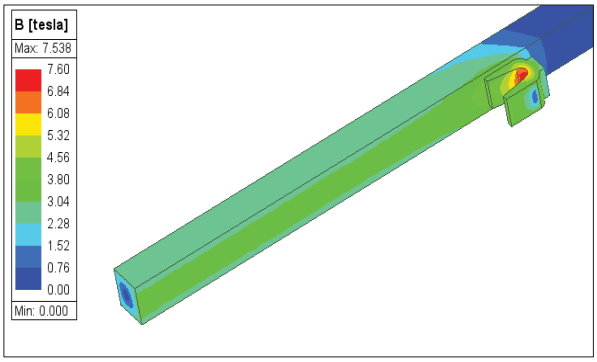


Fig. 11. Magnetic flux density field plot for rectangular railgun at armature distance of 40 mm.

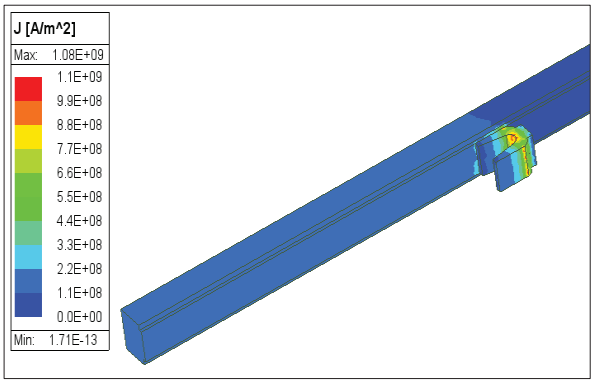


Fig. 12. Current density field plot for T-shaped railgun at armature distance of 40 mm.

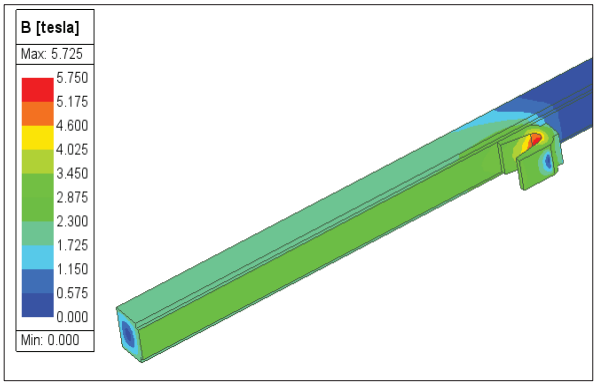


Fig. 13. Magnetic flux density field plot for T-shaped railgun at armature distance of 40 mm.

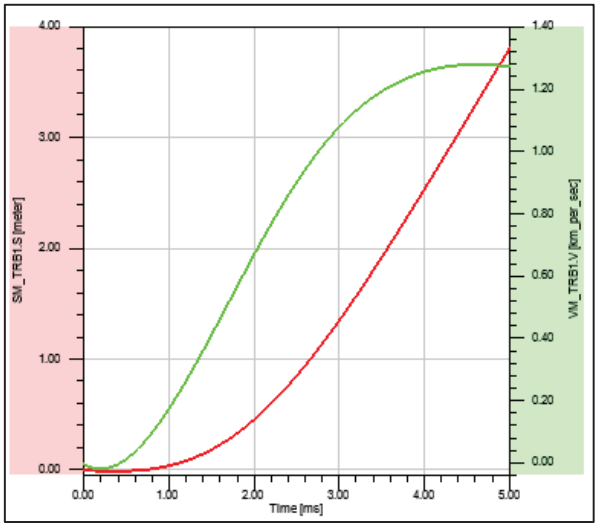


Fig. 14. Armature velocity (VM_TRB1.v) of 1.25 km/s for rectangular railgun.

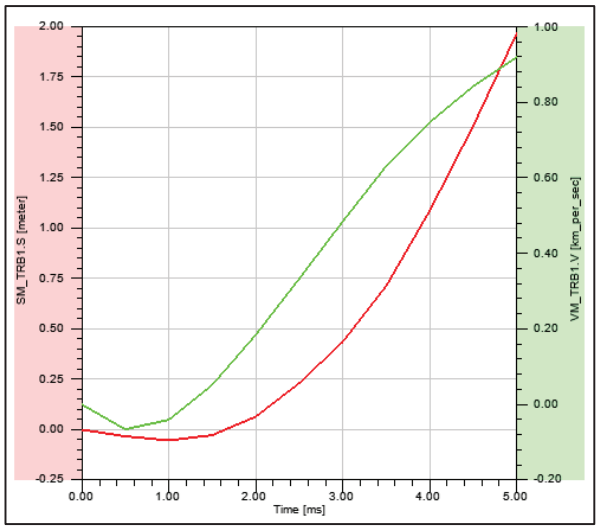


Fig. 15. Armature velocity (VM_TRB1.v) of 0.9182 km/s for T-shaped railgun.

## V. CONCLUSION

In this paper, the area's moment of inertia is investigated for rectangular and T-shaped rail cross-sections, and FEM simulations of railgun dynamics are done under identical circumstances. ANSYS MSC simulations are run for the two different rail geometries. The findings reveal the following:

1. The cross-sectional area was kept constant at 1500 $mm^2$ by modifying the rail's dimensional properties. T-shaped rails have a greater moment of inertia than flat rails for the same cross-sectional area and rail width. The high moment of inertia can delay the occurrence of maximum displacement, although this impact is subtle since the critical velocity is determined by the fourth root of the moment of inertia. As a result, the T-shaped rail cross-section has a higher mechanical strength (1.7 $mm^4$) and critical velocity (129 m/s), allowing it to withstand the launch.
2. Simulations of rail dynamics using a flat surface C-shaped armature show no significant changes in mechanical performance between the two rail designs. As a result, the benefits of bigger moments of inertia for a given cross-sectional area are limited.
3. Compared to rectangular and T-shaped rails, T-shaped rails have lower current density at the inner curvature but higher at the contact interface.

## REFERENCES

[1] Y. Zhou, P. Yan, W. Q. Yuan, J. Wang, and M. T. Li, "Current distribution and inductance gradient calculation at different rail geometric parameters," in *2009 IEEE Pulsed Power Conference*, Washington, DC, pp. 1290-1293, 2009.

[2] A. Keshtkar, "Effect of rail dimension on current distribution and inductance gradient," in *2004 12th Symposium on Electromagnetic Launch Technology*, Snowbird, UT, pp. 359-362, 2004.

[3] L. Jin, B. Lei, Q. Zhang, and R. Zhu, "Electromechanical performance of rails with different cross-sectional shapes in railgun," *IEEE Transactions on Plasma Science*, vol. 43, no. 5, pp. 1220-1224, May 2015.

[4] S. Liu, J. Ruan, Z. Du, D. Wang, and C. Zhao, "Calculation of railgun inductance gradient by 2-D finite element method," in *2008 International Conference on Electrical Machines and Systems*, Wuhan, pp. 4057-4060, 2008.

[5] L. Jin, B. Lei, Z. Li, and Q. Zhang, "Comparison simulation of friction heat and joule heat in electromagnetic railgun," *Applied Mechanics and Materials*, vol. 203, pp. 401-405, 2012.

[6] M. N. Saravana Kumar and R. Murugan, "Analysis of inductance gradient and current density distribution over different cross-section of rails," *International Journal of Electrical and Computer Engineering*, vol. 8, no. 02, pp. 723-729, 2018.

[7] M. N. Saravana Kumar, R. Murugan, and Shivkumar Poorani, "Inductance gradient and current density distribution for T-shaped convex and concave rail cross-sections," *International Journal of Engineering & Technology (UAE)*, vol. 7, no. 01, pp. 237-240, 2018.

[8] A. Keshtkar, Z. Jafari Khorrami, and L. Gharib, "Comparison of inductance gradient and electromagnetic force in two types of railguns with two projectiles by finite element method," *IEEE Transactions on Plasma Science*, vol. 45, no. 8, pp. 2387-2392, 2017.

[9] M. S. Bayati, A. Keshtkar, and S. V. A.-D. Makki, "Analyzing the current distribution, magnetic field and inductance gradient at the circular rail in comparison to rectangular rail," in *2012 16th International Symposium on Electromagnetic Launch Technology*, Beijing, China, pp. 1-5, 2012.

[10] K. Daneshjoo, M. Rahimzadeh, R. Ahmadi, and M. Ghassemi, "Dynamic response and armature critical velocity studies in an electromagnetic railgun," *IEEE Trans. Magn.*, vol. 43, no. 1, pp. 126-131, Jan. 2007.

[11] K. B. Lewis and N. V. Nechitailo, "Transient resonance in hypervelocity launchers at critical velocities," *IEEE Trans. Magn.*, vol. 43, no. 1, pp. 157-162, Jan. 2007.

[12] S. Timoshenko, "Method of analysis of statistical and dynamical stresses in rail," in *Proc. 2nd Int. Congr. Appl. Mech.*, Zürich, Switzerland, pp. 1-12, 1927.

[13] J. Gallant and P. Lehmann, "Experiments with brush projectiles in a parallel augmented railgun," *IEEE Transactions on Magnetics*, vol. 41, no. 1, pp. 188-193, 2005.

**M. N. Saravana Kumar** received a bachelor's degree in Electronics and Communication Engineering from Bhajarang Engineering College, Chennai, India, in 2009. He received his master's degree in Power Electronics and Drives from Rajalakshimi Engineering College, Chennai, India, in 2013, and Ph.D. degree in Electrical and Electronics Engineering from St. Peter's Institute of Higher Education and Research, Chennai, India, in 2019. His main areas of interest are power electronics and drives, electric machine designing, electromagnetic field computation and modelling.

**R. Murugan** received a bachelor's degree in Electrical and Electronics Engineering from University of Madras, Tamil Nadu, India, in April 1996. He received his master's degree in High Voltage Engineering from College of Engineering, Anna University, Guindy, Chennai, Tamil Nadu, India, in February 1999, and Ph.D. degree in Electrical and Electronics Engineering from Anna University, Chennai, Tamil Nadu, India, in 2011. His main areas of interest are electromagnetic field and high voltage engineering.

**J. Lydia** has completed her Ph.D. degree under the Faculty of Electrical Engineering, Anna University, Chennai, India. She received the B.E. degree in Electrical and Electronics Engineering from Easwari Engineering College, Chennai, India. She received the M.E. degree in Power Electronics and Drives from the Karunya Institute of Technology and Sciences, Deemed University, in 2006. She is currently an Assistant Professor with the Department of Electrical and Electronics Engineering, Easwari Engineering College, and works in the fields of electromagnetic fields and high-voltage engineering. She is a member of MISTE.

**S. Leones Sherwin Vimalraj** is a Professor in the Department of Electronics and Communication Engineering, Panimalar Engineering College, Chennai, India. He completed his B.E. in Electronics and Communication Engineering from Karunya Institute of Technology, Bharathiar University, India, in 2001. He obtained his M.E. in Optical Communication Engineering (2004) from College of Engineering, Guindy, Anna University, and Ph.D. in Wireless Communication Engineering (2015) from Dr. MGR Educational and Research Institute, Deemed University, Chennai, India. His research areas include wireless communication, network engineering, computing and evolutionary algorithms.

# Cable Interference Analysis of Gas Insulated Substation Based on Domain Decomposition Method-Multilevel Fast Multipole Algorithm

**Abdul Mueed[1], Weiqiang Tang[1], Muhammad Asif[2], and Rui Ma[1]**

[1]College of Electrical and Information Engineering
Lanzhou University of Technology, Lanzhou, GanSu 730022 China
engr.mueed@live.com, twqzjh@163.com, 18294916381@163.com

[2]Education Department
Khyber Pakhtunkhwa 25000, Pakistan
asifpk003@gmail.com

***Abstract*** **–** To explore cable interference in gas insulated substations (GIS), this paper proposes a reliable and efficient computational approach. The hybrid domain decomposition method-multilevel fast multipole algorithm (DDM-MLFMA) is presented herein. This technique determines the specifications of GIS cables for RG58 and AWG23. Self and mutual interference are identified utilizing very fast transient overvoltage (VFTO) transient interference signal.This hybrid technique offers a numerical simulation to replicate the impact of the VFTO interference signal. Utilizing the matrix-vector multiplication (MVX) product to address compression and approximation challenges, the hybrid approach proves reliable and pragmatic. Because of its computational nature and explicit factorization reduction, this strategy reduces computation time and memory requirements. Consequently, the system's complexity follows a linear trend under this proposed approach. The computed results are juxtaposed with traditional methodologies to validate the effectiveness of the proposed algorithm.

***Index Terms*** **–** Computational memory, computational time, domain decomposition, hybrid algorithm, interference measurement, multilevel fast multipole method, very fast transient overvoltage interference signal.

## I. INTRODUCTION

The substation is the hub of power transmission and transformation. The utilization of gas insulated substation (GIS) switching techniques has led to the generation of rapid transient events termed very fast transient overvoltages (VFTO). During the propagation of VFTO in GIS, catadioptric reflection takes place, subsequently coupling to the GIS shell and emitting outward into the external space.

The EM transient phenomena occurs in the GIS substation by the leakage of isolation gasses due to voltage level increases. This signal/behavior effects the secondary side due to its enormous amplitude and complicated composition of frequency (VFTO signal). This penetration occurs via power cable connection [1–4].

The automation of the secondary side in GIS substations has received significant attention over the past decade. Secondary equipment produces current or voltage through the transformation process and powerful transient EM fields are produced in space. Additionally, coupling is used to safeguard the cable through EM radiation. The surge VFTO signal effects secondary side equipment and becomes a key factor in the design of EMC in a GIS substation [5–8].

Due to continual advancements in digital and intelligent substation technology, GIS installations incorporate a greater number of secondary intelligent electronic devices equipped with control, protection, and communication capabilities. It is crucial to note that substation operations may generate electromagnetic interference that poses a risk to the safe and reliable functioning of the substation. This interference has the potential to cause malfunctions and damage to electronic equipment. The VFTO procedure and related risks are depicted in Figs. 1 and 2.

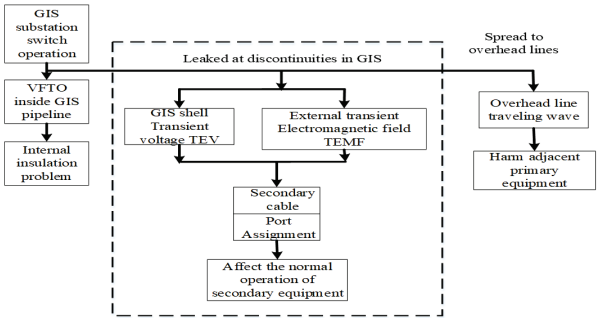


Fig. 1. The very fast transient process and its hazards.

*Submitted On: January 9, 2024*
*Accepted On: August 18, 2024*



https://doi.org/10.13052/2024.ACES.J.390909

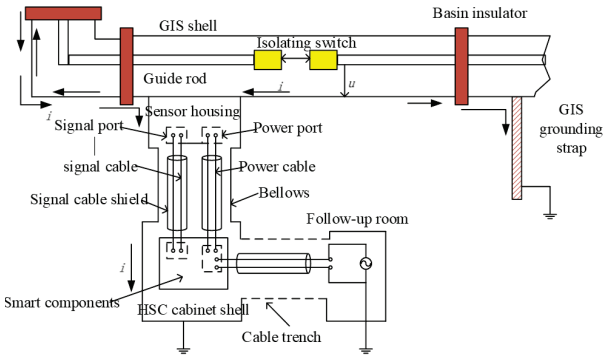


Fig. 2. The principle of interference voltage generated by GIS switch operation on equipment ports.

The next hazard is frequency components composed in this waveform. There are several types of high frequency components present in the power frequency components. The frequency range is 1 MHz-1 GHz and the current method is fast Fourier transform (FFT). In Fig. 3, the VFTO waveform also contains the frequency components 40 MHz, 56 MHz, and 88 MHz corresponding to the 5th, 7th, and 11th harmonic frequency components of 8 MHz, respectively.

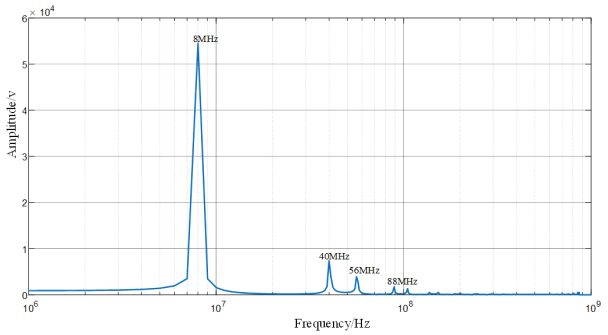


Fig. 3. The VFTO frequency components.

Numerous theories regarding EM interference in GIS substations have been explored. The concept of coupling transmission line field lines has been addressed [9–10], alongside Agrawal's theory on multiconductor transmission lines [11]. Additionally, discussions on lossy and lossless lines are included [12].

A time domain model has been developed to estimate secondary cable interference in GIS substations [13]. Yamamura et al. [14] presented a numerical calculation approach for determining the common-mode induced voltage of shielded cables in substations, utilizing the transmission line theory of the mirroring principle. Acatauassu et al. [15] have showcased the occurrence of transient overvoltage in shielded cables.

As per the study by Yan et al. [16], finite difference techniques have been investigated for scattering and radiation problems involving narrow wires. Recent advancements in high-frequency theories and research have led to a greater utilization of multi-conductor stranded cables. Calculating the electrical crosstalk/interference parameters for such cables at high frequencies is not particularly challenging [17–18].

In the GIS substation with multistrand cables, various numerical techniques such as the moment method [19–20], FDTD techniques [21–22], advanced modeling techniques [23], domain decomposition method [24], and traditional FEM approach [25] are employed to conduct interference analysis.

Due to the non-linear nature of the memory parameters, additional iterations are necessary for convergence, prompting the utilization of FEM for computation. This results in an increase in complexity. When employing standard FEM for analysis, the complexity in terms of memory size also escalates.

Domain decomposition is based on tetrahedra (triangles) to form a mesh. However, this method demands a considerable number of operations to solve the resulting equations.

The fast multipole method (FMM) [26–27] speeds up the matrix-vector multiply in the conjugate gradient (CG) method when it is used to solve the matrix equation iteratively. FMM with the formula of combined field integral equation (CFIE) has been derived, where the complexity of the matrix-vector multiplication reduces from O($N^2$) to O($N^{1.5}$), where $N$ is the number of unknowns. The ray-propagation fast multipole algorithm [28–29] with nonnested method, further reduces to O($N^{4/3}$). Hence, we implement the multilevel fast multipole algorithm (MLFMA), whose complexity reduced to O($NlogN$). As a result, we employ the hybrid domain decomposition method-multilevel fast multipole algorithm (DDM-MLFMA) technique to overcome the computational deficiencies inherent in conventional methods. This article focuses on analyzing interference/crosstalk in cables utilized within GIS substations. The DDM-MLFMA algorithm is employed to calculate both self and mutual interference. Additionally, computational parameters including computational time, memory usage, errors, and efficiency are evaluated.

This article is structured as follows. In section I, we attempt a GIS literature review. In section II, the mathematical equations of cable modelling parameters are described. Section III covers the comprehensive procedure about the hybrid algorithm (DDM-MLFMA). In section IV, proposed cable model simulation and validation of results are presented. Finally, section V concludes our work.

## II. CABLE MODEL BUILDING

The model is composed of a single-core wire and a shielded wire as mentioned in the two sets

of transmission line loops. The signal applies on the shielded wire core and induces current on the shielding layer. Hence, an induced voltage is generated at its port. The equivalent circuit model parameters are shown in Fig. 4. $Z_S$, $Z_L$, $Z_{SS}$, and $Z_{SL}$ are 50 Ω, and both ends of the shielding layer are directly grounded.

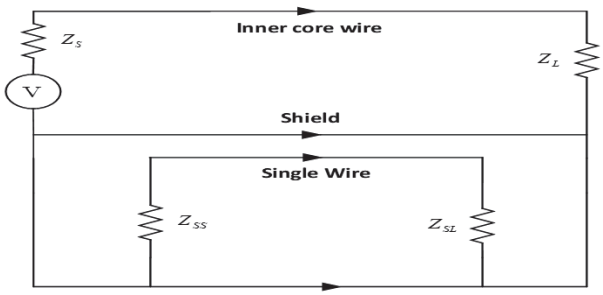


Fig. 4. Equivalent circuit model of shielded wire and single core wire.

According to transmission line theory, the current distribution on the inner core of the wire is:

$$I_1(z) = \frac{I_{01}Z_{01}}{Z_{C1}}\sinh(\gamma_1 z) + I_{01}\cosh(\gamma_1 z), \qquad (1)$$

where $I_{01}$ and $Z_{01}$ represent the excitation current and internal impedance of the inner core wire, and $Z_{C1}$ and $\gamma_1$ represent the characteristic impedance and propagation constant of the inner transmission line loop, respectively.

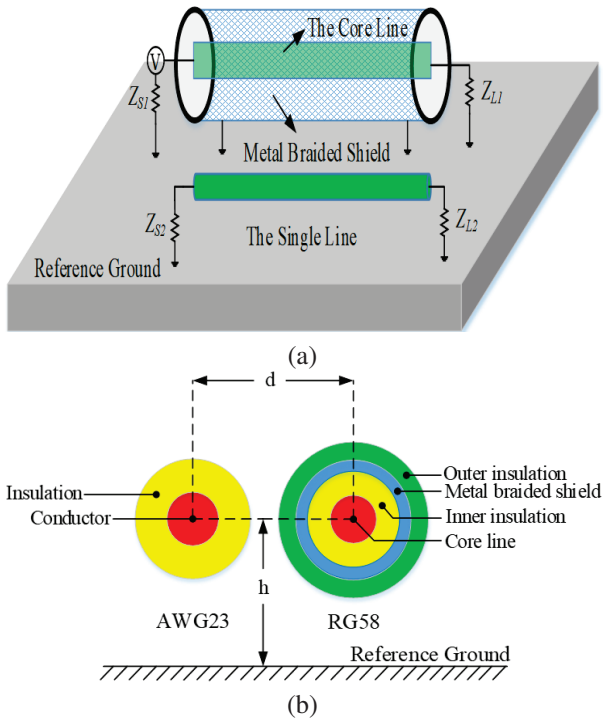


Fig. 5. Schematic diagram of crosstalk model: (a) radial diagram and (b) sectional view.

The shielding layer does not contain an excitation source. The voltage source generated by the current on the inner core wire at any position $z$ of the shielding layer is:

$$du = I_1(z)Z_t dz. \qquad (2)$$

In this section, the theoretical calculation and simulation verification of the crosstalk of the specific model are carried out. The model of the shielded wire is RG58 and the model of the single-core wire is AWG23. The radial and cross-sectional schematic diagrams are shown in Fig. 5. The specific parameters of the model are shown in Table 1.

Specific parameters of the model are shown in Table 1.

Table 1: RG58 and AWG23 cable parameters

| Parameter | Size |
|---|---|
| Relative distance between cables d | 3 mm |
| Height over the ground h | 10 mm |
| Single core conductor radius$r_{21}$ | 0.2865 mm |
| Insulation thickness of single core wire $t_{22}$ | 0.19 mm (PE) |
| Line length | 1 m |
| Inner core wire radius $r_{11}$ | 0.47 mm |
| Inner insulation layer thickness $t_{12}$ | 1.005 mm (PE) |
| Shield thickness $t_{13}$ | 0.325 mm |
| Outer insulation thickness $t_{14}$ | 0.5 mm (PVC) |
| Termination resistance | 50 Ω |

## III. HYBRID ALGORITHM

By combining one or more asymptotic and numerical techniques, the hybrid approach improves the accuracy of solving electromagnetic problems. Originally designed to improve algorithmic performance, the hybrid approach focused on fusing asymptotic and numerical techniques to address challenging structural problems. These methods can be used on large or small surfaces, depending on how complicated the issue is. This approach has the benefit of offering useful solutions for large and complex technical challenges. In our case, transient electromagnetic interference is estimated using huge and irregular structures. The hybrid algorithm is DDM-MLFMA.

This hybrid algorithm uses a hybrid approach. First, convert the irregular shapes that are decomposed into a regular surface (# of triangles). Then, use the matrix-vector multiplication (MVX) principle to compute the interference and computing parameters. The computation is done through the far and near interaction field, which is based on the domain specified by the domain decomposition method (DDM).

### A. Domain decomposition method

The non-overlapping DDM has become a potent and attractive tool for numerically rigorous solutions of

Maxwell's equations, which is based on the divide-and-conquer strategy. The original problem is divided into smaller, potentially repeating and simpler, subdomains rather of being addressed as a whole. To enforce the continuation of electromagnetic fields, some suitable boundary requirements known as transmission conditions are required at the interfaces between adjacent subdomains. Iteratively, these transmission requirements are imposed. Subdomains interact with one another, starting with arbitrary initial assumptions for each, until a specific convergence in the solution is achieved [30].

The straightforward geometrical multi-section method is used for domain decomposition. The domain can be divided into as many subdomains as desired, each of which has an equal number of cells per processor. To create the desired number of subdomains, the domain is divided along its largest dimension using the domain decomposition technique. This pruning can (and typically is) done recursively to newly created subdomains. Since each subdomain is stored in a distinct file and the cells are sorted using the quick-sort method, the process is extremely speedy.

Moreover, embedded DDM have many advantages, which can be to discretize one domain into subdomains. Thus, we can make an embedded mesh of complicated geometries by dividing them into many small subdomains, from which we get a good quality of mesh. Therefore, small subdomain meshes and matrix assembly are independent. Recomputing the DDM subdomain and adding another subdomain will support EM modeling and practical design solutions.

For electrically large EM problems, direct inversion methods such as Gaussian elimination or LU decomposition can no longer be applicable due to O($N^2$) memory and O($N^3$) central processing unit (CPU) time requirements, where $N$ is the number of unknowns. Iterative solution methods such as the conjugate gradient (CG) method are the only options but their convergences are often chaotic or failing. Much of the work in the DDM in this aspect is related to the selection of the transmission conditions to ensure the convergence of the DDM algorithm. When transmission conditions are properly devised, DDM becomes an effective preconditioner for such problems. Furthermore, memory requirements can be greatly reduced since DDM can be easily parallelized with MLFMA.

### B. Multilevel fast multipole algorithm

MLFMA is an iterative approach that accelerates MVX, resulting in lower memory requirements and faster computation. A multilevel solver, MLFMA is based on the working principle of MVX product. MLFMA is used to compute the number of operations and the memory usage by the extraction of sparse matrix. Additionally, it is an almost matrix-free solver and only needs ($NlogN$) memory. Furthermore, it has been demonstrated that the MLFMA can be applied to dense matrices with FEM up to 10 million unknowns. As a consequence, MLFMA minimizes complexity and memory requirements. In order to achieve ($NlogN$) complexity, the MLFMA employs aggregation, translation, and disaggregation.

The MLFMA algorithm is based on expansion and approximation of the first kind Hankel function. The integral equation can be solved iteratively, which involves the MVX product: MVX performed by the MLFMA solver and having (M+1)×(N+1) matrix-vector equation. This algorithm reduces the memory requirement from $\emptyset\left(N^2\right)$ to $\emptyset(NlogN)$. In MLFMA, the far-field is effectively calculated in a group-to-group for basis function and testing function. The MLFMA is a well-organized solver that can optimize computations. Additionally, the Lagrange interpolation method significantly improves the efficiency and accuracy of proposed solver. This Lagrange method is used to fill the translation matrix entries of large-scale EM problems, but the number of interpolation and sampling points are fixed. This speeds up the simulation i.e. reduces the computation time.

To develop the fast and hybrid multilevel algorithm (DDM-MLFMA), the whole geometry is composed of one big cube (known as a group). The big cube is divided into eight small cubes (subgroups/subblocks). Each subcube is divided into smaller cubes. This smaller cube is divided into the finest level with each cube having the length of half a wavelength. Every cube has to be categorized. By comparing the basis function of the center cube with other centered cubes, we may determine the cube at the highest level in which each basis function can be found, while checking for nonempty cubes.

### C. Implementation of DDM with MLFMA

To implement the hybrid DDM-MLFMA multilevel algorithm, the entire object is first decomposed into a larger cube, which is partitioned into eight smaller cubes. Each subcube is then recursively subdivided into smaller cubes until the edge length of the finest cube is about half of a wavelength. An index number is assigned to all levels of cubes. At the finest level, each basis function is assigned to a cube by comparing its center coordinates with the cube's center. We further find nonempty cubes by sorting. Only nonempty cubes are recorded using tree structured data at all levels. Thus, the computational cost depends only on the nonempty cubes.

The basic algorithm for matrix vector multiply is broken down into two sweeps. The first sweep consists of constructing outer multipole expansions for each nonempty cube at all levels. The second sweep consists

of constructing local multipole expansions contributed from the well-separated cubes at all levels. When the cube becomes larger as one progresses from the finest level to the coarsest level, the number of multipole expansions should increase. In the first sweep, the outer multipole expansions are computed at the finest level, and then the expansions for larger cubes are obtained using shifting and interpolation.

Let $r_{m'_l}$ and $r_{m'_{l-1}}$ be the cube centers at level $l$ and $l-1$, respectively, then the outer multipole expansions for coarser level $l-1$ should be:

$$V_{sm'_{l-1}} i\left(\hat{k}\right) = e^{ik.r_{m''_l m''_{l-1}}} V_{sm'_l} i\left(\hat{k}\right). \tag{3}$$

$V_{sm'_{l-1}} i\left(\hat{k}\right)$ has only $K_l$ values, and we need $K_{l-1}$ values of $V_{sm'_{l-1}} i\left(\hat{k}\right)$. Therefore, we will interpolate $V_{sm'_{l-1}} i\left(\hat{k}\right)$ to $K_{l-1}$ values first. That is:

$$V_{sm'_{l-1}} i\left(\hat{k}_{(l-1)n'}\right) = e^{ik_{(l-1)n'}.r_{m''_l m''_{l-1}}} \sum_{n=1}^{K_l} W_{n'n} V_{sm'_l} i\left(\hat{k}_{(l)n'}\right), \tag{4}$$

where interpolation matrix $W$ is a sparse matrix.

At the coarsest level, the local multipole expansions contributed from well-separated cubes are calculated using the basic multipole equation. At the second sweep, the local expansions for smaller cubes include the contributions from the parent cube using shifting and interpolation and from the well-separated cubes at this level but not well-separated at the parent level. If the local multipole expansions received by a cube center at level l-1 is $B\left(\hat{k}\right)$, then the contribution from all well-separated cubes can be written as:

$$\begin{aligned} I &= \int d^2\hat{k} V_{fm_{l-1}j}\left(\hat{k}\right).B\left(\hat{k}\right) \\ &= \sum_{n'=1}^{K_{l-1}} W_{n'} V_{fm_{l-1}j}\left(\hat{k}_{(l-1)n'}\right).B\left(\hat{k}_{(l-1)n'}\right), \end{aligned} \tag{5}$$

where $w_{n'}$ is the weighting function. If we put the interpolation expression for $V_{fm_{l-1}j}\left(\hat{k}_{(l-1)n'}\right)$ into equation (5) and change the order of two summations this leads to:

$$\begin{aligned} I = \sum_{n=1}^{K_l} w_n V_{fm_l j}\left(\hat{k}_{(l)n'}\right) . \sum_{n'=1}^{K_{l-1}} W_{n'n} B\left(\hat{k}_{(l-1)n'}\right) \\ e^{i\hat{k}_{(l-1)n'} r_{m'_l} r_{m''_{l-1}}} w_{n'}/w_n. \end{aligned} \tag{6}$$

The above operation is called interpolation. At the finest level, the contributions from non-well-separated cubes are calculated directly. Since only nonempty cubes are considered, the complexity for MLFMA is reduced to O(*NlogN*) and the memory requirements for MLFMA are of the order O(*NlogN*).

This method is instigated in three phases. First step is aggregation, second step is translation, and final step is disaggregation. At the first level of the group, the field of each group is acquired and connected with its center of geometry. Hence, this point is chosen as first aggression point. In the solution steps, this first level of group is amassed into a larger group. The principles of aggression of the lower group(s) contained in each high-level groups (cubes) are evaluated through shifting and interpolation to reduce computing resources. When the first step is completed, a translation occurs between separated groups, but the group belongs to the same level. Finally, when all the cubes have received a contribution from all other cubes of the same level, these influences are released to the inherited cubes through shifting and translation as mentioned in the aggression step. The flowchart of the hybrid algorithm is shown in Fig. 6.

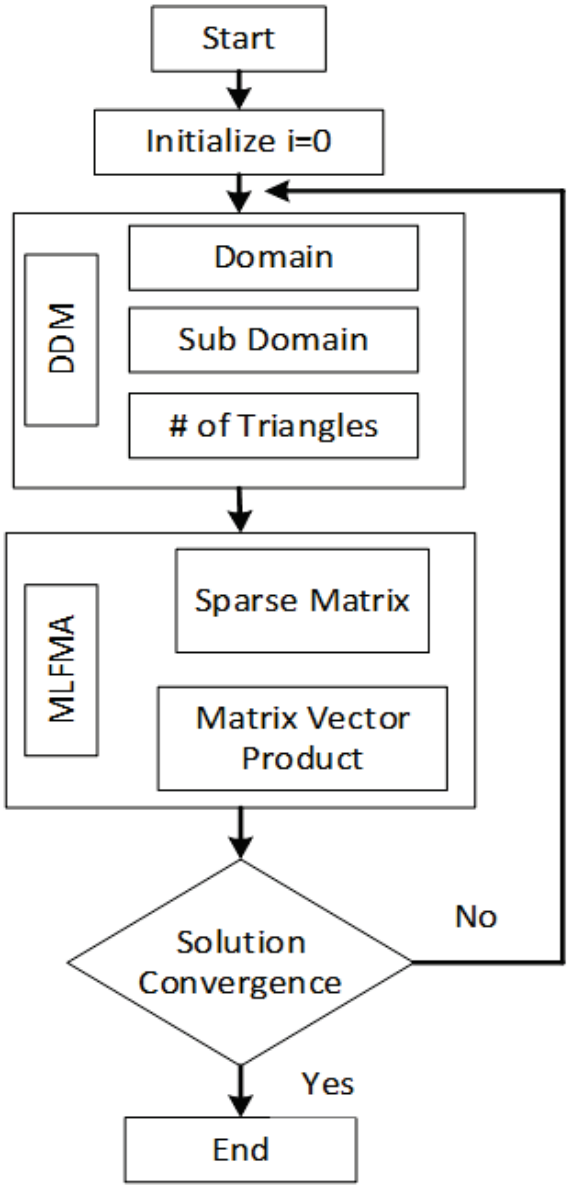


Fig. 6. Flowchart of hybrid DDM-MLFMA.

## IV. RESULTS AND DISCUSSION

### A. The numerical model

This section focuses on the power cable, exploring transient analysis for various cable pairs. Specifically, RG58 and AWG23 configured as a twisted pair is utilized for VFTO analysis.

Based on the geometrical dimensions and materials, the electromagnetic interference simulation model is built, as shown in Fig. 7. The characteristics and configurations of the bus bars and conductors, as well as their computational models, are important considerations when examining the electromagnetic interference and crosstalk properties of the GIS substation. Different tube/conductor thicknesses (5 mm, 10 mm) are taken into account throughout the estimating procedure, and their effect on electromagnetic shielding performance is investigated. There are two different kinds of cables in this model. Figure 6 has comprehensive explanations of the model, meshing, and surface field representation.

More meshes result in a greater confinement of convergence of the solution. In the hybrid technique suggested, mesh refinement reduces geometry factors that aid in solution prediction. Increasing the number of meshes also lowers system complexity. As a result, the suggested approach is dependable and improves the DDM-MLFMA algorithm's accuracy.

The algorithm needs the number of passes, number of iterations, and convergence value to estimate the solution. The hybrid algorithm must follow the criteria of admissibility for the conversion process. It means that the far-field and near-filed matrices are well-mannered to compute the assemblies of the matrix. The beauty of this algorithm requires a smaller number of operations for the estimation of interference parameters. The convergence is shown in the Fig. 8.

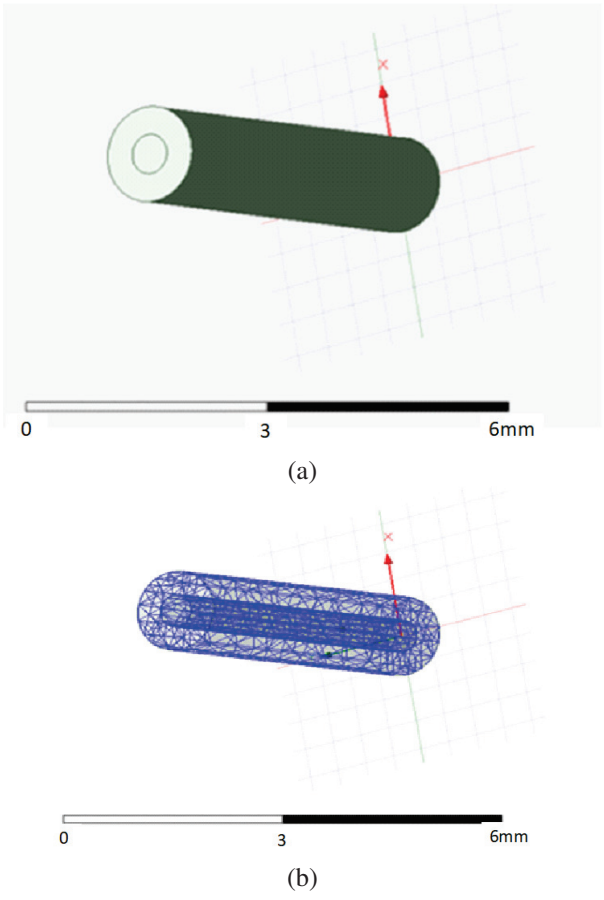


Fig. 7. Cable geometry: (a) the model and (b) meshed view.

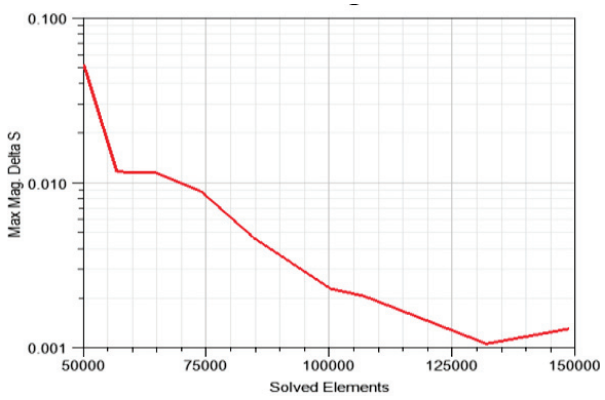


Fig. 8. Solution convergence criteria.

### B. Interference measurement

In such cases, there are two different types of crosstalk. When the effects are the same, there is self-pair/self-strand interference. Self-interference is shown in Fig. 9.

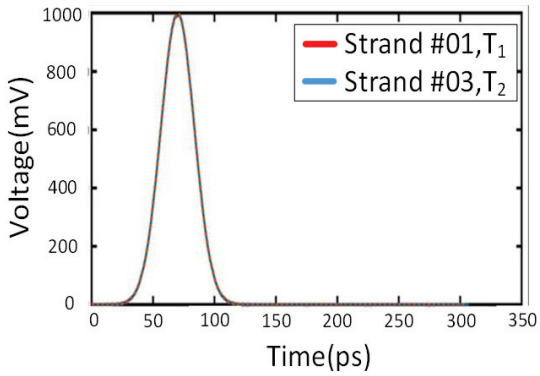


Fig. 9. Self-pair effect of VFTO signal.

Crosstalk refers to the mutual interference between pairs or strands, occurring when they interact. This type of interference manifests as transient effects on other pairs, as depicted in Fig. 10.

Figures 11 and 12 depict the electric and magnetic field distributions along the selected calculation line for a frequency of 100 MHz within the conductor and a casing thickness of 5 mm.

According to Figs. 12 and 13, the electric field magnitudes caused by the electromagnetic interference source are 35316.780 and 27822.773, respectively, while the corresponding magnetic field strengths are 154.277 and 113.440.

As the electromagnetic field moves approaching the shielding (second pair), the electromagnetic field variation curve shows noticeable attenuation. During switching operations, the GIS metal conductor exhibits efficient shielding against radiated electromagnetic fields produced by the electromagnetic interference source.

The GIS conductor's magnetic field shielding effectiveness reaches 240.5 dB at the same frequency of 100 MHz, while its electric field shielding effectiveness registers at -90 dB and -10 dB at a shell thickness of 2 mm. This emphasizes how effectively high-frequency electromagnetic radiations are shielded by the GIS conductor tube.

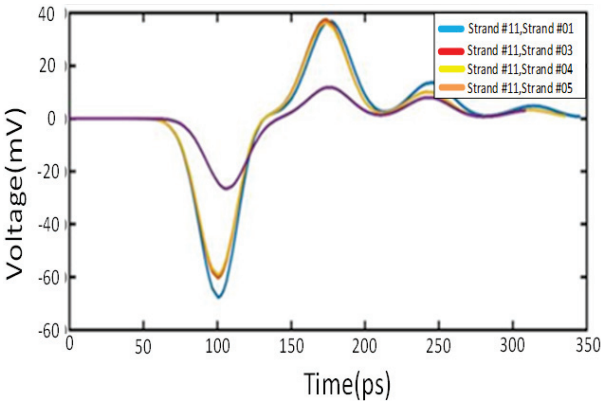


Fig. 10. Mutual pair effect of VFTO signal.

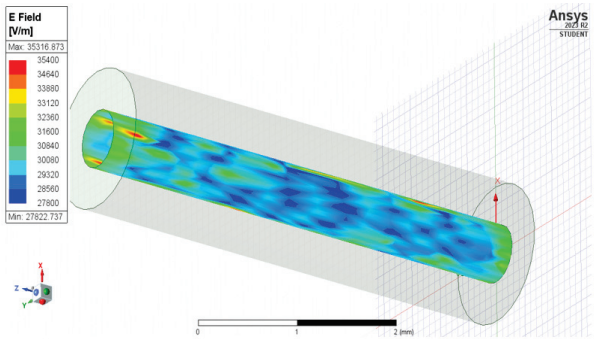


Fig. 11. Electric field of GIS EM interference.

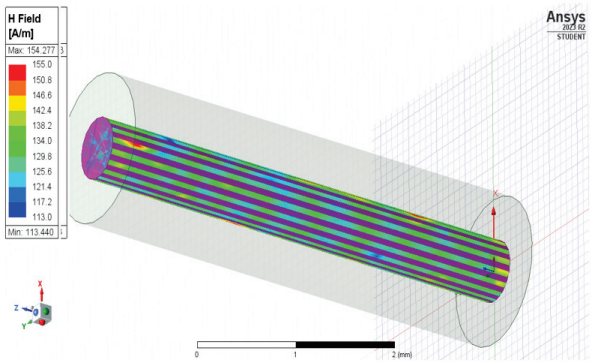


Fig. 12. Magnetic field of GIS EM interference.

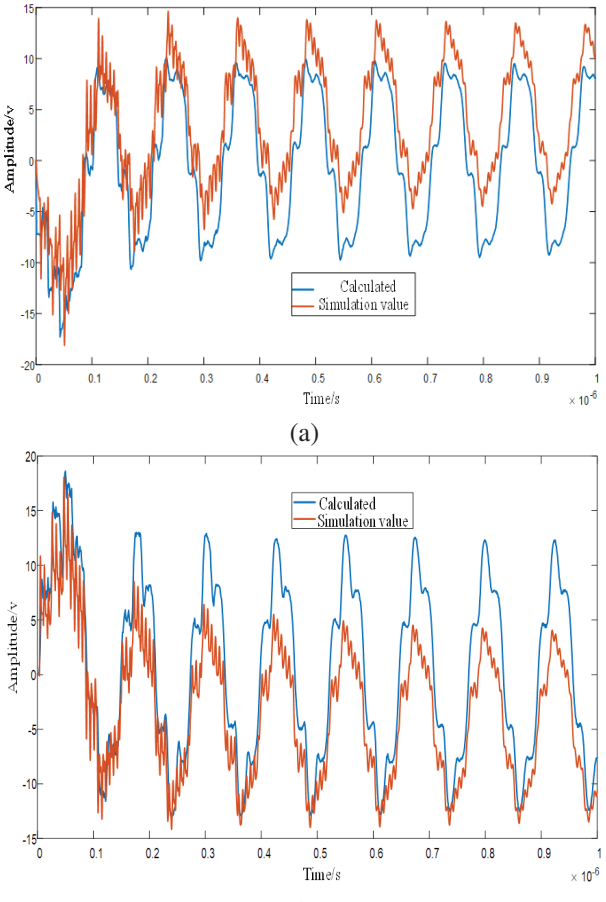


Fig. 13. Response voltage waveforms at two ports of a single-core wire: (a) near-end voltage waveform and (b) far-end voltage waveform.

The experimental procedures are adopted to calculate the interference in the proposed cables model in the GIS substation. The proposed power cable model is simulated and designed in the HFSS portfolio. The excitation signal is used as the VFTO signal to obtain the

crosstalk effect of the signal on the inner core. At the same time, the numerical simulation value is calculated through a hybrid algorithm. The comparison is made as shown in Figs. 13 (a) and (b).

There is an acceptable level of agreement between the hybrid algorithm and the HFSS simulation, even though the former oscillates less than the latter. This difference could be the result of radiation losses during computation, which the HFSS simulation did not take into consideration.

The voltage waveform is represented in Fig. 13. The red line is the simulated data and the blue line is a representation of the calculated data through the equations (proposed algorithm). Both results are compatible with each other. It means that the proposed algorithm is validated. The estimated value (experimental measurement) of the suggested approach is essentially consistent with the waveform size and trend of the simulated value, as can be seen in Fig. 13. This confirms the suggested method's efficacy. However, a few errors in the peak value are unavoidable and are shown for the following two aspects: (1) there will be some discrepancy between the theoretically estimated and actual measurements of the transmission impedance, and (2) there are specific errors in the interference parameter matrix that are determined by the ANSYS program.

### C. Computational parameters

In this section, the computing parameters are estimated through the hybrid algorithm. This hybrid algorithm reduces the number of operations to solve the matrix assembly. The graph is drawn between the numbers of unknowns (matrix assembly) and the computational memory. In Fig. 14, the x-axis represents the number of unknowns (matrix assembly needed to be solved) and y-axis represents the computational memory. Fig. 14 estimates how many matrix assemblies have to be solved: the blue line displays the result of the proposed method, and the red line represents the traditional MLFMA result.

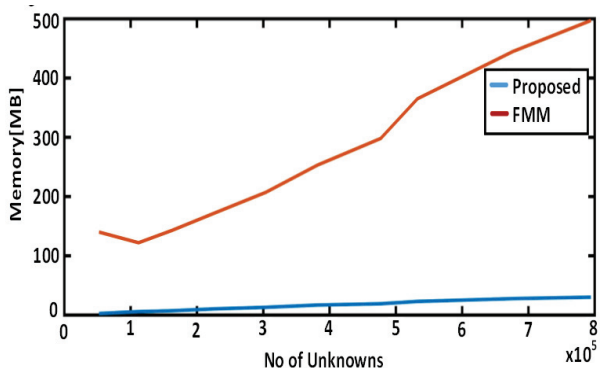


Fig. 14. Memory comparison of proposed method.

The matrix-vector product is employed by the MLFMA to calculate memory usage. As a result, the usual approach involves additional processes, which increases system complexity. The resulting slope is nonlinear. The suggested approach applies the Garlinken's function, which is independent. This function needs fewer steps to achieve solution convergence. As a result, the system's complexity becomes linear, as seen in Fig. 14. The computational memory is shown in Table 2.

Table 2: Computational memory parameters

| No of Unknowns | Memory (MBs) | No of Adaptive Passes |
|---|---|---|
| 349722 | 30.103 | 1 |
| 428992 | 32.337 | 2 |
| 428992 | 31.200 | 3 |
| 545330 | 42.343 | 4 |

## V. CONCLUSION

In this paper, the electromagnetic interference model of GIS is established. Based on electromagnetic computational theory, the effectiveness analysis of GIS cabling is analyzed. EMI interference and computing parameters are evaluated through the hybrid algorithm. The beauty of the hybrid algorithm is that it speeds up the estimation process due to the explicit nature of Garlinken's function. This reduces the computing time and memory size and, ultimately, the size of the system and cost is reduced because a smaller number of operations is required with comparison to the traditional FMA method. Hence, the system complexity becomes linear. As a result, the computed results validate the algorithm's cogency. The computing results are superior to traditional computing methods.

## ACKNOWLEDGEMENT

This work was supported by the National Natural Science Foundation of China (Grant numbers 62063018, 62463017).

## REFERENCES

[1] E. Kuffel, W. S. Zaengl, and J. Kuffel, *High Voltage Engineering: Fundamentals*. Amsterdam: Elsevier, 2000.

[2] B. Liu, G. Ye, and Y. Tong, "Influence of disconnector in gas insulated switchgear switching on/off on electromagnetic compatibility of electronic transformer," *High Voltage Engineering*, vol. 44, no. 4, pp. 1204-1210, 2018.

[3] S. Bai, L. Zeng, M. Rong, Y. Li, K. Chen, and Y. Zhang, "Interference analysis and protection of electronic current transformer caused by disconnect switch operation in GIS," *High Volt. Appar.*, vol. 52, pp. 54-62, 2016.

[4] M. Rao, M. Mohana, M. Joy Thomas, and B. P. Singh, "Insulated substation model during switching," *Journal of Electrical Engineering and Technology*, vol. 2, no. 3, pp. 306-311, 2007.

[5] M. Rao, M. Mohana, M. Joy Thomas, and B. P. Singh, "Transients induced on control cables and secondary circuit of instrument transformers in a GIS during switching operations," *IEEE Transactions on Power Delivery*, vol. 22, no. 3, pp. 1505-1513, 2007.

[6] T. Yang, L. Huang, J. Wu, J. Huang, K. Xu, Y. Zhu, and X. Wu, "Study on the electromagnetic shielding characteristics of GIS shell," *International Journal of Electrical Energy*, vol. 7, no. 1, pp. 31-35, 2019.

[7] J. Liu, F. P. Dawalibi, and B. F. Majerowicz, "Gas insulated substation grounding system design using the electromagnetic field method," in *2012 China International Conference on Electricity Distribution,* pp. 1-6, 2012.

[8] J. I. Jianfei, W. Lihui, Y. Yubo, and Y. Yifei, "Experimental analysis of EMC immunity for field installed intelligent equipment, of intelligent substation," in *2014 China International Conference on Electricity Distribution (CICED)*, pp. 1556-1564, 2014.

[9] Z. Ma, J. Jasni, M. Z. A. Ab Kadir, N. Azis, J. Xie, and Y. Ma, "Simulation of lightning strikes to 1000 kV UHV-AC double-circuit transmission lines," in *2023 IEEE International Conference on Power Science and Technology (ICPST)*, Kunming, China, pp. 980-985, 2023.

[10] H. Xue, A. Ametani, and J. Mahseredjian, "Very fast transients in a 500 kV gas-insulated substation," *IEEE Transactions on Power Delivery*, vol. 34, no. 2, pp. 627-637, 2018.

[11] A. K. Agrawal, H. J. Price, and S. H. Gurbaxani, "Transient response of multiconductor transmission lines excited by a nonuniform electromagnetic field," *IEEE Transactions on Electromagnetic Compatibility*, vol. 2, pp. 119-129, 1980.

[12] C. R. Paul, *Analysis of Multiconductor Transmission Lines*. Hoboken, NJ: John Wiley and Sons, 2007.

[13] D. Hui and Z. Liang, "Simulation of electromagnetic interference coupling to a substation secondary cable," in *2010 Asia-Pacific International Symposium on Electromagnetic Compatibility*, 2010.

[14] M. Yamamura, Y. Kami, K. Murano, and F. Xiao, "Analysis of transmission characteristics for twisted pair cables using the RLGC parameters of the cable," in *2015 Asia-Pacific Symposium on Electromagnetic Compatibility (APEMC)*, Taipei, Taiwan, pp. 720-723, 2015.

[15] D. Acatauassu, S. Höst, Chenguang Lu, M. Berg, A. Klautau, and P. O. Börjesson, "Simple and causal twisted-pair channel models for G.fast systems," in *2013 IEEE Global Communications Conference (GLOBECOM)*, Atlanta, GA, pp. 2834-2839, 2013.

[16] Y. Yan, L. Meng, X. Liu, T. Jiang, J. Chen, and G. Zhang, "An FDTD method for the transient terminal response of twisted-wire pairs illuminated by an external electromagnetic field," *IEEE Transactions on Electromagnetic Compatibility*, vol. 60, no. 2, pp. 435-443, Apr. 2018.

[17] Y. X. Sun, Q. Li, W. H. Yu, H. Jiang, and Q. K. Zhuo, "Study on crosstalk between space transient interference microstrip lines using finite difference time domain method," *The Applied Computational Electromagnetics Society Journal (ACES)*, vol. 30, no. 8, pp. 891-897, 2015.

[18] D. A. Weston, *Electromagnetic Compatibility: Methods, Analysis, Circuits, and Measurement*. Boca Raton: CRC Press, 2016.

[19] W. Xin, G. Zhang, W. Yuan, J. Wu, and Y. Geng, "Calculation of transient electromagnetic fields generated during switching operation in power substation by the method of moment and superposition principle," in *2013 2nd International Conference on Electric Power Equipment - Switching Technology (ICEPE-ST)*, Matsue, Japan, pp. 1-4, 2013.

[20] T. Lu, X. Cui, M. Ianoz, and D. Tabara, "Prediction of switching transient electromagnetic fields in gas-insulated substations," in *2002 3rd International Symposium on Electromagnetic Compatibility*, Beijing, China, pp. 182-185, 2002.

[21] Y. Yan, L. Meng, X. Liu, T. Jiang, J. Chen, and G. Zhang, "An FDTD method for the transient terminal response of twisted-wire pairs illuminated by an external electromagnetic field," *IEEE Transactions on Electromagnetic Compatibility*, vol. 60, no. 2, pp. 435-443, Apr. 2018.

[22] Q. Q. Liu, Y. Zhao, C. Huang, W. Yan, and J. M. Zhou, "A new method for stranded cable crosstalk estimation based on BAS-BP neural network algorithm combined with FDTD method," *The Applied Computational Electromagnetics Society Journal (ACES),* pp. 135-144, 2020.

[23] X. Pei, W.-W. Ran, and P.-A. Du, "An analytic method of determining a critical cable spacing for acceptable crosstalk," *The Applied Computational Electromagnetics Society Journal (ACES)*, pp. 237-244, 2020.

[24] S. Khan, Y. Zhao, Y. Wei, A. Mueed, Z. Ullah, and A. Khan, "Simulation of high frequency twisted pair cable using DDM-FEM hybrid algorithm," *The Applied Computational Electromagnetics Society Journal (ACES),* pp. 109-116, 2022.

[25] W. Yu, Z. Huang, S. Pan, J. Yan, K. Fu, B. Li, and Y. He, "Finite element analysis-based impedance calculation of GIS station horizontal pipeline considering magnetization curve," in *International Conference on Wireless Power Transfer*, Singapore, pp. 493-501, 2023.

[26] J. Barnes and P. Hut, "A hierarchical *O (N log N)* force-calculation algorithm," *Nature*, vol. 324, pp. 446-449, 1986.

[27] C. R. Anderson, "An implementation of the fast multipole method without multipoles," *SIAM Journal on Scientific and Statistical Computing*, vol. 13, no. 4, pp. 923-947, 1992.

[28] R. Coifman, V. Rokhlin, and S. Wandzura, "The fast multipole method for the wave equation: a pedestrian prescription," *IEEE Antennas and Propagation Magazine*, vol. 35, no. 3, pp. 7-12, June 1993.

[29] S. Velamparambil and W. C. Chew, "Analysis and performance of a distributed memory multilevel fast multipole algorithm," *IEEE Transactions on Antennas and Propagation*, vol. 53, no. 8, pp. 2719-2727, Aug. 2005.

[30] L. Yin and W. Hong, "A fast algorithm based on the domain decomposition method for scattering analysis of electrically large objects," *Radio Science*, vol. 37, no. 1, pp. 1-9, Jan. 2002.

**Weiqiang Tang** was born in Wuzhou, China. He received the B.S. degree in Automation from Lanzhou University of Technology, Lanzhou, China, in 2003; the M.S. degree in Control Theory and Control Engineering from Lanzhou University of Technology, Lanzhou, China, in 2008; and the D.S. degree in Control Science and Engineering from Xi'an Jiaotong University, Xi'an, China, in 2012. His research interests include advanced control theory and its application and robust control.

**Abdul Mueed** was born in Bhakkar, Pakistan. He received the master's degree in electrical engineering from the University of Engineering and Technology, Taxila, Pakistan, in 2015. From 2009 to 2017, he worked as a Lecturer in Electrical Engineering at the Dr. A. Q. Khan Institute of Technology, Mianwali, Pakistan. He is currently working as a Research Scholar at Lanzhou University of Technology, Lanzhou, China. His primary research interests include electromagnetic compatibility problems, computational electromagnetics, power system transients, EMC related application in biomedical engineering, and application of artificial intelligent in EMC.

**Rui Ma** was born in Gansu, China. He received the master's degree in control theory and engineering from Lanzhou University of Technology, Lanzhou, China, in 2024. He is currently studying for his Ph.D. at Lanzhou University of Technology, majoring in pattern recognition and intelligent systems. His main research focus are intelligent control and motion control.

**Muhammad Asif** was born in Khyber Pakhtunkhwa, Pakistan. He received his bachelor's degree from University of Science and Technology, Bannu, Pakistan. He has worked as BSS Engineer in ZTE. Currently working in the Education Department Khyber Pakhtunkhwa, Pakistan. His main research is related to electromagnetic computability, controller designing and power converters, and control systems.

# Integral Sliding Mode Control with Exponential Approximation Law for an AMB Rotor System Considering the Alford Force

**Siyuan Zhang[1] and Jin Zhou[2]**

[1]Department of Marine and Electrical Engineering
Jiangsu Maritime Institute, Nanjing 210000, China
zhangsiyuan@nuaa.edu.cn

[2]Department of Mechanical and Electrical Engineering
Nanjing University of Aeronautics and Astronautics, Nanjing 210000, China
zhj@nuaa.edu.cn

***Abstract –*** In order to deal with the nonlinear problems associated with the Alford force and active bearing rotor system in fluid machinery, an integral sliding mode control with exponential reaching law is proposed in this paper. An integral term is incorporated into the switching function, and an exponential approaching law, along with a boundary layer saturation function that replaces the symbolic function, is adopted to suppress the chattering and tracking error of sliding mode control. Simulation and experimental results show that, under the magnetic bearing force and Alford force, the system exhibits improved anti-disturbance performance compared to a PID controller. Moreover, the rotor amplitude is reduced by 33% when using this controller. The proposed controller demonstrates good dynamic performance and strong robustness, even when the parameters of the entire system are perturbed.

***Index Terms –*** Active magnetic bearings, Alford force, Sliding mode control, Vibration control.

## I. INTRODUCTION

An active magnetic bearing (AMB) is widely used in fluid machinery because of its advantages of no mechanical contact, no friction and wear, longer life, high efficiency and active control [1]. Nevertheless, issues during the manufacturing and assembly process can result in relative eccentricity between the impeller and volute. When the magnetic suspension fluid machinery operates at high speeds, a differential pressure is generated in the circumferential direction of the impeller. This differential pressure creates a transverse force acting on the rotor [2], commonly referred to as the Alford force. The Alford force can potentially induce instability in the equipment.

Generally, the rotor cannot remain suspended at the center due to multiple disturbances, which causes the electromagnetic force of the AMB to exhibit strong time-variant and nonlinear characteristics. What's more, the Alford force aggravates the nonlinearity which makes the controller more difficult and complicated. Shata et al. [3] and Anantachaisilp and Lin [4] applied a fractional order PID controller to the magnetic bearing rotor system and optimized the control parameters. The effect of the improved PID controller was verified by comparative experiment. Raafat and Akmeliawati [5] developed a robust H2/H∞ controller for AMB systems by employing adaptive neuro-fuzzy inference systems (ANFIS) for intelligent uncertainty estimation, thereby achieving wide bandwidth and enhanced performance while accurately compensating for modeling errors and nonlinearities Ran et al. adopted H∞ [6] and μ [7] controllers, and their research confirmed that by using these two controllers, rotor vibration was effectively suppressed and successfully passed through the critical speed. Di and Lin [8] applied the all-coefficient adaptive control (ACAC) to control the flexible magnetic bearing rotor and the orbit was smaller than μ. This method did not rely on modeling accuracy, which is simpler to realize compared with H∞ and μ. Guan et al. [9] introduced extended state observer (ESO) into the adaptive controller and used it in magnetic bearing rotor systems. Research showed that the controller can significantly suppress interference in the system.

As a robust controller, sliding mode control (SMC) is suitable for dealing with nonlinear systems and remains insensitive to variations in parameters and external disturbances. In recent years, SMC has been widely used in magnetic bearings. Chen and Lin [10] presented a robust nonsingular terminal sliding mode control. Compared with the conventional sliding mode control with linear sliding surface, it provides faster, finite time convergence, and higher control precision. Huynh and Tran [11] designed a new integral sliding mode control for the

*Submitted On: June 20, 2024*
*Accepted On: October 12, 2024*



https://doi.org/10.13052/2024.ACES.J.390910

3-pole AMB system and demonstrated the efficacy of the proposed method. Rong and Zhou [12] built an adaptive backstepping sliding mode control for a zero-bias current AMB system and the effectiveness was verified by simulation and experiment. Mystkowski [13] dealt with sliding mode nonlinear observers and designed a Lyapunov sliding mode observer for a flux-controlled AMB. The stability and effectiveness of the proposed observer-based feedback were verified by means of numerical simulations. Rahmatullah and Serteller [14] employed SMC for DC motor speed control, investigating its performance and parameter effects in MATLAB/Simulink, and compared its effectiveness with Fuzzy Logic Control, PID and PI methods.

However, the aforementioned research primarily focuses on internal disturbance within the AMB rotor system, with relatively little attention given to the effects of external disturbance. In this paper, an integral sliding mode control with an exponential approximation law is implemented to solve the Alford force disturbance in magnetic suspension fluid machinery. The switching function is augmented with an integral term, and an exponential approach, along with a boundary layer saturation function, is adopted in place of the symbolic function. This approach suppresses chattering and tracking errors in the sliding mode control, thereby enhancing the system's anti-disturbance performance. Using a five degrees of freedom AMB rotor system rig as the test object, the effectiveness of this controller is demonstrated through comparison with a PID controller.

## II. FUNDAMENTALS

### A. Modeling of the AMB rotor system considering the Alford force

The AMB rotor system is divided into five degrees of freedom in radial and axial directions. The radial AMB offers two translational and two rotational degrees of freedom, while the axial AMB provides one translational degree of freedom. The axial rotational degree of freedom is enabled by the motor. In this paper, modeling analysis and controller design for the AMB rotor system are conducted to validate the effectiveness of the controller. Figure 1 shows the model of an AMB rotor system.

By using Newton's law and ignoring the influence of gravity, the dynamic model of a magnetic bearing rotor system can be described as follows:

$$m\ddot{x} = F_{AMB} + F_A + \Delta F, \tag{1}$$

where $\ddot{x}$ is acceleration, $m$ is the mass of the rotor, $F_{AMB}$ is the electromagnetic force and defined in equation (3), $F_A$ is Alford force and defined in equation (4), and $\Delta F$ is various disturbances.

The electromagnetic force of a magnetic bearing is driven by the power amplifier in the form of current difference [1]:

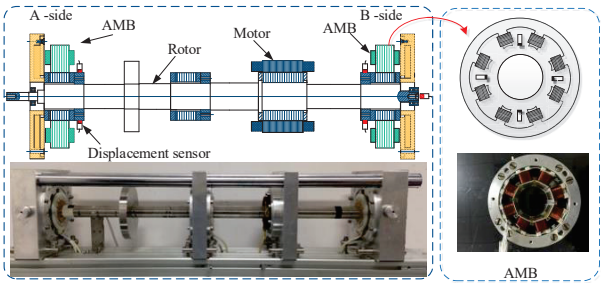


Fig. 1. AMB rotor system.

$$F_{AMB} = f_{x1} - f_{x2} = \frac{\mu_0 A N^2 \cos\alpha}{4} \left[ \left( \frac{i_0 + i_x}{C_0 + x_0 \cos\alpha} \right)^2 - \left( \frac{i_0 - i_x}{C_0 - x_0 \cos\alpha} \right)^2 \right], \tag{2}$$

where the Taylor expansion of the above equation at $i_x = 0$, $x_0 = 0$ and ignoring the higher-order term, the magnetic bearing force on the rotor can be expressed as:

$$F_{AMB} = \frac{\mu_0 A N^2 i_0^2 \cos^2\alpha}{C_0^3} x + \frac{\mu_0 A N^2 i_0 \cos\alpha}{C_0^2} i_x, \tag{3}$$

where $\mu_0$ is vacuum permeability, $A$ is area of a single magnetic pole, $N$ is total number of turns of the coil on a pair of magnetic poles, $C_0$ is unilateral air gap when the rotor is at the magnetic center, $i_0$ is coil bias current, $i_x$ is coil control current, $x_0$ is rotor displacement, $k_h$ is displacement stiffness coefficient, $x$ is displacement signal, and $k_i$ is current stiffness coefficient.

The Alford force model can be expressed as [15]:

$$F_A = A_1 \cdot e + A_3 \cdot e^3, \tag{4}$$

$$A_1 = \left(R_T{}^2 - R_B{}^2\right)^2 \pi C R_T / \left(R_T{}^2 - R_B{}^2 + 2R_T\overline{\delta}\right)^2, \tag{5}$$

$$A_3 = 3\left(R_T{}^2 - R_B{}^2\right)^2 \pi C R_T{}^3 / \left(R_T{}^2 - R_B{}^2 + 2R_T\overline{\delta}\right)^4, \tag{6}$$

$$C = V^2 \sin\beta_1 \rho_0 \left(\cos\beta_1 + \zeta\cos\beta_2\right), \tag{7}$$

where $e$ is eccentricity, $R_T$ is tip radius, $R_B$ is root radius, $\beta_1$ is inlet angle, $\beta_2$ is outlet angle, $\rho_0$ is airflow density, $\zeta$ is speed coefficient, $\overline{\delta}$ is average tip clearance, and $V$ is inlet speed.

If equation (3) is substituted into equation (1):

$$m\ddot{x} = k_h x + k_i i_x + F_A + \Delta F \tag{8}$$

then, according to the state-space representation of the system, equation (9) is obtained as follows:

$$\dot{x} = Ax + Bu + CF_A + D\Delta F \tag{9}$$

where $A = \begin{bmatrix} 0 & 1 \\ \frac{k_h}{m} & 0 \end{bmatrix}$, $B = \begin{bmatrix} 0 \\ \frac{k_i}{m} \end{bmatrix}$, $C = \begin{bmatrix} 0 \\ \frac{1}{m} \end{bmatrix}$, $D = \begin{bmatrix} 0 \\ \frac{1}{m} \end{bmatrix}$, $x = \begin{bmatrix} x \\ \dot{x} \end{bmatrix}$, $u = [i_x]$.

The block diagram of an AMB rotor system considering the Alford force is shown in Fig. 2. In the AMB rotor system, significant nonlinear perturbations arise from a variety of disturbances. This paper presents the design of a sliding mode controller equipped with an exponential approach law, which can still maintain the characteristics of low overshoot, rapid response, and strong robustness in the case of multi-source external disturbances.

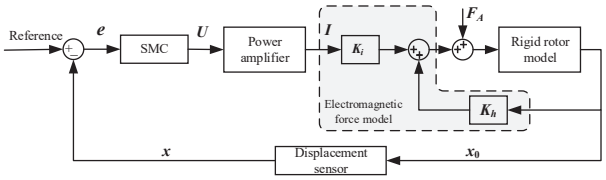


Fig. 2. AMB rotor system considering the Alford force.

### B. SMC design for an AMB system

Exponential reaching law sliding mode control can guarantee the quality of sliding mode control and weaken chattering to a certain extent [16]. Guo and Bo [17] proposed a new exponential reaching law based on the traditional exponential reaching law, enhancing the robustness of the control system. Wang et al. [18] designed a new variable exponential reaching law, introducing system state variables into the constant velocity term, which accelerates the reaching speed while reducing the system chattering, but the overshoot issue was not resolved. Wang et al. [19] introduced a weighted integral term based on the variable exponential reaching law, eliminating the system overshoot.

Based on the above analysis, an exponential reaching integral sliding mode control method will be utilized to design the controller, including the design of the sliding surface function and the control law for the sliding mode reaching phase, and further analysis of the system's robustness will be conducted.

(1) Controller design

According to the control objectives of the system, the sliding mode switching function is designed as follows:

$$s(t) = ce(t) + \dot{e}(t) \tag{10}$$

where $c$ must satisfy the Hurwitz condition, meaning that $c>0$, and its numerical value determines the exponential convergence rate of the error.

To enhance the tracking performance of the control system and to eliminate the steady-state error, integral action is incorporated into the sliding mode switching function. Equation (10) can be rewritten as follows:

$$s(t) = ce(t) + \dot{e}(t) + c_i \int_0^{\infty} e(t)dt \tag{11}$$

where $c_i$ is integral sliding mode gain.

If we define the tracking error $e(t) = x_r - x$ and its derivative $\dot{e}(t)$, where $x_r$ is 0 in the ideal state, then the sliding mode switching function is defined as:

$$\dot{s} = c\dot{e}(t) + (\ddot{x}_r - \ddot{x}) + c_i e(t). \tag{12}$$

Neglecting other external interference factors, substituting this into the preceding equation yields:

$$\dot{s} = c\dot{e}(t) - \frac{k_h x + k_i i_x + F_A}{m} + c_i e(t). \tag{13}$$

Due to the characteristics of the AMB rotor system, the rotor deviates from the equilibrium position when the system boots. To ensure the system reaches the sliding surface without chattering in a short time, an exponential approach law is adopted. The designed exponential approach law is:

$$\dot{s} = -\varepsilon sgn(s) - ks. \tag{14}$$

By combining and simplifying equations (13) and (14), the subsequent equation is derived:

$$u = \frac{m}{k_i}\left[\varepsilon sgn(s) + ks + c_i e(t) + c\dot{e}(t)\right] - \frac{k_h x}{k_i} - \frac{F_A}{k_i}. \tag{15}$$

In practical applications, the use of a symbolic function can result in high-frequency chatter, which may excite additional vibrations within the system, potentially leading to instability. Consequently, it is imperative to mitigate this chatter. In this paper, the saturation function of the boundary layer is used to replace the symbolic function:

$$\text{sat}\left(\frac{s}{\varphi}\right) = \begin{cases} +1, s > \varphi \\ \frac{s}{\varphi}, |s| \le \varphi \\ -1, s < -\varphi \end{cases} \tag{16}$$

where $\varphi$ is boundary layer thickness, which indicates that the trajectory of the system is limited to a neighborhood of $\varphi$ and the larger the value, the smaller the chattering, but it will make the static error larger and the control effect worse.

(2) Stability analysis

Integrating the designed SMC, the robustness of the system is investigated. In accordance with the stability criteria for control systems, the subsequent Lyapunov function is selected:

$$V = \frac{1}{2}s^2. \tag{17}$$

The sufficient condition for ensuring the stability of the system is that the derivative of the Lyapunov function must be less than or equal to zero, which is then substituted into equation (13):

$$\dot{V} = s\dot{s} = s\left(c\dot{e}(t) - \frac{k_h x + k_i i_x + F_A}{m} + c_i e(t)\right). \tag{18}$$

Substitute (12) into (18) and simplify to:

$$\dot{V} = -\varepsilon s sgn\left(\frac{s}{\varphi}\right) - ks^2 \approx -\varepsilon|s| - ks^2. \quad (19)$$

Since the parameters $\varepsilon$, $k$ are positive, when $s \neq 0$, the equal sign applies, and the aforementioned equation remains consistently less than 0, thus satisfying the Lyapunov stability condition. Consequently, the controller is capable of stabilizing the system.

## III. SYSTEM SIMULATION ANALYSIS

In order to test the effect of the SMC proposed in this paper, the controller is verified by Matlab/Simulink. In the simulation, the AMB rotor system parameters are as shown in Table 1.

Table 1: Parameters of an AMB rotor system

| Parameter | Value |
|---|---|
| $m$ (kg) | 14.56 |
| $k_i$ (N/A) | 338.54 |
| $k_h$ (N/μm) | 2.502e6 |
| $R_T$ (mm) | 29 |
| $R_B$ (mm) | 7.5 |
| $\beta_1$ (°) | 25 |
| $\beta_2$ (°) | 30 |
| $V$ (m/s) | 42 |

To facilitate the tuning process, the impact of three parameters on the controller's performance was investigated through the application of a step response. The results are depicted in Fig. 3. As observed from Fig. 3, the rise time of the step response tracking decreases with an increase in $\varepsilon$. Variations in $k$ exhibit minimal influence on the system's behavior. However, as $\varphi$ increases, the overshoot becomes more pronounced, and a certain degree of chattering is observed. The optimized parameters for the improved SMC controller are presented in Table 2.

Table 2: Parameters of SMC

| Parameter | Value |
|---|---|
| $\varepsilon$ | 80 |
| $k$ | 3000 |
| $\varphi$ | 10 |
| $c_i$ | 500 |

Following the controller tuning, its performance was simulated and experimentally validated. The system was accelerated to 100 Hz, and the rotor orbit was subsequently obtained, as depicted in Fig. 4. The figure illustrates that the radial vibration is effectively controlled within 0.02 V by the improved SMC, signifying the controller's robust control performance.

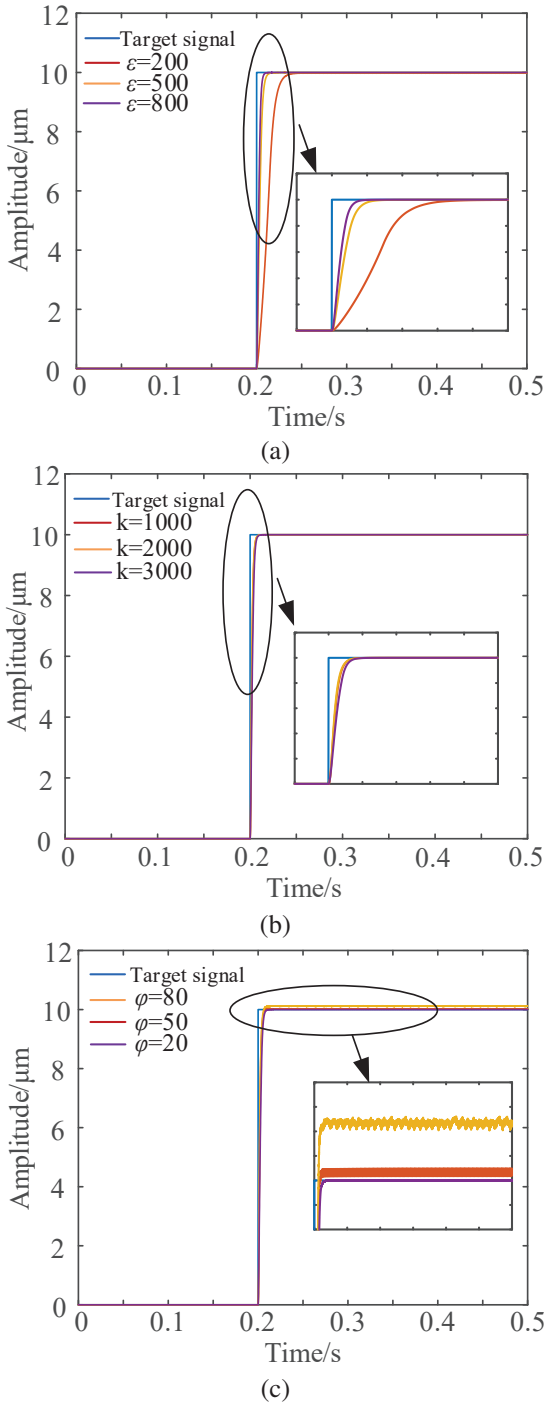


Fig. 3. Influence of different parameters on SMC:(a) influence of parameter $\varepsilon$ on SMC, (b) influence of parameter $k$ on SMC, and (c) influence of parameter $\varphi$ on SMC.

Subsequently, the anti-interference performance of the improved SMC was simulated. The Alford force model was introduced for comparison with the PID controller. The rotor's response to this is presented in

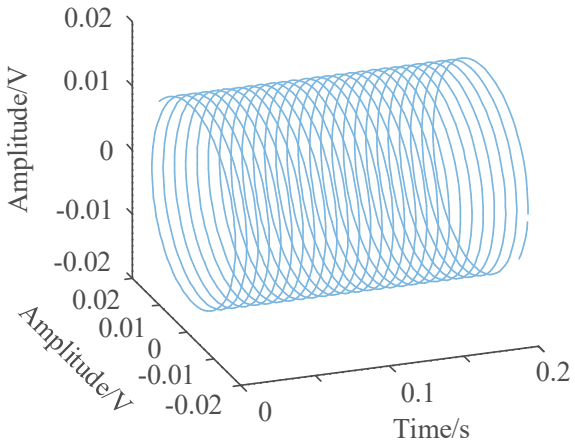


Fig. 4. Rotor orbit under SMC.

Fig. 5. The simulation results indicate that both controllers influence the Alford force, although the improved SMC exhibits a more pronounced effect. In comparison with the PID controller, the amplitude reduction achieved by the enhanced SMC is approximately 25%.

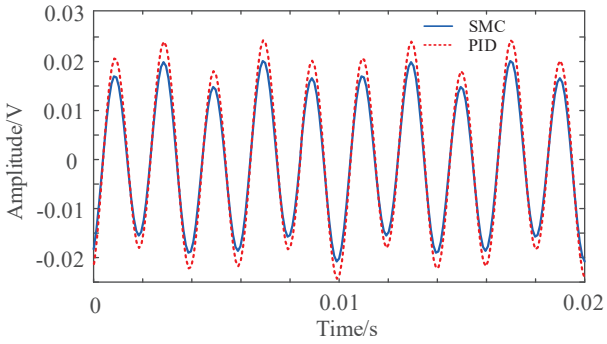


Fig. 5. Comparison of rotor responses of different controllers.

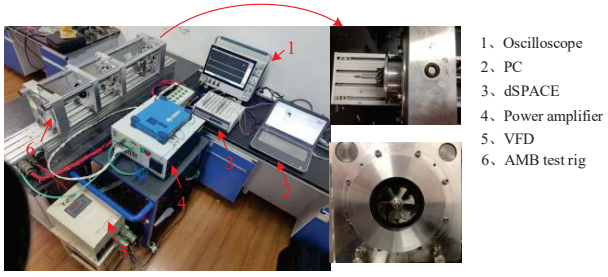


Fig. 6. Experimental equipment.

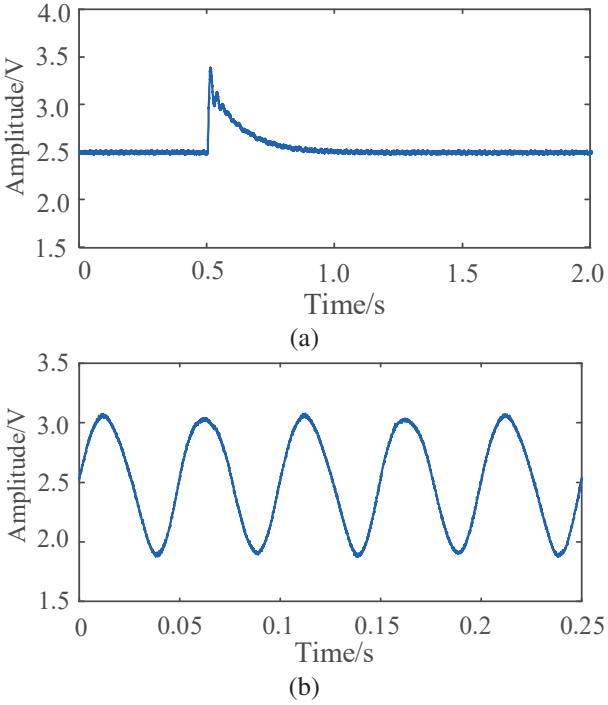


Fig. 7. Rotor response to different disturbances under suspension: (a) step interference and (b) sinusoidal interference.

## IV. EXPERIMENT

To validate the accuracy of the preceding analyses, an AMB test rig was employed for experimental purposes. The experimental apparatus is depicted in Fig. 6.

Initially, step and sinusoidal disturbances were introduced to the rotor while in the suspended state, and the resulting displacement response of the rotor was recorded, as depicted in Fig. 7. The figure clearly indicates that, in the suspended state, the controller exhibits robust performance in the presence of disturbances. The rotor returns to the suspended position within 0.35 s following perturbation by the step signal.

To further substantiate the efficacy of the controller, a rotation experiment was conducted. The rotor's response to the introduction of step and sinusoidal disturbances is illustrated in Fig. 8. The figure reveals that, in the rotating state, the amplitude is reduced compared to that in the suspended state. This discrepancy is attributed to rotor imbalance and external disturbances present in the rotating state, which necessitate a control effort that generates a compensation quantity counteracting the interference. As a result, the interference is manifest in the vibration displacement, characterized by a quicker response and reduced vibration amplitude.

Finally, the AMB test rig was utilized to simulate the Alford force and to compare the suppression effects of the PID and SMC controllers. The rotor orbit at 100 Hz under the influence of both controllers is depicted in Fig. 9. As shown in Fig. 9 (a), due to the Alford force and flow field effects, the rotor orbit at the impeller side is larger than that at the non-impeller side. Furthermore,

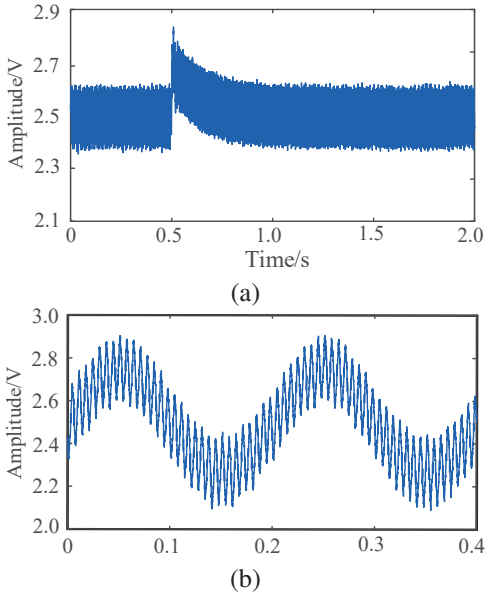


Fig. 8. Rotor response to different disturbances under rotating: (a) step interference and (b) sinusoidal interference.

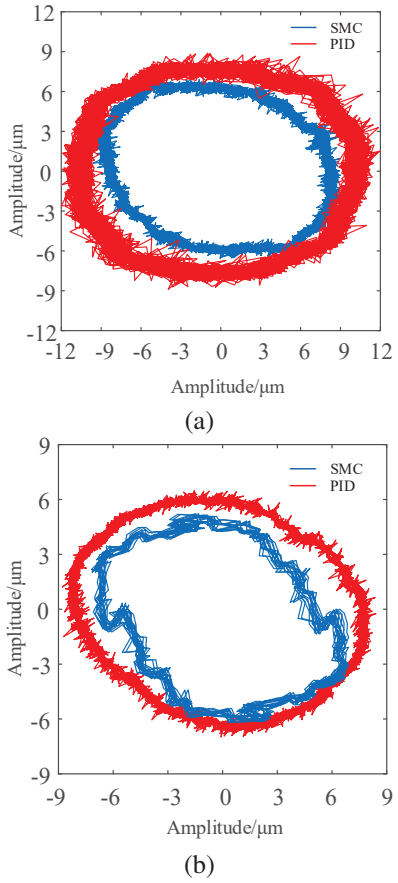


Fig. 9. Comparison of rotor orbit of different controllers considering the Alford force: (a) impeller side and (b) non-impeller side.

the SMC controller outperforms the PID controller, as indicated by a 33% decrease in the rotor orbit amplitude shown in Fig. 9 (b). This demonstrates the superiority and reliability of the designed SMC controller.

## V. CONCLUSION

A model of a magnetic bearing rotor system considering the Alford force is established in this paper. On this foundation, an integral sliding mode control with exponential approximation law is designed to solve the system nonlinear and chattering. Moreover, a stability analysis of the system is carried out. Experimental results show that the proposed controller can effectively mitigate chattering and exhibits robust anti-interference ability. It is noteworthy that the rotor orbit at the impeller side is reduced by 33% under the controller presented here, when compared to the performance of the PID controller, highlighting the superiority and significance of this approach for the AMB rotor system.

## REFERENCES

[1] G. Schweitzer and E. Maslen, *Magnetic Bearing: Theory, Design, and Application to Rotating Machinery*. Berlin: Springer, 2009.

[2] J. S. Alford, "Protecting turbomachinery from self-excited whirl," *Journal of Engineering for Power*, vol. 87, pp. 333-343, 1965.

[3] A. Shata, R. Hamdy, and A. Abdel-Khalik, "A particle swarm optimization for optimum design of fractional order PID controller in active magnetic bearing systems," *IEEE MEPCON*, 2016.

[4] P. Anantachaisilp and Z. Lin, "Fractional order PID control of rotor suspension by active magnetic bearings," *Actuators*, vol. 6, no. 1, 2017.

[5] S. M. Raafat and R. Akmeliawati, "Intelligent H2/H∞ robust control of an active magnetic bearings system," *Al-Khwarizmi Engineering Journal*, vol. 11, no. 2, pp. 1-12, 2015.

[6] S. Ran, Y. Hu, and H. Wu, "Design, modeling, and robust control of the flexible rotor to pass the first bending critical speed with active magnetic bearing," *Advances in Mechanical Engineering*, vol. 10, no. 2, pp. 1-13, 2018.

[7] S. Ran, Y. Hu, H. Wu, and X. Cheng, "Resonance vibration control for AMB flexible rotor system based on $\mu$-synthesis controller," *Mathematical Problems in Engineering*, pp. 1-16, 2018.

[8] L. Di and Z. Lin, "Control of a flexible rotor active magnetic bearing test rig: A characteristic model based all-coefficient adaptive control approach," *Control Theory and Technology*, vol. 12, pp. 1-12, 2014.

[9] X. Guan, J. Zhou, C. Jin, and Y. Xu, "Disturbance suppression in active magnetic bearings with adaptive control and extended state observer," *Proceed-*

*ings of the Institution of Mechanical Engineers Part I: Journal of Systems and Control Engineering*, vol. 234, no. 2, pp. 272-284, 2020.

[10] S. Y. Chen, and F. J. Lin, "Robust nonsingular terminal sliding-mode control for nonlinear magnetic bearing system," *IEEE Transactions on Control Systems Technology*, vol. 19, no. 3, pp. 636-643, 2011.

[11] V. V. Huynh and M. H. Q. Tran, "Integral sliding mode control approach for 3-pole active magnetic bearing system," *Applied Mechanics & Materials*, vol. 829, pp. 128-132, 2016.

[12] H. Rong and K. Zhou, "Nonlinear zero-bias current control for active magnetic bearing in power magnetically levitated spindle based on adaptive backstepping sliding mode approach," *Proceedings of the Institution of Mechanical Engineers Part C Journal of Mechanical Engineering Science,* 2016.

[13] A. Mystkowski, "Lyapunov sliding mode observers with application for active magnetic bearing operated with zero-bias flux," *Journal of Dynamic Systems Measurement and Control*, vol. 231, no. 20, 2018.

[14] R. Rahmatullah and N. F. O. Serteller, "SMC controller design for DC motor speed control applications and performance comparison with FLC, PID and PI controllers," in *Intelligent Sustainable Systems (Lecture Notes in Networks and Systems)*, vol. 579. Singapore: Springer, 2023.

[15] S. Chai, Y. Zhang, and Q. Qu, "An analysis on the air exciting-vibration force of steam turbine," *Engineering Science*, vol. 3, no. 04, pp. 68-72, 2001.

[16] W. B. Gao, *Theory and Design Method for Variable Sliding Mode Control*. Beijing: Science Press, 1996.

[17] X. D. Guo and D. Bo, "A PMSM sliding mode control system based on a novel exponential reaching law," *Control Engineering of China*, vol. 25, no. 10, pp. 1865-1870, 2018.

[18] A. Wang, X. Jia, and S. Dong, "A new exponential reaching law of sliding mode control to improve performance of permanent magnet synchronous motor," *IEEE Transactions on Magnetics*, vol. 49, no. 5, pp. 2409-2412, 2013.

[19] Q. M. Wang, C. H. Jiang, and M. J. Xie, "Permanent magnet synchronous motor control with composite variable exponent reaching law," *Micromotors*, vol. 54, no. 7, pp. 99-103, 2021.

**Siyuan Zhang** was born in Jiangsu, China, in 1992. He received the Ph.D. degree from the Nanjing University of Aeronautics and Astronautics (NUAA). He has been working in the Jiangsu Maritime Institute (JMI) since 2023. His research interests include magnetic bearings and vibration control.

**Jin Zhou** was born in Jiangsu, China, in 1972. She received the Ph.D. degree in mechanical engineering from the China University of Mining and Technology (CUMT), China, in 2001. From 2012 to 2013, she was a Visiting Scholar in the Rotating Machinery and Control Laboratory (ROMAC) of the University of Virginia. She was the member of Program Committee of the 14th International Symposium on Magnetic Bearings (2014) and the Program Chair of the 16th International Symposium on Magnetic Bearings (2018). She was an elected member of International Advisory Committee for ISMB in 2018. Her research interests include magnetic bearings and vibration control.